

# **Effects of Wall Impingement and Multiple Injection on Mixture Formation and Combustion Processes of Diesel Spray**

(ディーゼル噴霧の混合気形成と燃焼過程に及ぼす壁面衝突と多段噴射の影響)

**by**

**LI Kuichun**

**Dissertation**

Submitted to the Graduate School of Engineering

Hiroshima University

in Partial Fulfillment of the requirements

For the Degree of

Doctor of Engineering

Hiroshima University

September, 2014

## ABSTRACT

The objective of this work is to get a better understanding of the effects of impingement and multiple injection on the mixture formation process, combustion and soot emission characteristics of D.I. Diesel sprays. The experimental study, focusing on the characteristics of impinging Diesel spray flames, was carried out in a high-temperature high-pressure constant volume vessel. A flat wall and a two-dimensional (2-D) piston cavity which has the same shape with small-bore diesel engine were employed to form the impinging spray flame. An ordinary injection pressure range (100-200 MPa) of current Diesel engines was selected. Various impinging distances (30, 40, 50, 60 mm and free) were selected to analyze the effect of impinging distance. Different injection amounts (0.27, 0.89 and 2.97 mg) which represent pilot injection, main injection of light load, and main injection of middle load respectively were used. The ambient gas density of  $16 \text{ kg/m}^3$ , which is representative of a low compression ratio Diesel engine at top dead center, was adopted. A single nozzle hole injector with conventional size (0.133 mm) and a three holes injector with liner arrangement were applied as the test nozzles in this study.

Mie scattering method and laser absorption-scattering (LAS) technique were employed to qualitatively and quantitatively characterize the spray development. The blend fuel of  $\alpha$ -MN and n-tridecane with volumetric percentages of 2.5 and 97.5 respectively was used for LAS technique. The spray evolution characteristics such as spray tip penetration, ambient gas entrainment, evaporation and concentrations of liquid and vapor were paid attentions. The effects of shape of the impinging wall, injection pressure, impinging distance and injection amount were taken into account.

The characteristics of the combustion process of Diesel spray were investigated by adopting a color camera which directly perceived the flame natural luminosity,  $\text{OH}^*$  chemiluminescence recording system, and two-color perometry techniques. The effects of the impinging wall shape, injection pressure, impinging distance and injection amount were also taken into account and the combustion behaviors were related to the previously measured spray mixture characteristics.

In addition, the combustion and soot emission behaviors were investigated in this study. Tiny amount (0.27 mg) and normal amount (2.97 mg) were selected as the pilot (as well as post) and main injections respectively. The effects of the intervals between pilot and main injections and between main and post injections and the pilot injection frequency on combustion and soot formation were taken into account.

# TABLE OF CONTENTS

ABSTRACT .....	i
TABLE OF CONTENTS .....	ii
NOMENCLATURES .....	v
CHAPTER 1 INTRODUCTION.....	1
1.1 BACKGROUND AND MOTIVATIONS.....	1
1.2 OBJECTIVES AND APPROACHES.....	4
1.3 OUTLINES .....	4
1.4 REVIEW OF PREVIOUS WORKS.....	5
1.4.1 Diesel Spray Evolution and Combustion Processes .....	5
1.4.2 Homogeneous Charge Compression Ignition.....	21
1.4.3 Multiple Injection .....	25
1.4.4 Optical Diagnostic Technique for Diesel Spray and Process .....	27
1.5 SUMMARY.....	36
CHAPTER 2 EXPERIMENTAL APPERATUS AND MEASURING METHODS .....	38
2.1 FUEL INJECTION SYSTEM.....	38
2.2 HIGH TEMPERATURE AND HIGH PRESSURE AMBIENT CONDITON ACQUIRING SYSTEM .....	40
2.3 OPTICAL MEASUREMENT TECHNIQUES.....	42
2.3.1 Mie Scattering Method .....	42
2.3.2 OH* Chemiluminescence Recording System .....	43
2.3.3 Natural Luminosity Recording System and Two-Color Pyrometry.....	44
2.3.4 Laser Absorption-Scattering Technique .....	48
2.4 SUMMARY.....	57
CHAPTER 3 EFFECT OF SOOT INCADESENCE ON OH* SINGAL AND THE EFFECT OF SOOT ABSOTPTION AND SCATTERING ON THE PRECISION OF LINE-OF-SIGHT TECHINIQUE ....	58
3.1 INTRODUCTION .....	58
3.2 EXPERIMENTAL CONDITIONS .....	58
3.3 SYNCHRONOUSLY OBSERVE OH* CHEMILUMINESCENCE AND SOOT INCANDESCENCE.....	60

3.4 LIGHT ATTENUATION BY THE SOOT ABSORPTION OR SCATTERING IN THE LIGHT PATH.....	68
3.5 SUMMARY.....	70
CHAPTER 4 A COMPARISON OF DIESEL SPRAY FLAME CHARACTERISTICS OF FREE AND IMPINGING INJECTIONS.....	72
4.1 INTRODUCTION.....	72
4.2 EXPERIMENTAL CONDITIONAL.....	72
4.3 MIXTURE FORMATION.....	73
4.3.1 Spray Structure.....	73
4.3.2 Spray Concentration Distribution.....	78
4.4 COMBUSTION FLAME CHARACTERISTICS.....	82
4.4.1. Flame Natural Luminosity and OH* chemiluminescence.....	82
4.4.1 Two-Color Method Results.....	87
4.5 SUMMARY.....	94
CHAPTER 5 CHARATERISTICS OF DIESEL IMPINGING SPRAY FLAME UNDER VARIOUS INJECTION PRESSURES.....	96
5.1 INTRODUCTION.....	96
5.2 EXPERIMENTAL CONDITIONS.....	96
5.3 FLAT WALL IMPINGIGN SPRAY FLAMES CHARACTERISTICS UNDER DIFFERENT INJECTION PRESSURES.....	97
5.3.1 Mixture Formation Process.....	97
5.3.2 Combustion Process.....	102
5.4 SUMMARY.....	106
CHAPTER 6 CHARACTERISTICS OF DIESEL IMPINGING SPRAY FLAME UNDER VARIOUS IMPINGING DISTANCES.....	108
6.1 INTRODUCTION.....	108
6.2 EXPERIMENTAL CONDITIONS.....	108
6.3 MIXTURE FORMATION CHARACTERISTICS.....	109
6.4 COMBUSTION CHARACTERISTICS UNDER DIFFERENT IMPINGING DISSTANCES..	113
6.5 SUMMARY.....	119

CHAPTER 7 CHARACTERISTICS OF DIESEL SPRAY FLAME UNDER VARIOUS INJECTION AMOUNTS .....	121
7.1 INTRODUCTION .....	121
7.2 EXPERIMENTAL CONDITIONS .....	121
7.3 SPRAY STRUCTURE .....	122
7.3.1 Free Spray.....	122
7.3.2 2-D Cavity Impinging Spray.....	129
7.4 VAPOR AND LIQUID PHASE DISTRIBUTION OF EVAPORATING SPRAY .....	131
7.4.1 Free Spray.....	131
7.4.2 2-D Cavity Impinging Spray.....	134
7.5 COMBUSTION PROCESSES .....	136
7.5.1 Free Spray Flame.....	136
7.5.2 2-D Piston Cavity Impinging Spray Flame.....	140
7.6 SUMMERY .....	142
CHAPTER 8 COMBUSTION AND EMISSION CHATACTERISTICS OF MULTIPLE INJECTION SPRAY .....	144
8.1 INTRODUCTION .....	144
8.2 EXPERIMENTAL CONDITIONS .....	144
8.3 FLAME CHARACTERISTICS OF SPRAY WITH PILOT AND POST INJECTIONS.....	146
8.3.1 Combustion Behaviors under Different Intervals.....	146
8.3.2 Combustion Behaviors of Three Times Injections.....	151
8.4 SUMMARY .....	153
CHAPTER 9 CONCLUSIONS .....	154
9.1 MAIN FINDINGS OF THIS STUDY .....	154
9.2 RECOMMENDATIONS FOR FUTURE WORKS .....	159
REFERENCE .....	161
ACKNOWLEDGEMENTS.....	175

## NOMENCLATURES

ASOI	After start of injection
ASOMI	After start of main injection
ASOPostI	After start of post injection
$C_a$	Coefficient of area contraction
$C_v$	Velocity coefficient
$C_n$	Droplet number density
$C_d$	Discharge coefficient
CH	methylidyne
C/R	Low compression ratio
CCD	Charge-coupled device
CH	methylidyne
CO	Carbon monoxide
DME	Dimethyl ether
DMN	Dimethyl naphthalene
ECU	Electronic control unit
EGR	Exhaust gas recirculation
EOI	End of injection
$Eq_a$	Equivalence ratio of liquid
$Eq_v$	Equivalence ratio of vapor
fps	Frames per second
FWHM	Full-width-half-maximum
HC	Hydrocarbon
HCCI	Homogeneous charge compression ignition
HCHO	Formaldehyde
HCPC	Homogenous charge progressive combustion
HiMICS	Homogeneous charge intelligent multiple injection combustion system
$l$	Eddy size
$L$	Nozzle hole length
$L_0$	Lift-off-length
LAS	Laser absorption-scattering

LDA	Laser doppler anemometer
LDV	Laser doppler velocimetry
LIEF	Laser induced exciplex fluorescence
LIF	Laser induced fluorescence
LII	Laser induced incandescence
LRS	Laser rayleigh scattering
LTO	Low temperature oxidation
MK	Modulated kinetics
MULDIC	Multiple stage diesel combustion
NO <sub>x</sub>	Oxides of nitrogen
NTC	Negative temperature coefficient
OH	Hydroxyl
$P_a$	Ambient pressure
PAH	Polycyclic aromatic hydrocarbons
PCCI	Premixed charge compression ignition
PDA	Phase doppler anemometry
PDPA	Phase doppler particle analysis
PIV	Particle image velocimetry
PLIF	Planar laser-induced fluorescence
PM	Particulate matters
PREDIC	Premixed lean diesel combustion
$Q_{ext}$	Extinction efficiency
RoRH	Rate of heat release
S	Spray tip penetration
SCR	Selective catalytic reduction
SMD	Sauter mean diameter
SOI	Start of injection
SRS	Spontaneous Raman Scattering
$t$	Times after start of injection
T	Temperature
$T_a$	Ambient temperature
TDC	Top dead center

$u$	Initial jet velocity
UHC	Unburnt hydrocarbon
UNIBUS	Uniform bulky combustion system
UV	Ultra-violet
VETC	Variable valve timing and valve life electronic control system
VGT	Variable geometry turbo
Vis	Visble
We	Weber number
$\alpha$	Spray cone angle
$\varepsilon$	Molar absorption coefficient
$D$	Nozzle hole diameter
$\lambda$	Wavelength
$\sigma$	Liquid surface tension
$\phi$	Equivalence ratio
$u_{rel}$	Relative velocity between droplets and gas
$x^+$	Characteristic length for the spray
$\varepsilon_\lambda$	Monochromatic emissivity
$\rho_a$	Ambient density (Kg/m <sup>3</sup> )
$\rho_f$	Fuel density
$\tau_i$	Transmittance of neutral filter
$\Delta P$	Difference of injection pressure and the ambient pressure (MPa)
2-D	Two dimensional

# CHAPTER 1 INTRODUCTION

## 1.1 BACKGROUND AND MOTIVATIONS

Diesel engine was first invented by Rudolf Diesel in 1892. During the past more than 120 years, because diesel engine has been continually developed and ceaselessly assembled with the advanced technology, it has become one of the most popular products which has the superior economic efficiency, power performance and dependability, and it is the main power source of vehicle and engineering machinery [Heywood, 1988]. However, diesel engine is facing enormous challenges which are coming from reduction of oil reserves and the more and more stringent exhaust emission regulations.

As we all know that the oil is the nonrenewable resources, while the oil demand had been expanding rapidly with the global developing of industrialization. Figure 1.1 shows the global oil consumption (by region in the reference scenario) from past to future [Matsuo et al., 2013], it reveals that the global oil consumption is gradually increasing. As one of the most common consumption sources, the traditional vehicle will face the situation of little fuel useable in the future. There for, as the most widely used commercial vehicle, diesel engine should enhance fuel economy performance, which can effectively relieve the pressure caused by the shortage of the resources.

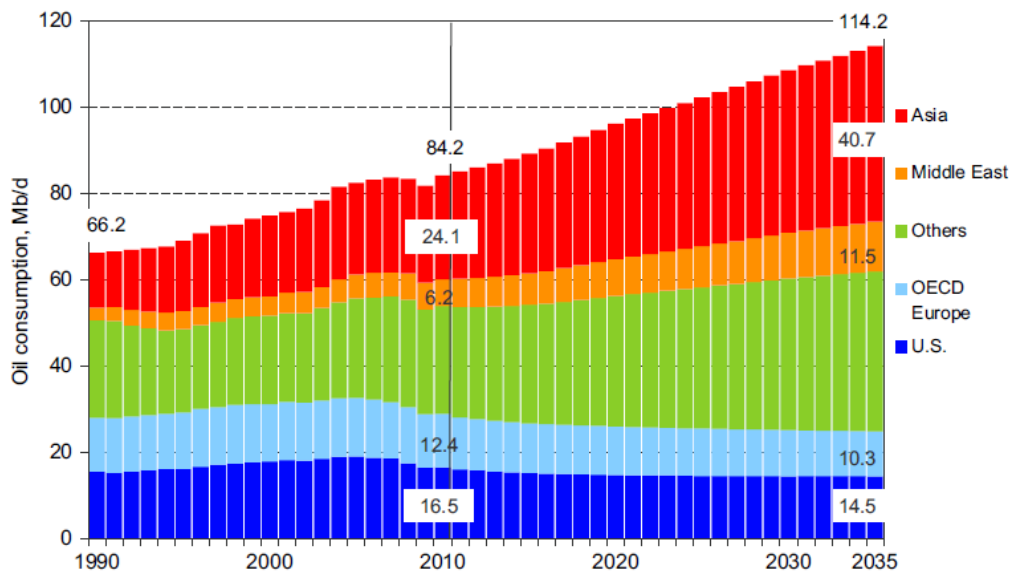


Figure 1.1 Global oil consumption (by region in the reference scenario) [Matsuo et al., 2014].

In recent years, because more and more attentions are paid to environmental protection, emission regulations gradually become stringent. Figure 1.2 exhibits the global emission regulation

of on road diesel engine from past to the future [Endo, 2011]. Thanks to the new techniques such as multi-injection strategy, high pressure common rail injection system, VGT (Variable Geometry Turbo), VETC (Variable Valve Timing and Valve Life Electronic Control System), EGR (Exhaust Gas Recirculation), and SCR (Selective Catalytic Reduction) system et al., the modern diesel engine can satisfy the present emission law. However, compared with gasoline engine, diesel engine still has high NO<sub>x</sub> and soot emissions which can encourage the photochemical smog and PM 2.5 increment respectively, thus the clean diesel engine is pursued persistently by engine researchers.

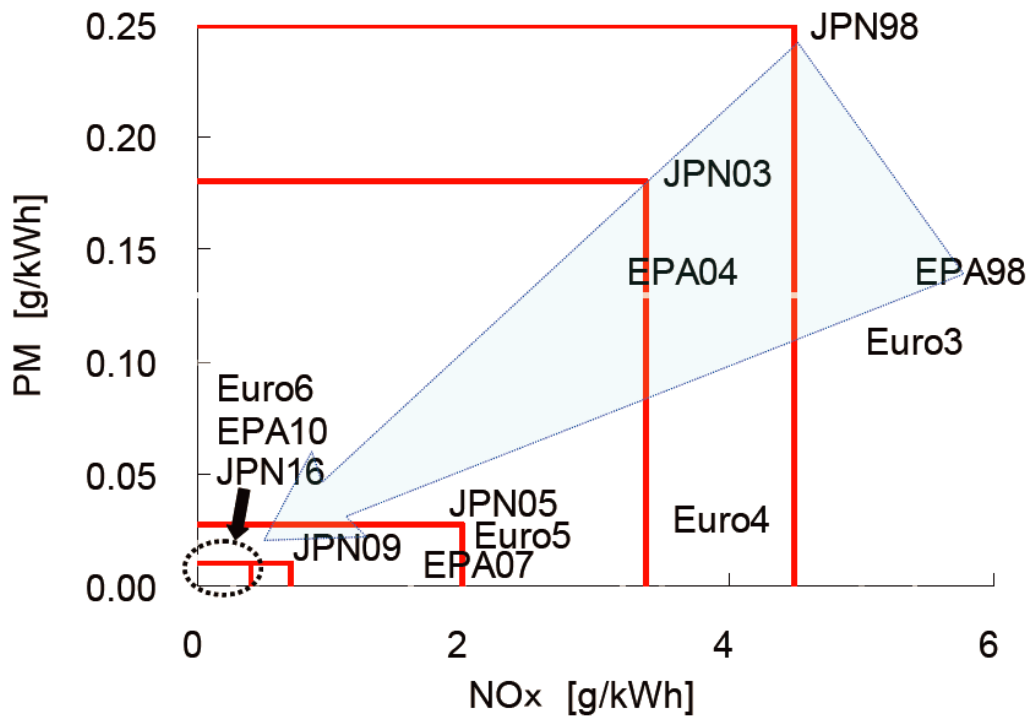


Figure 1.2 Global regulation of NO<sub>x</sub> and PM emissions for on-road diesel engines [Endo, 2011].

As introduced above, the diesel engine accompanied with advanced techniques can achieve satisfied performance, however, without doubt that the engine cost must be forced to raise up. Nowadays, more attentions are still paid to improve diesel engine performance without increasing engine cost too much, but the traditional diesel combustion mode called diffusive combustion has the deficient of that the NO<sub>x</sub> and PM emissions cannot be reduced simultaneously which attributes to the formation mechanisms of NO<sub>x</sub> and PM. Thus the advanced combustion concepts which are thought possible to reduce NO<sub>x</sub> and PM emission simultaneously are proposed such as HCCI (Homogeneous Charge Compression Ignition), PCCI (Premixed Charge Compression Ignition), HCPC (Homogenous Charge Progressive Combustion) et al. These clean diesel engine concepts are based on the same intention which is the homogeneous combustion.

As one of the key factors of the subsequent combustion and emission processes, mixture formation should be improved excellently to realize clean diesel combustion. There were numerous investigations which focused on the optimization of Diesel spray mixture formation, and it is an agreement that increasing injection pressure [Kato et al., 1989; Yokota et al., 1991; Su and Farrell, 1998; Varde and Watanabe, 2000] or applying small orifice injector [Montgomery et al., 1996; Bergstrand and Denbratt, 2001] can improve the mixture quality which contributes to superior combustion behaviors. Eliminating the effect of injection rate, by increasing injection pressure is more effective than decreasing orifice size to improve the combustion behaviors [Wang et al., 2011]. Therefore, the high pressure common rail system is always applied in the commercial diesel engine. In the small-bore diesel engine which is widely used in the passenger car, combined with high injection pressure, avoiding interaction between spray and cylinder wall (or piston cavity) is difficult. It has been proved that the spray/wall interaction has strong influences on mixture formation, combustion and emission processes inside the combustion chamber [Song and Abraham, 2003; Ko and Arai, 2002; Bruneaux, 2005; Pickett and López, 2005]. The effects of spray wall interaction on the mixture formation have become the subject of plenty of research works during the past decades, for simplicity, the flat wall was always selected to form impinging spray. However, the structure of impinging wall is complicated in a real engine and the spray often impinges on the piston crown and then forms impinging spray, the mixture formation and combustion process are different from that of flat wall impinging spray. Thus it is worthwhile to investigate the spray and combustion behaviors using two-dimensional (2-D) piston cavity and forming an engine like impinging spray flame. What's more, under impinging condition, so far most of the researches which were concentrated on the injection pressure effect or impinging distance effect paid significant attentions on the mixture formation process, the combustion characteristics influenced by injection pressure and by impinging distance still need profound understanding.

To realize homogeneous combustion, decreasing compression ratio is thought as one effective way for diesel engine. However, the combustions under cold start process and idle mode are unstable in a low compression ratio diesel engine. As a solving method, the multi-pilot injection strategy is always employed [MacMillan et al., 2009] under the cold start and idle modes. Under multi-pilot injection condition, the pilot injection mass is always selected as tiny to restrain the uncontrollability of ignition timing. Up to present, there is little investigation focused on tiny mass injection spray flame, therefore, the spray behaviors of tiny mass injection is worthwhile to be concentrated on. Meanwhile, the combustion behaviors of spray with pilot injection and with post

injection which enhances soot oxidation [Bobba et al., 2010] are necessary to be observed to provide references for engine design and modeling in the future.

## **1.2 OBJECTIVES AND APPROACHES**

The target of this study is to investigate the D. I. Diesel spray mixture formation and the combustion characteristics in a high pressure high temperature constant volume test rig, the specific objectives of this research are shown as follows:

- 1) Analyze the effects of flat wall and 2-D piston cavity impingements on Diesel spray flame characteristics, compared with the criterion which is defined as the free spray flame.
- 2) Clarify the influence of injection pressure on Diesel spray flame behaviors, especially under impinging conditions.
- 3) Study the spray and combustion features of pilot injection which is characterized by tiny injection amount.
- 4) Observe the Diesel spray flames' characteristics of pilot-main injection and main-post injection. Investigate the effect of pilot injection number and also the effect of interval on combustion.
- 5) Explain the effect of multi-injection strategy on combustion by keeping that the single injection and the couple injections have the same injection amount and the same total injection duration.

In this study, the Mie Scattering technique was applied to obtain the qualitative information of Diesel spray. And the Laser Absorption-Scattering (LAS) technique was adopted to qualitatively and quantitatively analyze the mixture formation process of Diesel spray. The flame features which were estimated from natural luminosity and OH\* chemiluminescence were concentrated on by employing a high speed video color camera and a high speed black/white video camera coupled with an image intensifier system respectively. In addition, Two-Color Pyrometry was used to quantitatively measure the soot concentration and flame temperature.

## **1.3 OUTLINES**

To present this work, the dissertation is organized as follows: a review of previous work such as mixture formation characteristics and combustion concepts of D. I. Diesel spray, multi-injection strategies, and optical diagnostic techniques for spray and combustion is given in Chapter 1. Chapter 2 describes the experimental apparatus such as fuel injection system and constant volume vessel, and the observation techniques adopted in this work such as LAS technique and Two-Color method

will also be introduced. The influence of soot incandescence on OH\* chemiluminescence intensity and the effect soot existence on optical attenuation when applying line-of-sight image recording techniques are shown in Chapter 3. Chapter 4 illuminates the effects of flat wall impingement and 2-D piston cavity impingement on Diesel spray mixture formation, combustion and soot emission by applying LAS, OH\* recording, and Two-Color techniques respectively. Chapter 5 states the atomizing features and combustion characteristics of impinging spray under different injection pressures by analyzing Mie scattering, OH\* chemiluminescence and Two-Color results. The mixture formation and combustion characteristics of tiny injection amount is given in Chapter 6. Chapter 7 shows the combustion behaviors with pilot spray injection and also with post spray injection by describing the natural luminosity KL factor and temperature distributions images. Chapter 8 deals with the combustion process of multi-injection, several injection cases are selected, and the single injection has the same injection amount and the same total injection duration with those of couple injections. Finally, general conclusions on mixture formation and combustion processes of Diesel spray under impingement are summarized in Chapter 9.

## **1.4 REVIEW OF PREVIOUS WORKS**

### **1.4.1 Diesel Spray Evolution and Combustion Processes**

#### **1.4.1.1 Free Spray Flame**

##### **Spray Mixture Formation**

The mixture formation process is undoubtedly thought as one of the most important key factors for the subsequent combustion process. Therefore, it is necessary to deeply understand the spray atomization process which is thought as contribution to improve combustion and emission properties. Even plenty of researches focused on spray atomization were carried out, because of the complexity, it has been a lengthy process before an agreement was researched. Initially, the internal turbulent [DeJuhasz, 1931; Schweitzer, 1937], internal flow cavitation [Bergwerk, 1959], mutation of boundary condition at nozzle exit [Rupe, 1953], and aerodynamic forces [Castleman, 1931] were separately proved to be the determinants for atomization. In recent decades, thanks to the development of optical diagnostics techniques, the fundamental experiments especially the visualization of the spray evolution have made great process. It is found that the each determinant described above cannot individually explain the spray atomization, however, the atomization depends on the combined effect of many factors in which the internal flow cavitation, turbulence instability and aerodynamic forces are paramount [Smallwood and Gülder, 2000; Arcoumanis et al.,

1997]. Therefore, the previous works concentrated on those three paramount factors will be emphatically introduced.

It is believed that the phenomenon of coherent liquid disintegrating into ligaments and large droplets is defined as primary break-up occurs during the internal flow stage even the spray does not come out of the nozzle hole because of the turbulence and cavitation. Usually, the break-up mechanisms of turbulence and cavitation occur simultaneously. Wu et al. [1995] found that even under small aerodynamic condition just like nozzle hole internal flow, the droplets are formed from turbulent eddies when the surface energy is smaller than the kinetic energy of radial fluctuations of the eddy, which is described as follow,

$$C_l(4\pi l^2)\sigma \leq \rho_f v_l^2 (\pi l^3 / 6) / 2 \quad (1.1)$$

Where  $l$  is the eddy size,  $\sigma$  is the liquid surface tension,  $C_l$  is an empirical factor,  $\rho_f$  is the liquid density and  $v_l$  is the radial fluctuation velocity. It is clear that the turbulent effect highly depends on the flow velocity. Meanwhile, when the flow velocity is strong enough, the cavitation occurs, this is because that the liquid phase instantaneously vaporizes when the local static pressure (decreases with velocity increasing) is lower than vapor pressure. Hence a two-phase flow exists inside the nozzle hole after cavitation formed. In Diesel spray, cavitation mainly attributes to the low temperature vaporization of the more volatile components [Whitelaw and Payri, 2000]. Figure 1.3 shows the schematic representation of the different flow regimes for a real-size nozzle [Arcoumanis et al., 2000].

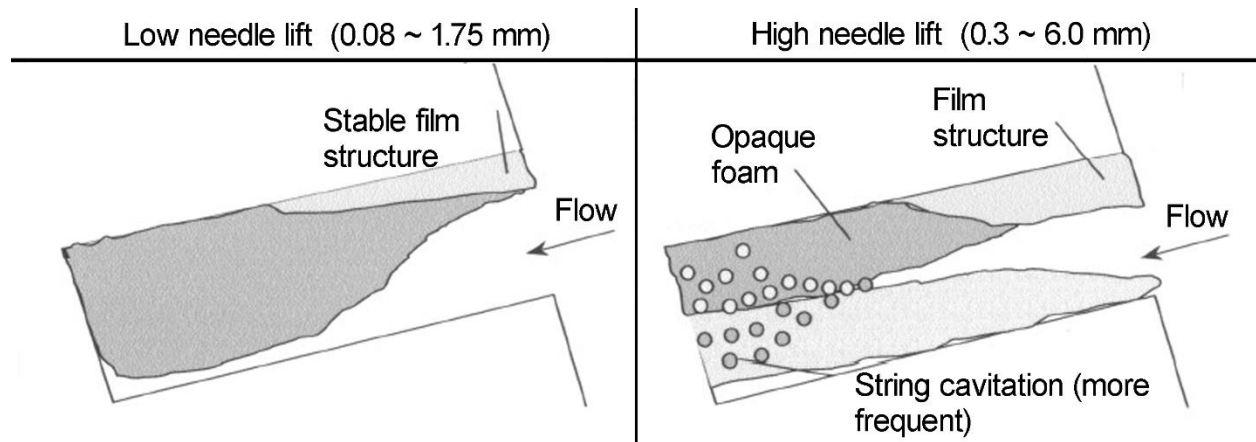


Figure 1.3 Schematic representation of the different flow regimes for a real-size nozzle [Arcoumanis et al., 2000].

To completely comprehend the effect of internal cavitation on the spray atomization behaviors, numerous investigations were carried out by former researchers. And plenty of available theories were developed. It is common accepted that the intensity of cavitation highly depends on the nozzle hole inlet geometry [Schugger and Renz, 2001 and 2003] and as exhibited in Fig 1.3 [Arcoumanis et al., 2000]. The implosions of cavitation bubbles needle lift accelerate the spray disintegration, several studies [Arai et al., 1991; Hiroyasu et al., 1991; Soterious et al., 1995; Tamaki et al., 2001] shown that the nozzle hole cavitation results in spray angle increasing and spray tip penetration decreasing. Until now, it does not reach an agreement whether the cavitation plays a positive or negative role in engine performance. One side, the atomization is enhanced by cavitation, however, the other side, the effective cross-sectional flow area is reduced by cavitation which contributes to deterioration of combustion especially under large amount injection condition. Therefore, the engine researchers persistently spare no effort to find the optimal situation of cavitation when the most excellent engine performance is reached. However, to realize it, there is still a long way to go.

When the spray comes out of the nozzle hole, aerodynamic-induced break-up gradually plays a role in mixture formation. Studies [Hiroyasu et al., 1990 and 1991;] indicate that the coherent liquid does not disintegrate into small droplets immediately, there is a region closed to nozzle exit with ligaments and dense large droplets, this process is also included in the primary break-up because the internal turbulence and cavitation still play a more decisive effect than aerodynamic forces on fuel disintegration in this process. And the axial length of the external break-up region could be calculated by applying Equation 1.2 which is given by Hiroyasu and Arai [1990].

$$L_b = 7 \cdot D \cdot (1 + 0.4 \frac{r}{D}) \cdot \left(\frac{P_a}{\rho_l u^2}\right)^{0.05} \cdot \left(\frac{L}{D}\right)^{0.13} \cdot \left(\frac{\rho_l}{\rho_a}\right)^{0.5} \quad (1.2)$$

Where  $L$  and  $D$  are the length and diameter of the nozzle hole respectively,  $r$  is the radius of the nozzle hole inlet,  $u$  is the initial jet velocity,  $P_a$  represents the ambient pressure density and  $\rho_l$  and  $\rho_a$  mean liquid and gas density respectively. When the spray goes beyond this break-up length, aerodynamic force leads to the formation of smaller droplets which is called as secondary break-up. And secondary break-up process highly depends on the ratio of aerodynamic and surface tension which is defined as gas phase Weber number,

$$We_a = (\rho_a \cdot u_{rel}^2 \cdot d) / \sigma \quad (1.3)$$

In which  $d$  means droplet diameter and  $u_{rel}$  is the relative velocity between droplets and gas. It is well known that different break-up models exist according to different Weber numbers. Pilch and Erdman [1987] investigated the partition of break-up regimes on the basis of Weber number as

shown in Fig 1.4. In engine sprays, all of those break-up mechanisms occur. The disintegration process contributed by high Weber number takes place in upstream region, correspondingly, the break-up process resulted from low Weber number arises in the downstream region.

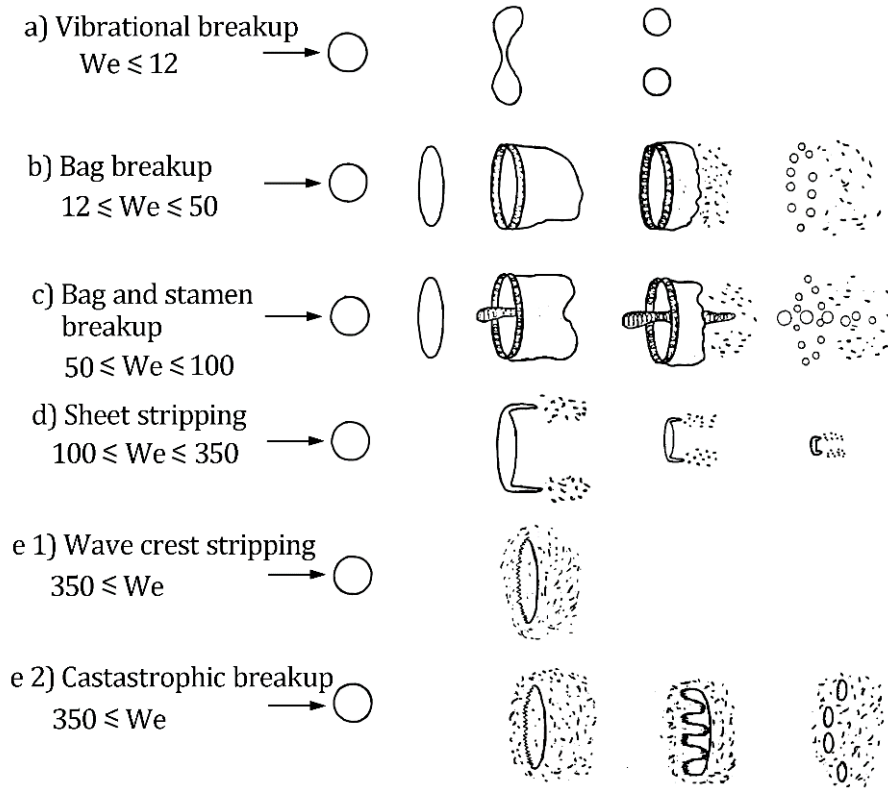


Figure 1.4 Drop break-up regimes [Pilch and Erdman, 1987].

Compared with the investigation of microscopic characteristics of spray, the experiment of macroscopic characteristics of spray is easier to taken place. The most accepted macroscopic characteristics of spray are spray penetration and spray cone angle. Figure 1.5 exhibits a schematic representation of traditional Diesel spray propagation and the definitions of spray tip penetration and spray cone angel [Baumgarten, 2006].

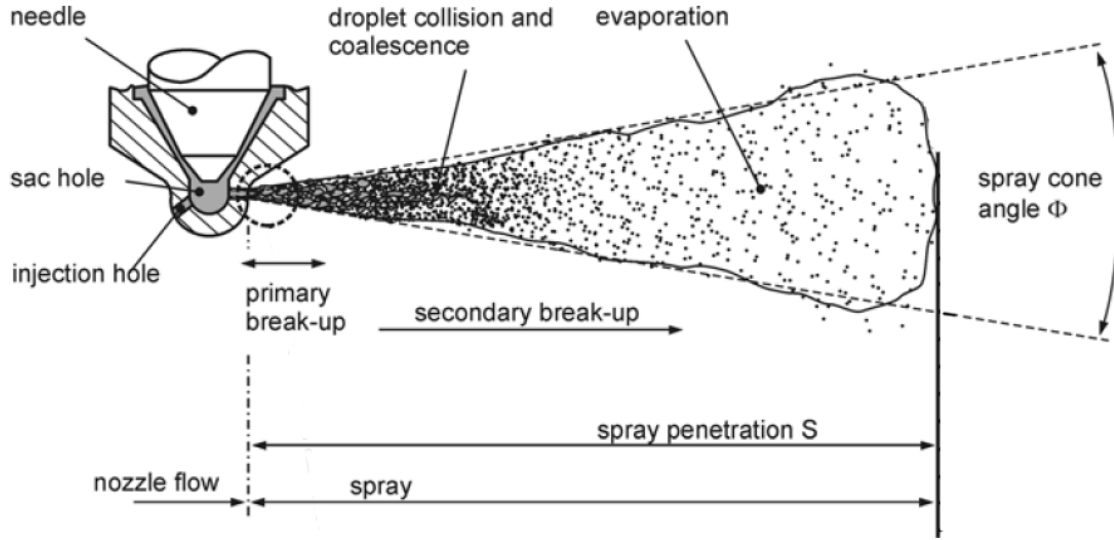


Figure 1.5 Schematic representation of spray propagation [Baumgarten, 2006].

Spray tip penetration and spray angle play significant role on ambient gas utility and the mixture formation rate. For Diesel spray, overlong spray tip penetration results in high hydrocarbon (HC) and carbon monoxide (CO) emissions, low fuel economy, and consumption of lubricant because wall wetting effect. However, on the contrary, the utilization of chamber gas will be deteriorated attributed to short spray tip penetration. During the past several decades, plenty of researches which paid attention to study semi-empirical relations about spray cone angle and spray tip penetration as a function of the boundary conditions have been carried out by different researchers. Based on the fuel mass balance and an overall momentum conservation, and also based on the supposition of relative velocity between droplets and air contained in the spray is negligible, Wakuri et al. [1960] developed the spray penetration empirical equation as follow,

$$S = \left(\frac{2C_a \cdot \Delta P}{\rho_a}\right)^{0.25} \cdot \left(\frac{t \cdot D}{\tan(\alpha/2)}\right)^{0.5} \quad (1.4)$$

$C_a$  is the coefficient of area contraction,  $\Delta P$  is the pressure drop at the nozzle exit,  $\alpha$  means the spray cone angle and  $t$  stands for evolution timing.

Dent [1971] took into account of the effect of ambient temperature  $T_a$  on spray tip penetration in a constant volume rig, and concluded that the spray penetration length inversely proportional to the fourth root of ambient temperature as Equation (1.5) shows.

$$S = 3.07 \cdot \left(\frac{\Delta P}{\rho_a}\right)^{0.25} \cdot (t \cdot D)^{0.5} \cdot \left(\frac{294}{T_a}\right)^{0.25} \quad (1.5)$$

Hiroyasu and Arai [1990] divided the time-dependence of the spray penetration length into two phases. The first phase is the spray core without integration because the low needle lift and the low flow mass. And the spray tip penetration is proportional to the evolution timing. During the second phase, the spray consists of droplets. Even the spray still continue penetrate into further destination due to impetus from the latter injected high momentum fuel, the penetrating velocity is decreased, and the penetration length follows a square root function over  $t$ .

$$t < t_{break} : S = 0.39 \cdot \left(\frac{2\Delta P}{\rho_l}\right)^{0.5} \cdot t \quad (1.6)$$

$$t > t_{break} : S = 2.95 \cdot \left(\frac{\Delta P}{\rho_a}\right)^{0.25} \cdot (t \cdot D)^{0.5} \quad (1.7)$$

$$\text{where } t_{break} = \frac{28.65 \cdot \rho_l \cdot D}{(\rho_a \cdot \Delta P)^{0.5}} \quad (1.8)$$

More recently, Naber and Siebers [1996] derived a penetration correlation for non-evaporating spray based on the idealized model proposed by Wakuri et al. [1959] as shown in Fig 1.6 but including significant modifications. Those modifications include estimation for the arbitrary constant that appears in the penetration. Based on the fuel mass balance and overall momentum balance in the axial direction in a control surface, they gave the spray tip penetration as follows:

$$S < S_r : S = C_v \cdot \left(\frac{2\Delta P}{\rho_l}\right)^{0.5} \cdot t \quad (1.9)$$

$$S > S_r : S = \sqrt{\frac{C_v \cdot \sqrt{2C_a}}{\tan(\alpha/2)}} \cdot \left(\frac{\Delta P}{\rho_a}\right)^{0.25} \cdot (t \cdot D)^{0.5} \quad (1.10)$$

$$\text{where } S_r = \frac{\sqrt{C_a \cdot D}}{\tan(\alpha/2)} \cdot \sqrt{\frac{\rho_l}{\rho_a}} \quad (1.11)$$

$C_v$  is the velocity coefficient. It is clear that the equations are similar with the equations (1.6-1.8) proposed by Hiroyasu and Aria, however, Naber and Siebers replaced time-length by physical length in definition of the transition of the spray, and also the flow coefficient was taken into account.

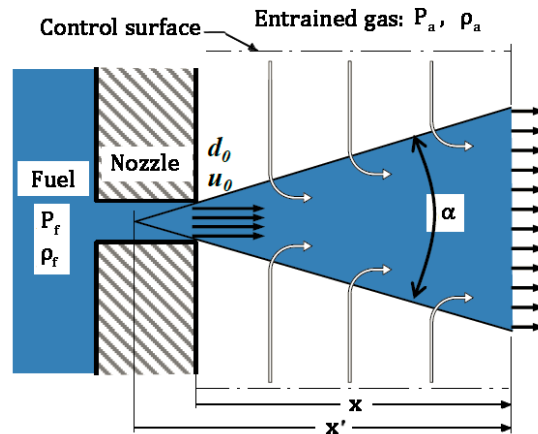


Figure 1.6 Schematic of the idealized model fuel jet [Naber and Siebers, 1996].

As introduced above, the secondary break-up process is mainly induced by aerodynamic forces which have highly dependence on the air entrainment, thus air entrainment was widely investigated. In 1961, Ricou and Spalding proposed an air entrainment coefficient of a turbulent gaseous jet injected into stagnant air at uniform pressure by applying the “porous-wall technique”. Ha et al. [1984] investigated the gas velocity distribution around the spray and the time history using a hot wire anemometer, and announced that the ambient air mainly entrains into the spray through the upstream, while the air is pushed away at the spray tip region. Cossali et al. [1991, 1996] studied the air entrainment in transient Diesel spray adopting Laser Doppler Velocimetry (LDV), one of the observations from those studies was that the entrainment rate during the main injection period is constant, and they also described the surrounding gas flow behaviors and the relationships between the gas entrained rate and ambient gas density and also ambient gas temperature. In recent decades, the development of Particle Image Velocimetry (PIV) technique promotes a further research of mixture formation. Thanks to PIV technique, it is a common acceptance that the surrounding airflow could be divided into three regions based on the flow property [Araneo et al., 1999; Rajalingam and Farrell, 1999; Rhim and Farrell, 2002; Sepret et al., 2010]: the gas is first pushed apart by the spray head front (region 1: head vortex zone), then recirculated along the head side (region 2: gas recirculation zone), finally entrained into the following spray zone (near quasi static zone).

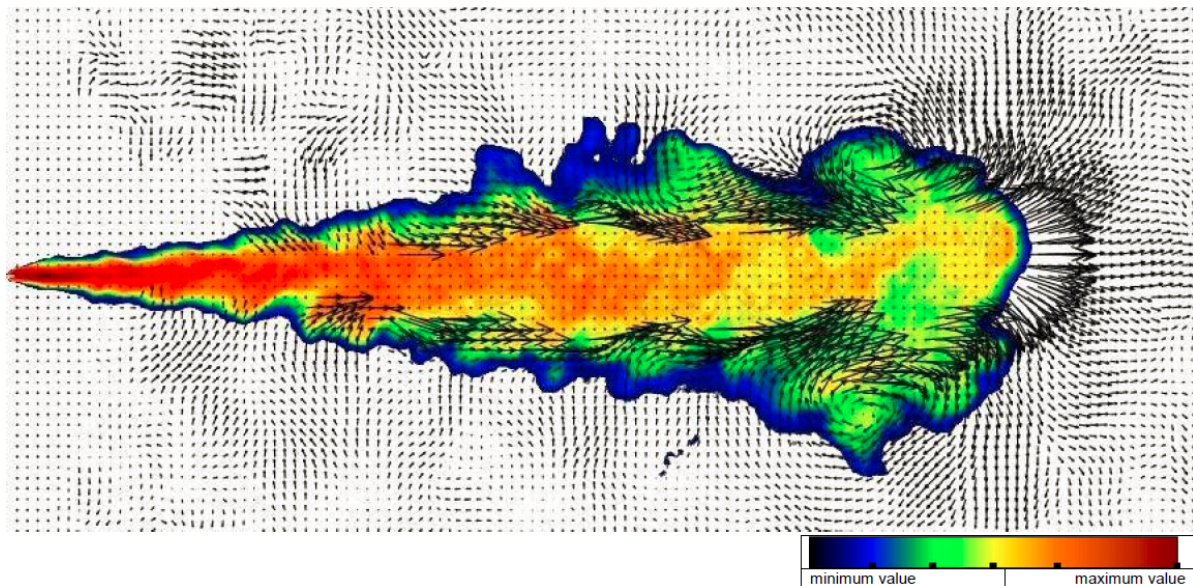


Figure 1.7 Air entrainment and fuel concentration image of Diesel-liked gas spray. Fuel concentration in color scale and flow velocity in black vectors [Bruneaux et al., 2011].

Bruneaux et al. [2011] applied Laser Induced Fluorescence (LIF) and PIV techniques simultaneously and discussed the relationship between air entrainment and fuel concentration, different with former researchers' conclusions, they found that air entrainment in the recirculation zone is also evident as shown in Fig 1.7.

Recently, separate observation of the distributions of vapor and liquid phases of Diesel spray is widely focused on. Schmalzing et al. [1999] applied Shadowgraph and Schlieren Photography technique and found that the liquid phase penetrates much shorter than vapor phase under engine condition. Yeh et al. [1994] described the vapor concentration has function with fluorescence intensity by applying Laser Induced Exciplex Fluorescence (LIEF) technique. Bruneaux [1999] made an investigation on the vapor phase mixing using LIEF and announced that the mixing of the vapor phase is improved by increasing injection pressure and reducing orifice diameter. Quantitative images of fuel vapor concentrations were obtained in an evaporating Diesel spray by using Laser Rayleigh Scattering (LRS) technique by Espey et al., [1997]. Spontaneous Raman Scattering (SRS) technique was also used to obtain air-fuel ratio distribution of Diesel spray, by applying this method, Heinze [1989] and Rabenstein [1998] found that the mixture formation highly depends on the propagation velocities of inner and front spray. Zhang [2001] achieved the equivalence ratio distributions of vapor phase and liquid phase of Diesel-like spray simultaneously by applying Laser Absorption-Scattering technique (LAS) as shown in Fig 1.8, the results revealed that the upstream region is mainly occupied by high equivalence ratio liquid phase and the high equivalence ratio vapor region where the auto-ignition is possible occurred locates at near the spray tip.

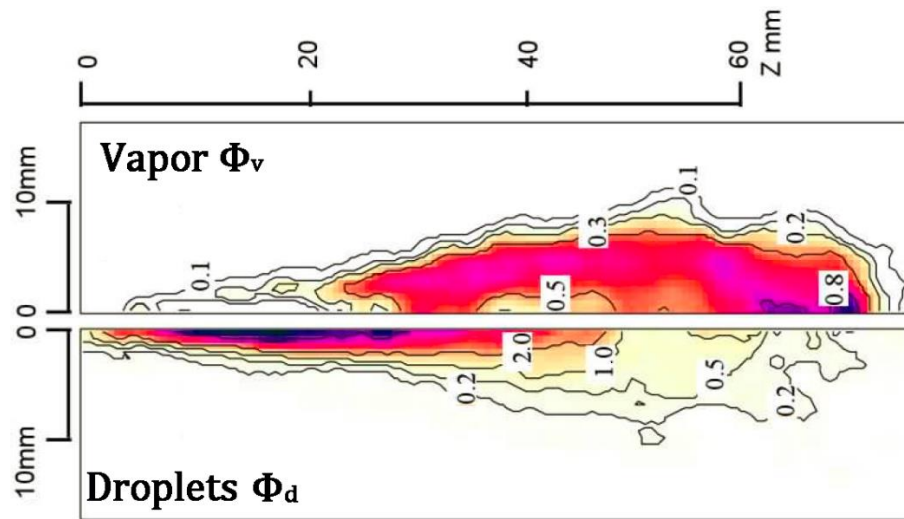


Figure 1.8 Equivalence ratios of vapor and droplets achieve by LAS technique [Zhang,2001].

## Combustion and Emissions

In a D.I. Diesel engine, the combustion process is initiated by auto-ignition which is resulted from the increasing gas pressure during the compression process. Due to the high compression ratio and high calorific value, the temperature and pressure at the compression top dead center (TDC) are ranged in 1000~2000 K and 4~12 MPa respectively [Kaminoto and Kobayashi, 1991]. A typical relationship diagram of heat release, cylinder pressure and fuel injection rate for D.I. Diesel engines is shown in Fig 1.9 [Baumgarten, 2006].

According to Fig 1.9, the combustion process is divided into three phases. The phase 1 is called as premixed combustion, the premixed mixture which is formed during the ignition delay undergoes reaction during this process, and the heat release rate and flame temperature increase quickly. The heat being released during the premixed combustion depends on the premixed mixture formed during the ignition delay. During this process, the flame luminosity mainly comes from chemical radicals which are very weak or even transparent. Following premixed phase, the combustion phase 2 is defined as diffusion combustion. The combustion during the diffusion phase mainly occurs in the periphery region of the spray, and the flame luminosity is much higher because of the soot incandescence. The last combustion phase occurs after the end of injection (EOI), and the soot oxidation rate is higher than production rate in the combustion phase.

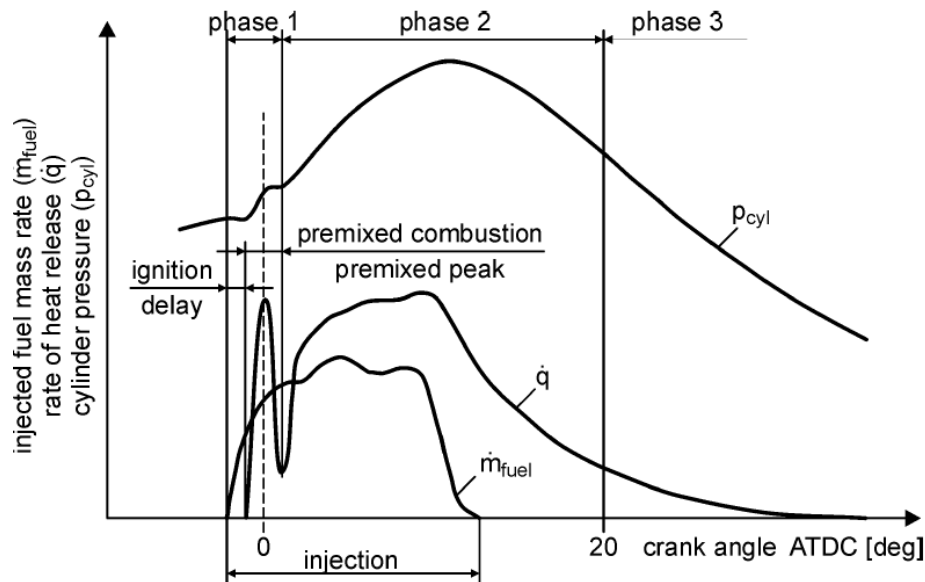


Figure 1.9. Phases of the conventional diesel combustion process [Baumgarten, 2006].

The earliest systematic description of the D.I. Diesel engine combustion concept was summarized by Dec [1997] and Flynn et al., [1999]. They carried out the investigation in an optical

engine by adopting chemiluminescence imaging system to observed auto-ignition, by applying Planar Laser-Induced Fluorescence (PLIF) technique to determine polycyclic aromatic hydrocarbons (PAH) and by using Laser Induced Incandescence (LII) method to measure soot concentration. The results show those: after the fuel injected into the chamber, a sheath of fuel vapor and hot air is formed around the spray and also at the leading edge of the spray; auto-ignition is occurring at multi points nearly simultaneously at the downstream region, the premixed burn mainly occurs volumetrically throughout the cross section of the leading portion of the jet; during the mixing controlled combustion, as shown in Fig 1.10, the injected fuel is heated to 825 K by mixing with entrained hot gas and reactions occur which consume 15% of the total combustion heat, a thin diffusion flame is formed surrounding the burning plume and the rich combustion products (CO, UHC and particles) are completely burnt in this region, the high temperature and high oxygen concentrations at the diffusion flame interface provide an ideal environment for NO<sub>x</sub> formation reactions [Zeldovich, 1946]. In traditional D.I. Diesel engines, it is impossible to both reduce soot and NO<sub>x</sub> emissions simultaneously, this phenomenon is called as soot -NO<sub>x</sub> trade off [Baumgarten, 2006].

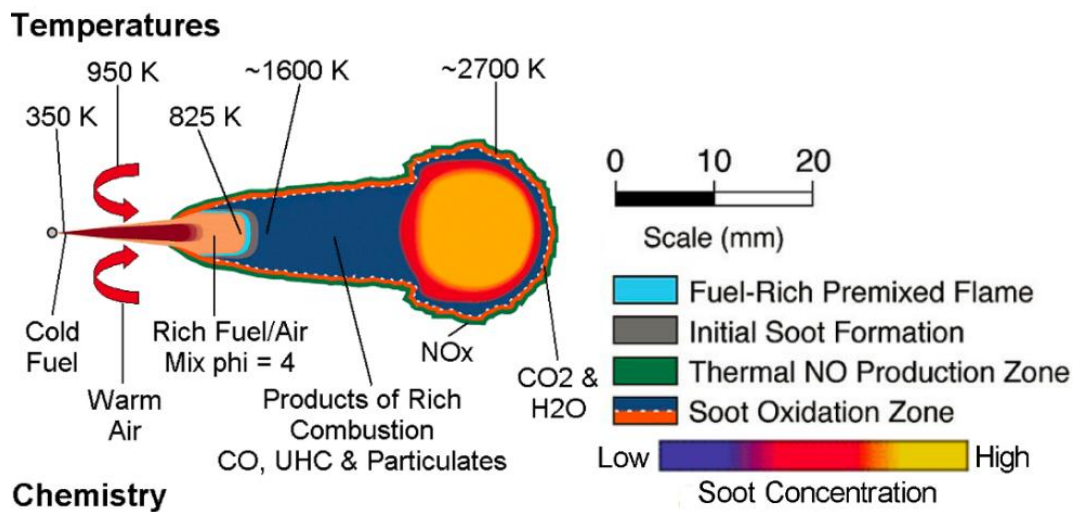


Figure 1.10 Schematic of conceptual model of Diesel spray combustion described by Dec [1997] and Flynn et al., [1999].

In the conceptual combustion model introduced above, the ignition process was detected by applying a line-of-sight technique of chemiluminescence recording which unable to provide spatially resolved information, what's more, the soot formation processes of soot particles from their precursors have not been investigated deeply. Therefore, to make clear ignition process spatially and to make an extensive research on soot formation and oxidation processes, Kosaka et al. [2005] presented a detail combustion model as shown in Fig 1.11. The ignition position is detected by applying formaldehyde (HCHO) LIF method, because the formaldehyde is one of the intermediate

species marking the start of oxidation reactions [Kosaka et al., 2000]. It is found that the auto-ignition region has highly dependence on the ambient gas temperature. As the soot precursor, PAH [Tree and Svensson, 2007] form the hole leading edge of the spray at the start of mixing controlled combustion timing. During the diffusion combustion, PAH and young soot are formed in sequence in the central fuel rich region, and growth during convection to the spray tip, finally, the soot particles are delivered to the upstream side by the head vortex, and oxidized rapidly by the lean side combustion.

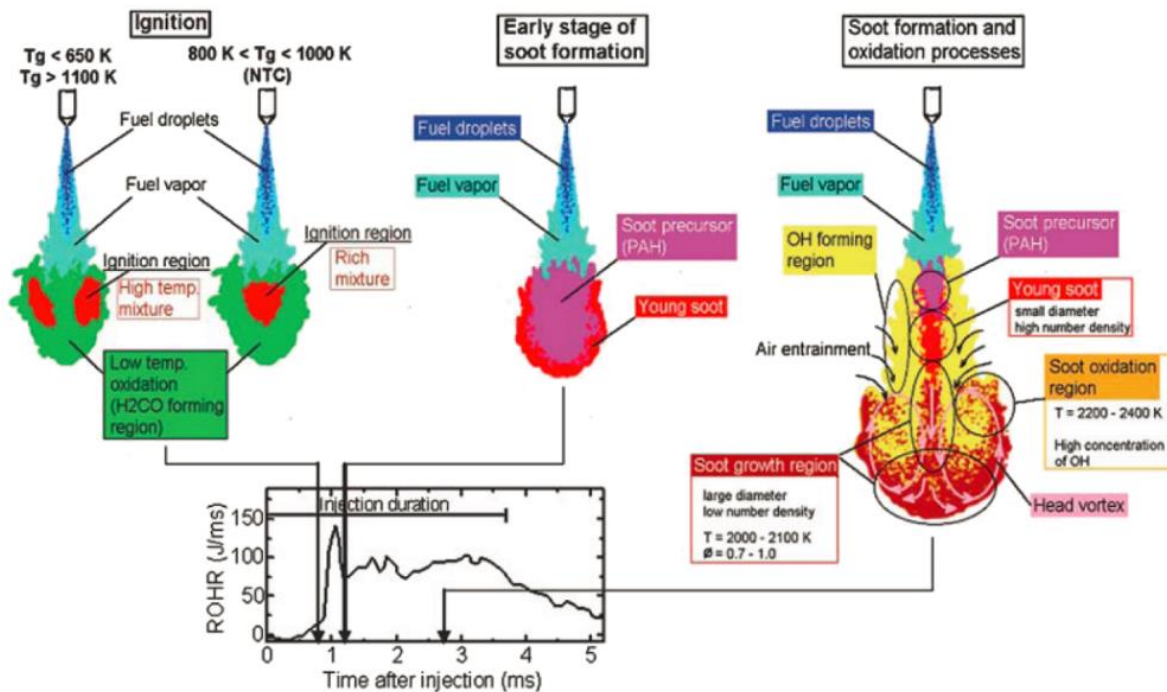


Figure 1.11 Conceptual model of ignition, soot formation, and oxidation process in a diesel spray flame depicted by Kosaka et al [2005].

The latest description of the D.I. Diesel engine combustion model was described by Bruneaux [2008] as shown in Fig 1.12. Compared with the former combustion models, it was paid more attention on the low temperature fuel decomposition and high temperature burnt gases by applying LIF 355 and hydroxide (OH) LIF techniques respectively. It is found that the hot ignition occurs inside the HCHO cloud. At the initial stage of diffusion combustion, the low temperature reaction still occurs in the peripheral region. During the whole mixing controlled combustion process, there is a shell-shaped region of OH between reaction zone of diffusion flame and soot cloud.

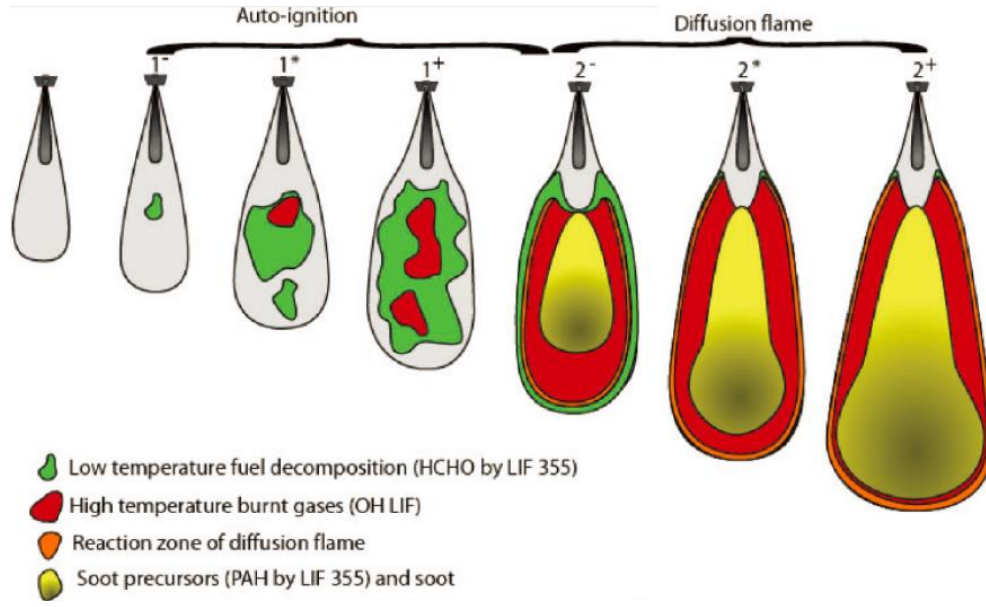


Figure 1.12 Conceptual Diesel spray combustion model developed by Bruneaux [2008].

From all the diesel combustion models, it is evident that there is a distance between nozzle tip and the most upstream stable combustion region during the quasi-steady combustion process. This distance is defined as flame lift-off length [Siebers and Higgins, 2001; Higgins and Siebers, 2001]. The flame lift-off length plays a significant role in combustion and emission processes because the premixing of injected fuel and entrained gas which has important effect on the subsequent combustion occurred just downstream of the lift-off length [Chomiak and Karlsson, 1996] is taken place within this region. The percentage of total air required to burn the fuel being injected which is defined as the percent of stoichiometric air ( $\zeta_{st}$ ) was depicted by Siebers and Higgins [2001] as follow,

$$\zeta_{st}(\%) = \frac{100}{\phi} = \frac{10}{3} \cdot \left( \sqrt{1 + 16 \cdot \left( \frac{L_0}{x^+} \right)^2} - 1 \right) \quad (1.12)$$

$\phi$  is the cross-sectional average equivalence ratio,  $L_0$  is the lift-off-length and  $x^+$  is the characteristic length for the spray, defined by,

$$x^+ = \sqrt{\frac{\rho_l}{\rho_a} \cdot \frac{\sqrt{C_a} \cdot D}{0.66 \cdot \tan(\alpha/2)}} \quad (1.13)$$

Siebers and Higgins [Whitelaw et al., 2000] investigated the relationship of the liquid length and the lift-off length with different injection pressures and orifice diameters as shown in Fig 1.13. It is concluded that the interaction between cold liquid phase and premixed interaction and the ambient gas entrainment through the lift-off length region are weakened and enhanced respectively,

which are thought as the effective methods to reduce soot formation, by either increasing injection pressure or decreasing orifice diameter.

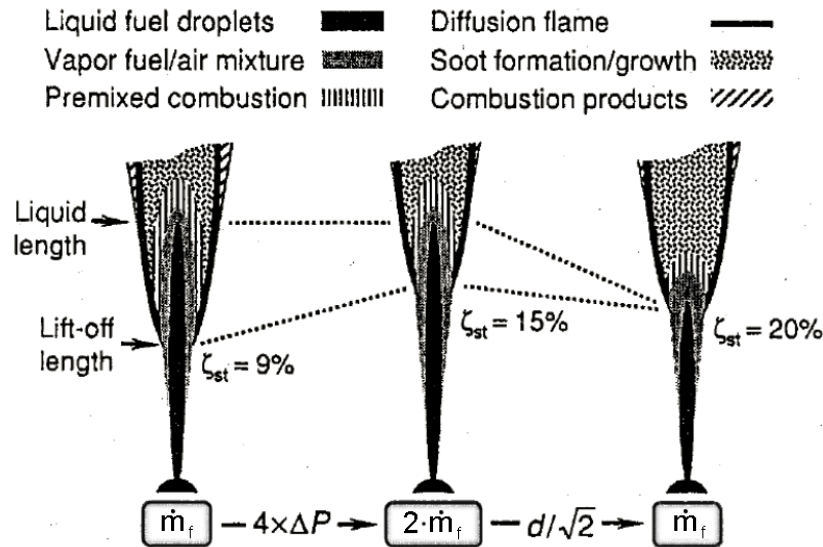


Figure 1.12 Schematic of spatial relationship between various regions in the spray change with injection pressure and orifice diameter described by Siebers and Higgins [Whitelaw et al., 2000].

#### 1.4.1.2 Impinging Spray Flame

##### Spray Mixture Formation

Spray/wall interaction occurs in a small-bore high speed diesel engine, it has been paid wide attention from the automobile engineers. It is found that the impingement between spray and wall has a significant influence on mixture formation, combustion and emission. The atomization processes under impinging condition are much different with those of free spray. The difference comes from two aspects: on the one hand, the impingement between large Weber number droplets and wall contributes to small droplets formation, and the secondary break-up process is improved; on the other hand, the impingement between the low Weber number droplets and wall results in liquid film formation which plays a negative effect on UHC and soot emissions. The schematic of various regimes of a droplet/wall interaction is shown in Fig 1.13 [Bai and Gosman, 1995].

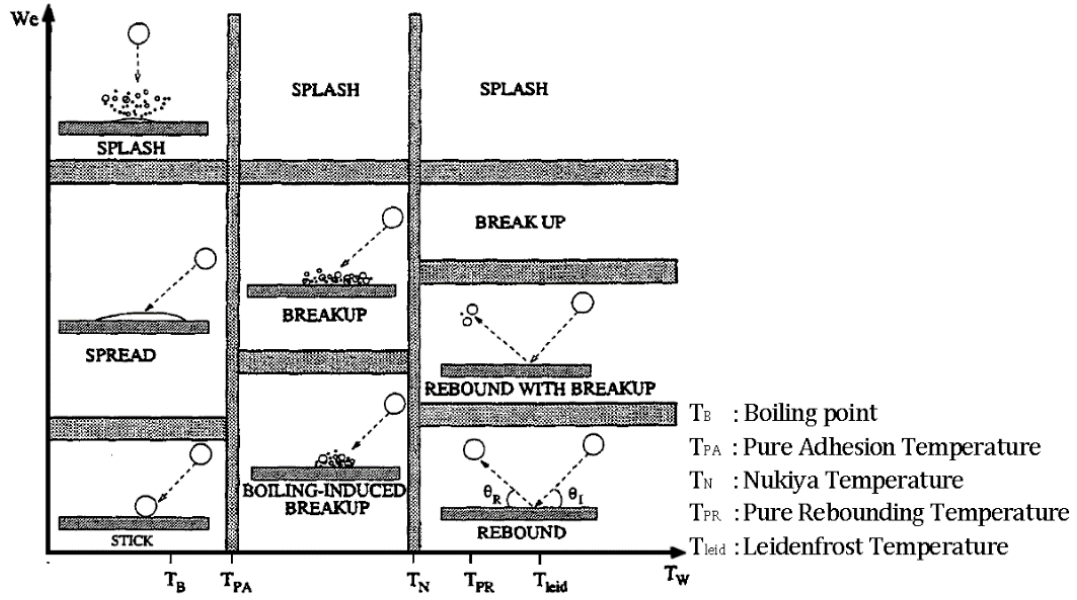


Figure 1.13 Schematic illustration of different impact regimes [Bai and Gosman, 1995].

The impinging Diesel spray under room temperature condition was initially investigated by Fujimoto et al. [1987], after that, Katsura et al. [1990] made a further research on the impinging spray and proposed a typical model for flat wall impinging spray as shown in Fig 1.14. It is observed that the spray flow radially along the surface wall after impingement. A head vortex region is formed in the spray tip region due to the ambient gas resistance. And the vortex rolls up the droplets which results in spray volume enlarging. The droplets density is increased with the measuring point goes nearer the plate. However, droplets concentration in the radial direction is varying according to the spray height, considering the total region, it is dense in the impinging point and head vortex regions.

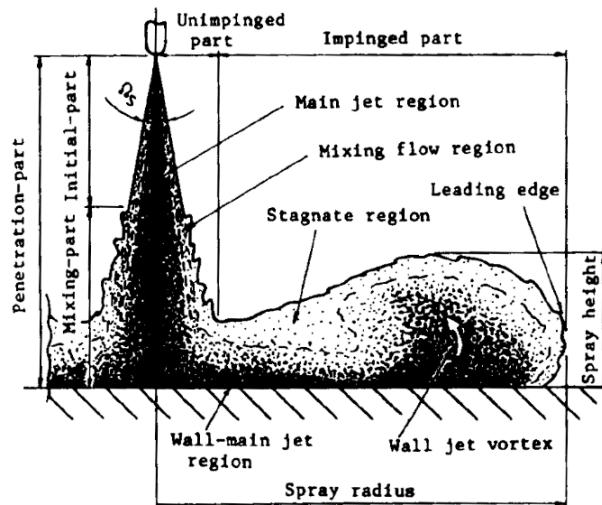


Figure 1.14 Model of a flat wall impinging spray [Katsura et al., 1990].

Senda et al. [1992] and Meingast et al. [2000] extended the impinging spray investigation to the evaporative conditions. It is found that the head vortex enhances the evaporation. The liquid phase is confined within 2 mm height near the wall, and the liquid phase penetration does not grow during the stable injection duration. The influence of wall temperature on mixture formation processes is concentrated on by Arcoumanis and Chang [1994], and they found that as wall temperature increasing, the intensity of wall-jet head vortex is increased, and the droplet size is decreased at the leading edge but increased at the behind the wall-jet head region attributed to the changing of competitive effect of droplet collision and coalescence [Reitz and Diwakar, 1986].

Cossali et al. [1993] studied the air entrainment of impinging spray by using Laser Doppler Anemometry (LDA) and found that the spray/wall interaction plays a role in air entrainment even before impingement occurs. Mohammadi et al. [2002] investigated the ambient air entrained processes in detail by applying Laser Sheet Imaging method. It is concluded that either with increasing injection pressure or with enlarging orifice diameter, the gas entrainment is enhanced under impinging condition. And the gas entrainment is also improved by decreasing impinging distance. Bruneaux et al. [2011] measured the velocity and streamlines of impinging spray, as shown in Fig 1.15, by applying PIV technique. It is concluded that compared with free spray, the impinging spray has more air entrainment in the vortex region contributed by large normal velocities, however, the total entrained mass of air is reduced attributed to penetration reduction under impinging condition.

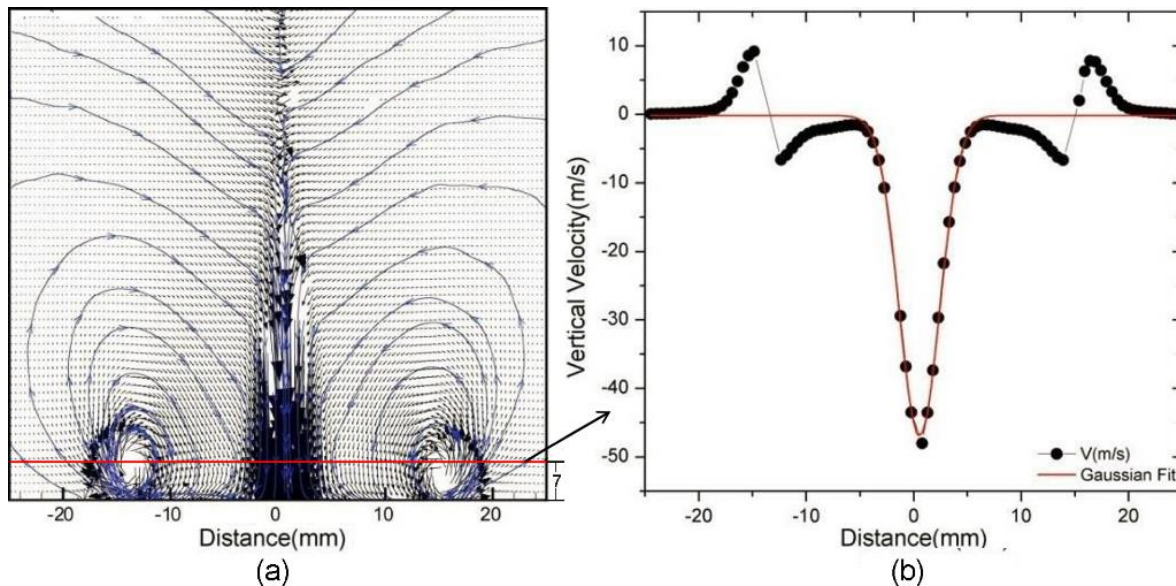


Figure 1.15 Typical velocity field and streamlines of impinging spray (a) and velocity profile at the center of wall-jet vortices (b) [Bruneaux et al., 2011].

As the direct results of air entrainment, the concentration and equivalence ratio of impinging spray were numerously studied [Fujimoto et al., 1997; Senda et al., 1997; Egermann et al., 2001; Bruneaux, 2005]. A typical vapor phase concentration of impinging spray is shown in Fig 1.16 measured by Bruneaux [2005]. It is commonly accepted that the dense or rich region of impinging spray appears in the near impinging point region, and the leading edge of impinging spray forms leaner mixture than that of free spray.

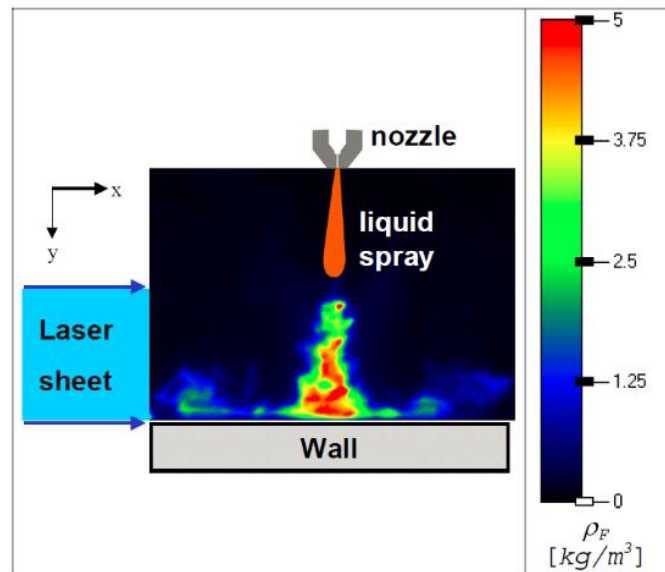


Figure 1.16 Typical fuel concentration of impinging spray [Bruneaux, 2005].

### Combustion and Emissions

The combustion process of impinging spray is complicated. Pickett and López [2005] investigated the OH\* chemiluminescence and soot emissions of impinging flame and free flame and described that the combustion was enhanced and soot emission was improved by impingement. However, Wang et al. [2011] showed that the impingement deteriorates combustion and Dec and Tree [2001] also concluded that spray/wall interaction may increase particulate and unburned hydrocarbon emissions and reduce thermal efficiency. Until now, the effects of impingement haven't yet been agreed upon. However, it is a common acceptance that the impinging spray combustion and emission are resulted from integrative effect of many factors such as wall temperature, impinging distance, liquid/wall interaction and et al.

A schematic diagram depicting the conceptual model of diesel jet combustion under impinging condition during the stabilized diffusion-limited combustion phase was given by Bruneaux [2008] as shown in Fig 1.17. During the diffusion combustion phase, the diffusion flame and OH\*

radical appear at the spray periphery which are the same with those of free spray as shown in Fig 1.12, while the soot particles are confined at the near flat wall region.

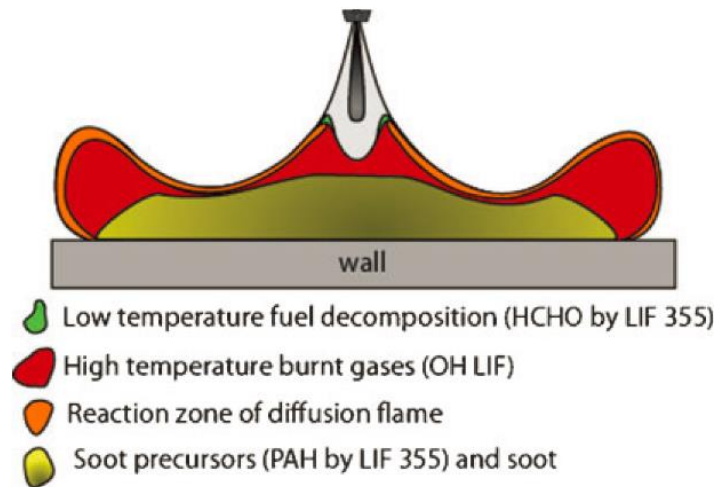


Figure 1.17 Schematic conceptual model of impinging Diesel spray under stable diffusion combustion phase [Bruneaux, 2008].

### 1.4.2 Homogeneous Charge Compression Ignition

In a traditional D.I. Diesel engine, as discussed above, the combustion mode results in the impossibility of simultaneously reduce the NO<sub>x</sub> and soot emissions. To overcome this soot-NO<sub>x</sub> trade off effect, the Diesel combustion mode should be changed. According to the soot and NO<sub>x</sub> formation mechanisms, the lean mixture is thought as an effective method to reduce soot emission, and the low temperature combined with high burning-rate is a valid approach to eliminate NO<sub>x</sub> emission. Therefore, the spontaneous ignition of the lean homogeneous fuel/air mixture throughout the whole combustion chamber can offer a significant reduction of soot and NO<sub>x</sub> emissions.

HCCI concept was firstly proposed and operated by Onishi et al. [1979] and Nouguchi et al. [1979] in a two-stroke gasoline engine, and it was initially investigated for four-stroke engines by Najt and Foster [1983]. After proposed, HCCI concept drew great attention and was extensively investigated by engine researchers. Early studies of HCCI combustion were mainly focused on SI engine, in 1990s, the HCCI combustion was initially carried out in Diesel engines [Ryan and Callahan, 1996; Gray and Ryan, 1997]. The typical combustion stages of Diesel HCCI is shown schematically in Fig 1.18 [Baumgarten, 2006]. The first stage of heat release is attributed to low temperature oxidation (LTO), and the second stage of heat release is associated with high temperature oxidation (HTO). The interval between the first stage and second stage is contributed by negative temperature coefficient (NTC) effect. From Fig 1.18, it is also found that compared with mixing controlled

combustion of traditional D.I. Diesel engine, HCCI has shorter heat release duration, and all the injected fuel simultaneously burnt around the top dead center (TDC) rather than expansion stroke.

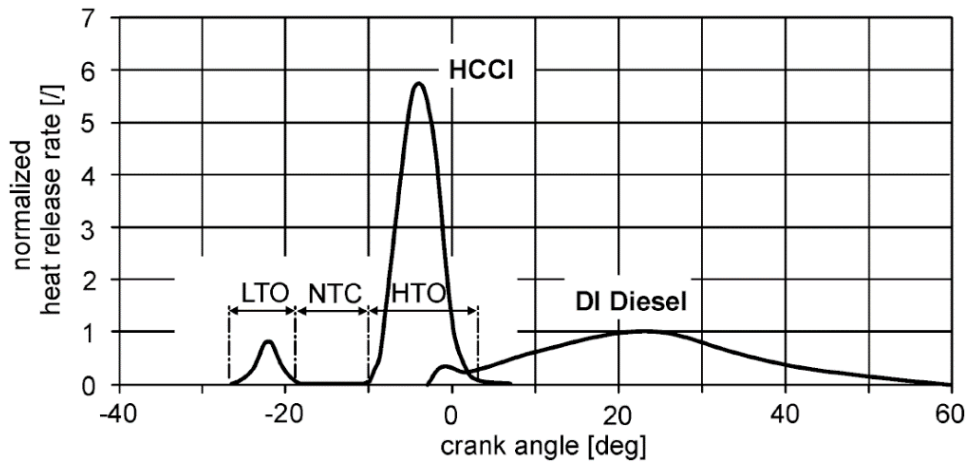


Figure 1.18 Schematic diagram of heat release of HCCI Diesel combustion [Baumgarten, 2006]

Altogether, HCCI combustion has been proved that it can reduce soot and NO<sub>x</sub> emissions without fuel economy deterioration. However, excellently apply HCCI combustion in Diesel fueled engines is still limited due to the several challenges: ① homogeneous mixture is difficult to form due to low volatility of Diesel fuel; ② high CO and UHC emissions caused by low temperature combustion; ③ contribute by self-ignition property, auto-ignition takes place immediately if the chamber temperature higher than 800 K [Peter et al., 2000], which results in difficulty of combustion phase controlling and knocking combustion; ④ due to the uncontrollable and premature knock-like combustion at higher loads and partial burning or even miss fire [Peng et al., 2003] at very low load or high engine speed, until now, HCCI is only possible at moderate loads and engine speeds. To overcome those difficulties and realize HCCI in diesel engines, appropriate spray injection strategies which enhances homogeneous mixture formation and effective approaches which make combustion process controllable should be applied.

#### 1.4.2.1 Homogeneous Mixture Formation

According to the forming process of homogeneous mixture, Diesel HCCI combustion is divided into three categories: port injection, early direct injection and late direct injection [Stanglmaier and Roberts, 1999].

Port injection is thought as the simplest way to achieve homogeneous in-cylinder mixture. Just like Gasoline engine, the mixture is formed inside the intake port. Ryan and Callahan [1996], Gray

and Ryan [1997] and Osses et al., [1998] adopted external mixture formation method to study Diesel HCCI combustion. It is found that the HCCI combustion can be achieved by applying port injection, as a result, the NO<sub>x</sub> and Soot emissions are reduced. However, wall wetting effect which results in poor evaporation is inevitable under Diesel port injection condition, this contributes to high CO and UHC emissions and low fuel economy. Besides, another drawback of port injection is that injection timing cannot be used to influence the start of ignition.

Early direct injection is the mostly used method for HCCI Diesel applications. The homogeneous mixture is achieved during the long ignition delay. By applying early injection method, many combustion systems have been developed such as PREDIC (premixed lean diesel combustion) [Takeda et al.,1996], MULDIC (multiple stage diesel combustion) [Hashizume et al., 1998;1999; Akagawa et al., 1999 ], HiMICS (Homogeneous charge intelligent multiple injection combustion system) [Yokota et al., 1997;1998] and UNIBUS (uniform bulky combustion system) [Yanagihara,2001; Hasegawa and Yanagihara, 2003]. However, every combustion model described above is either suffered by wall wetting effect (high CO and UHC emissions and low fuel economy) or suffered by the difficulty of combustion phase controlling under full load condition.

Late direct injection can be described as that the Diesel fuel injected into the combustion chamber at the near TDC timing such as the traditional combustion mode. By applying heavy cooled EGR, compression ratio reduction and high swirl ratio approaches to control the ignition delay longer than injection duration. The most famous HCCI concept of late injection are MK (modulated kinetics) combustion [Kimura et al., 1999; 2001] and PCI (premixed compression ignition) combustion [Shimazaki et al., 2003]. The onset of heat release of late injected HCCI technique is clearly after TDC and thus peak pressure and combustion noise is reduced. Even the mixture is inhomogeneous, NO<sub>x</sub> emission is very low. However, because it is impossible to achieve a further ignition delay to inject larger fuel mass, the application of late injected HCCI under full load condition have not been resolved.

#### **1.4.2.2 Control of Ignition Timing and Heat Release Rate**

As discussed above, even numerous injection strategies are tried to realize Diesel HCCI combustion mode, the operating range of HCCI still is a serious challenge. Under high load, the HCCI applications with Diesel fuel always suffer from premature ignition, which not only damages the engine, but also vanishes the emission benefits [Stanglmaier and Roberts, 1999]. Therefore, enlarging ignition delay, especially under full load condition, to control ignition timing and heat release rate is extremely urgent. It is recognized that the cooled EGR and reduction of compression ratio are effective approaches to enlarge ignition delay.

Cooled EGR is included in the external EGR system. The exhaust gas pass through the cooler and entrance the combustion. The cooled EGR offers an additional possibility to reduce combustion temperature and prolongs ignition delay which are crucial factors for HCCI Diesel combustion mode application under full load. Figure 1.19 shows a typical operating region of Diesel-liked HCCI under cooled RGR condition [Peng et al., 2003]. It is shown that with the cooled EGR increasing, the Diesel-liked HCCI operating has higher realized possibility under high load.

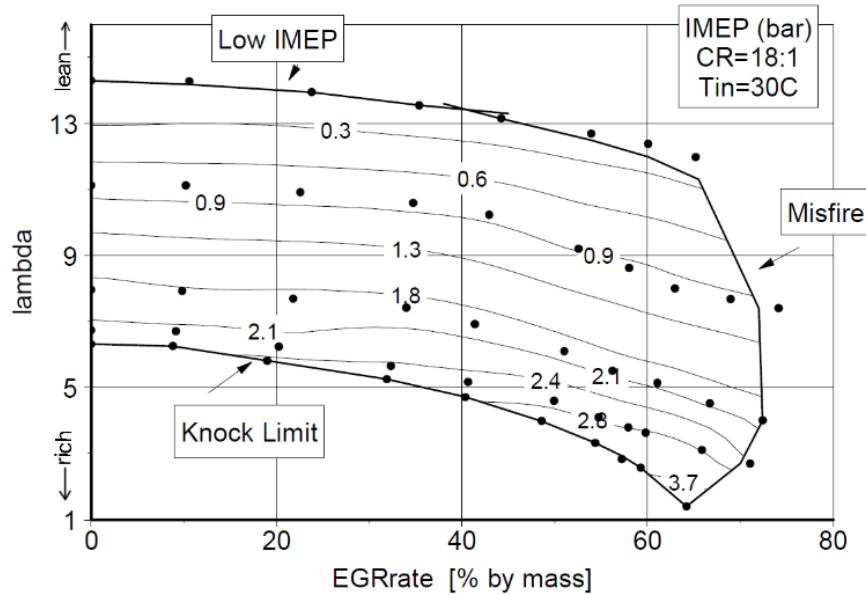


Figure 1.19 Typical operating region of Diesel-liked HCCI under cooled RGR condition [Peng et al., 2003].

The external cooling system must be applied to realize cooled EGR which enhances cost and the complexity, therefore, reduction compression ratio to realize Diesel HCCI is paid attention. Being directly related to charge temperature, compression ratio is important to determine the start of ignition (SOI) and heat release rate. In the case of Diesel HCCI combustion mode, the conventional compression ratio should be reduced in order to delay the SOI and to prevent excessive heat release rate. Figure 1.20 shows the temporal variations of cylinder pressure under different compression ratios [Velji et al., 2003], it is clearly that reduction compression ratio is an effective approach to enlarge ignition delay and to moderate heat release. However, the low compression contributes to the low thermal efficiency, what's more, the combustion has low stability under partial load and cold start conditions when low compression ratio is applied. Recently, thanks to the modern injection system, multiple injection strategy is always adopted to resolve combustion instability under low compression ratio Diesel engine which will be introduced in next section.

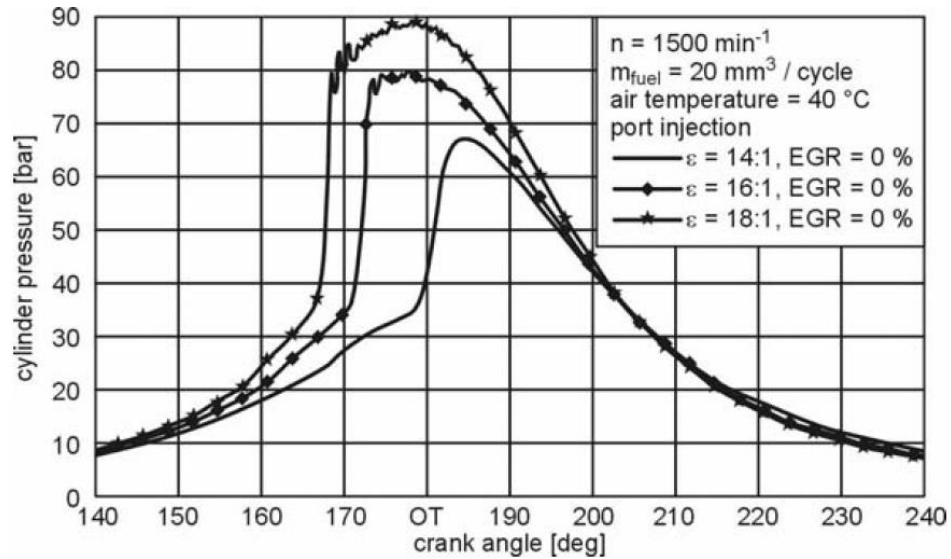


Figure 1.20 Typical Effect of compression ratio on HCCI combustion [Velji et al., 2003].

### 1.4.3 Multiple Injection

Multiple injection, nowadays, is using widely because its advantages [Ricaud and Lavoisier, 2004]: (1) reduce combustion noise and NO<sub>x</sub> emissions through pre-injection or pilot injection of a small fuel quantity; (2) optimize the torque release without producing excessive particles through the main injection and (3) enhance soot oxidation rate through post injection of another small fuel mass.

#### 1.4.3.1 Pre-injection

Diesel spray with pre-injection has been proved as an effective method to enhance fuel/gas mixing and to decrease sauter mean diameter (SMD) [Farrell et al., 1996; Su et al., 1996], subsequently, the NO<sub>x</sub> emission and combustion noise are weakened [Helmantel and Denbratt, 2004]. However, it is a common recognition that the pre-injection deteriorates the soot emission because of the shortening ignition delay of main injection. Wonderful effect achieving of pre-injection highly depends on the pre-injected mass fraction, the injection interval and the pre-injection frequency, detailed investigations concerning such an optimization are reported by Ricaud and Lavoisier [2004]. It is stated that the shorter interval has more advantages, and smaller pre-injected mass should be selected under higher speed and load.

In a low compression ratio Diesel engine which is aimed at the realization of HCCI, the combustion is always unstable or even misses under cold start and low load working conditions. In order to resolve these problems, a small amount of fuel injected (pilot injection) before main injection is usually

employed [Macmillan et al., 2009; Payri et al., 2010]. A schematic diagram of heat release rates under pilot injection strategies of low compression ratio (C/R) Diesel engine and conventional Diesel engine is shown in Fig 1.21. It is recognized that the pilot injection especially multi-pilot injections can extend HCCI combustion mode into cold start and partial load conditions of low compression ratio Diesel engine [Pacaud et al., 2008; Mendez and Thirouard, 2008].

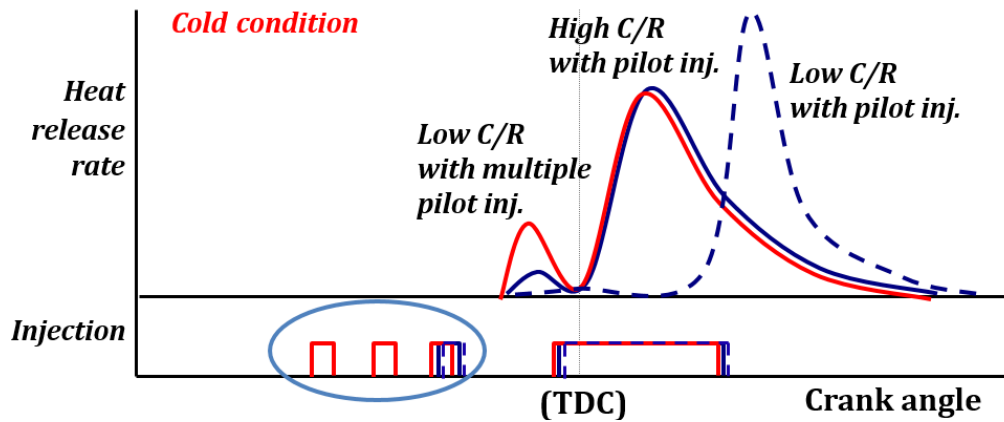


Figure 1.21 Schematic diagram of heat release rates under pilot injection strategies.

### 1.4.3.2 Post-injection

Post-injection which is a short injection follows the main injection is an effective measure to reduce engine-out soot while maintaining efficiency. It is found that the post injection not only enhances mixing with in the cylinder [Bobba et al., 2010; Yun and Reitz, 2007], but also increase the flame temperature during the late combustion phase [Chmela et al., 1999; Benajes et al,2001; Payri et al., 2002] which contributes to soot oxidation enhancing. Figure 1.22 gives a typical flame temperature variations versus crank angle with and without post-injection.

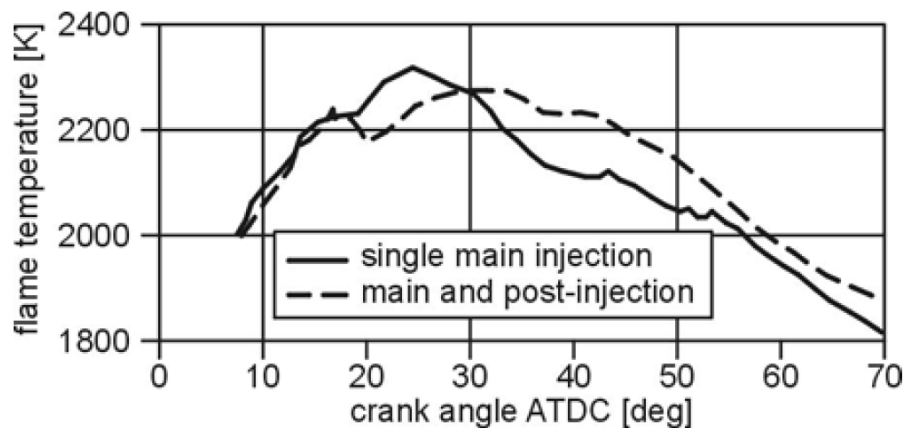


Figure 1.22 Typical flame temperature variations versus crank angle [Chmela et al., 1999].

However, the effect of post-injection on combustion depends on injected mass fraction, timing interval and also operating conditions. In order to achieve optimized effects, it is important to adjust post-injection mass and dwell time between main and post-injection carefully. O'Connor and Musculus [2013] reported a review of post-injection technique in which the soot emissions with a post-injection investigated by previous researchers were collected as Fig 1.23 shows. It is evident that the engine-out soot results are inconsistent. While it is a common acceptance that the shorter-dwell injection reduces engine-out soot more than longer-dwell injection [Hotta et al., 2005] and the low post-injected mass fraction (approximately 10%-20% of the total fuel) reduces soot emission [Payri et al.,2002].

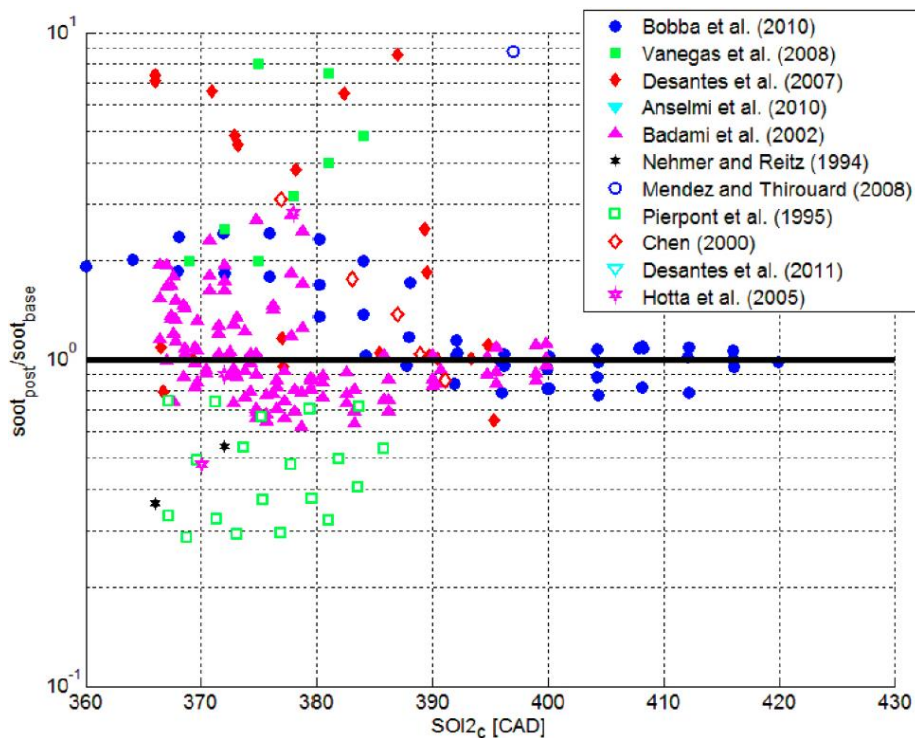


Figure 1.23 Ratio of engine-out soot with a post-injection to that without a post-injection versus timing [O'Connor and Musculus, 2013].

## 1.4.4 Optical Diagnostic Technique for Diesel Spray and Process

### 1.4.4.1 Spray Visualization Diagnostic Techniques

Optical diagnostic techniques have been widely applied to understand the nature of Diesel sprays. Those techniques have been summarized excellently by Zhao and Ladommatos [1998; 2001] as shown in Tab 1.1. In this section, those spray visualization diagnostic techniques will be briefly reviewed.

Table 1.1 Summary of optical techniques for in-cylinder mixture formation measurement [Zhao and Ladommatos, 1998; 2001].

Technique	Applications	Advantages	Limitations
Mie Scattering	Liquid fuel distribution	Simple setup	Sensitive to large droplets
Schlieren and Shadowgraph	Observation of overall spray	Simple setup	Sensitive to both liquid and vapor phases
LRS	Density measurement Vapor concentration	Strong signal Simple setup 2-D imaging	Interference from Mie and spurious scattering Limited to gaseous fuel
SRS	A/F ratio Residual gas fraction	Multi-species detection Multi-point detection Most accurate A/F readings Unaffected by windows fouling	Weak signal
LIF	Fuel concentration	Strong red shifted signal 2-D image of fuel	Quenching at high pressures Difficult to calibrate
FARLIF	A/F ratio	Direct A/F measurements 2-D imaging	Careful calibration required High pressure operation
LIEF	Fuel vaporization & atomization	2-D imaging Simultaneous detection of vapor and liquid	Quenching by oxygen
LEA (LAS)	Fuel vaporization & atomization	Quantitative concentration measurements Droplet size information	Poor spatial resolution

Mie scattering method is extensively applied to detect the liquid phase of the spray for its simplicity and explicitness. According to the Lorenz-Mie theory, the intensity of Mie scattering is determined by the square of the droplet diameter and the droplets concentration when droplets remain spherical and droplets diameter larger than  $1 \mu\text{m}$  [Kim et al., 2002]. Mie scattering method was used to measure droplet size and concentration by Hodges et al., [1991] by applying ensemble-scattering polarization ratio method. Meanwhile, Kosaka et al., [1992] quantitatively measured the fuel concentration by using a 2-D Mie scattering technique. However, the results of the droplet diameter and droplets concentration analyzed from Mie scattering intensity are not very accurate especially compared with those from recently developed techniques. Therefore, the Mie scattering is usually applied to identify liquid phase penetration [Siebers, 1998] and the spray structure [Gulder et al., 1992].

Schlieren and shadowgraphy, as two of the earliest optical diagnostics, can simultaneously observe the vapor phase and liquid phase of spray. The details of those two techniques have been summarized by Settles [2001]. The same as Mie scattering method, they are usually adopted to measure the structure of spray because of the limitation of quantitative analysis. However, the superiority of them compared with Mie scattering method is that they can not only detect liquid phase but also observe vapor phase, what's more, the interface between liquid and vapor can be roughly estimate through the intensity gradient. Recently, schlieren has been used to identify spray boundary under evaporating conditions [siebers, 1998; Pickett et al., 2009].

When a beam light is passed through the gas mixture, a small amount of light energy will be scattered. When the scattered light consists mostly of the incident wavelength, the phenomenon is called as Rayleigh scattering, when the scattered light wavelength is far away from the incident wavelength, the effect is referred as Raman scattering. Thanks to the laser technique, which is considered as monochromatic illuminant, the elastic scattering method could be effectively adopted in spray vapor phase measurement.

Laser Rayleigh Scattering (LRS) is possible to analyze vapor phase concentration because the scattered light intensity is proportional to the number density of gas molecules, what's more, it could be applied to measure vapor concentration under low gas density because of the larger scattering cross section. Arcoumanis et al., [1985] firstly demonstrated the availability of LRS for fuel concentration measurement, subsequently, Arcoumanis and Enotiadis [1991] measured fuel vapor concentration in a port injected SI engine applying LRS. It was found that the vapor concentration depends on the injection time and duration. Espey et al., [1997] used planar LRS technique successfully to obtain the quantitative images of fuel vapor concentration, the experimental setup is shown in Fig 1.24. They analyzed distribution of vapor concentration and the behaviors of auto-ignition, which provided theoretical foundations for the subsequent combustion model supposed by Dec [1997]. However, it is difficult to eliminate noise which comes from Mie scattering for LRS technique. It is meaningless if Mie scattering occurs when applying LRS technique because the energy of Mie scattering is ten to twenty orders of magnitude stronger than that of Rayleigh scattering. Thus the LRS technique must be applied in the environment of virtually free of particles.

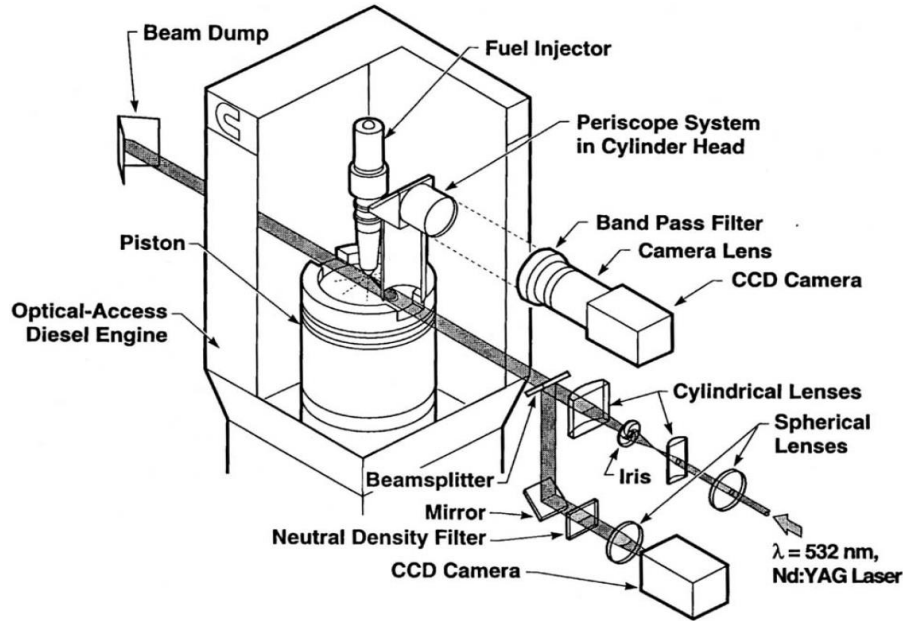


Figure 1.24 Schematic of the optical setup for LRS measurements [Espey et al., 1997].

Spontaneous Raman Scattering (SRS) is a technique to identify molecular species, measure gaseous species concentrations and calculate air/fuel ratio. The scattered intensity depends on the number of molecules that are thermally populated at particular rovibronic energy levels. In 1979, Johnston obtained air/fuel ratio by applying SRS technique, and concluded that the air/fuel ratio distribution changes hugely after fuel injection. Heinze and Schmidt [1989] also applied this technique to measure air/fuel ratio, quantitatively ensemble-averaged 2-D images of air/fuel ratio were obtained, and they claimed that the precision of result is within  $\pm 8\%$ . For species detection, Sawersyn et al., [1986] investigated spatial distributions of different species, later, investigation of molar fraction of gaseous species was successfully carried out by Miles and Hinze [1998]. However, the signal energy of SRS is very attributed by the low scattering cross section, and then SRS is always suffered by the noises which come from background and Mie scattering.

Laser Induced Fluorescence (LIF) is an electronic absorption and emission process that produces relative strong signal intensity with high spatial resolution. Atom or molecule absorbs the specified laser light energy and then electronic state energy is excited to an upper level, because of the instability, electronic back to state ground immediately accompanied with emission light which is called as fluorescence. The fluorescence intensity can be used to estimate concentration because it is proportional to the molecular density [Andresen et al., 1990]. As a result, LIF is widely used to measure mass distribution [Yeh et al., 1994; Bruneaux, 2002]. However, under engine-like condition,

the quantitative measurements are difficult because the quenching effect plays a significant role in reduction of fluorescence intensity.

Laser Induced Exciplex Fluorescence (LIEF) which was developed by Melton and Verdick [1985] is an available method to quantitatively measure vapor phase and liquid phase of spray simultaneously. In this method, a fluorescence molecule at excited state called monomer reacts with another molecule and then a second fluorescent species called exciplex is formed. It is possible to record monomer and exciplex fluorescence individually based on the difference between them, besides, the monomer is the dominant emitter in the vapor phase and the exciplex is the dominant emitter in the liquid phase. The fluorescence intensity is directly proportional to the fuel concentration, as a result, LIEF technique can achieve information of liquid and vapor concentrations. Senda and his coworkers [1992; 1994; 1997] carried out a series investigations on vapor concentration of impinging spray, and gave some fundamental principles of imping spray evolution. More recently, Bruneaux [2001] measured the structures of concentrations of liquid phase and vapor phase by applying LIEF and reported the effect of injection pressure on atomization at the nozzle outlet and the vapor distribution. It should be noted that the LIEF technique suffers from the limitation of quenching by oxygen, careful considerations of used fuel type and ambient conditions must be spent before applying LIEF technique.

Laser Absorption-Scattering (LAS) technique is based on the principle of that the optical thickness of absorption light attribution to the attenuation by droplets scattering and vapor absorption, and the optical thickness of transmitted light only contributed by droplet scattering. Because extinctions of absorption light and transmitted light contributed by droplet of Diesel spray are equal to each other, therefore, by subtracting optical thickness of transmitted light from that of absorption light, the optical thickness which is only contributed by vapor phase is received. As the optical thickness of vapor phase is directly proportional to the vapor concentration and the optical thickness of transmitted light is correlated to droplets density and distribution of their diameters, the simultaneous measurements of fuel vapor concentration, liquid phase concentration and droplets' diameters can be achieved. LAS technique was firstly proposed by Chraplyvy [1981], he applied 3.39  $\mu\text{m}$  and 0.6328  $\mu\text{m}$  to measure vapor and liquid scattering respectively. Suzuki et al., [1993] developed LAS technique and simultaneously measured vapor concentration and liquid droplets by applying 280 nm (absorption) and 560 nm (scattering) light beams pass through an evaporative  $\alpha$ -methyl naphthalene ( $\alpha$ -MN) spray. The most comprehensive applications of LAS technique were carried out by Zhang [2001] and Gao et al., [2007], they selected Dimethyl naphthalene (DMN) as the test fuel and used the second harmonic and fourth harmonic of a neodymium-doped yttrium

aluminum garnet (Nd: YAG) laser to serve as scattering and absorbed beams respectively, and systematically described the analyzing methods of symmetric and non-symmetric sprays.

There are also several techniques which are available for the measurements of ambient gas flowing velocity, spray droplet size and spray flow velocity. Laser doppler velocimetry was well developed and widely applied. It includes Laser Doppler Anemometer (LDA) and Phase Doppler Anemometry (PDA) which is also known as Phase Doppler Particle Analysis (PDPA) techniques. LDA is based on the measurement of the Doppler shift of laser light scattered from small particles carried along with the moving fluid, it is usually used to measure the flow velocity or turbulent scale. There are some researchers adopted LDA to engine measurement [Corcione and Valentino, 1990; Baby and Floch, 1997], however, the drawback of that one component of velocity at single point can be recorded at one time obstructs the wide range of applications of LDA technique. PDA or PDPA can receive the size and velocity data, number density, volume flux and time resolved information based on the principle of that when the spray moves through the detected volume, the dispersed beam signal can be obtained as modulations of time and space which are related to the droplet velocity and droplet size respectively. PDA technique has received wide acceptance as a reliable means of characterizing sprays. This method is limited by the number density of the droplets, thus it faces challenge to detect diesel spray which is dense. However, there are many researches which are concentrated on the diesel spray by applying PDA technique [Desantes et al., 1998; Payri et al., 2008]. Suh et al., [2007] applied PDPA technique to analyze the effects of injection characteristics such as injection rate and injection delay profile on droplet size, the experimental setup is shown in Fig 1.25, and concluded that compared with solenoid-driven system, the piezo-driven can obtain smaller droplet size.

Particle Image Velocimetry (PIV) is a measurement technique for obtaining the instantaneous whole field velocities. It uses a double-pulsed laser light sheet to illuminate the specified flow field, and the scattered light is detected camera placed at a right angle to the light sheet, and the velocity can be simply obtained by dividing time interval from the variations of the two images. The detailed descriptions of PIV was introduced by Kompenhans and Kähler [2002]. It is widely applied to the measurements of air flow and spray evolution processes [Rhim et al., 2002; Lee et al., 2004; Wu et al., 2006]. With several decades development, some advanced PIV techniques are developed such as FPIV (Fluorescent-PIV) [Sepret et al., 2010], UV-PIV [Fajardo et al., 2009] and LIF-PIV [Lee et al., 2002].

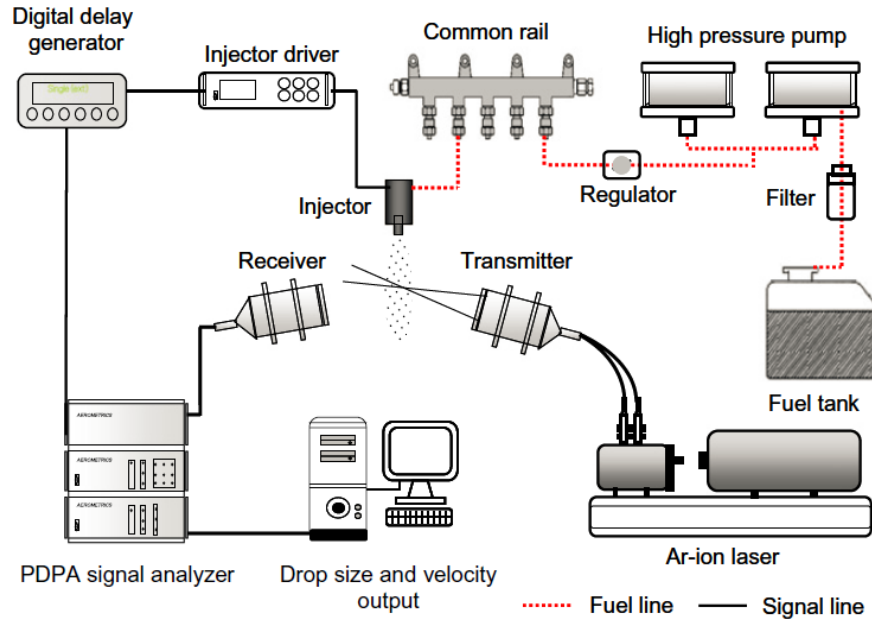


Figure 1.25 A typical PDPA system for analyzing droplets size and velocity [Suh et al., 2007].

#### 1.4.4.2 Diesel Combustion Diagnostic Techniques

The ultimate goals of engine research are to obtain the optimized combustion processes which are related to the maximum power output, maximum efficiency and the minimum pollutant emissions. Therefore, the engine researchers have been sparing no effort to realize the combustion visualization. D.I. Diesel engine combustion visualization was firstly realized by Rothrock and Waldon [1935], and it was rapidly developed in the 1960s [Alcock and Scott, 1962; Nagao and Kakimoto, 1962; Scott, 1969]. In recent decades, thanks to the developments of image recording system and the laser technique, the multiple diagnostics such as laser-elastic scattering, OH-PLIF, fuel-PLIF, chemiluminescence recording, natural luminosity recording and laser induced incandescence (LII) can be realized simultaneously [Espey and Dec, 1993; Musculus, 2006]. The development and applications of Diesel combustion optical diagnostic techniques were summarized by Zhao and Ladammatos [2001], Kohse-Hoinghaus and Jeffries [2002]. In this section, the background of combustion diagnostic techniques used in this dissertation will be briefly reviewed, including the imaging of flame chemiluminescence and natural luminosity.

#### Flame Chemiluminescence

Flame chemiluminescence is the emission of light, as a result of a chemical reaction. It is widely used to offer the temporal and spatial initial combustion reactions in primary premixed flame. In hydrocarbon-air flames, the strongest chemiluminescence intensity peaks are produced by OH\*

(here the asterisk denotes an electronically excited state) at 280 to 310 nm, methylidyne radical (CH\*) at 431 nm and C<sub>2</sub>\* at 516 and 473 nm. The primary path for forming CH\* is the reaction C<sub>2</sub> + OH → CH\* + CO. Succeeding this process, OH\* is produced by the reaction O<sub>2</sub> + CH → OH\* + CO [Gaydon, 1974]. Figure 1.26 gives the emission intensity of spatially resolved flame spectra [Kojima et al., 2000]. It is clear that the chemiluminescence intensity has correlation with equivalence ratio, thus there are some researchers paying attentions in estimating equivalence ratio from the chemiluminescence, Ikeda et al., [2001] found that the intensity ratios of CH\*/OH\* and C<sub>2</sub>\*/OH\* can calculate local equivalence. Imperial College London researchers carried out a series investigations [Hardalupas and Orain, 2004; Panoutsos et al., 2009; Hardalupas et al., 2010] and they claimed that the intensity ratio of OH\*/CH\* exhibits a monotonic dependence on the equivalence ratio  $\phi$ , what's more, an empirical equation was supposed,

$$\frac{OH^*}{CH^*} = 0.497 + 2.107 \exp\left(-\frac{\phi-0.7}{0.26}\right) \quad 1.12$$

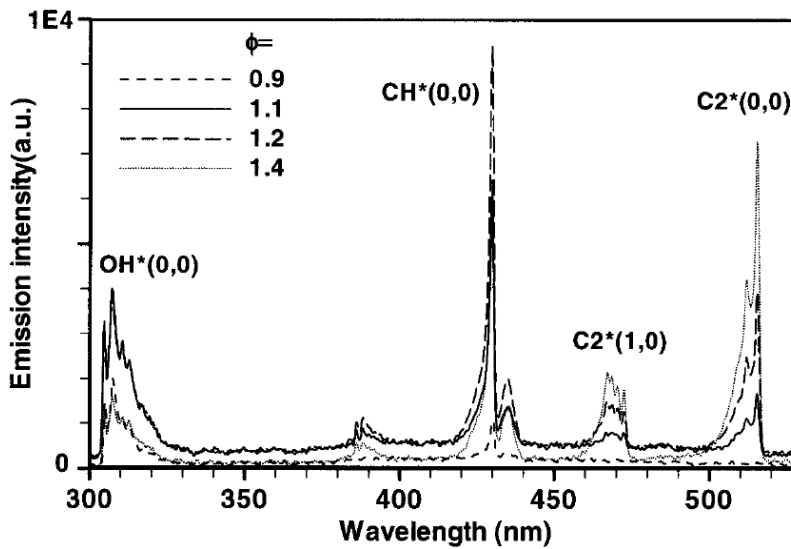


Figure 1.26 Emission intensities of OH\*, CH\* and C<sub>2</sub>\* combustion flame [Kojima et al., 2000].

As the equivalence ratio directly relates to the flame adiabatic temperature [Mueller and Martin, 2002] and combustion velocity [Lee et al., 2000], the chemiluminescence intensity can be a good marker of the rate of heat release (RoHR) [Hurle et al., 1968]. Najm et al., [1998] found that mole fraction of formyl radical (HCO) has excellent correlation with flame RoHR, Panoutsos et al., [2009] described that CH\* and OH\* can be used as RoHR markers, especially OH\*, since the negligible distance between the maximum of RoHR profile and their maximum intensity as shown in Fig 1.27. Tinaut et al., [2011] detected n-heptane flame and also concluded that the peak of OH\* chemiluminescence emission is coinciding with the highest RoHR and the ratio of CH\* to OH\* is

linearly proportional to the equivalence ratio. However, the chemiluminescence especially that wavelength longer than 340 nm (e.g.  $\text{CH}^*$  and  $\text{C}_2^*$ ) is suffered by soot incandescence after soot formed, and it is found that the chemiluminescence is much lower than soot incandescence in Diesel flames [Dec and Espey, 1998]. Karnani and Dunn-Rankin [2013] measured  $\text{CH}^*$  chemiluminescence in sooting flames and claimed that more than 95% of the  $\text{CH}^*$  intensity obtained by traditional method is emitted from soot incandescence. Thus, careful attention should be paid when applying chemiluminescence recording system in sooting flames.

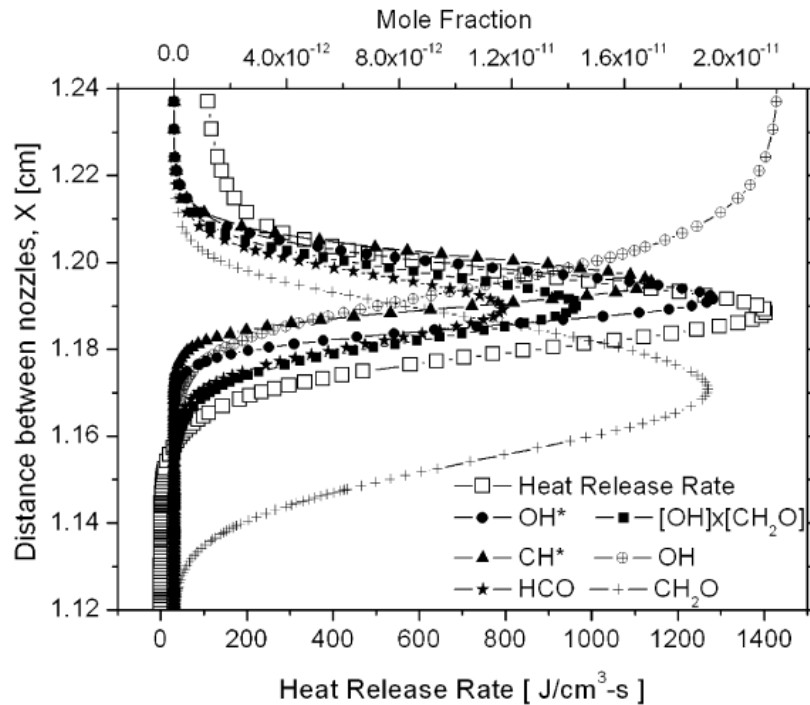


Figure 1.27 Mole fractions and heat release rate for a premixed  $\text{CH}_4$ -air flame [Panoutsos et al., 2009].

The chemiluminescence imaging of  $\text{CH}^*$  and  $\text{OH}^*$  have been widely implanted in Diesel combustion to investigated the cool-flame reaction, auto-ignition and flame structure [Fujimoto et al., 1994; Higgins et al., 2000; Costa et al., 2005]. It is found that the  $\text{HCO}^*$  and  $\text{CH}^*$  appeared during the cool reaction process, while the  $\text{OH}^*$  appears in correspondence to the intense reaction [Dec and Espey, 1998]. Because the  $\text{OH}^*$  is occurred under high temperature and stoichiometric conditions, it provides the best trade-off between image quality and detectability of the most upstream combustion zone, therefore the  $\text{OH}^*$  chemiluminescence is always selected to determine the flame lift-off length [Siebers and Higgins, 2001]. In this research,  $\text{OH}^*$  is applied to analyze the auto-ignition process and flame structure, in addition, to estimate combustion RoHR.

## Broadband Natural Flame Luminosity

The natural flame luminosity recording is one of the most widely used techniques for its simplicity and explicitness. It can be used to investigate the auto-ignition process as well as the flame structure. Even though the line-of-sight images cannot reflect the local combustion behaviors, however, global information which is valuable is obtained. In highly soot flames like those of Diesel engines, the natural luminosity is dominated by gray body emission [Dec, 1992; Dec and Espey, 1995; 1998] which depends on temperature and soot concentration [Zhao and Ladommatos, 1998], thus the perceived natural luminosity intensity reflects the flame characteristics and emission behavior. This is also the basis for the two-color method which has been often used for the analysis diesel combustion. The detailed principle of two-color method will be described in detail in Chapter 2.

Oguma and his coworkers [2002] investigated the flame chemiluminescence and natural luminosity comprehensively by applying optical engine as shown in Fig 1.28 with a dimethyl ether (DME) spray, and analyzed the appearing durations and spatial distributions of natural luminosity and chemiluminescence which consisted of  $C_2^*$ ,  $HCHO^*$ ,  $OH^*$ ,  $CH^*$ ,  $HCO^*$  and  $NO^*$ .

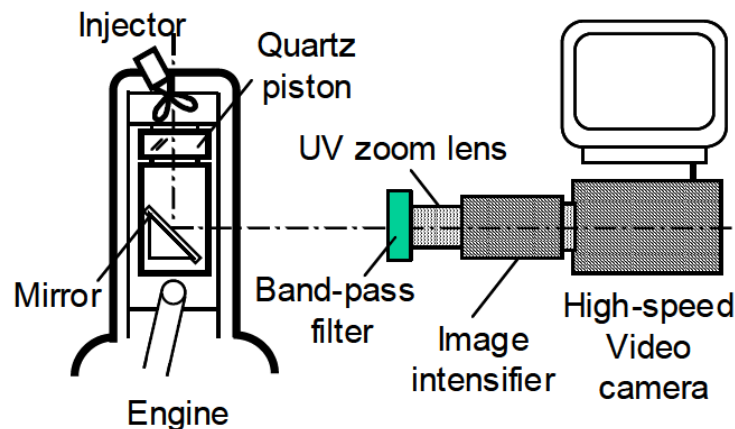


Figure 1.28 Typical experimental setup for flame observation [Oguma et al., 2002].

In summary, both the chemiluminescence and the natural luminosity images offer the possibility of flame visualization for engine researcher to comprehend the complicated combustion processes, as a result, to improve combustion behaviors.

## 1.5 SUMMARY

In order to realize the simultaneous reductions of soot and  $NO_x$  emissions, as well as to enhance the fuel efficiency, it is necessary to improve mixture formation and combustion processes. The injection parameters such as injection pressure, injection mass and multiple injection are

recognized as key factors for Diesel HCCI realization. What's more, in a small-bore Diesel engine, the wall impingent effect plays a significant role in mixture formation, combustion and emissions. Therefore, the target of this study is to clarify the effects of injection pressure, injection mass, multiple injection and impingement on mixture formation and combustion processes, and then provide fundamental theories to realized clean Diesel combustion in passenger cars.

This chapter firstly gives the background and employed approaches of this study. And then the previous works of mixture formation and combustion concepts are reviewed subsequently. Finally, the diagnostics especially applied in this research are simply introduced.

# CHAPTER 2 EXPERIMENTAL APPERATUS AND MEASURING METHODS

## 2.1 FUEL INJECTION SYSTEM

Figure 2.1 shows the schematic of injection system employed in this research work. A manually operated piston screw pump was used to suck the fuel from fuel reservoir and then generate the fuel injection pressure up to 200 MPa. The handle of the high pressure generator was pressed repeatedly or rotated counter-clockwise to give the sucked fuel pressure, there was a pressure reservoir in the injection system to play a role in pressure stability, which had the similar function with common rail system. The injection pressure was observed through an electronic meter which revealed pressure sourced from the signal of pressure transducer. The injector was controlled by the injector electronic control unit (ECU). Injection timing, injected mass and image taken timing were controlled by a delay pulse generator (Stanford Inc., DG 535 or DG645).

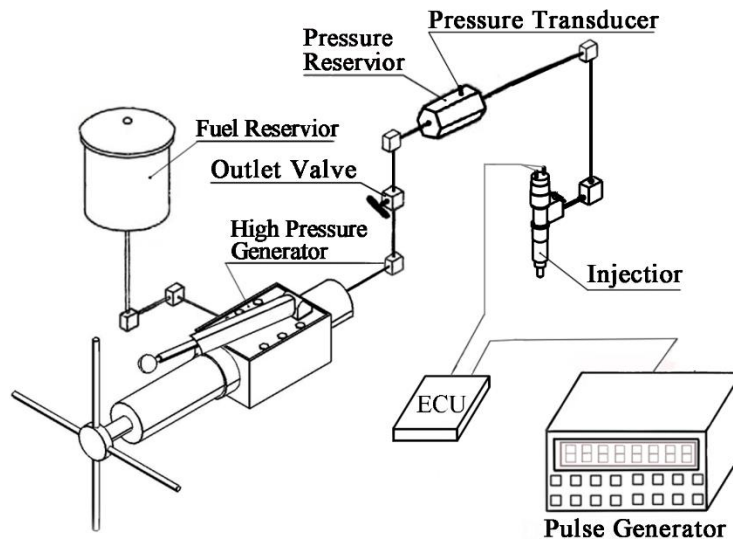


Figure 2.1 Schematic diagram of high pressure injection system.

An electrical controlled piezo Diesel injector with sac-hole nozzle was employed in this study. A cross-sectional schematic diagram of the nozzle tip is shown in Figure 2.2. The diameter of the orifice used in this study was selected as 0.133 mm which is within the normal size region of the

injector used in commercial Diesel engine. The orifice length of was 0.8 mm, as a result, the L/D of the orifice was around 6. The diameter of the sac hole was 0.8 mm and the sac volume was 0.18 mm<sup>3</sup>.

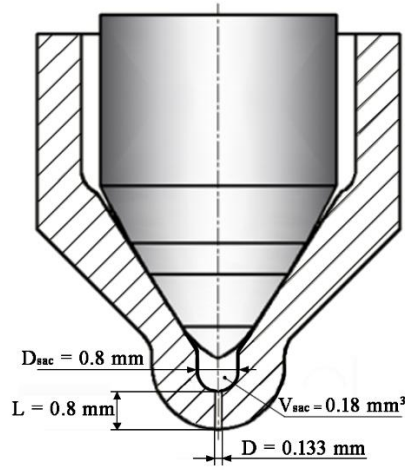


Figure 2.2 Schematic of nozzle tip

The mass injection rate measurement based on Zeuch method [Takamura et al., 1992] was performed to confirm the fuel delivery and injection rate shape by applying injection rate meter (Onosokki Co. Ltd, FJ-7000). The flow rates of 0.27, 0.89 and 2.97 mg under 100 MPa injection pressure and 100, 150, and 200 MPa under 2.97 mg injected mass are shown in Fig 2.3 (a) and (b) respectively. The injection masses were also verified by an electronic balance with a precision of 0.1 mg.

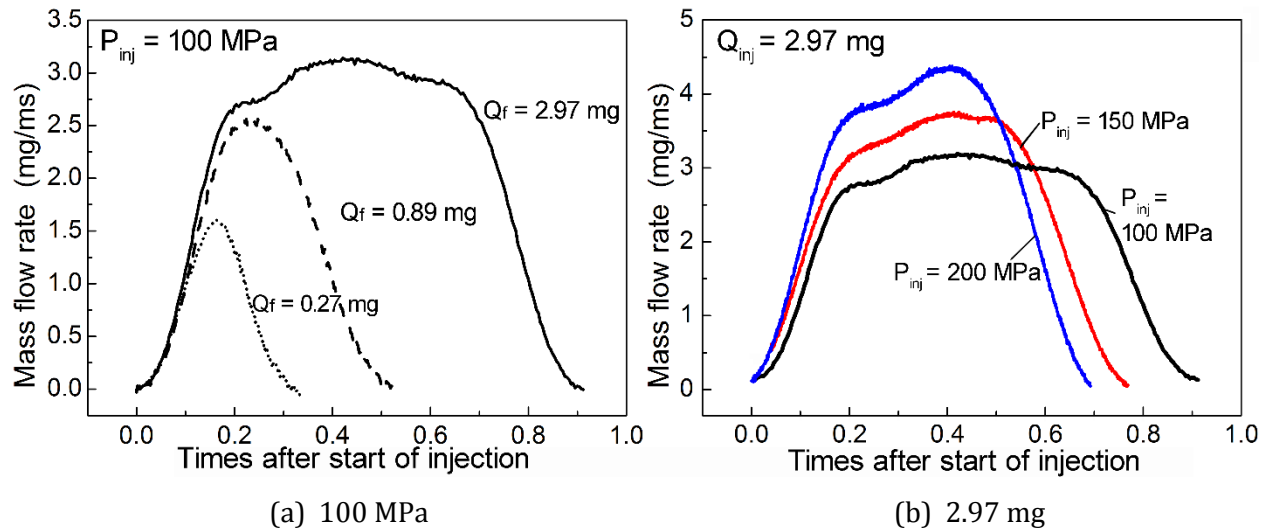


Figure 2.3 Fuel flow rate curves.

## 2.2 HIGH TEMPERATURE AND HIGH PRESSURE AMBIENT CONDITION ACQUIRING SYSTEM

The injector was mounted in a constant volume vessel which can sustain the high temperature and high pressure to carry out the experiments in an engine-like conditions. The schematic structure of the combustion vessel is shown in Fig 2.4. The vessel has four available windows, and the utilized window was decided according to the specific experiment. The quartz glass with diameter of 120 mm and thickness of 170 mm was mounted in the utilized window adaptor. At most six thermocouples could be fixed by the thermocouple adaptor. By disperse distribution, the thermocouples can detect temperatures at different positions of the chamber. The internal and external surfaces of the chamber are covered by the thermal insulator to avoid the heat conduction and maintain the stable environment. A kanthal alloy heating unit was placed inside the chamber to produce the engine like high temperature and high temperature condition as high as 900 K. There were cooling water circulations inside the injector adaptor and the quartz glass adaptor to avoid overheating.

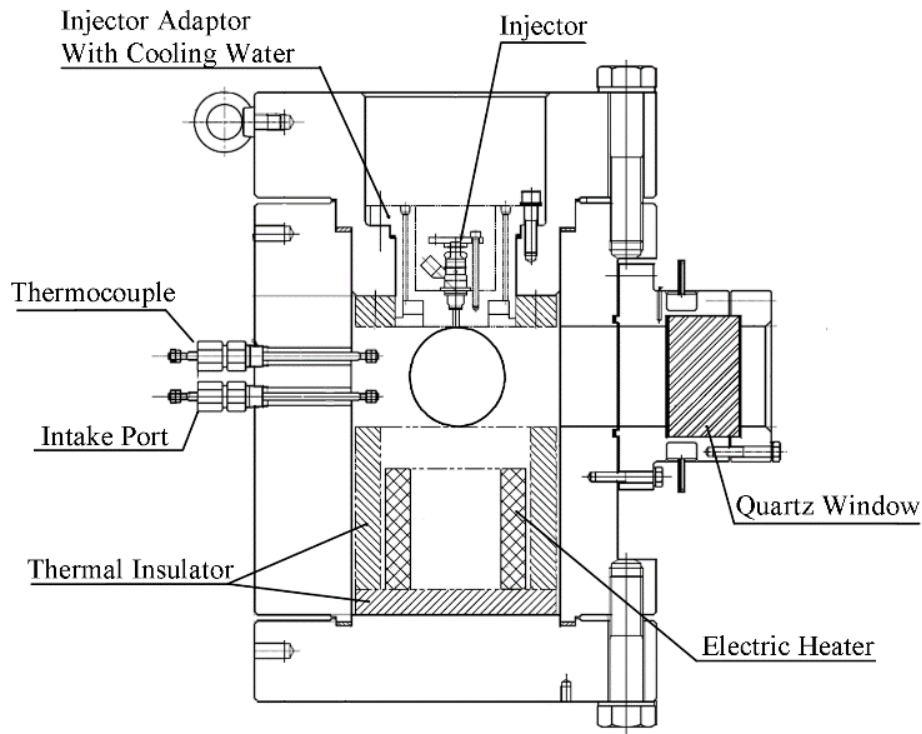


Figure 2.4 Schematic diagram of constant volume vessel.

The high pressure condition inside the combustion chamber was produced by applying a gas cylinder. The high pressure gas inside cylinder quickly entered into the chamber through the intake

port. To avoid the overload of the electric heater due to the low temperature high pressure gas, and also to receive the stable ambient condition during the fuel injection and combustion processes, a preheater was employed, and the schematic diagram of it is shown in Fig 2.5. The preheat equipment had a “room” which was produced by surrounding heaters, the temperature in the “room” can reach to 700 °C. The gas passed through the helical pipe which was mounted in the high temperature “room”, and it can be heated to 480-500 °C. Then the high temperature gas entered into the combustion chamber.

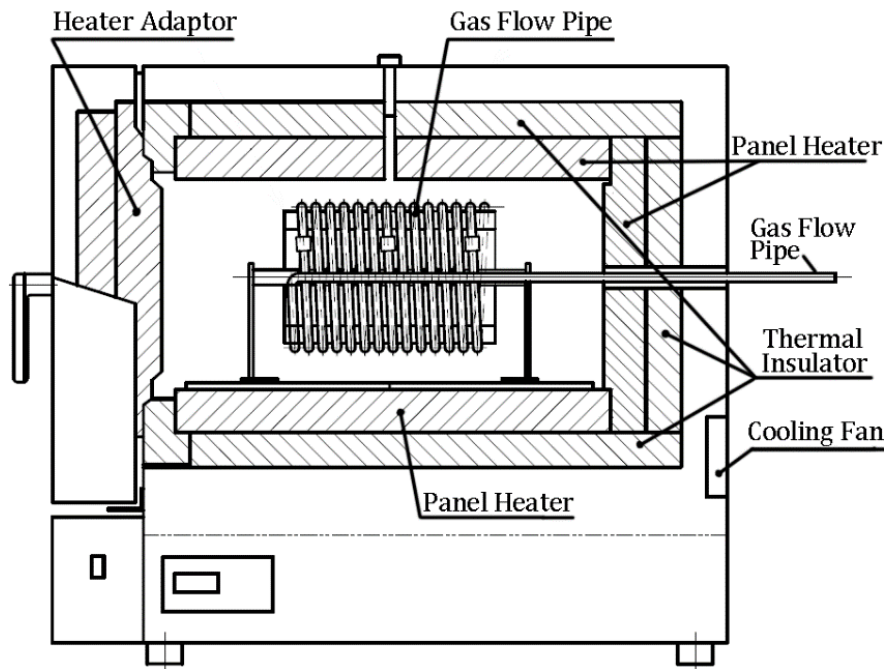


Figure 2.5 Schematic diagram of preheater.

In this study, two kinds of impinging walls were applied, flat wall and two-dimensional (2-D) piston cavity. The schematic diagram of them are shown in Fig 2.6.

The flat wall impinging system consisted of two steel plates, one was used to impinge with the spray flame, and the other one was applied to resist the thermal radiation from the electronic heater directly. Between the two flat walls, there was a layer of heat insulator which was also used to reduce thermal radiation effect. Therefore, the impinging wall has the same temperature with ambient gas. Two connecting rods whose length were adjustable were employed to mount the impinging wall in the injector adaptor.

In the 2-D piston cavity impinging system, the flat surface which plays a role as the cylinder head has a 13.5 degree angle with the injector axis and the impinging point was located 30mm away from the nozzle tip. The squished distance at top dead center was defined as 0.8 mm.

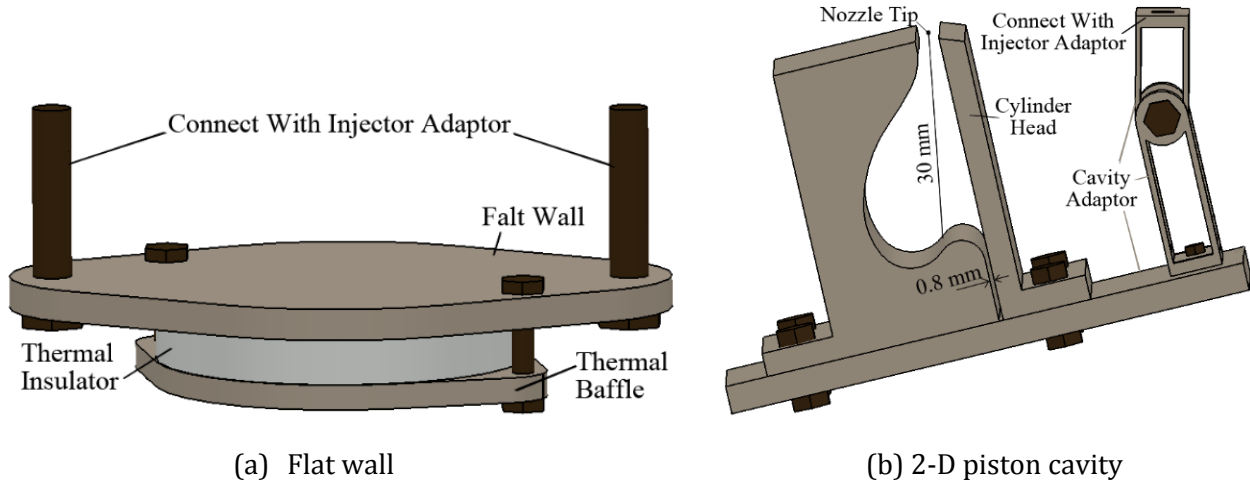


Figure 2.6 Schematic diagram of flat wall and two dimensional piston cavity.

## 2.3 OPTICAL MEASUREMENT TECHNIQUES

### 2.3.1 Mie Scattering Method

The spray structure and the droplets distributions were initially observed by applying Mie scattering method. As shown in Fig 2.7, a high speed video camera (Photron Co., ultima APX RS) was applied to record the reflected light from the spray droplets. The camera provide full mega pixel resolution images at frame rates up to 3000 frames per second (fps), 512 x 512 pixels resolution at 10000 fps, and at reduced pixels resolution to the fastest frame rate of 25000 fps, by utilizing 10-bit CMOS sensor with 17  $\mu\text{m}$  pixels. The visible-Nikkor 105 mm f/4.5 lens was mounted in front of the camera. A Xenon lamp (Ushio Inc., SX-UID 510XAMQ) was employed to form the incident light, under two dimensional piston cavity impinging condition, two reflect mirrors were applied to form the incident light as Fig. 2.7 shown, while under free injection and flat wall impinging conditions, the light from the Xenon lamp illuminated the spray through the sideward transparent quartz window. The experiments were carried out in both non-evaporating and evaporating conditions to detect the droplets characteristics.

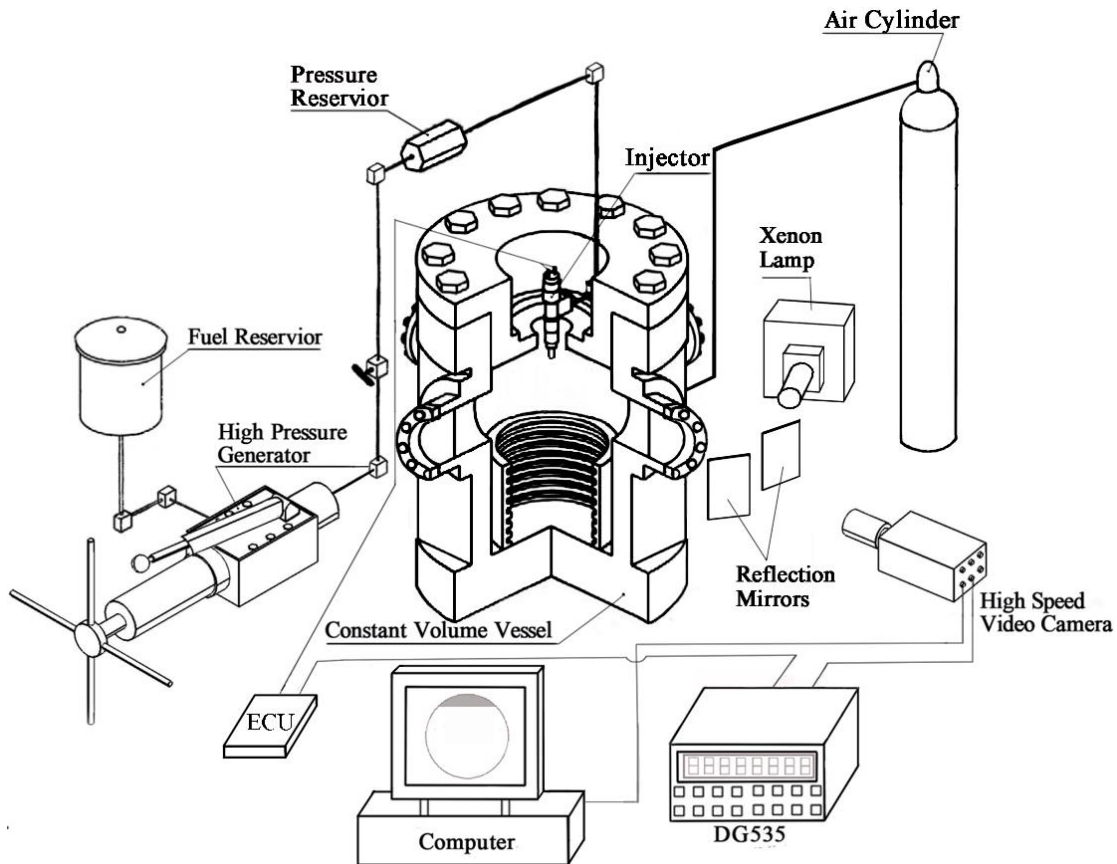


Figure 2.7 Experimental setup for Mie scattering method.

### 2.3.2 OH\* Chemiluminescence Recording System

In order to observe the flame development, OH\* chemiluminescence was applied. In a diesel flame, the stoichiometric and high temperature combustion gives rise to the excited state OH\* formation, and this excited OH\* will rapidly return to its ground state and this process is accompanied with chemiluminescence emission. Figure 2.8 shows the experimental apparatus of OH\* recording experiments, the high speed video camera in this experiment was the same with that of Mie scattering experiment, however, an UV Nikkor lens (Nikon, 105 mm, f/4.5) coupled with a narrow band pass filter with a centre wavelength of 310 nm and a band pass of 10 nm at full-width-half-maximum (FWHM) were used. An image intensifier system (LaVision Inc., HS-IRO) was employed because the OH\* intensity is too weak to detect. The gain and the gate were carefully selected as 75 and 80  $\mu$ s. As discussed in Chapter 1, OH\* chemiluminescence in this study was used to analyze the flame structure, reaction intensity and the heat release behaviors.

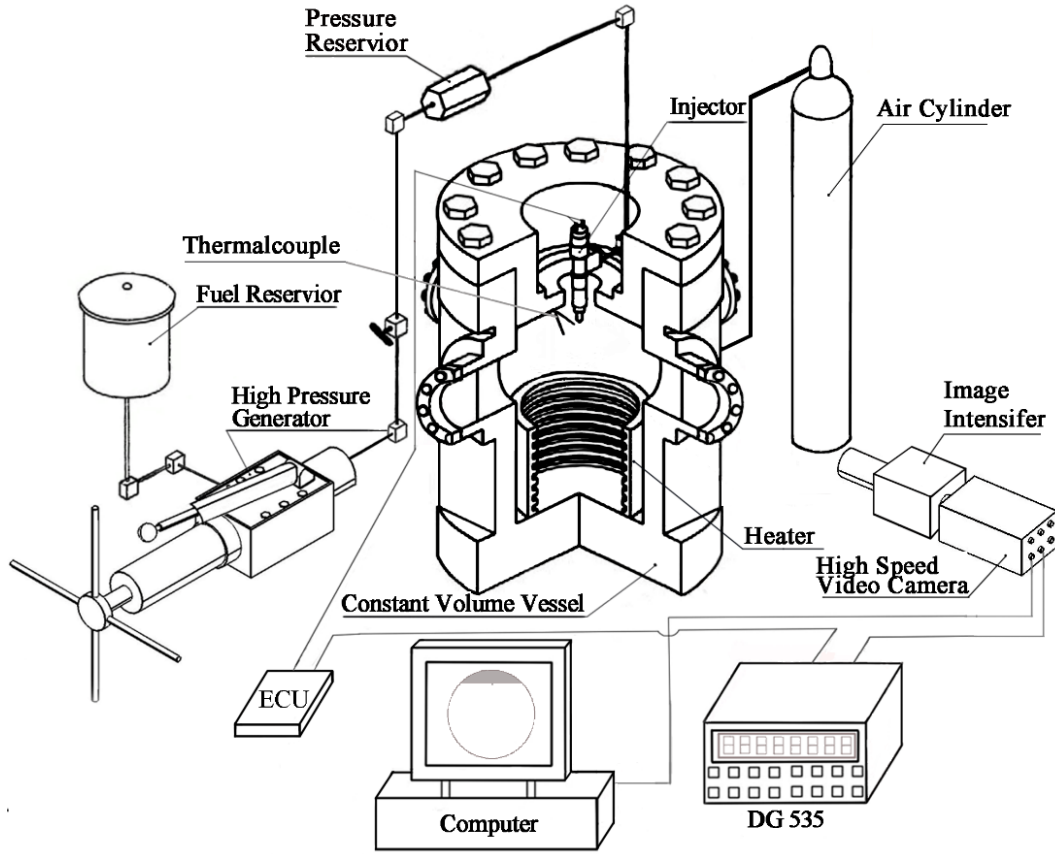


Figure 2.8 Experimental set up of OH\* chemiluminescence recording.

### 2.3.3 Natural Luminosity Recording System and Two-Color Pyrometry

The flame natural luminosity was also focused on in this study because it can not only be used to observe the global flame structure and combustion behaviors, but also be viewed as the basic of two color method. The experimental setup for natural luminosity recording system and two-color pyrometry is shown in Fig 2.9. In this observation, a high speed color camera (Nac Image Technology Inc. GX-8) was applied to record the images. The sensitivity of the camera was ISO 5,000. A neutral density filter of 5% transmittance was located before the visible-Nikkor 105 mm f/4.5 lens to avoid image saturation which results from diesel combustion and high camera sensitivity.

#### 2.3.3.1 Principle of Two-color Pyrometry

According to the Wien's equation, the monochromatic emissive power of a black body  $N(\lambda, T)$  depends on the temperature and the specific wavelength, which can be expressed as:

$$N(\lambda, T) = C_1 \lambda^{-5} \exp(-C_2 / \lambda T_a) \quad (2.1)$$

Where  $C_1$  and  $C_2$  are the first Planck's constant and the second Planck's constant respectively;  $\lambda$  is the wavelength and  $T_a$  is the temperature of the black body.

Under non-blackbody emission condition, the mission power is expressed as:

$$N(\lambda, T) = \varepsilon_\lambda C_1 \lambda^{-5} \exp(-C_2/\lambda T) \quad (2.2)$$

Where T is the temperature of the non-black body;  $\varepsilon_\lambda$  is the monochromatic emissivity of a non-black body.

In practice,  $\varepsilon_\lambda$  is estimated for soot particles based on the empirical correlation developed by Hottel and Broughton [1932],

$$\varepsilon_\lambda = 1 - e^{(-KL/\lambda^\alpha)} \quad (2.3)$$

Combining Eq (2.1), Eq (2.2) and Eq (2.3) gives,

$$KL = -\lambda^\alpha \ln[1 - \exp(-C_2/\lambda \cdot (\frac{1}{T_a} - \frac{1}{T}))] \quad (2.4)$$

If there are two specific wavelengths  $\lambda_1$  and  $\lambda_2$  that are measured simultaneously, the value KL which is proportional to the integrated soot concentration can be eliminated:

$$[1 - \exp(-C_2/\lambda_1 \cdot (\frac{1}{T_{a1}} - \frac{1}{T}))]^{\lambda_1^\alpha} = [1 - \exp(-C_2/\lambda_2 \cdot (\frac{1}{T_{a2}} - \frac{1}{T}))]^{\lambda_2^\alpha} \quad (2.5)$$

Provided the black body temperatures  $T_{a1}$  and  $T_{a2}$  at two specific wavelength  $\lambda_1$  and  $\lambda_2$  can be obtained according to the calibration data, the actual temperature and the KL value calculated.

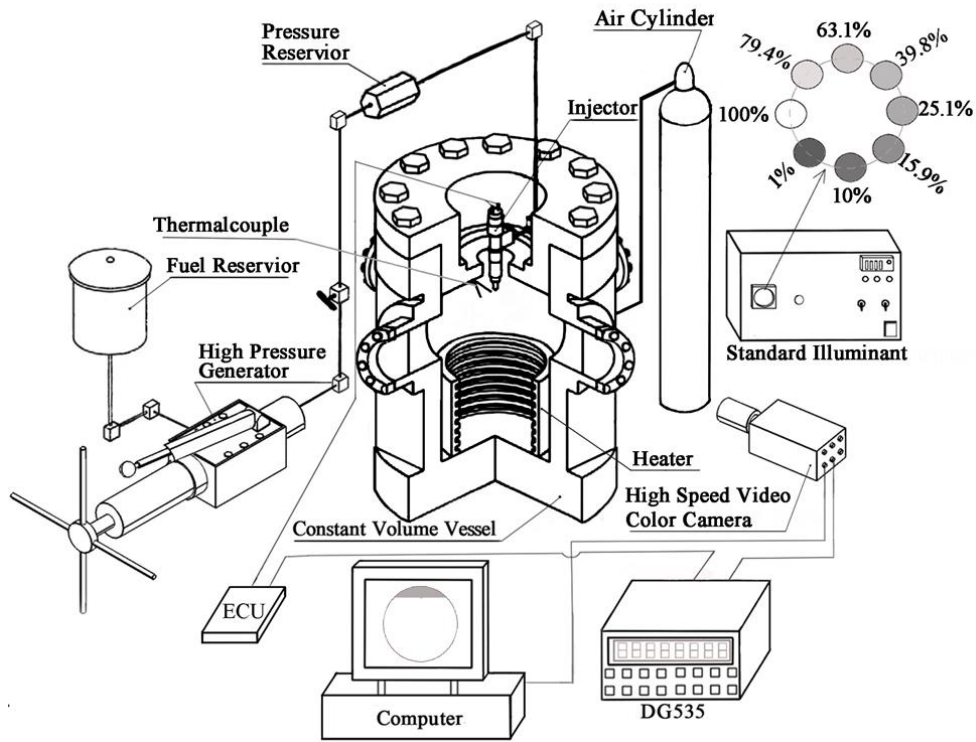


Figure 2.9 Experimental setup for natural luminosity and two-color pyrometry.

### 2.3.3.2 Calibration Method

According to the Eq (2.2), the power of monochromatic emissive after passed through the neutral filter with transmittance of  $\tau_i$  can be expressed as,

$$N(\lambda, T) = \tau_i \varepsilon_\lambda C_1 \lambda^{-5} \exp(-C_2/\lambda T) \quad (2.6)$$

Combining Eqs (2.1) and (2.6) gives:

$$1/T - 1/T_a = \lambda/C_2 \cdot \ln(\tau_i \varepsilon_\lambda) \quad (2.7)$$

When the transmittance is 1, the temperature  $T$  will be received by using a thermodetector and then  $T_a$  will be calculated through equation 1. The empirical correlation of  $\varepsilon_\lambda = a_0 + a_1 \lambda + a_2 T + a_3 \lambda T$  is used in this calculation.

The luminous intensity  $I$  perceived by camera sensor could be defined as:

$$I = a \varepsilon_\lambda C_1 \lambda^{-5} \exp(-C_2/\lambda T) + b \quad (2.8)$$

Where  $a$  and  $b$  are constants which depend on the camera sensor. Taking the logarithm at both sides of Eq (2.8) gives,

$$\ln(I - b) = -C_2/\lambda T + \ln(a\varepsilon_\lambda C_1 \lambda^{-5}) \quad (2.9)$$

According to this equation, the relationship between  $\ln(I - b)$  and  $1/T$  follow linearity when the illuminant happens. The slope equals to  $-C_2/\lambda$ , in reverse, the effective wavelength of this system could be defined as follows:

$$\lambda_{effective} = -C_2/\text{slope} \quad (2.10)$$

In this investigation, a high speed video color camera is used and the intensity of Red, Green and Blue channels could be obtained. Three effective wavelengths of color camera (GX-8, Nac Image Technology Inc.) could be acquired:

$$\lambda_{red} = 577.38\text{nm}, \lambda_{green} = 541.12\text{nm}, \lambda_{blue} = 517.82\text{nm}$$

Only the red and blue channels are selected for our two-color calculation because these two channels have spectral responses with insignificant overlap [Svensson et al., 2005].

When the source of the light is a standard illuminant as shown in the right top part of Fig 2.9, the  $\varepsilon_\lambda$  in will becomes the value of 1, and the  $T$  will be replaced by  $T_a$ . After the camera recorded eight kinds of luminous intensity which are attenuated by eight kinds of neutral filters, and calculate those data by using the Eq (2.10) then the calibration line like Fig 2.10 will be obtained.

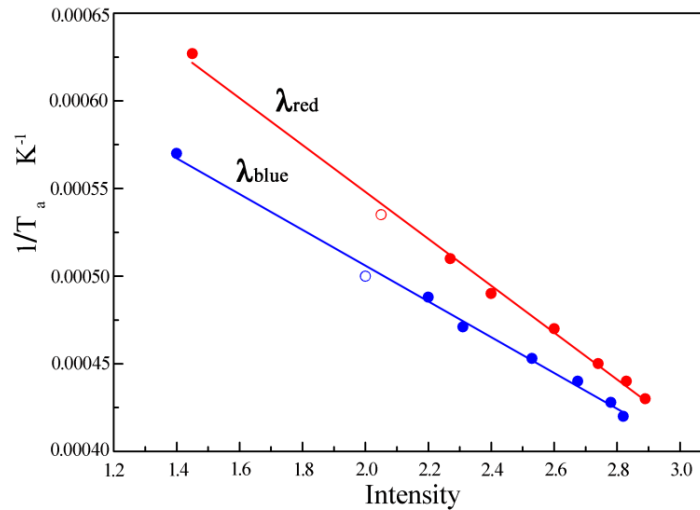


Figure 2.10 Calibration graph sample. The vertical axis represents the black body's temperature; the horizontal axis represents the actual intensity  $\ln(I - b)$  which is received by camera sensor,  $b$  is a constant of the camera.

From Fig 2.10 the temperatures of black body at two effective wavelengths are received. And the actual temperature could be calculated by applying Eq (2.5).

In this study, In fact, some natural luminosity, as a result, the two color experiments were carried out by applying another high speed color camera (Nac Image Technology Inc. GX-1). In this system, the actual temperature was calculated by two apparent temperatures at two specific wavelengths. The calibration method was different with that of GX-8 camera as introduced above which was implemented employing standard illuminant. The calibration process of GX-1 camera used a tungsten lamp to play a role as standard illuminant. The correlation of the voltage and the apparent temperature at the wavelength of 662 nm of the tungsten lamp was identified in advance, then the apparent temperature at the effective wavelength can be calculated by Eq (2.11):

$$T_{effective} = \frac{1}{\frac{1}{T_{662}} + \frac{\lambda_{662} \ln \epsilon_{662} - \lambda_{effective} \ln \epsilon_{effective}}{C_2}} \quad (2.11)$$

The effective wavelengths were calculated by Eq (2.10), and the result revealed that the effective wavelength of red channel and green channel of GX-1 camera are 754 nm and 596 nm respectively. The emissivity  $\epsilon$  is a function of wavelength and the tungsten temperature, it can be calculated by the Larabee empirical equations as shown in Tab 2.1.

Table 2.1 Larabee empirical equations.

350 to 450 nm	$\epsilon_{\lambda T} = 0.6075 - 0.3000\lambda - 0.3265 \times 10^{-4}T + 0.5900 \times 10^{-4}\lambda T$
450 to 680 nm	$\epsilon_{\lambda T} = 0.4655 - 0.01558\lambda - 0.2675 \times 10^{-4}T - 0.7305 \times 10^{-4}\lambda T$
680 to 800 nm	$\epsilon_{\lambda T} = 0.6552 - 0.2633\lambda - 0.7333 \times 10^{-4}T + 0.7417 \times 10^{-4}\lambda T$
$\lambda$ is the effective wavelength and T is the tungsten temperature	

## 2.3.4 Laser Absorption-Scattering Technique

### 2.3.4.1 Experiment Setup

The optical agreement of LAS equipment and injection system are shown in Fig 2.11. Inside the chamber, transparent quartz windows were employed to make the inside observable and optically accessible. A pulsed YAG laser (Continuum NY61-10) was used to form the Vis (second harmonic, 512 nm) and UV (fourth harmonic, 266 nm) lights. The two beams were separated by a dichroic mirror, then the UV and Vis beam were expended respectively. Before pass through the chamber, the two beams were made coaxial again. After being attenuated by the spray, the beams were separated again and were recorded by two CCD cameras (C4880, Hamamatsu Photonics). The light extinction at the

two wavelengths was recorded as 14 bit images by CCD camera chips, and the mathematical algorithm processing of the image was carried out by an IPLab (Spectrum Signal Analytic) system.

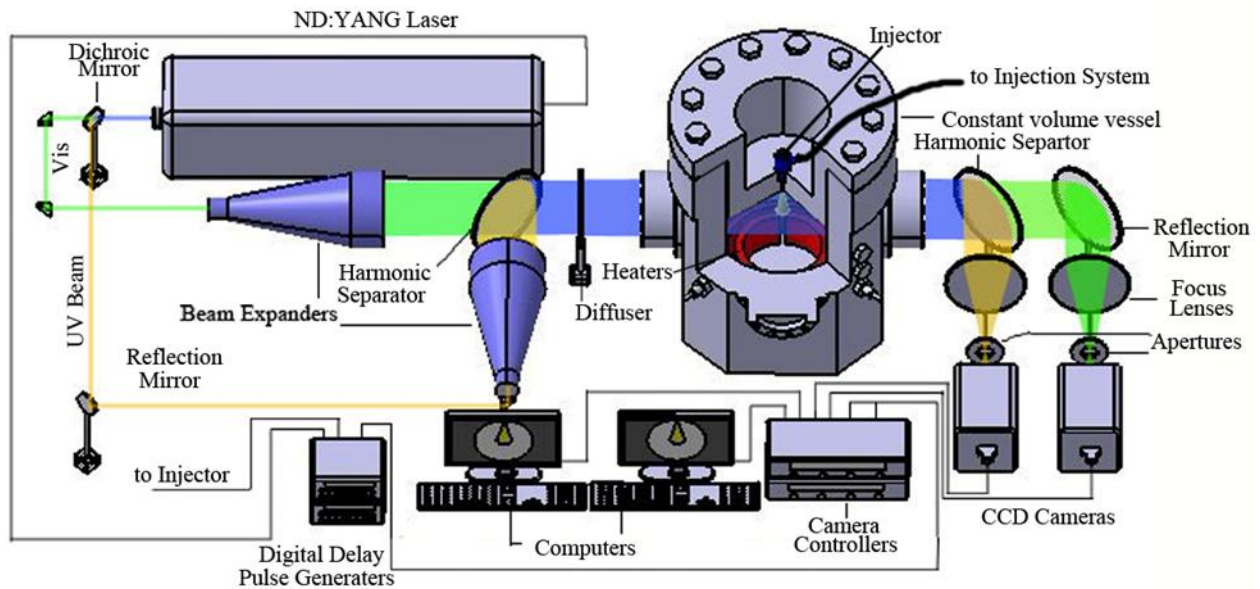


Figure 2.11 Experimental setup of LAS system.

### 2.3.4.2 Principles of LAS Technique

Two kinds of laser beams are applied in LAS method, 512 nm (visible,  $\lambda_T$ ) and 266 nm (ultraviolet,  $\lambda_A$ ). Those two incident laser beams pass through the spray as the principle which is showing in Fig 2.12. The intensities are decreased due to the attenuation effect. In the ultraviolet (UV) image, the intensity attenuation is because of liquid scattering, liquid absorption and vapor absorption, the effect of liquid absorption is negligible; in the visible (Vis) image, the extinction is only resulted from droplets scattering.

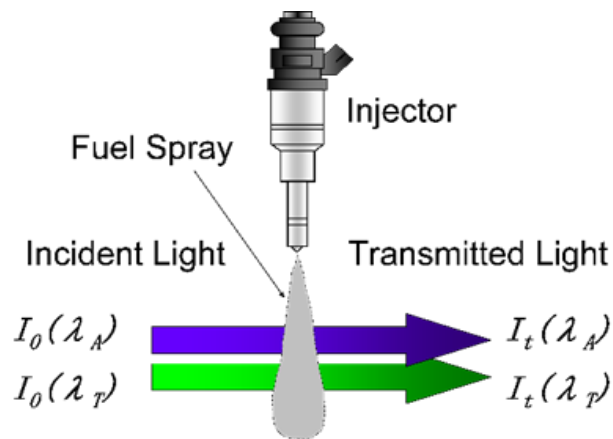


Figure 2.12 Principle of LAS technique.

The light extinction of UV can be expressed as,

$$\ln \left( \frac{I_0}{I_t} \right)_{\lambda_A} = \ln \left( \frac{I_0}{I_t} \right)_{L_{sca}+L_{abs}} + \ln \left( \frac{I_0}{I_t} \right)_{V_{abs}} \quad (2.11)$$

where subscript of  $L_{sca}$ ,  $L_{abs}$  and  $V_{abs}$  represent light attenuation contributed by liquid scattering, liquid absorption and vapor absorption respectively.

The light extinction of Vis can be expressed as,

$$\ln \left( \frac{I_0}{I_t} \right)_{\lambda_T} = \ln \left( \frac{I_0}{I_t} \right)_{L_{sca}} \quad (2.12)$$

It has been proved that the droplet plays the same role on the attenuations of absorption and scattering wavelengths [Zhang, 2001], which implies that the first items of the right sides of Eqs (2.11) and (2.12) are equal to each other. Therefore, by subtracting Eq (2.12) from Eq (2.11), the attenuation of UV result from the vapor absorption can be achieved:

$$\ln \left( \frac{I_0}{I_t} \right)_{V_{abs}} = \ln \left( \frac{I_0}{I_t} \right)_{\lambda_A} - \ln \left( \frac{I_0}{I_t} \right)_{\lambda_T} \quad (2.13)$$

Taking Lambert-Beer theory into account, the vapor phase concentration can be calculated. The analytic process is shown as followings:

Based on Lambert-Beer theory, the attenuation of UV by vapor phase absorption can be expressed as

$$\ln \left( \frac{I_0}{I_t} \right)_{V_{abs}} = \int_0^L \alpha dx = \int_0^L \frac{\varepsilon \times 10^2}{MW} \cdot C_v dx \quad (2.14)$$

where  $L$  : optical path length

$\alpha$  : the absorption coefficient

$C_v$  : vapor mass concentration

$\varepsilon$  : molar absorption coefficient

MV: mole weight

Supposing the vapor in the defined field is homogeneous, the vapor phase concentration can be given as

$$C_v = \frac{MW \cdot \ln(I_0/I_t)_{V_{abs}}}{\varepsilon \cdot L \times 10^2} \quad (2.15)$$

In addition, the vapor phase equivalence ratio can be calculated by

$$\Phi_v = \frac{AF_{stoich}}{AF_v} = \frac{AF_{stoich}}{\left(\frac{C_a}{C_v}\right)} \quad (2.16)$$

where the  $AF_{stoich}$  is the stoichiometric air-fuel ratio and the  $AF_v$  is the vapor actual air-fuel ratio and  $C_a$  is the entrained gas concentration.

Based on Bouguer's law, the attenuation of Vis can be expressed as

$$\ln\left(\frac{I_0}{I_t}\right)_{\lambda_T} = \int_0^L \int_0^\infty \frac{\pi}{4} R_K Q_{ext} C_n N(D) D^2 dD dx \quad (2.17)$$

Where the  $R_K$  represents the correction factor for extinction efficiency  $Q_{ext}$ ,  $N(D)$  is the droplet size distribution function and  $C_n$  is the droplet number density.

The concentration of the liquid phase fuel  $C_d$  is given by

$$C_d = \frac{1}{L} \int_0^L \int_0^\infty \frac{\pi}{6} \rho_f D^3 C_n N(D) dD dx \quad (2.18)$$

$\rho_f$  is the liquid fuel density.

Assuming that the diameter of droplets in the entire spray plume can be replaced by Sauter mean diameter  $D_{32}$ , combining Eq (2.17) and the definition of  $D_{32}$ ,

$$D_{32} = \frac{\int_0^\infty D^3 C_n N(D) dD}{\int_0^\infty D^2 C_n N(D) dD} \quad (2.19)$$

Then the liquid phase concentration can be re-expressed as

$$C_d = \frac{2}{3} \rho_f D_{32} \frac{1}{L} \int_0^L \int_0^\infty \frac{\pi}{4} D^2 C_n N(D) dD dx = \frac{2}{3} \rho_f D_{32} \frac{\ln\left(\frac{I_0}{I_t}\right)_{\lambda_T}}{R_K Q_{ext} L} \quad (2.20)$$

In Eq (2.20), the  $D_{32}$  can be calculated by applying light extinction method which was proposed by Kamimoto et al [1989],

$$D_{32} = \frac{0.63 R_K Q_{ext} M_d}{\rho_f \sum_S \ln[I_0(\lambda_T)/I_t(\lambda_T)] \cdot \Delta S} \quad (2.21)$$

where  $S$  is the project area over the entire area spray,  $\Delta S$  means the unit project area and  $M_d$  is the fuel mass of liquid phase.

Therefore, the ling-of-sight equivalence ratio of the liquid phase fuel  $\Phi_d$  can be expressed as

$$\Phi_d = \frac{AF_{stoich}}{AF_d} = \frac{AF_{stoich}}{\left(\frac{C_a}{C_d}\right) - \left(\frac{C_a}{\rho_f}\right)} \quad (2.22)$$

where  $AF_d$  is the actual line-of-sight air-droplet mass ratio.

### 2.3.4.3 Image Processing Processes

There are two kinds of image processing processes, axisymmetric analysis process and the non-axisymmetric process which are used to analyze cross section and line-of-sight characteristics respectively.

For axisymmetric spray, an onion-peeling model [Hammond, 1981] can be applied to deal with the line-of-sight image and then the spatial distribution can be calculated. The onion-peeling model applied in LAS technique was systematic introduced by Zhang [2001]. In the processing model, the spray radial cross section was divided into numerous concentric rings. When the width of each ring was very narrow, the concentration inside the ring can be considered as homogeneous. The vapor phase and liquid phase concentrations in each ring can be calculated by deconvolution method on the basis of given value of temperature distribution. The temperature was evaluated by enthalpy conservation in each ring. The analytical process is simply presented in Fig 2.13.

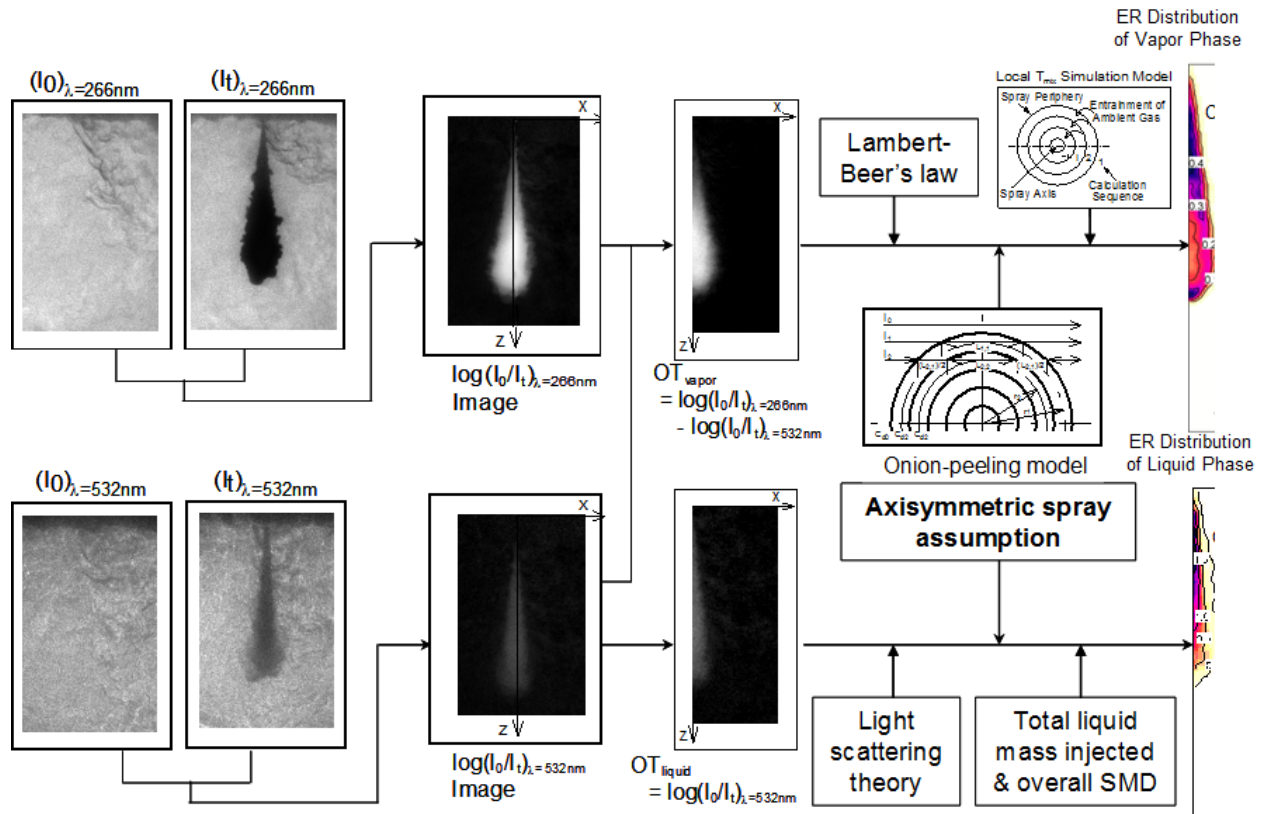


Figure 2.13 Flow diagram of data processing for axisymmetric sprays.

In fact, the spray is always non-axisymmetric in a Diesel engine. When LAS technique is applied to analyze a non-axisymmetric spray, the onion-peeling model is unavailable. Therefore, Zhang and Nishida [2004] extended the LAS technique to analyze the concentrations of non-axisymmetric sprays. The principle will be introduced as followings:

According to Eq (2.14), if the molar absorption coefficient keeps constant along the line of sight, vapor concentration could be described as

$$m_V = \frac{1}{(\varepsilon\lambda_A)} \{Ln[I_0(\lambda_A)/I_t(\lambda_A)] - Ln[I_0(\lambda_T)/I_t(\lambda_T)]\} \quad (2.23)$$

The mass of fuel vapor in one pixel could be calculated by multiplying the vapor concentration and the area of one pixel, and the total vapor mass  $M_V$  is the vapor mass over the whole spray. The total liquid mass  $M_d$  could be calculated by subtracting  $M_V$  from the total injected fuel.

When the droplet size does not vary so greatly along the line-of-sight, the following equation could be obtained

$$Ln[I_0(\lambda_T)/I_t(\lambda_T)] = \frac{3R_K Q_{ext}}{2\rho_f D_{32}} \cdot m_d \quad (2.24)$$

Combining Eqs (2.21) and (2.24),  $m_d$  can be received as

$$m_d = M_d \cdot \frac{Ln[I_0(\lambda_T)/I_t(\lambda_T)]}{\sum_S Ln[I_0(\lambda_T)/I_t(\lambda_T)] \cdot \Delta S} \quad (2.25)$$

The flow diagram of non-axisymmetric analyzing process is shown in Fig 2.14

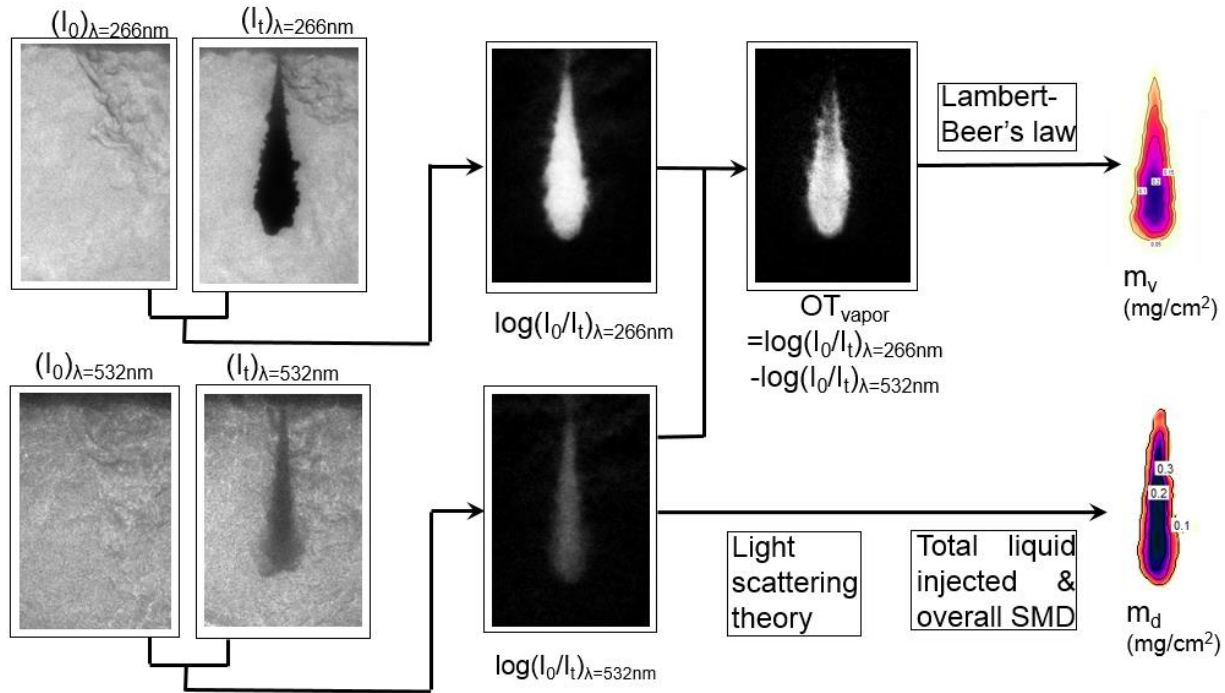


Figure 2.14 Flow diagram of non-axisymmetric analyzing process.

#### 2.3.4.4 Fuel for LAS Technique

Taking the LAS principle into account, the test fuel type is very important for the precision of LAS technique, and the fuel must have the characteristics of: (1) the similar chemical and physical properties with Diesel fuel; (2) absorbs UV light but not absorbs visible light. Previously, 1, 3-dimethylnaphthalene (1, 3-DMN) was thought as a substitute fuel of Diesel for LAS technique [Zhang, 2001], however, it was found that the UV absorption ability of 1, 3-DMN is very strong which results in absorbance saturation as shown in Fig 2.15. In Fig 2.15, left is the absorbance image of UV beam at 1.0 ms ASOI under 760 K, 3.6 MPa ambient conditions, right is the absorbance distribution along the red horizontal line defined in the left figure. It was found that the variations of the absorbance along the red line is unobvious, and the distribution approaches the flat shape. In fact, the absorbance along the horizontal line such as shown in Fig 2.15 should follow Gaussian distribution in an unsaturated image. This kind of saturation image leads to large error when applying LAS technique. Thus it is necessary to find out another substitute fuel which has appropriate absorptive ability on UV beam for LAS technique.

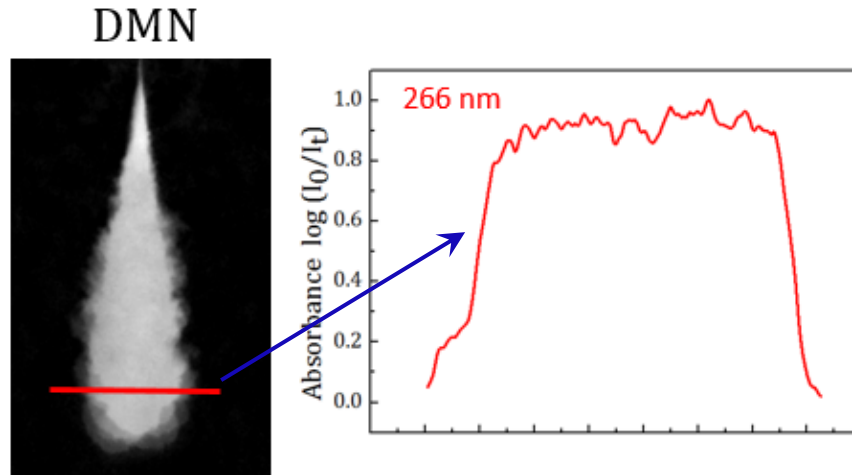


Figure 2.15 Typical absorbance distribution image of 1, 3- DMN spray.

The absorption spectra of liquid fuels with physical properties similar to those of Diesel fuel are shown in Fig 2.16. Nearly all of the candidates were applied in LAS technique, however, the 1, 3-DMN and  $\alpha$ -MN strongly absorb the UV beam, and as a result, the absorbance saturation occurred. The other fuels such as n-pentadecane, n-tetradecane, n-tridecane and n-cetane do not absorb UV light powerfully, which results in the unclear spray region. Until now, the pure fuel which can be perfectly adopted for LAS technique is not discovered. Thus the attentions were paid to blend fuel.

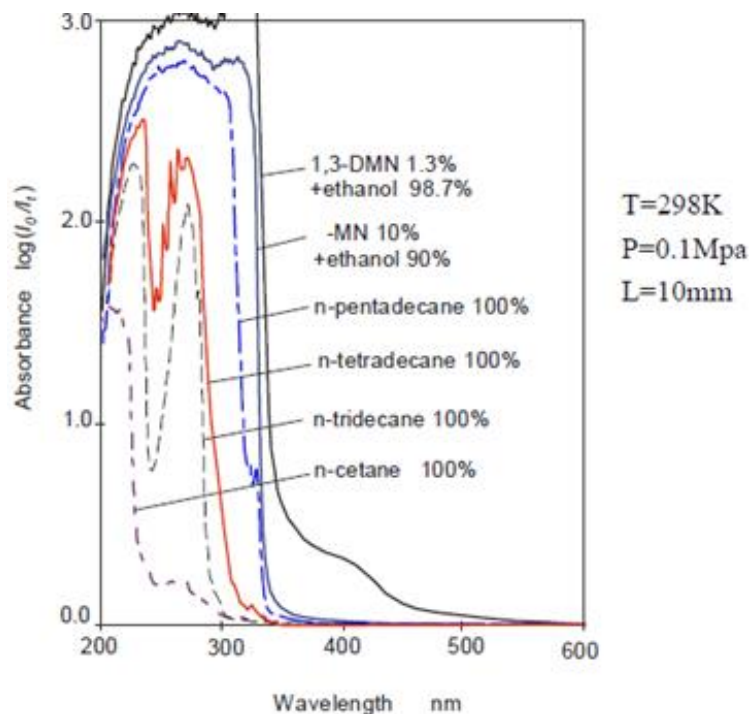


Figure 2.16 Absorption spectra of liquid fuels with physical properties similar to those of Diesel fuel.

The blend fuel for LAS technique must meet that: first, applied fuels have intersolubility; second, the selected fuels should have the similar vaporizing velocity, and have the similar properties with Diesel; third, the appropriate ability of UV beam absorbance. According to the above requirements, a blend fuel with 2.5 volumetric percentage of  $\alpha$ -MN and 97.5 volumetric percentage of n-tridecane was proposed. This is because that the evaporation characteristics of  $\alpha$ -MN and n-tridecane are nearly the same, and the properties of them are similar with Diesel fuel. Fig 2.17 gives the vapor pressures of  $\alpha$ -MN and n-tridecane which was published by Reid et al., [1985], it is found that the vapor pressures are correspond with each other perfectly.

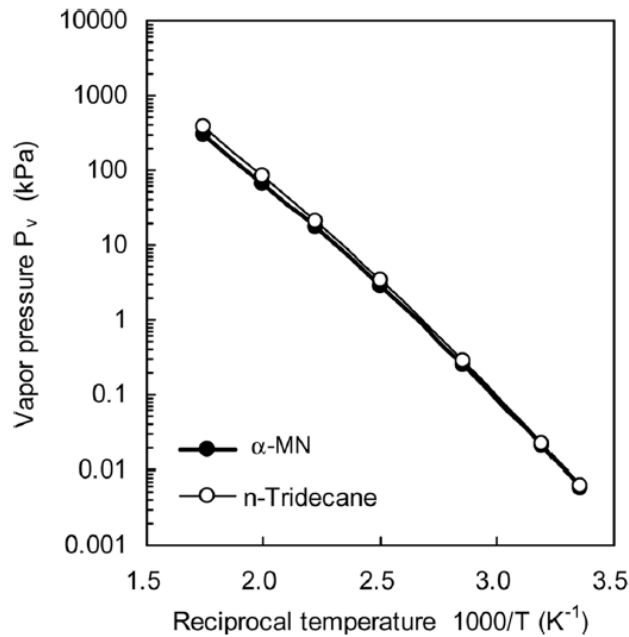


Figure 2.17 Vapor pressure of fuel  $\alpha$ -MN and n-tridecane [Reid et al., 1985].

The blend fuel absorbance image and the distribution along the horizontal red line is shown in the Fig 2.18 under the same condition with that of Fig 2.15. It is clear the red curve is close to Gaussian distribution without losing image sharpness. Therefore, the blend fuel of  $\alpha$ -MN and n-tridecane with volumetric percentages of 2.5 and 97.5 respectively is the ideal test fuel for LAS technique.

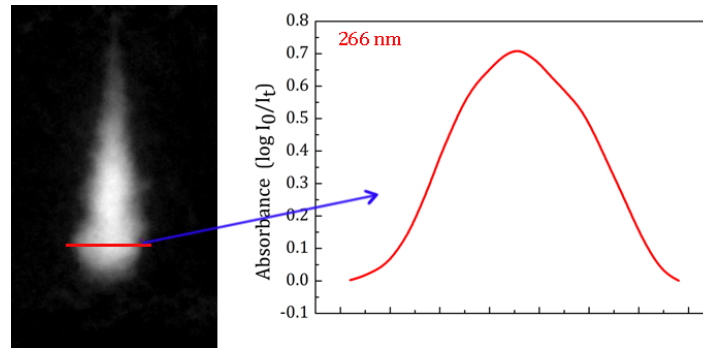


Figure 2.18 Typical absorbance distribution image of  $\alpha$ -MN and n-tridecane blend fuel spray.

## 2.4 SUMMARY

In this dissertation work, the spray and combustion were carried out in a high speed combustion chamber, a manual injection system was employed to support the high injection pressure. The spray structure and the mixing process were observed by applying Mie scattering method and LAS technique. In LAS technique, a blend fuel with 2.5 volumetric percentage of  $\alpha$ -MN and 97.5 volumetric percentage of n-tridecane was employed. The OH\* chemiluminescence which can be used to analyze combustion behaviors and be regarded as hear release indicator was detected by a high speed camera coupled with an image intensifier system. And the flame temperature and soot concentration were calculated by applying two-color pyrometry, which was based on the flame natural luminosity result perceived by high speed video color camera.

# **CHAPTER 3 EFFECT OF SOOT INCANDESCENCE ON OH\* SIGNAL AND THE EFFECT OF SOOT ABSORPTION AND SCATTERING ON THE PRECISION LINE-OF-SIGHT TECHNIQUE**

## **3.1 INTRODUCTION**

In this dissertation study, OH\* chemiluminescence and two color pyrometry were employed to detect the combustion and soot emission behaviors. These results were received using line-of-sight technique, which intensities are the accumulated value along the optical path length. Therefore, the soot in the flame is thought as a potential source of light attenuation especially in a diesel spray flame. This attenuation effect could be described as that the soot near the camera could scatter or absorb the remote light, and then partial of the remote light could not be recorded by the camera. This kind of attenuation is a source of error in the line-of-sight recording system. Different flame structures which are prominent in this study have different light path lengths. Therefore, before the discussions of later Chapters, it is better to check the soot attenuation effect on the precision of the image intensity results.

What's more, the soot incandescence intensity is much larger than that of chemical radicals, and soot incandescence spectrum occupies large range of the wavelength (even in the IR and UV region). Thus, the soot incandescence has influence on the image intensity when the chemical radical recording method is carried out. Karnani and Dunn-Rankin [2013] described that thermal emission may account for 90% of the light collected by a CH\*-specific narrowband filter. Even the OH\*-specific region is locating at the shorter wavelength position compared with that of CH\*, the soot influence is substantial. Therefore, it is useful to analyze soot effect on the OH\* chemiluminescence detecting when applying OH\* chemiluminescence to observe combustion behaviors.

In order to analyze the influence of soot incandescence on OH\* chemiluminescence, the OH\* chemiluminescence experiment and the two color method were conducted synchronously. However, in the experiments of the soot effect on line-of-sight image recording system and impinging effect on combustion, the OH\* chemiluminescence and two color method were not carried out synchronously.

## **3.2 EXPERIMENTAL CONDITIONS**

The experimental conditions were decided according to a real small-bore diesel engine operation. The ambient pressure and temperature for combustion and evaporating experiments

were selected as 4.1 MPa and 873 K to reproduce the thermodynamic environment near top dead center in combustion chamber of a low compression ratio diesel. Table 3.1 shows the detail conditions of this experiment. In all the experiments, the injected quantity was kept to be 9 mg by using a piezo actuator type three nozzle holes injector with diameter of 0.113 mm. The JIS#2 diesel was selected as the injected fuel, the physical and chemical properties were also shown in Table 1.

Table 3.1 Experimental Conditions.

Nozzle Type	Three Holes Nozzle
Hole Diameter (mm)	0.113
Injector Type	Piezo Actuator Type
Injection Pressure (MPa)	100
Injection Quantity (mg)	9
Fuel Type	Diesel JIS#2
Density (kg/m <sup>3</sup> , 300 K)	~830
Boiling Point (°C, 1 atm)	~273
Kinetic Viscosity ((10 <sup>-6</sup> ) m <sup>2</sup> /s, 20 °C, 1 atm)	~3.86
Cetane Index	>=45
Sulfur (ppm)	10
Surface Tension (N/M, 300 K)	0.025
Ambient Gas	Air (21% O <sub>2</sub> )
Ambient Temperature (K)	873
Ambient Pressure (MPa)	4.1
Ambient Density (kg/m <sup>3</sup> )	16
Camera for OH*	Photron High Speed Video Black/White Camera
Lens Type	UV-Nikkor 105 mm f/4.5
Recording Speed (fps)	10000
Image Resolution (pixels)	512 x 512
Camera for Two-Color Method	Nac GX-1 High Speed Video Color Camera
Lens Type	Visible-Nikkor 105 mm f/4.5
Recording Speed (fps)	10000
Image Resolution (pixels)	464 x 464

### 3.3 SYNCHRONOUSLY OBSERVE OH\* CHEMILUMINESCENCE AND SOOT INCANDESCENCE.

In this part, the aperture size for OH\* chemiluminescence was selected as F 4.5. Figure. 3.1 shows the false-colored OH\* chemiluminescence at first row, the natural luminosity images at the second row and the KL factor and temperature images which were calculated from natural luminosity at the third row and fourth row. In the OH\* chemiluminescence and natural luminosity images, the background have been cut. The experiment was carried out three times.

From Fig.3.1, it is clear that the OH\* chemiluminescence and the natural luminosity are detected nearly at the same time (1.0 ms ASOI). At initial stage, it is different to distinguish the soot location from the OH\* chemiluminescence location. When it goes to 1.5 ms ASOI, the OH\* chemiluminescence intensity becomes strong and the soot concentration becomes dense. According to the black line at the OH\* chemiluminescence image of 1.5 ms ASOI, the particles mainly locate at the midstream and downstream of the flame, and at the upstream of the flame, there is a region with OH\* chemiluminescence but without KL factor. It implies that in a diesel flame, the OH\* flame upstream region is not influenced by soot incandescence. The soot locates at the flame leading region is because that the soot particles has larger momentum than burning mixture. What's more, the ambient gas mainly entrain into the spray through the upstream region, and the mixture in this region is lean, the lean combustion in this region results in no soot emission. At 2.0 ms ASOI, the OH\* chemiluminescence and soot incandescence regions are shrunken, the OH\* intensity is enlarged but the KL factor intensity is decreased. This reveals that near this timing, the combustion is the soot oxidation dominant process because the OH\* chemiluminescence is a potential indicator of soot oxidation [Moon et al., 2008]. When it comes to 2.5 ms ASOI, only tiny soot could be observed, however, the OH\* radical still has strong intensity. At 3.0 ms ASOI and 4.0 ms ASOI, there is no soot combustion, only the OH\* radical could be detected. This implies that, at the post stage of diesel combustion, no soot is forming and there is no influence from soot incandescence on OH\* chemiluminescence intensity.

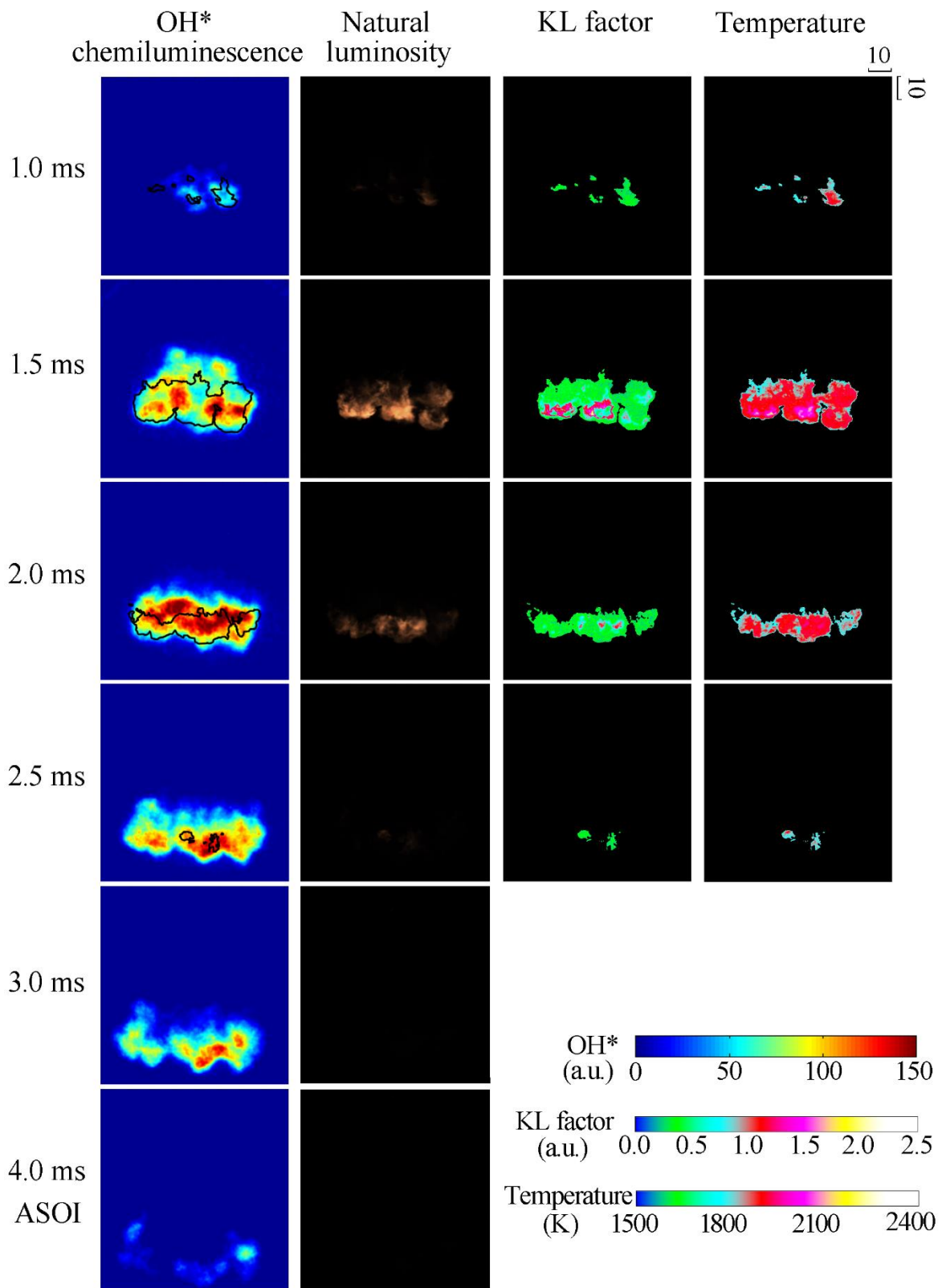


Figure 3.1. Spatial distributions of OH\* chemiluminescence, natural luminosity, KL factor and temperature.

In this part, in order to make a comparison between different magnitudes parameters, such as KL factor, intensity of natural luminosity and temperature, an intensity scaling method was applied as shown in Eq (3.1).

$$\text{Scaled value} = \frac{I - I_{\min}}{I_{\max} - I_{\min}} \quad (3.1)$$

where  $I$  is the original value in the valid pixel,  $I_{\min}$ , and  $I_{\max}$  are the minimum and maximum value inside the specific region, respectively. This scaled method can put the different data into one diagram without losing their features.

The scaled integrated intensity of OH\* chemiluminescence, natural luminosity and KL factor are shown in Fig 3.2. In this paper, integrated intensity is defined as the accumulated value of every valid pixel in flame image. The natural luminosity image is a color image which include three color channels. In order to calculate the scaled integrated intensity, the color image was converted to gray scale image by applying the well known NTST transmission standard [Jain, 1989].

According to Fig. 3.2, before 1.5 ms, OH\* intensity has the same increasing trend as that of natural luminosity and KL factor, it seems that the soot incandescence or natural luminosity has influence on OH\* intensity at this stage. However, the interval between the maximum timings of integrated KL factor and OH\* chemiluminescence is larger than 0.2 ms, after 1.5 ms ASOI, soot decreases but OH\* still increase, which means that the effect of soot incandescence on OH\* intensity is not significant. What's more, the velocity of soot decreasing is much faster than that of integrated OH\* intensity decreasing. Therefore, even the precise influence degree of effect of soot incandescence on OH\* intensity could not be calculated, the received intensity of OH\* recording camera mainly comes from OH\* radical rather than soot incandescence. At the post combustion stage (after 2.5 ms ASOI), no sooting flame is detected, and it is safe to say that the OH\* chemiluminescence is pure.

The changings of natural luminosity and KL factor nearly have the same trend. This confirms that the natural luminosity mainly comes from the soot incandescence [Dec and Espey, 1998]. Actually, there is a tiny difference of the maximum timing between natural luminosity and KL factor. Even this difference is difficult to distinguish in Fig 3.2, it is subsistent because that the natural luminosity not only depends on the soot incandescence, but also depends on the flame temperature, the degree of temperature dependence reaches to 11 orders of magnitude [Mueller and Martin, 2002]. It will be discussed in detail next.

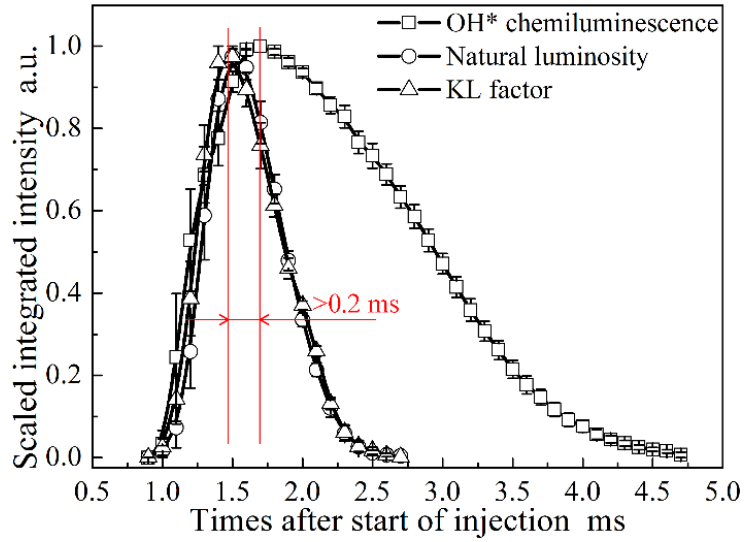


Figure 3.2. Temporal deviations of scaled integrated intensity of OH\* chemiluminescence, natural luminosity and KL factor.

The spatial distributions of scaled intensities of natural luminosity, temperature and KL factor at different axial distances is shown in Fig 3.3. The timing is 1.5 ms ASOI around when the integrated natural luminosity and KL factor are maximum according to Fig 3.2. Three kinds of axial distances: 48, 54 and 60 are defined to reflect the upstream, midstream and downstream of the sooting flame respectively.

From Fig 3.3, at the upstream of sooting flame, it is clear that the timing variation of natural luminosity has the same trend with that of sooting flame temperature, which reveals that the temperature is a dominant influence factor on luminosity intensity. When it comes to midstream of the sooting flame 54 mm, the natural luminosity seems have superior dependence on the soot intensity especially in smaller radial distance region (-15 to 15 mm). In the downstream of the sooting flame, the temperature plays a significant role in natural luminosity intensity, the KL factor reveals opposite trend with natural luminosity and temperature. According to those variations, it can be conclude that temperature play a dominant role in natural luminosity intensity at the periphery (not only the upstream and downstream, but also the large radial distance of the midstream) of sooting flame, while, in the inner region of the spray, the natural luminosity has superior dependence on soot concentration. This is because that the periphery of the sooting flame has high possibility of reaction with ambient gas, and the temperature is high according to Dec [1997], however, the inner region is occupied by high soot concentration and relative low temperature, therefore, the natural luminosity appears different dependences on soot and temperature in different regions.

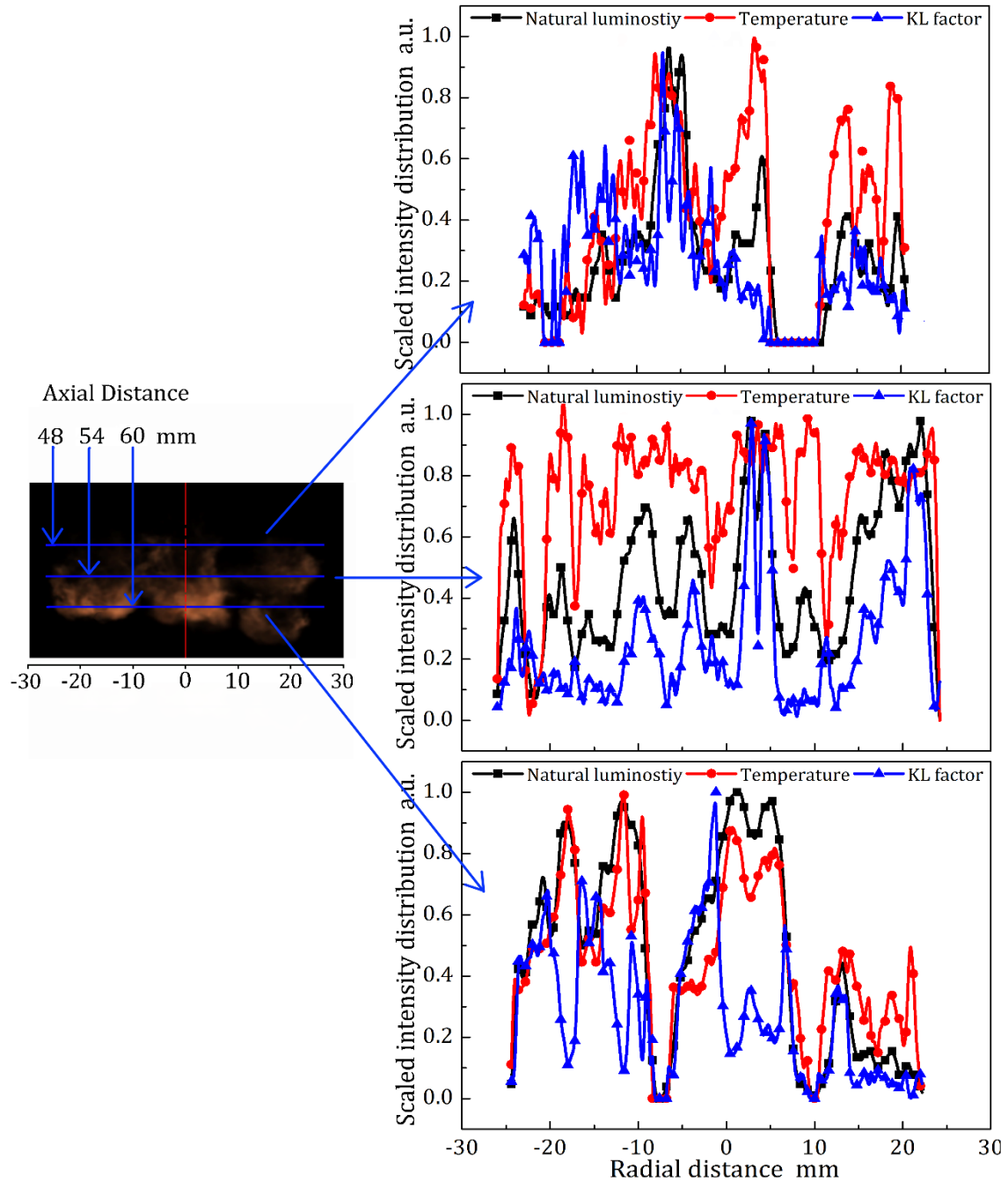


Figure 3.3 Spatial distributions of scaled intensities of natural luminosity, temperature and KL factor at different axial distances.

Figure 3.4 gives the global distribution of the correlation between the natural luminosity and the KL factor at 1.5 ms ASOI. The correlation is estimated by subtracting scale KL factor from the scaled natural luminosity. Confirming the above discussion, the sooting flame periphery has relative large variations of the scaled intensity, especially in the spray tip region, the scaled intensity variation

is significant. The variations at the inner region of the sooting flame is unobvious which is reflected by the near value of zero in Fig 3.4.

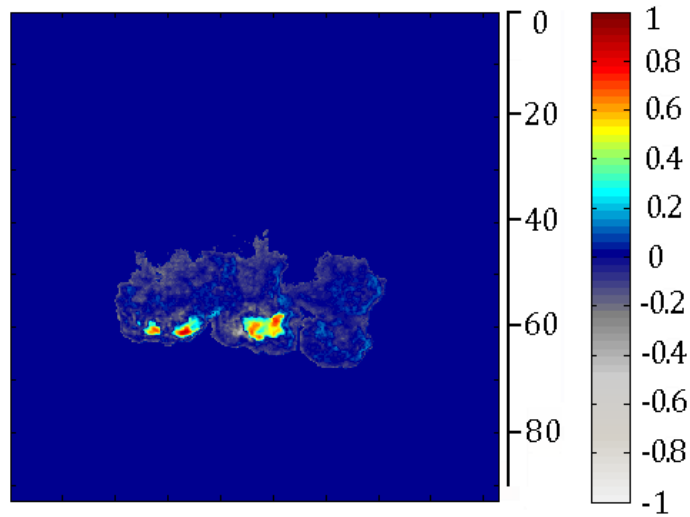


Figure 3.4 Global distribution of the correlation between the natural luminosity and the KL factor (scaled natural luminosity subtracts KL factor) at 1.5 ms ASOI.

The correlations between natural luminosity and soot concentration, between the natural luminosity and the temperature have been discussed above. In Diesel combustion research, the chemiluminescence especially the OH\* chemiluminescence can be applied to scrupulously analyze the flame behaviors but not the natural luminosity. As shown in Figs 3.1 and 3.2, the post combustion is pure OH\* chemiluminescence, however, under the sooting flame condition, the correlation between the OH\* chemiluminescence and the KL factor was not given. In order to observe the correlation, the scaled OH\* chemiluminescence subtracts the scaled KL factor was employed. Three timings were selected as 1.1, 1.5, 2.0 ms ASOI to analyze the initial combustion stage, soot maximum forming stage and soot oxidation dominant stage respectively. The results are shown in Fig 3.5.

In Fig 3.5, the color approaches red means the OH\* intensity strong region, while the color approaches white represents the soot dominant region, the color blue means the scaled OH\* the same with scaled KL factor. It is found that at 1.1 ms ASOI when the combustion just started, the pattern is varicolored, what's more, inside the flame, zero value region is small. These reveal that at the initial stage, even the increasing trend agree with each other as shown in Fig 3.2, the OH\* does not depend on the soot concentration. When it comes to 1.5 ms ASOI, the high soot region and the high OH\* chemiluminescence region are mutually exclusive: OH\* strong region has low soot and soot dense region has low OH\*, which confirms that the soot and OH\* can not appear in the same region [Jakob et al., 2012]. The soot mainly distributes in the down and inner region of the flame, however, the high

OH\* mainly occupies at the connecting region between the individual spray flames. At 2.0 ms ASOI, the soot is oxidized fast, and the high soot concentration regions are dispersedly distributed at the near flame tip region, and the high intensity OH\* distributes at the upstream flame region which is because that the formed soot is oxidized and the OH\* also is an indicator of soot oxidation.

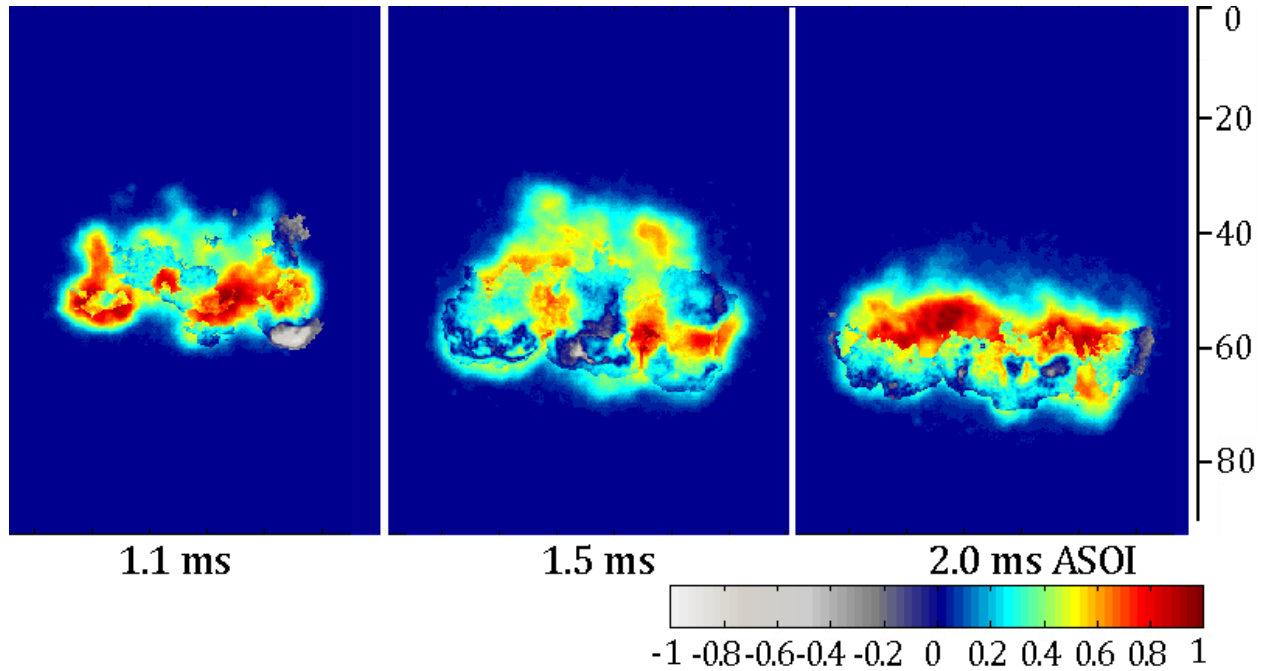


Figure 3.5 Global distribution of the correlation between the OH\* chemiluminescence and the KL factor (scaled OH\* subtracts scaled KL factor).

In general, even under sooting combustion condition, the OH\* intensity does not depend on the soot concentration or soot incandescence, therefore, in this dissertation study, the recorded OH\* chemiluminescence is thought as pure OH\* radical.

When applying two-color method, it should be note that the integrated KL factor is not the soot formation at the specific timing, it is the soot existence by accumulating. The soot formation and oxidation at specific timing can be calculated by applying the principle that when the soot formation process occurring, the KL factor increase and the temperature decrease (soot oxidation is endothermic process), however, the KL factor decrease and temperature increase region means soot oxidation (soot oxidation is the exothermic process). In addition, the OH\* chemiluminescence intensity increases with KL factor increasing because of the reaction intensity increasing, and the OH\* chemiluminescence intensity decreases at the soot oxidation process because the soot oxidation consumes OH\*. Therefore, by comparing the sequential two-color results and OH\* chemiluminescence result, the KL increasing, temperature decreasing and OH\* increasing region

represents the soot formation, and the KL decreasing, temperature decreasing and OH\* intensity decreasing region represents soot oxidation, the regions where the KL factor and temperature have the same variation trend (both increasing or both decreasing), this means the formed soot flowed into or flowed out of this region [Anezaki et al. 2013].

Figure 3.6 shows the distributions of KL factor variations at different combustion stage. The 1.0-1.1, 1.5-1.6 and 2.0-2.1 ms ASOI represent soot formation dominant, the maximum soot existence and soot oxidation dominant stage respectively. The positive value is the KL increasing which gives the soot formation level, and the negative value is the KL decreasing which reveals the soot oxidation level. And the white line is the flame boundary at this timing which is deduced from OH\* chemiluminescence. It is found that at initial combustion stage (1.0-1.1 ms ASOI), the particles are significantly formed but the oxidation is weak. When it comes to main combustion stage (1.5-1.6 ms ASOI), it is found that the soot forms at the inner region of the sooting flame, and the oxidation mainly takes place at the sooting flame tip region and the upstream region. This is because that soot formed in the inner rich region comes to the sooting flame tip periphery, and subsequently, is burned by the burning flame which is reflected by the OH\* boundary. In addition, the upstream where the mixture is lean undergoes the pure OH\* combustion, thus the particles which are formed or stagnated in the sooting flame upstream region are also oxidized in the sooting flame upper region. At the post combustion stage of the sooting flame (2.0-2.1 ms ASOI), the soot oxidation is dominant, and the soot still forms dispersedly inside the sooting flame, however, the soot formation is feeble.

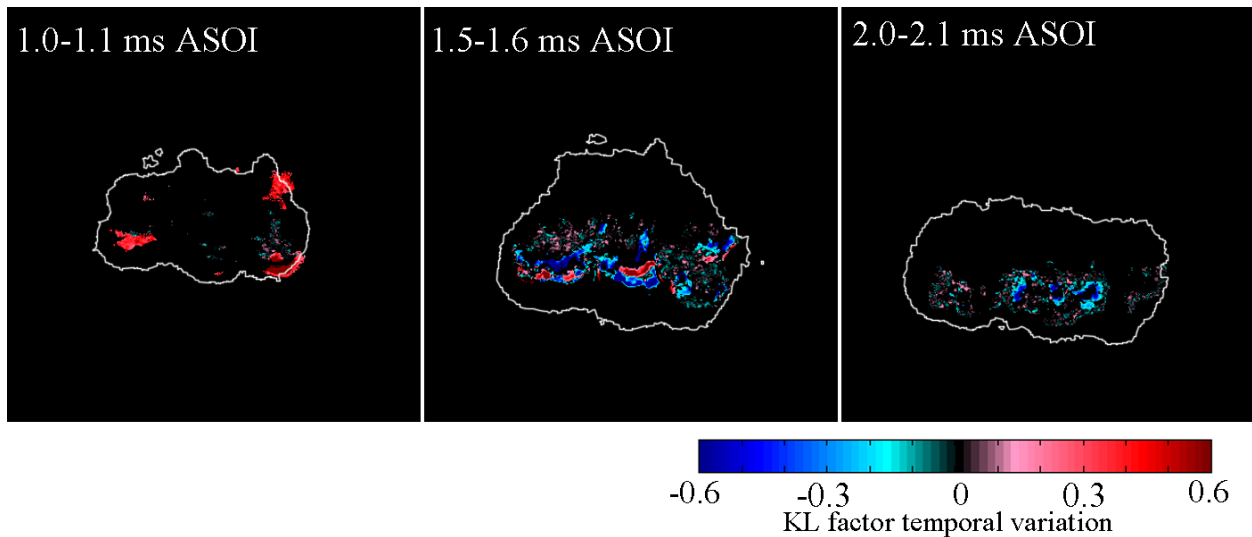


Figure 3.6 The KL factor variations at different combustion stage.

### 3.4 LIGHT ATTENUATION BY THE SOOT ABSORPTION OR SCATTERING IN THE LIGHT PATH

In this part, only the OH\* chemiluminescence experiment was carried out. And the frontal view and side view of the three holes injector which are defined in Fig 3.7 were concentrated on. The aperture size of this investigation was selected as F8. In order to accurately illustrate the common characteristics, every OH\* experiment were carried out at least 30 times.

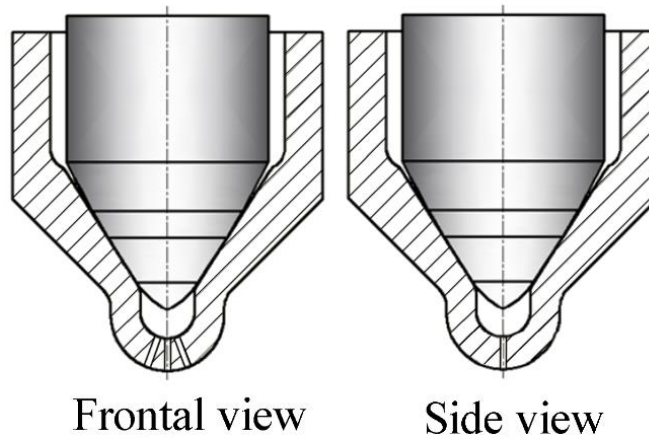


Figure. 3.7 The view definition of the injector.

Figure 3.8 shows the false-colored OH\* chemiluminescence images of side view (left row), frontal view (middle row) and the variations of the integrated OH\* intensity along the same axial distance (right row). The OH\* chemiluminescence is the average image which is calculated from 30 images.

In Fig 3.8, the OH\* integrated intensity was defined as the the integrated intensity along the same axial distance. The calculating process is samplely shown in the 1.0 ms images of Fig 3.8. The same axial distance integraed intensity was selected is because that it could reflect soot effect on line-of-sight technique directly, the integrated intensities of frontal view and side view should equal to each other if there is no soot effect. The value of axial distance in the right graph is corresponding to the vertical locations of left and middle images.

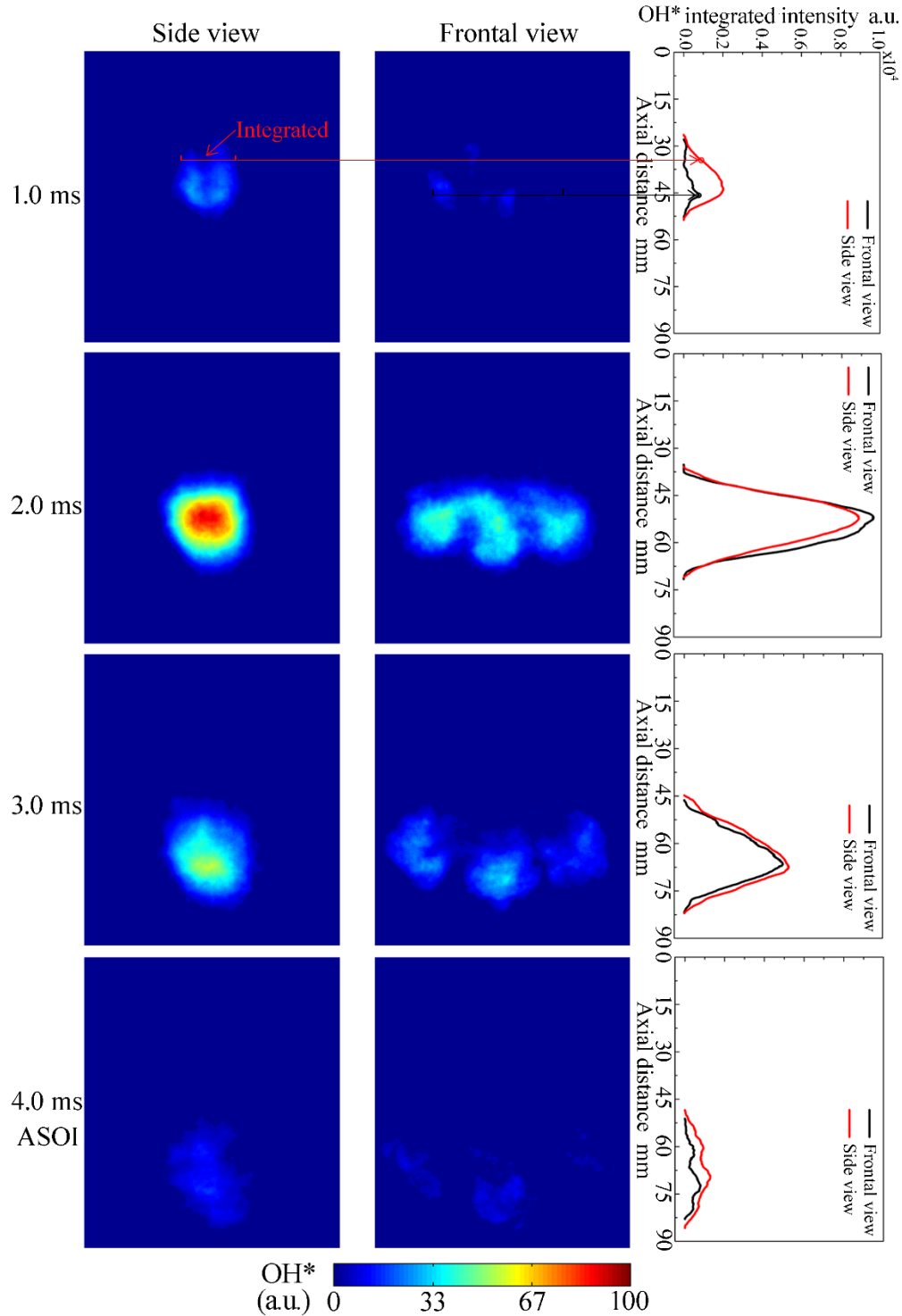


Figure 3.8 OH\* chemiluminescence images of side view (left row), frontal view (middle row) and the variations of the integrated OH\* intensity along the same axial distance (right row).

According to Fig 3.8, the received intensity of OH\* chemiluminescence is enhanced under side view condition because the flame optical path length enlarging. At 1.0 ms ASOI, the OH\* integrated intensity of side view image is much higher than that of frontal view. This is because 1: at this timing,

soot and OH\* radical appear simultaneously according to Fig 3.1, but the soot concentration is low, thus the soot attenuation effect is negligible; 2: the OH\* intensity is not strong enough to be recorded by camera under frontal view condition which is contributed by small aperture size, and the very low intensity could not be distinguished by the camera. However, each pixel intensity of side view image is accumulated from deeper flame depth, the intensity is high enough to be recorded. At 2.0 ms ASOI, the upstream integrated OH\* intensities of side view and frontal view images nearly have the same value, at midstream and downstream regions, the integrated OH\* intensity of frontal image is higher than that of side view image. This is because the soot plays a role on optical attenuation. As Fig 3.1 shows, the soot distribute at the flame midstream and downstream at 2.0 ms ASOI. Thus at these regions, shorter optical path length means higher received intensity. However, the soot attenuation effect is not significant. When it comes to 3.0 and 4.0 ms ASOI, the flame is pure OH\* chemiluminescence, the side view image OH\* integrated intensity is a little higher than that of frontal view image. As above discussed, this is contributed by combined effect of camera sensitivity and low OH\* intensity. But this kind of unobvious difference could be thought as negligible when applying line-of-sight technique under no soot emission condition.

Therefore, this part investigation can be concluded as that: the soot attenuation does not have significant effect on precision of line-of-sight technique. Under no soot existence condition, the longer optical path length has a little larger OH\* intensity, but the error also can be neglected.

### **3.5 SUMMARY**

The characteristics of Diesel flame were concentrated on by analyzing the results of OH\* chemiluminescence and two color pyrometry synchronously. And the light attenuation by the soot absorption and scattering in the light path was focused on by employing OH\* results of the frontal view and side view of a linearity arrayed three holes injector respectively. The main conclusions are summarized as follows:

1. The Diesel flame natural luminosity both depends on the soot concentration and temperature. In the sooting flame periphery region, the temperature plays a significant role in natural luminosity, while in the sooting flame inner region, the natural luminosity is predominantly decided by soot concentration.
2. The upstream flame is a no soot region, and the natural luminosity is always surrounded by OH\* chemiluminescence. And the strong OH\* region and the strong soot incandescence region are

complementary. The strong OH\* intensity mainly appears in the upstream flame and the individual flames connecting region.

3. The effect of soot incandescence on OH\* chemiluminescence intensity is negligible at all the timings. The intensity received by applying 310 nm band pass filter (10 nm FWHM) couple image intensity intensifier system is dominated by OH\* radical emission.

4. There is indeed attenuation of intensity caused by soot which exists between the camera and the optical source under further optical distance when applying line-of-sight technique, but this kind of attenuation effect is not significant enough to reduce the precision of line-of-sight technique.

# **CHAPTER 4 A COMPARISON OF DIESEL SPRAY FLAME CHARACTERISTICS OF FREE AND IMPINGING INJECTIONS**

## **4.1 INTRODUCTION**

Spray wall interaction occurs in small-bore high speed diesel engines and has strong influences on mixture formation, combustion and emission processes inside the combustion chamber. In order to clarify the effect of impingement on spray flame behaviors, flame wall was always selected to form the impinging spray flame. However, the structure of impinging wall is complicated in a real engine and the spray often impinges on the piston crown and then forms impinging spray, the mixture formation and combustion process are different with that of flat wall impinging spray. Thus the target of this Chapter's investigation is to clarify the mixture formation, combustion and soot formation characteristics by analyzing two-dimensional piston cavity and flat wall impinging spray flame in an engine liked high pressure and high temperature constant volume vessel. To make a comparison, the free spray flame was also carried out to play a role as the base condition.

## **4.2 EXPERIMENTAL CONDITIONAL**

The injection condition are summarized in Tab 4.1. In this investigation, all the cases have the same injected quantity of 2.97 mg by using a piezo actuator type injector with 0.133 hole diameter. Two kinds of impinging wall were employed to form impinging sprays: flat wall and 2-D piston cavity. The impinging distance between the nozzle tip and the impinging point is 30 mm. For Las technique, a blend fuel with 97.5 volume percent of n-tridecane and 2.5 volume percent of 1-methylnaphthalene was employed. To avoid reaction, nitrogen was selected as the ambient gas under evaporating condition. The ambient gas pressure was 3.6 MPa and temperature was 760 K, which had the densities with non-evaporating experiment. And for the other experiments, such as combustion and Mie scattering, JIS #2 was employed as the test fuel. In the combustion experiments, the ambient gas pressure was decided as 4.1 MPa and the temperature was decided as 873 K, the ambient density was kept at 16 kg/m<sup>3</sup>.

Table. 4.1 Injection conditions.

Nozzle Type	Single Holes Nozzle
Hole Diameter (mm)	0.133
Injector Type	Piezo Actuator Type
Injection Pressure (MPa)	100
Injection Quantity (mg)	2.97
Impinging Wall	Non-Impinging Flat Wall 2-D Piston Cavity
Impinging Distance (mm)	30

Table. 4.2 Experimental conditions for LAS technique.

Ambient Condition	Evaporating
Ambient Gas	Nitrogen
Ambient Temperature (K)	760
Ambient Pressure (MPa)	3.6
Ambient Density (kg/m <sup>3</sup> )	16
Fuel Type	97.5% n-Tridecane +2.5% 1-Methylnaphthalene

Table. 4.3 Experimental conditions for other techniques.

Ambient Condition	Non-Evaporating	Evaporating
Ambient Gas	Nitrogen	Nitrogen (for Spray) Air (O <sub>2</sub> ) (for Combustion)
Ambient Temperature (K)	300	873
Ambient Pressure (MPa)	1.4	4.1
Ambient Density (kg/m <sup>3</sup> )	16	
Fuel Type	JIS # 2	

## 4.3 MIXTURE FORMATION

### 4.3.1 Spray Structure

Before the discussion of this section, the spray structure especially spray tip penetration should be introduced. Spray tip penetration is thought as an important parameter. Enlarge spray tip

penetration is an effective method to enhance the utility of the ambient gas. The spray tip penetration definition is shown in Fig 4.1. The recording timings are selected as 0.2, 0.3, 0.5, 1.0, 1.5 and 2.0 ms (ASOI). The threshold of 50 (saturation value is 255) is selected to define the spray boundary. As shown in Fig 4.1, the spray tip penetration of free spray is defined as the axial distance, the spray tip penetration of 2-D piston cavity impinging spray is calculated by adding the axial penetration and the arc length along the cavity wall, and the penetration of flat wall impinging spray is defined as the summation of axial and radial penetrations.

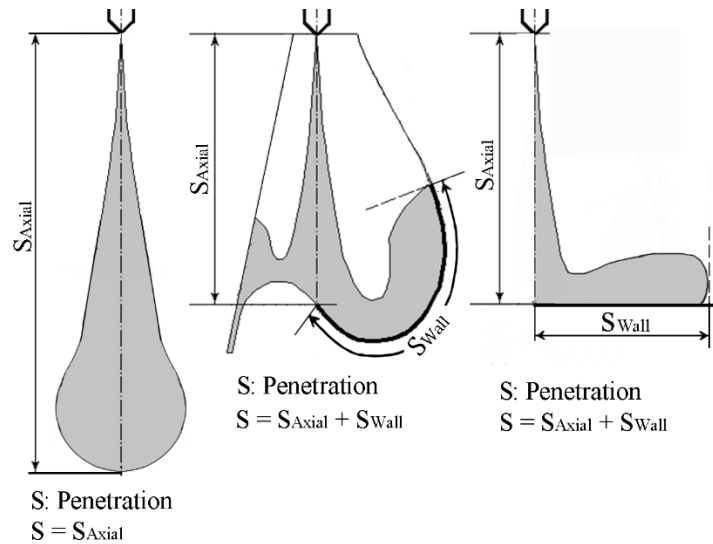


Figure 4.1 Definition of spray tip penetration.

The optical thicknesses of the UV beam, vapor phase (denoted as Vap) and liquid phase (denoted as Liq) of free, flat wall impinging and 2-D piston cavity impinging sprays under evaporating condition are shown in Fig 4.2. It is found that, under all the spray conditions, the vapor phase and the liquid phase nearly have the same tip penetration at 0.5 ms ASOI. When time increases to 1.0 ms AOSI, when the injection has been finished, the free spray has unobvious liquid phase optical thickness which implies that the injected fuel is mainly evaporated, and the spray tip and tail regions are occupied by fuel vapor. Under flat wall impinging condition, the dense liquid phase region distributes at the wall vicinity region, and the intensity of the liquid optical thickness seems weaker than that of free spray which reveals that the evaporation velocity under flat wall impinging condition is lower than that of free spray. Under 2-D piston cavity impinging condition, it is clear that large amount of liquid phase is still observed at the close wall region, especially at the large curvature region a bright liquid optical thickness region is appeared. This means that compared with other two spray conditions, the 2-D piston cavity impinging has the lowest evaporation velocity. It should be note that the liquid film cannot be detected by LAS technique, thus the real unevaporated fuel under

impinging conditions is larger than the image exhibition. At 1.5 ms ASOI, the injected fuel of free spray is completely evaporated, and it is difficult to estimate the scattered droplets exist or not under flat wall impinging condition because noise, however, under 2-D impinging condition, it is clear that the scattered droplets still exist inside the chamber especially at the wall vicinity region. Therefore, even the liquid film is not taken into account, the liquid phase combustion has high tendency to occur under 2-D impinging condition.

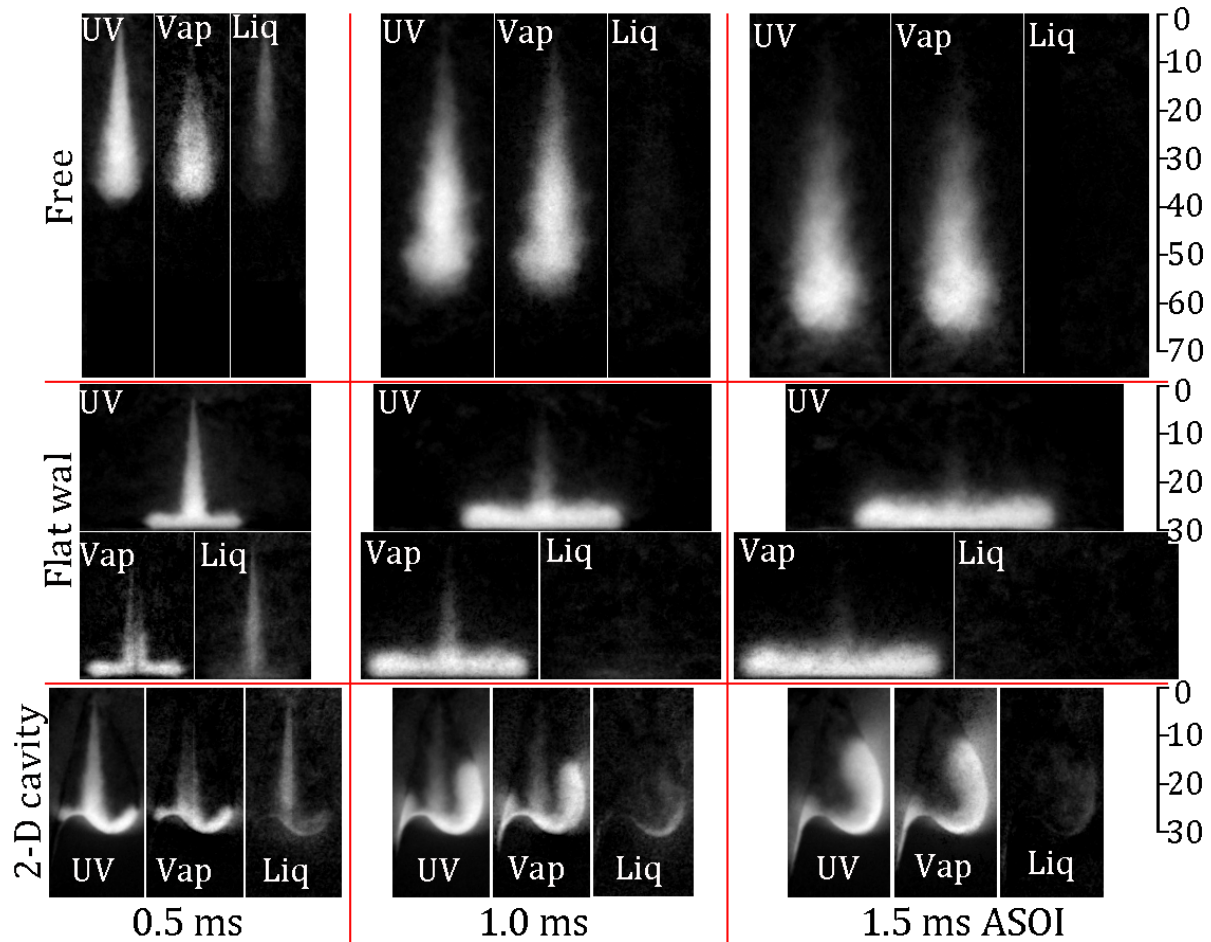


Figure 4.2 Optical thicknesses of UV, vapor (Vap) and liquid (Liq) of free, flat wall impinging and 2-D piston cavity impinging sprays under evaporative condition.

The temporal distributions of spray tip penetration and ratio of vapor to total fuel are shown in Fig 4.3 (a) and (b) respectively. It should be note that in Fig 4.3 (b), only the free spray and flat wall impinging spray are described, 2-D impinging spray is not shown, this is because that the cavity boundary is difficult to distinguish which results in large error when calculating the vapor mass. The results show that the penetration of free spray is the longest one among the three kinds of spray impinging conditions, and the flat wall impinging spray can penetrate to the shortest distance

because of the largest momentum losing. Coincides with the spray tip penetration, the free spray has the fastest evaporation velocity, at around 1.2 ms ASOI, the injected fuel is completely evaporated. The evaporation ratio of flat wall impinging spray at 2.0 ms ASOI is around 70 percent, this means that even large time (2.0 ms) has been elapsed, near 30 percent of the injected fuel exist as the scattered droplets or as the liquid film. According to Fig 4.2, the evaporation velocity of 2-D piston cavity impinging spray is the lowest one, thus it can be deduced that the liquid fuel percentage of 2-D impinging spray is even higher than 70 percent at 2.0 ms ASOI.

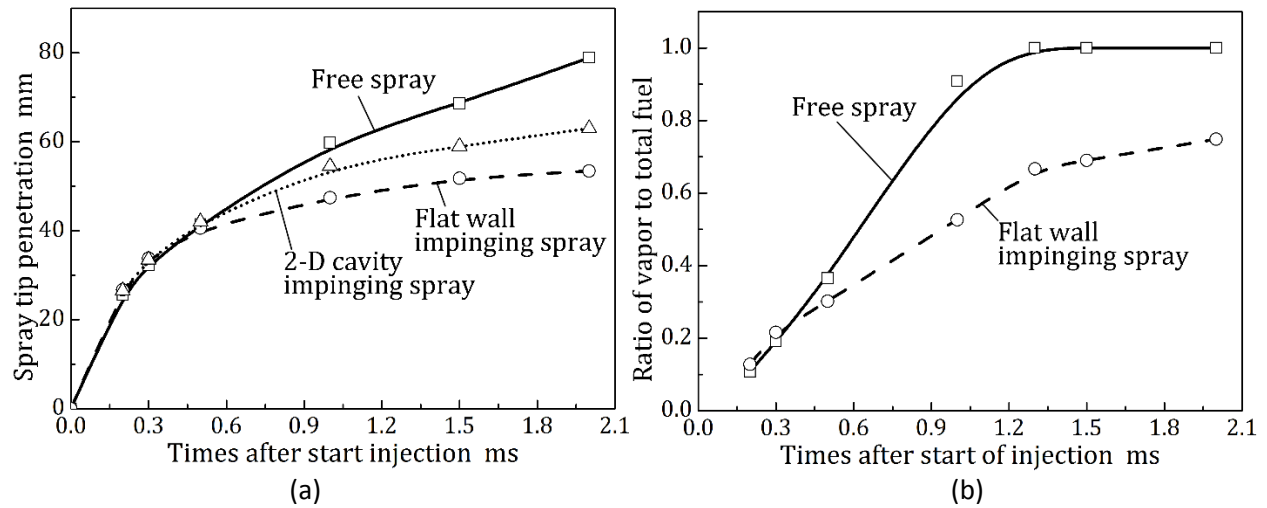


Figure 4.3 Temporal distributions of spray tip penetration and ratio of vapor to total fuel.

To clarify the droplets distribution, the Mie scattering method was applied to detect the droplets devolution processes under evaporating condition. Under free spray and flat wall impinging conditions, the incident light illuminated the droplets through the sideward window of the chamber vessel to insure the strong enough light intensity. However, because of the opaque 2-D cavity, mirrors are necessary to reflect the illuminant light and this process can result in energy losing which makes the illuminant light not strong enough to illuminate the small droplets. Therefore, in this section, only the free and flat wall impinging sprays are described.

Figure 4.4 shows the liquid phase distribution of free spray (upper row) and impinging spray (lower row) which were achieved by applying Mie scattering method under evaporating conditions. During the main injection period, the scattering light intensity is high enough to be clearly observed. However, after the end of injection, the scattering light is too weak to be observed, therefore, those weak intensity images are intensified three times to be observed clearly.

As shown in Fig 4.4, same results with LAS image which is shown in Fig 4.2, the liquid/wall interaction occurs under impinging condition. The droplets pileup on the flat wall and splash along

the surface. At 1.0 ms ASOI, the existing droplets of free spray are limited which coincides with Fig 4.2, however, in impinging spray, a large amount of liquid phase of fuel is still surviving along the flat wall surface. At 1.5 and 2.0 ms ASOI, the liquid phase of impinging spray still exists upon the surface, but the free spray is completely evaporated. Which confirms that the evaporating velocity of impinging spray is slower than that of free spray as described in Fig 4.3. The deposited droplets take a long time to be evaporated completely because the Leidenfrost phenomenon [Tomonaga et al, 1996; Xiong and Yuen, 1991] occurs. The existing liquid phase of impinging spray includes droplets and liquid film.

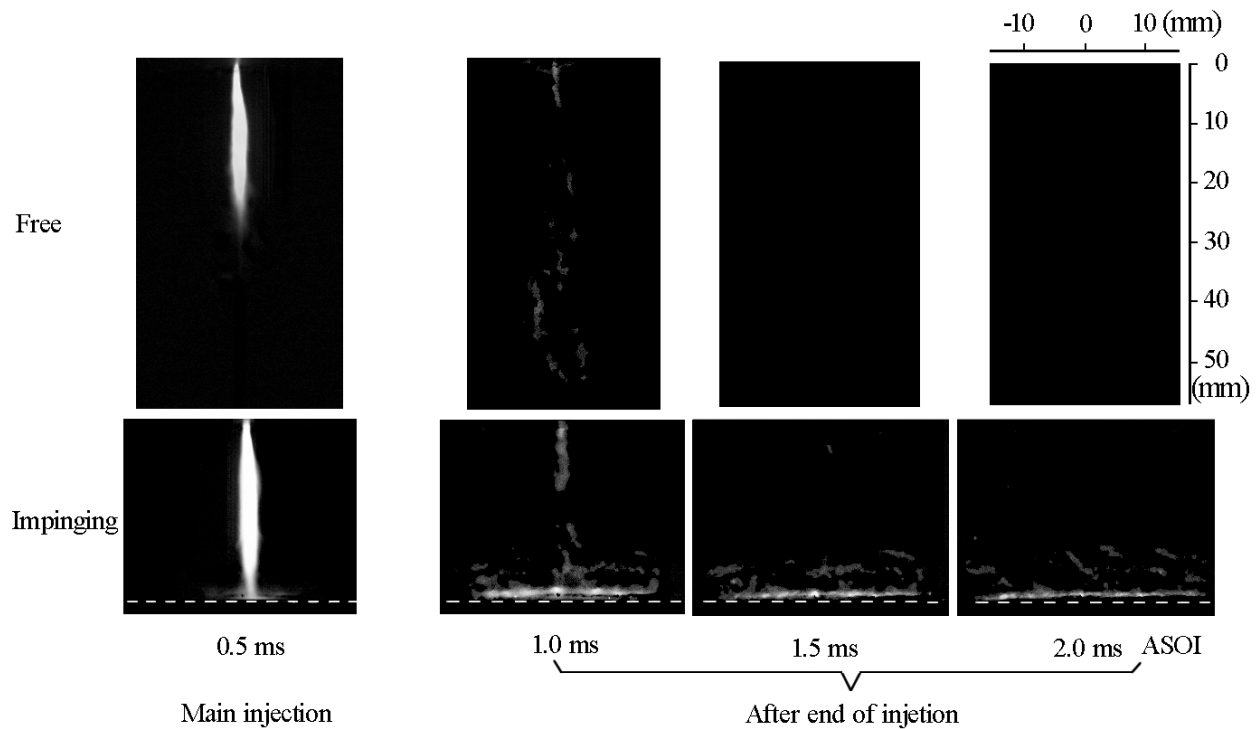


Figure 4.4. Temporal distributions of Mie scattering image of liquid phase in evaporating sprays. White dashed line represents the flat wall surface. The image intensity of 1.0, 1.5 and 2.0 ms are intensified.

From Fig 4.4, a thin black layer can be seen close to the wall, this is possibly attributed to the existence of liquid film because the continuous droplets have weak ability to scatter incident light. After flame formed, the film undergoes pool flame [Stojkovic et al., 2005] which could results in high particles emission and low thermal efficiency. What's more, the droplets combustion also could results in large particles formation.

### 4.3.2 Spray Concentration Distribution

Spatial distributions of fuel mass per unit area of free, flat wall impinging and 2-D piston cavity impinging sprays are shown in Fig 4.5. In each pair of the images of free spray and flat wall impinging spray, the left side is the droplet concentration and the right side is the vapor phase concentration. In the 2-D piston cavity impinging spray, only the vapor mass per unit area is shown. As discussed above, the calculated vapor mass of 2-D piston cavity impinging spray has large error because of the difficulty of cavity boundary definition, as a result, the liquid phase concentration is incorrect. However, it should be note that the vapor mass per unit area at the specific point is believable.

Figure 4.5 gives the fuel distribution information. It is found that during the main injection process (0.5 ms ASOI), vapor phase fuel mainly distributes in the mid-downstream of the spray under free and impinging conditions. The dense liquid regions of free and flat wall impinging spray locates at the spray middle region which are directly analyzed from Fig 4.5 (a) and (b), and the dense liquid fuel region of 2-D piston cavity impinging spray also appears in the spray middle region which is detected from Fig 4.2 (a). Therefore, the global fuel (vapor and liquid) dense region distributes at the spray midstream during the main injection duration. At 1.0 ms AOSI, which is around EOI, the vapor phase dominates the fuel mass distribution of free spray, and the dense fuel region is observed at the spray downstream. Under flat wall impinging condition, the droplets are stagnated at the impinging point region, and the vapor fuel mainly distributes at the wall vicinity region. Combined with Fig 4.2, it is found that the dense fuel region of 2-D impinging spray appears at the large curvature and head vortex regions. Under all the timings, it seem that the global vapor concentration of 2-D piston cavity impinging spray is higher even the evaporation velocity is slower than the other two conditions. This is because the spray is confined inside the piston cavity and projected area is small.

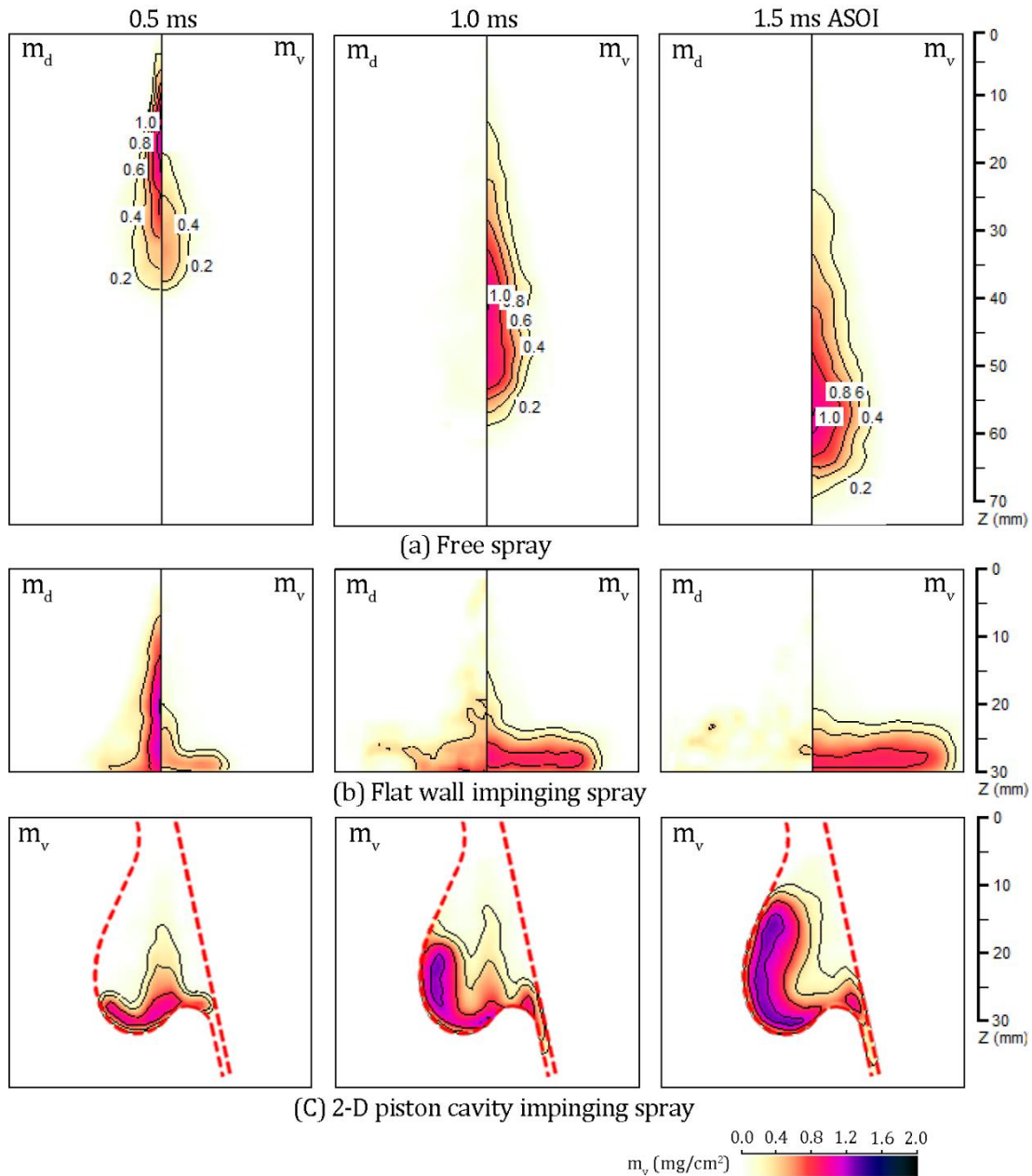


Figure 4.5 Spatial distributions of liquid and vapor masses per unit area .

Figure 4.6 gives the vapor mass per unit area along the spray flow path at 1.0 ms ASOI, the flow path of impinging spray after impingement is defined as the streamline which is 2 mm away from the wall surface. It is clear that the vapor phase dense regions of free and flat wall impinging sprays appear at the spray downstream region. And two peaks of vapor concentration were detected at the downstream of 2-D impinging spray, which represents the dense vapor fuel at the large curvature region and spray tip region respectively.

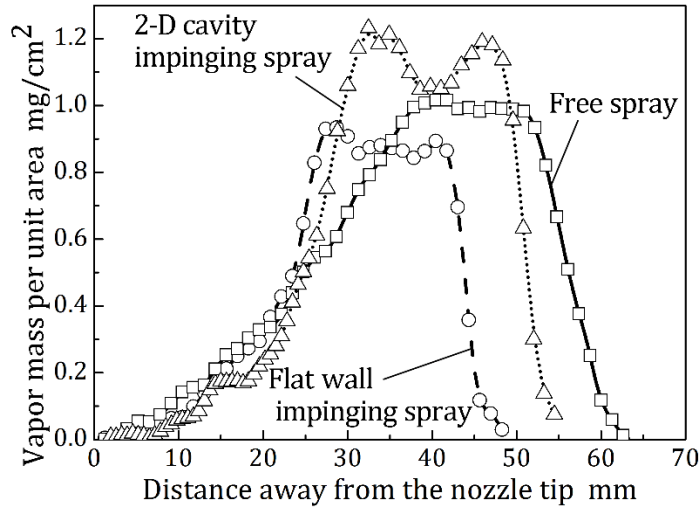


Figure 4.6 Distribution of vapor mass per unit area along the spray flow path at 1.0 ms ASOI.

The sectional vapor phase equivalence ratio distributions of free and flat wall impinging spray are shown in Fig 4.7. The equivalence ratio of 2-D impinging spray cannot be analyzed by LAS technique because of the unsymmetrical spray structure.

From Fig 4.7, it is found that the during the main injection process, the vapor phase equivalence ratio free spray is mainly ranged between 0.4 and 0.6. However, the equivalence ratio of flat wall impinging spray at the near impinging point region is higher than 0.8, it higher than free spray, besides, the equivalence ratio at the wall vicinity region is below 0.4, it is lower than the free spray at the same location. Which are corresponding with the LIEF results published by Bruneaux [2005]. Around end of the injection, the global vapor phase equivalence ratios of free and flat wall impinging spray are enlarged, the central region is higher than 1.6 and 0.8 for free spray and flat wall impinging spray respectively. The equivalence ratio at wall vicinity region is much lower than 0.4, and the relatively rich vapor region appears at the spray head vortex, between the head vortex and the impinging point, the vapor equivalence ratio is very small. At 1.5 ms ASOI, the maximum equivalence ratio of vapor phase is decreased, the inner region of free spray is between 0.4 and 1.4, however, the vapor-air mixture is very lean for impinging condition at this timing, this possibly because the combined effect of low evaporation velocity and the enhanced ambient gas entrainment which will be discussed next.

Vapor phase equivalence ratio distributions along the flow path at 1.0 ms ASOI and ratio of entrained gas to total fuel of free and flat wall impinging spray are shown in Fig 4.8 (a) and (b) respectively. As shown in Fig 4.8 (a), the impingement effect on the distributions of equivalence ratios of free and flat wall impinging spray at the un-impingement region (0-25 mm) are not significant.

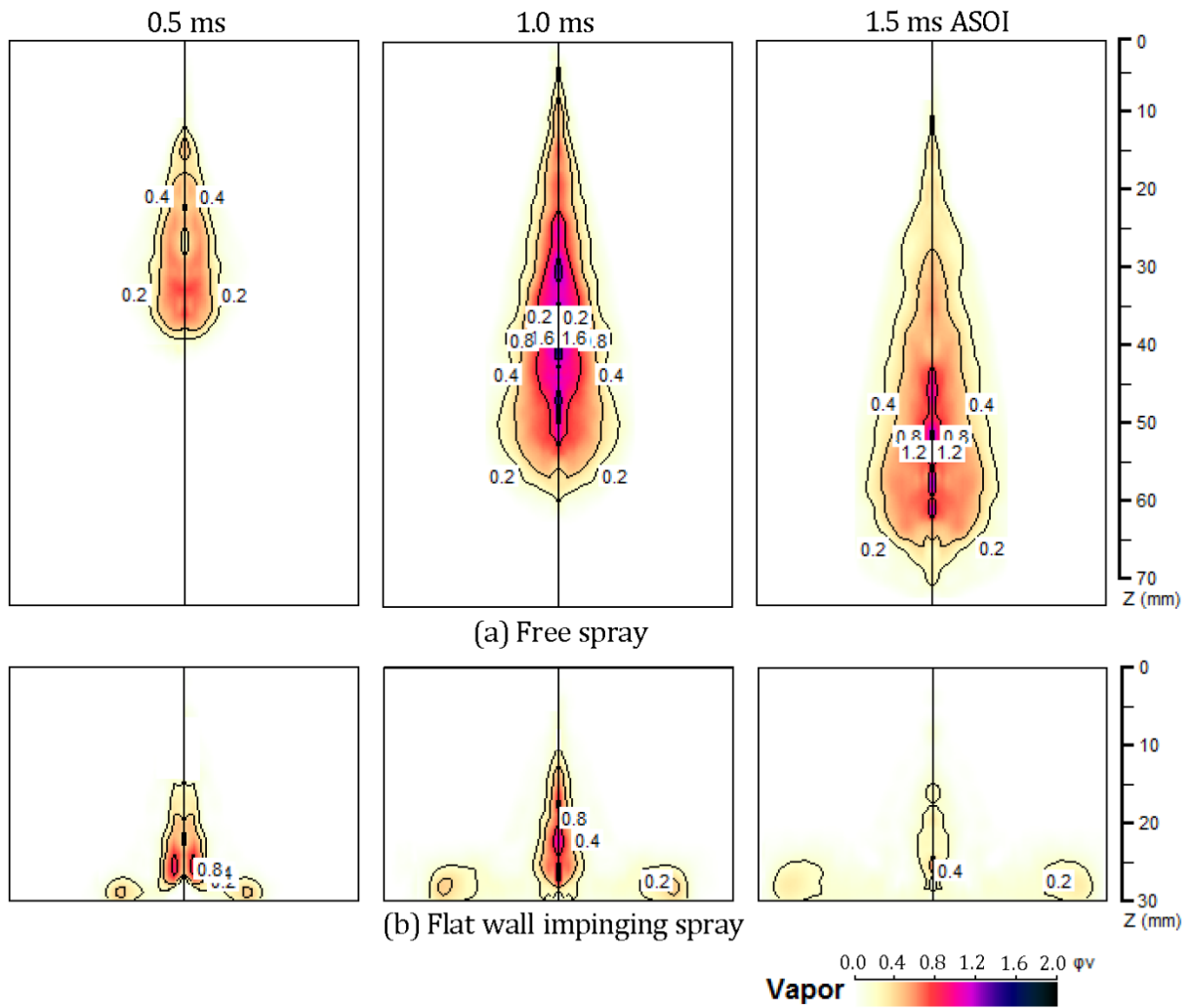


Figure 4.7 Vapor phase equivalence ratio distributions of free and flat wall impinging spray.

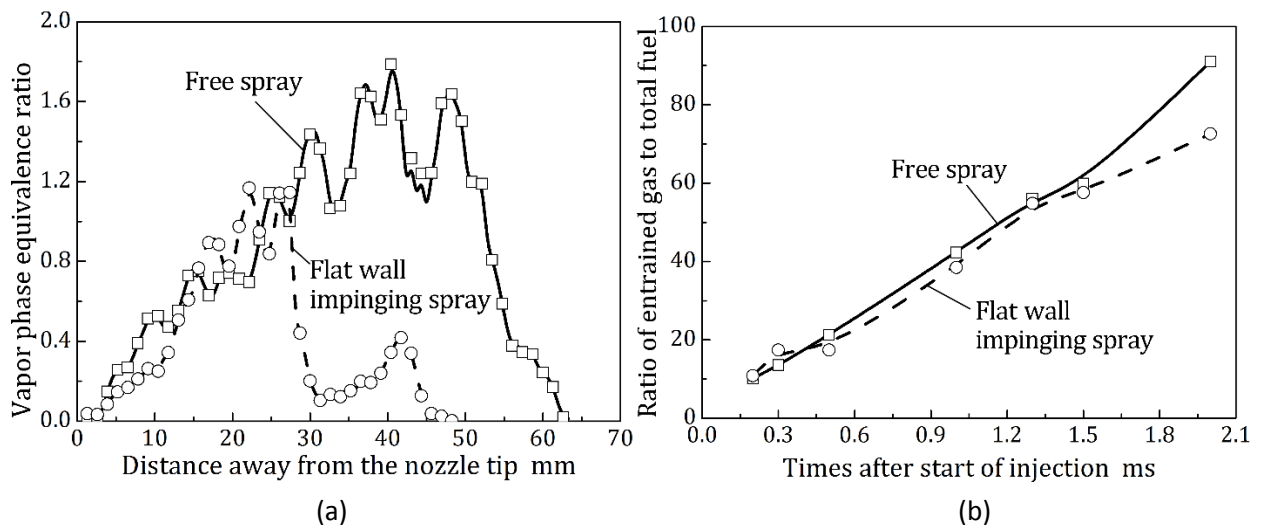


Figure 4.8 Vapor phase equivalence ratio distributions along the flow path at 1.0 ms ASOI and ratio of entrained gas to total fuel of free and flat wall impinging spray.

However, after impingement occurs, significant variations of vapor phase equivalence ratios at the spray downstream between free and flat wall sprays are observed. The flat wall impinging vapor-air mixture at wall impinging region is much leaner than that at the same location of free spray. Combined with the vapor mass image (Fig 4.5) and the equivalence image (Fig 4.7), it can be concluded that compared with free spray, the ambient gas entrainment at the wall impinging region is enhanced by impingement, but at the free spray region, the ambient gas entrainment is reduced. Fig 4.8 (b) gives the temporal variations of the ratio of entrained gas to total fuel under free and flat wall impingement conditions. It is found that the ambient gas entrainment of free spray is more than that of flat wall impinging spray under all the timings except the initial stage of injection. Thus the conclusion is that even the gas entrainment at wall impinging region is enhanced by impingement, but the enhancement cannot offset the entrainment reduction at the spray free region and the ambient gas entrainment reduction contributed by short spray tip penetration. This also has been confirmed by former researcher [Bruneaux et al., 2011].

It is interesting that the ratio of total fuel to total fuel image (Fig 4.3 (b)) and the ratio of entrained gas to total fuel image ( Fig 4.8 (b)) exhibit the same tendency during the injection initial stage (before 0.3 ms ASOI), which is that the impingement has a positive effect on the evaporation and ambient gas entrainment. It should be note that the impingement occurs at around 0.3 ms, therefore, even before impingement, the existence of wall plays a role in mixture formation. This wall existence effect is realized by enlarging the reaction between the spray tip and the ambient gas.

## **4.4 COMBUSTION FLAME CHARACTERISTICS**

### **4.4.1. Flame Natural Luminosity and OH\* chemiluminescence**

Figure 4.9 shows flame natural luminosity and OH\* chemiluminescence spatial distributions of free spray flame, flat wall impinging spray flame and 2-D impinging spray flame. All the images have been cut off the background and the boundary of OH\* chemiluminescence is defined as the 5/256 of the image intensity. The white lines in the natural luminosity figures represent the OH\* chemiluminescence boundaries at the same timing.

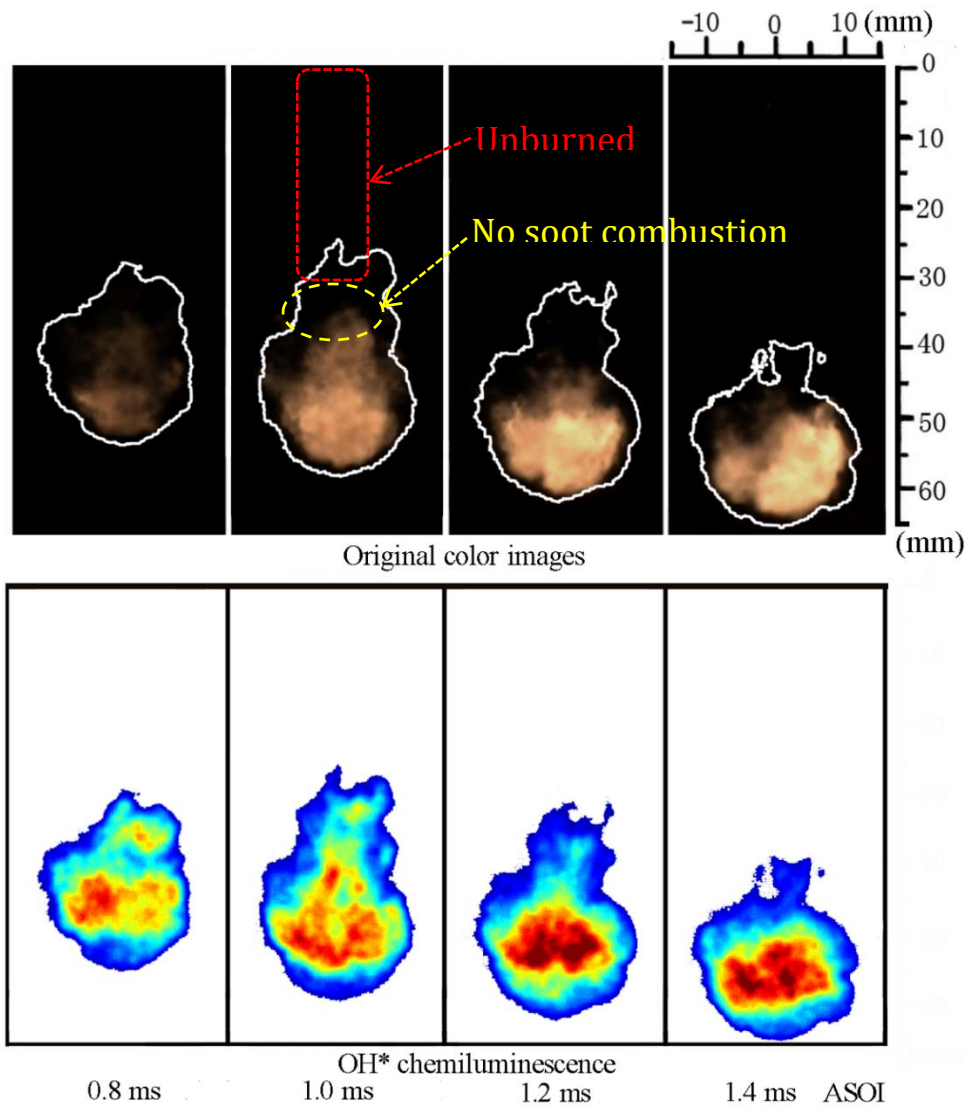
Under free spray combustion condition, both the high OH\* intensity and the high soot concentration region appear at the downstream of the spray, which coincides with the described diesel combustion models of Dec [1997] and Kosaka et al., [2005]. According to the white OH\* boundary lines in the original color image and KL factor image, the OH\* chemiluminescence projected area is larger than that of natural luminosity and KL factor. At the upstream region of the flame, there

is an obvious part which has OH\* chemiluminescence but no natural luminosity as typically pointed out by yellow arrow in the original color image at 1.0 ms after start of injection (ASOI). This implies that there is a no soot combustion region at the upstream of the flame, which is because the air entrains into the spray mainly through upstream region of the spray and the burnable mixture in this region is lean. The flame spreads to downstream with the moving of spray, and it spreads to the most upstream at 1.0 ms ASOI which is deduced by the OH\* chemiluminescence distribution. This is because that after the injection (injection duration is 0.91 ms), the momentum reduced suddenly, then much ambient gas entrained and fuel evaporated more quickly [Moon et al., 2009]. As a result, the flame reached to the maximum upstream as the 1.0 ms ASOI shows. It should be noted that even at 1.0 ms ASOI, there is a no OH\* chemiluminescence and no natural luminosity region at the upstream as the red arrow pointed out. According to the spray image in Fig 4.2, the ended injected fuel exists in this region for a long time, therefore, this spray tail region can be regarded as unburned region. This phenomenon is contributed by combined effects of (1) as discussed above, ambient gas entrainment is enhanced after the end of injection and a lean mixture which is unable to auto-ignition forms near the nozzle exit, and (2) the flame goes down with the spray, and this velocity is faster than that of diesel flame spreading (spray velocity at this flame maximum upstream location is about 30 m/s at 1.0 ms ASOI which is calculated from Mie Scattering results, however, the diesel burning velocity is between 7 and 13 m/s calculated by Arcoumanis et al [1994]) which results in flame quenching at the interface of burning and unburned region.

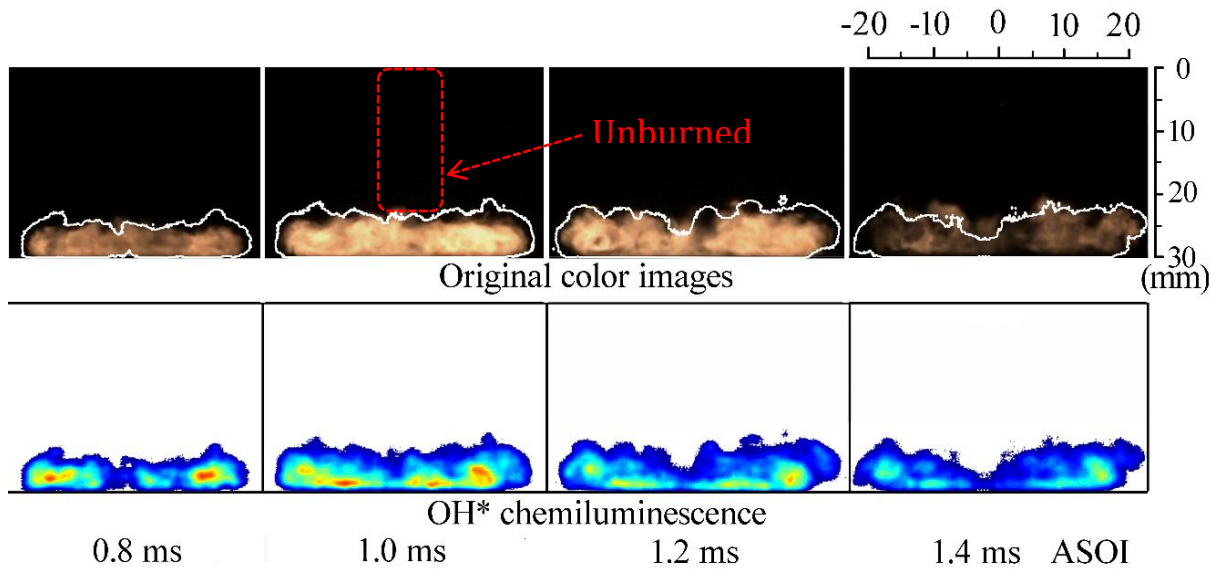
When it comes to flat wall impingement, as shown in Fig 4.9 (b), the combustion process seems moderate. The flame is confined in the near surface area, and the relative high OH\* intensity region is close to the wall surface. There is no OH\* chemiluminescence and natural luminosity in the free region, therefore, the same with free spray flame, the mixture existed in the upstream region cannot be burned, this result agrees with the results of Bruneaux [2005] and Pickett and López [2005] which show that the mixture and combustion are not influenced by flat wall impinging at free region respectively. It should be note that the OH\* chemiluminescence has low intensity at the impinging point projected region even it is a line-of-sight image, this will be discussed next.

When 2-d impingement occurs, the intense reaction region is close to the chamber wall and it is disconnected at the connected point of flame tip and wall jet region. This connecting region is the main way through where the ambient gas entrained, therefore the lean unstable mixture is formed which would results in low OH\* intensity. Different with the free spray flame and the flat wall impinging flame whose later injected fuel are unburnt, the later injected fuel of the 2-D piston

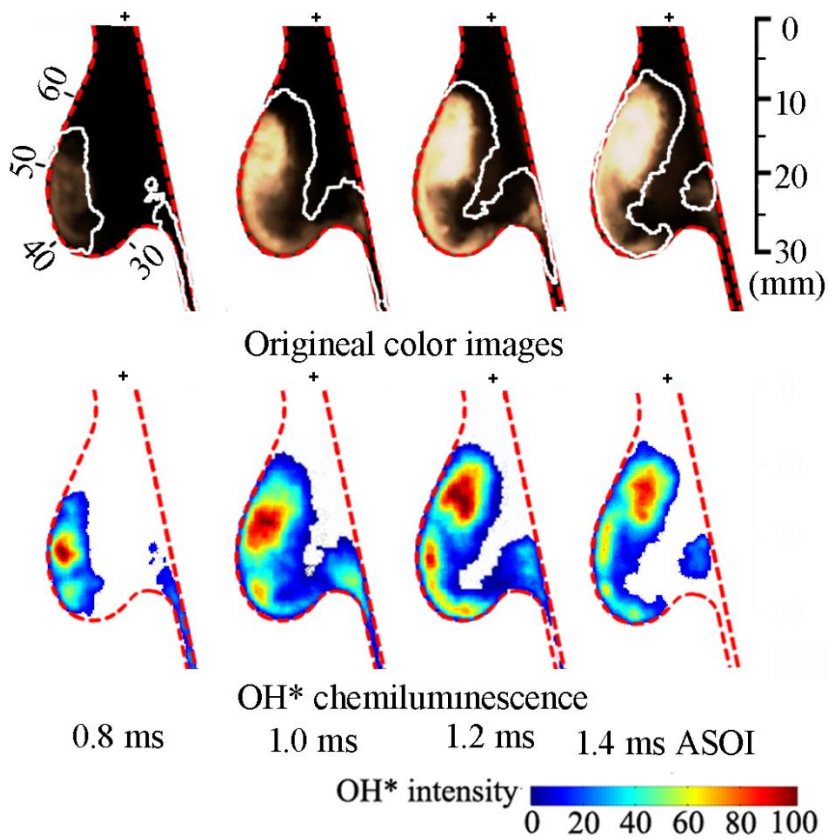
impinging spray partially entrained into the spray flame tip and subsequently is burned by the burning flame.



(a) Free flame



(b) Flat wall impinging flame



(c) 2-D piston impinging flame

Figure 4.9 Flame natural luminosity and OH\* chemiluminescence images of free flame, flat wall impinging flame and 2-D piston cavity impinging flame.

The temporal distribution of integrated OH\* intensity is shown in Fig 4.10. It is clear that the integrated OH\* intensity is much higher than the other two impinging spray flames. As the OH\* could act as the indicator of heat release of combustion [Tinaut et al., 2011] and could reflect the combustion behavior, this figure implies that the impinging combustion is not as complete as that of free spray flame. This is because that lean mixture is formed after impingement, and some regions are not rich enough to be burned; the wall wetting effect results in the incomplete combustion in the near wall region, because the liquid/wall interaction is happening in this experiment. The OH\* intensities of 2-d impinging flame and flat wall impinging flame are nearly the same at the initial combustion process, from 0.8 ms ASOI, the OH\* intensity of 2-d impinging flame becomes higher than that of flat wall impinging flame. Two possible reasons for this phenomenon are that: first, the fuel in the free region is burned by the head vortex flame because the tip flame turns back to the spray upstream by using the egg type piston cavity; second, the piston cavity restricts the mixture distribution and the rotatory flame results in more mixture burned especially the fuel that is injected into the chamber around the end of the injection. As discussed in Fig 4.9, there is no OH\* chemiluminescence at the free region of flat wall impinging spray flame, thus this region could not be burned as that of 2-d impinging spray flame, what's more, the OH\* intensity around the impinging point is low, from which it could be deduced that near the impinging point region, the fuel is also incompletely burned.

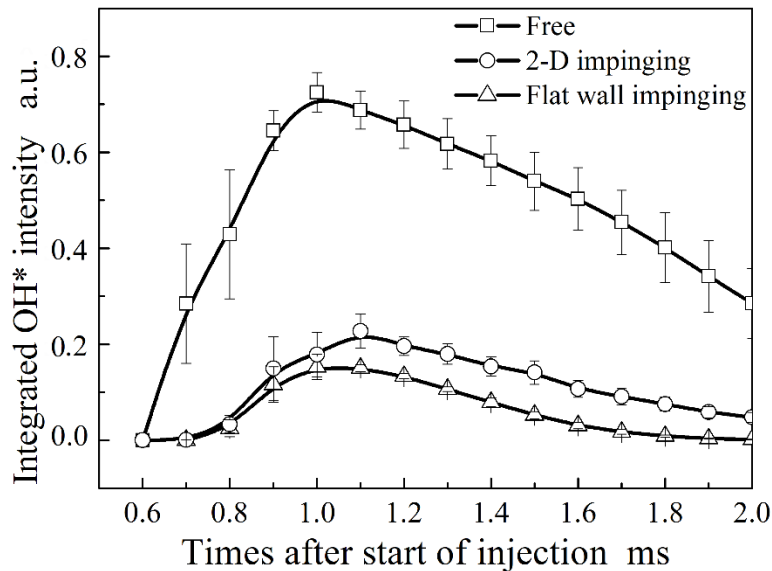


Figure 4.10 Temporal distribution of integrated OH\* intensity.

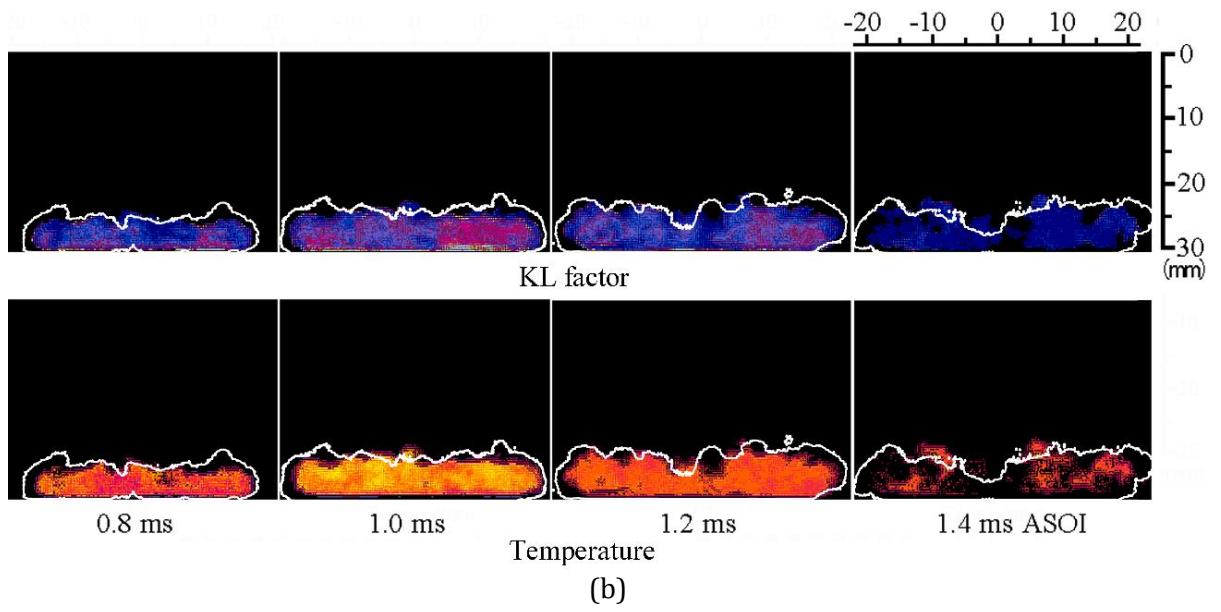
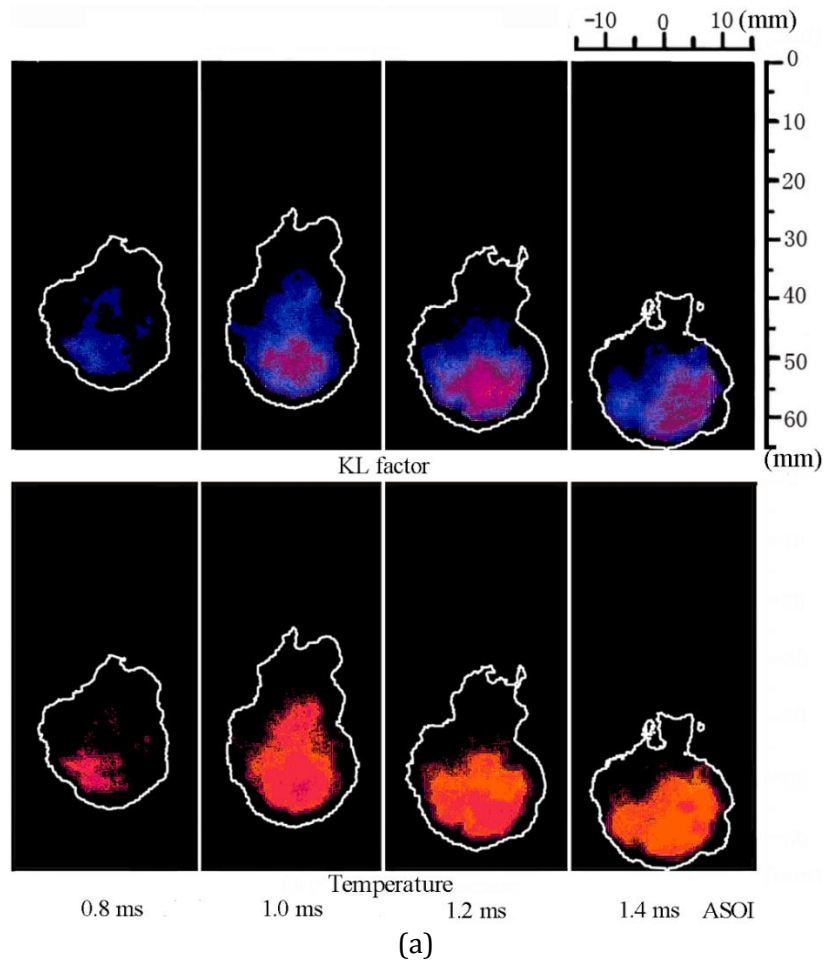
#### 4.4.1 Two-Color Method Results

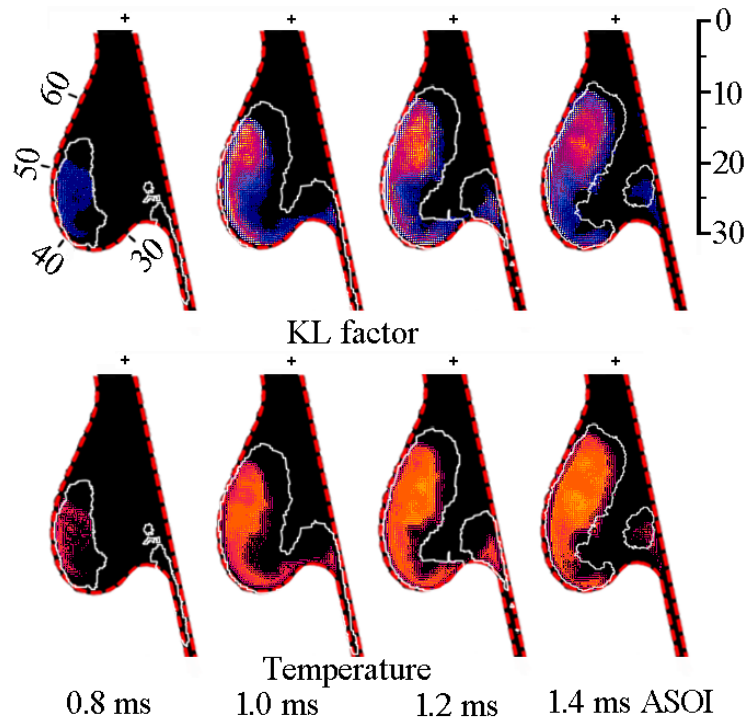
The KL Factor and temperature distributions of free flame, flat wall impinging flame and 2-D piston cavity impinging flame are shown in Fig 4.11, in each pair of the figure, the above is the KL factor image and the bottom is the temperature image. The white lines mean the OH\* chemiluminescence boundaries at the same timing.

The Fig 4.11 (a) shows that the soot of free spray flame mainly locates in the intense reaction region as Fig 4.10 shows, the large KL factor (0.5-0.7) region is in the near tip region because the large momentum. Same with the flame natural luminosity, the soot is surrounded by OH\* radical. In the temperature image, at 1.0 ms ASOI, the relative high temperature appears in at the midstream region of the sooting flame, it is because the soot is oxidized in this region [Kosaka et al, 2005] which is a exothermic process. After 1.2 ms SOI, the combustion is dominated by oxidation process, thus, the temperature increase slightly. Generally, the temporal and special temperature distributions are within 1850-2050 K.

The flat wall impinging flames are shown in Fig 4.11 (b). In the KL factor figures, a thin high KL factor layer appears close to the wall surface as a result of the liquid phase combustion as shown in Figs 4.2 and 4.4, this means that along the surface, the combustion is incomplete and high particle concentration is produced. And it seems that the right side and the left side of the projected flame image have high KL factor, it implies that large soot concentrations also appear inside the head vortex. This is both contributed by the rich combustion inside head vortex and by the soot motion caused by vortex. The temperature in the near wall region is relative low because the low heat release resulted from incomplete combustion and the heat transfer from the flame to the flat wall.

When 2-d impingement happens, the KL factor could reach more than 1.0 in the flame tip region because of the confined chamber type and long path L. A thin high KL factor layer coupled with low temperature are found near wall surface after impingement especially in the evident curvature region, this is because the liquid droplets are stagnated in this region as shown in Fig 4.2 and the low heat transfer hinders the formed soot oxidation.





(c)



Figure 4.11 KL factor and temperature images of free flame, flat wall impinging flame and 2-D piston cavity impinging flame.

Figure 4.12 shows the spatial distribution of OH\* chemiluminescence intensity and KL factor at 1.0 ms ASOI. In Fig 4.12, the left one is the spatial distributions (averaged results) of OH\* intensity (upper) and KL factor (lower), the right one is the definition of horizontal axis of the left figure. This kind of horizontal definition is aim to analyze the variations of combustion behaviors of impinging and free spray flames along the spray flowing path.

From Fig 4.12, compared with flat wall impinging spray flame, the OH\* chemiluminescence intensity of free flame is higher in all regions except for the initial flame appeared region along the horizontal axis. This implies that the reaction intensity of free spray flame is higher than that of flat wall impinging spray flame. Even this is line-of-sight image, the impinging OH\* chemiluminescence intensity has two peak values along the horizontal line (right padding circle), which corresponds to the two rich mixture structures of impinging spray at cross section [Katsura et al., 1989]. Both of the

OH\* intensity and the KL factor of impinging flame have their troughs near the projected impinging point (the start point of the half-padding circle). This can deduce that the impinging flame near the impinging point region undergoes fire missing because (1) if intense reaction occurs, high KL factor will be produced, for the reason that there is a certain amount of liquid fuel in the impinging point region and the mixture in this region is rich since air entrainment is limited [Bruneaux, 2005], however, the result shows that this region has the local minimum KL value in the radial distribution; (2) if this region is burned, the OH\* intensity should reach its relatively high value because of the line-of-sight image and the relative rich mixture. According to the deduction, the impinging flame has lower ability of upstream spreading than that of free flame (impinging spray unburned length >30 mm, free spray unburned length < 25 mm). Even though the combustion in this experiment doesn't have the quasi-steady period, the OH\* chemiluminescence could also reflect the lift-off-length (transient). Therefore, it comes to be the conclusion that the flame lift-off-length is influenced by flat impingement which is inconsistent with Pickett and López [2005] who claimed that the lift-off-length isn't influenced by impingement. This is possibly resulted from the influence of liquid/wall interaction, it could be explained as follows: (1) dense fuel stagnated at the impinging point region [Bruneaux, 2005] which results in low temperature due to evaporation, then the ignition cannot occur automatically; (2) different from free spray whose structure can be assumed as successional, the impinging spray seems disconnect between head vortex and the impinging region (as shown in Fig 4.6) caused by a large velocity gas entrainment [Bruneaux et al., 2011], therefore the mixture in the impinging point region is difficult to be ignited by the burning gas near the spray tip.

When it comes to the 2-d piston cavity impingement flames, the upmost flame is observed around 25 mm distance, different from flat wall impingement, the flame depth in this region is thin. Therefore, the upmost flame should come from the combustion near the impinging point. The KL factor and the OH\* intensity has two evident peaks along the flow path. One peaks of them is occurred correspondingly in the head vortex region, the other evident peaks of OH\* and KL factor are observed subsequently in the large curvature region. Which is corresponding perfectly with the vapor mass distribution as shown in Fig 4.6.

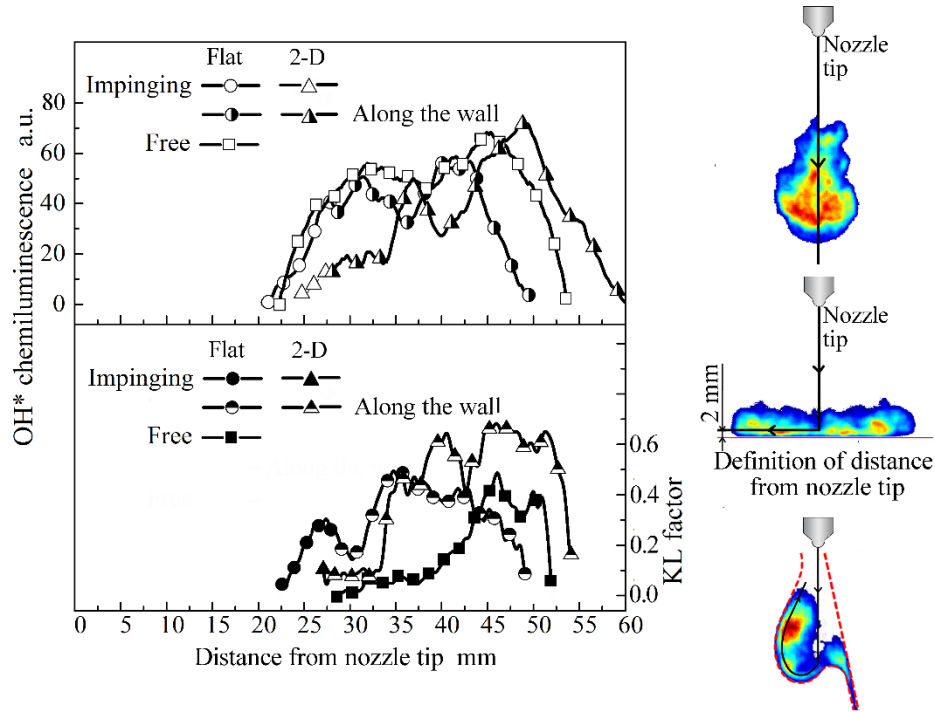


Figure 4.12. Distributions of OH\* chemiluminescence and KL factor along the defined line at 1.0 ms ASOI.

The temporal distribution of integrated KL factor and mean temperature are shown in Fig 4.13 (a) and (b) respectively.

Fig 4.13 reveals that the flat wall impingement has the most soot formation, the 2-d impingement takes the second place and free spray flame has the least. However, the soot emission trend is reversed. This is because that more air entrained into the spray after impingement and results in more available oxygen atom. From Fig 4.13 (b), the average temperatures of impinging spray flames are low because the heat transfers from the flame to the wall as well as the non-ideal combustion is not capable to achieve the maximum flame temperature as free flame shows.

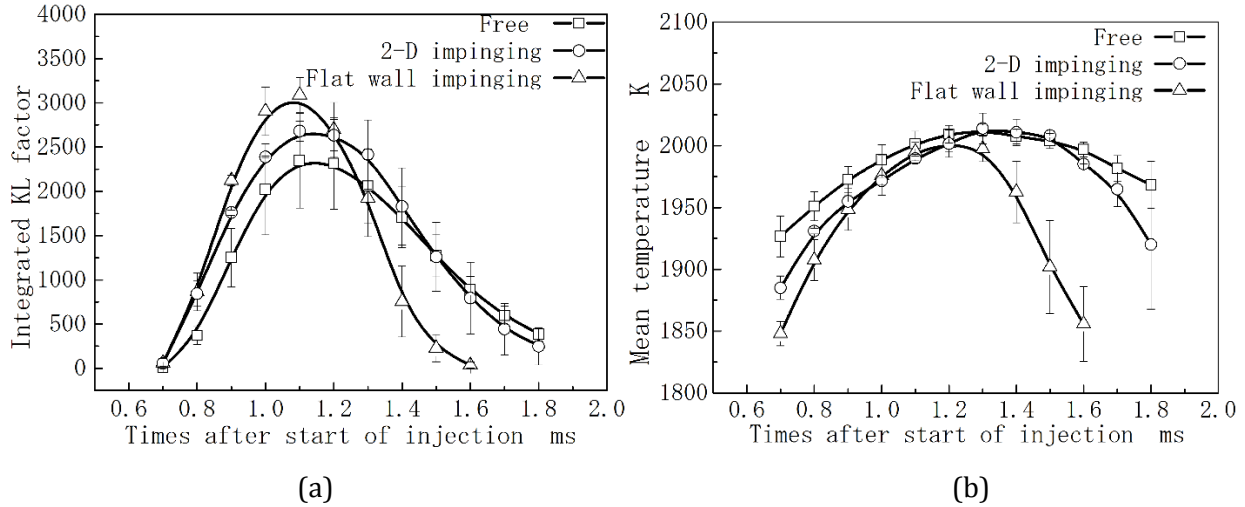


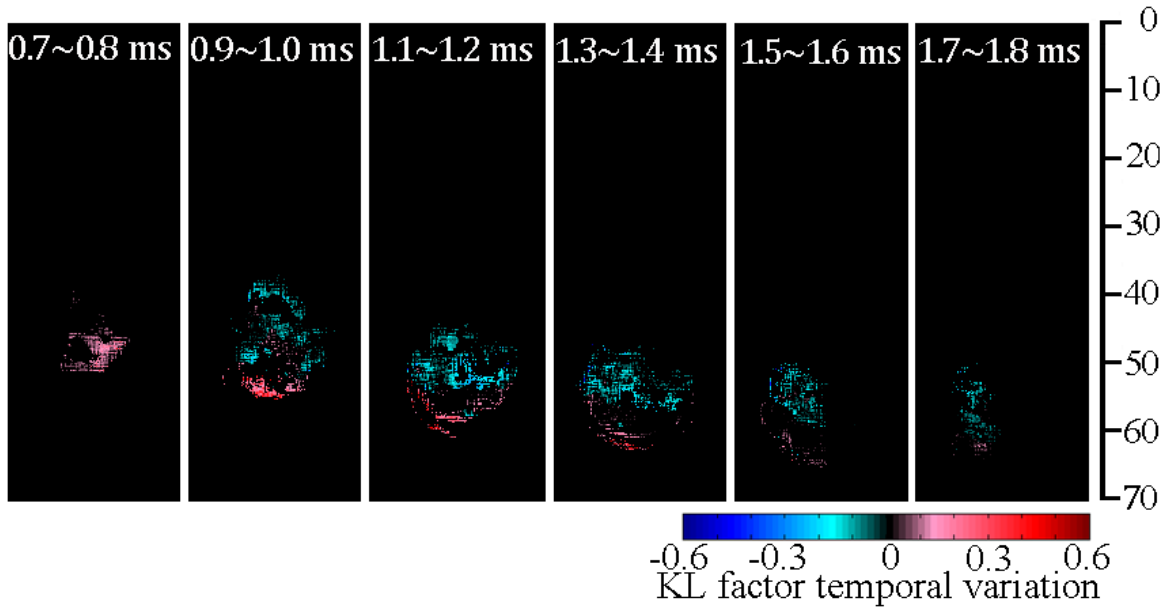
Figure 4.13 Temporal variations of integrated KL factor and mean temperature of free spray flame, 2-D impinging spray flame and Flat wall impinging flame.

The temporal KL factor variations of free spray flame, flat wall impinging spray flame and 2-D piston cavity impinging spray flame are shown in Fig 4.14. The calculating method was introduced in Chapter 3. In this figure, the color blue and red represent soot oxidation and formation respectively.

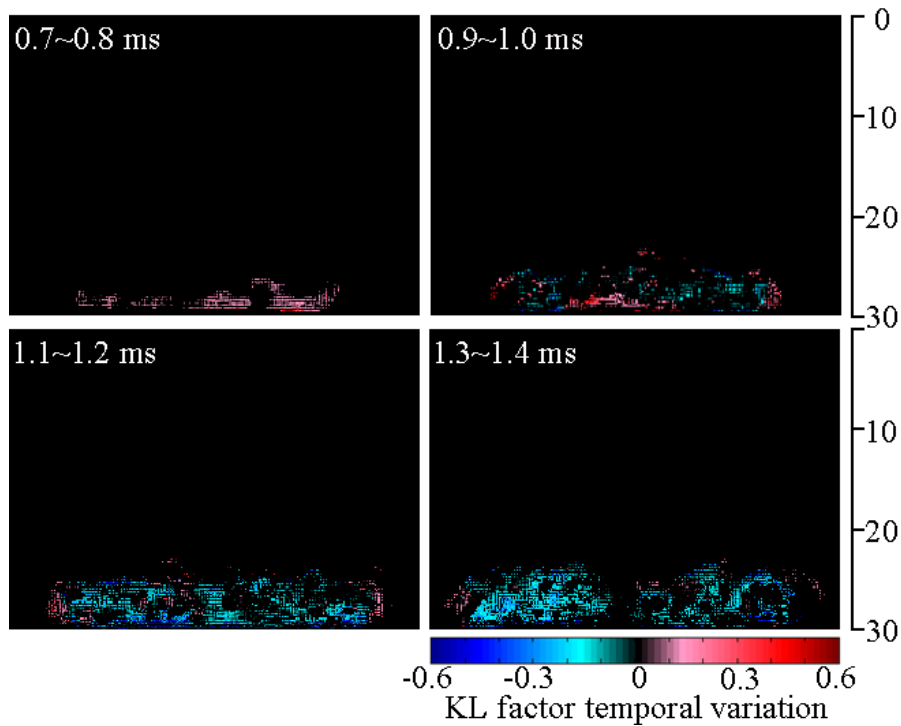
According to Fig 4.14 (a), at soot formation dominant stage, the soot is formed in the sooting flame downstream region, where the mixture is rich. And the soot oxidation region is located at the upstream of the sooting flame, this is because the air entrained into the spray mainly through the upstream, and the combustion in the flame upstream is no soot (just OH\* chemiluminescence). And at the post sooting combustion stage, the soot formation is very limited, and the soot oxidation is dominant at the whole soot flame region.

Under flat wall impinging combustion region, particles are initially formed at the wall vicinity region, this is because the droplet combustion and pool flame contributed by the droplets and liquid film respectively. When time increases, the KL variation image of 0.9~1.0 ms ASOI, the soot is formed in the close wall region and the sooting flame tip region. The soot formation at the sooting tip region is because that the head vortex results in the rolling up of droplets which are deposited at wall vicinity region as shown in Fig 4.4, what's more, the droplet size is relative large at the head vortex because of the coalescence [Arcoumanis and Chang, 1994]. At later stage, the oxidation cover the whole sooting flame except at the tip region. When it comes to 2-D piston cavity impinging spray flame, at the soot formation dominant stage, the soot is formed at the wall vicinity region and the periphery of the head vortex, and soot is oxidized at the inner region of the head vortex, the soot formation is coinciding with the liquid optical thickness at the wall spray region as shown in Fig 4.2 (c). At the

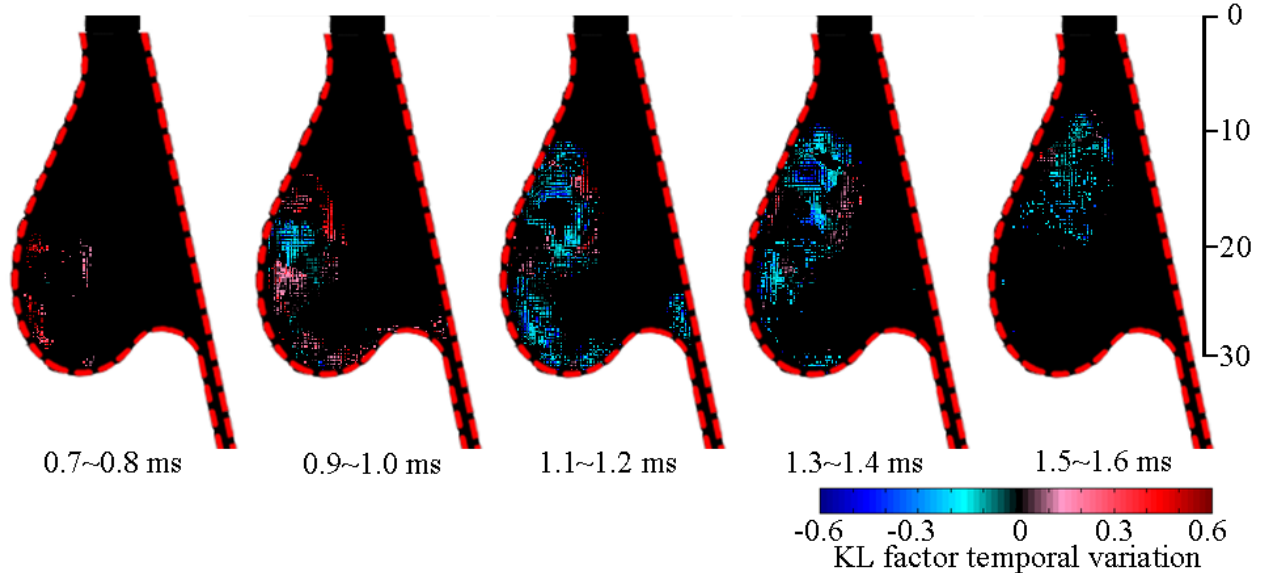
soot oxidation dominant stage of 2-D piston cavity impinging spray flame, the soot is still formed at the right periphery region of the head vortex, this is because the rolled up droplets combustion and also because the later injected fuel directly burned by the flame tip. And the soot flame luminosity is mainly emitted by soot oxidation.



(a) Free spray



(b) Flat wall impinging spray



(c) 2-D piston cavity impinging spray

Figure 4.14 Soot formation and oxidation denoted by KL factor temporal variation.

## 4.5 SUMMARY

The mixture formation combustion and soot emission processes were investigated by applying LAS technique, Mie scattering method, OH\* chemiluminescence and two color method in this Chapter. The free spray flame, flat wall impinging spray flame and 2-D piston cavity spray flame were concentrated on to study the effect of impingement on spray evolution, combustion and soot emission process. The main conclusions are summarized as followings:

1. The free spray has the longest tip penetration and the flat wall impinging spray has the shortest tip penetration. The free spray evaporates faster than the impinging spray, the liquid fuel is evaporated immediately after the EOI. Between the impinging spray, the flat wall impinging spray evaporates faster than 2-D impinging spray. Droplets still exist after a long time of EOI, and the liquid fuel locates at the wall vicinity region.
2. Compared with free spray, the ambient gas entrainment is enhanced at the wall spray region, however, the ambient gas entrainment is reduced at the free spray region. Generally, the air entrainment of free spray is higher than flat wall impinging spray. The vapor phase equivalence ratio of mixture at the wall spray region is much lower than the free spray.
3. The mixture formation characteristics were influenced by the flat wall impingement even before the impingement. The evaporation velocity and the air entrainment at the initial stage

(before impingement) of injection of flat wall impinging spray is higher than those of free spray.

4. The impinging spray flame could not be completely burned like the free spray flame because of the liquid combustion and also because some lean nonflammable regions are formed. The 2-d impinging effect could results in more end injected fuel burned compare with flat wall impinging flame.
5. Both the flat wall impinging spray flame and the 2-D piston cavity impinging spray flame cannot spread to the upstream as upper as the free spray flame, this is because the vapor phase distribution and liquid phase existence are influenced by impingement.
6. Impingement spray flame produces more soot but also enhances the soot oxidation velocity, so the soot emission of impinging spray flame is lower than that of free spray flame.
7. Under free spray combustion condition, the soot is mainly formed in the sooting flame downstream region, and oxidized at the upstream region of the sooting flame. Under the flat wall impinging spray combustion and 2-D piston cavity impinging spray combustion conditions, the soot is formed in the wall vicinity region and the head vortex periphery region. The soot formation regions are corresponding with the liquid phase region and the with the dense vapor phase region.

# CHAPTER 5 CHARACTERISTICS OF DIESEL IMPINGING SPRAY FLAME UNDER VARIOUS INJECTION PRESSURES

## 5.1 INTRODUCTION

Injection pressure increasing is thought as an effective method to improve the combustion characteristics. High-pressure fuel injections are recommended for improving the D.I. Diesel engine performance and reducing particulate matter [Su and Farrell, 1998]. In addition, the increased injection pressures usually shorten the time required for the droplet vaporization and combustible mixture preparation and then reduce the ignition delay. In this Chapter, the attentions were paid to investigate the effect of injection pressure on Diesel impinging spray flame characteristics.

## 5.2 EXPERIMENTAL CONDITIONS

The injector and impinging wall specifications are shown in Tab 5.1. The experimental conditions for LAS technique and the experimental conditions for combustion experiment are shown in Tabs 5.2 and 5.3 respectively. In this part of study, only the flat wall and the 2-D piston cavity impinging sprays were carried out, the impinging distance was kept at 30 mm. It should note that the maximum injection pressure for LAS technique was 170 MPa, this is because that n-tridecane will become solid when the injection pressure higher than 170 MPa under room temperature [Morawski et al., 2005]. Therefore, 100, 150 and 170 MPa were selected for LAS technique to investigate the effect of injection pressure on mixture formation.

Table 5.1 Injector and impinging wall specifications.

Nozzle Type	Single Holes Nozzle
Hole Diameter (mm)	0.133
Injector Type	Piezo Actuator Type
Impinging Wall	Flat Wall
Impinging Distance (mm)	30

Table. 5.2 Experimental conditions for LAS technique.

Ambient Gas	Nitrogen
Ambient Temperature (K)	760

Ambient Pressure (MPa)	3.6
Ambient Density (kg/m <sup>3</sup> )	16
Fuel Type	97.5% n-Tridecane +2.5% 1-Methylnaphthalene
Injection Pressure (MPa)	100, 150 ,170
Injection Quantity (mg)	2.97

Table. 53 Experimental conditions for combustion.

Ambient Gas	Air (O <sub>2</sub> )
Ambient Temperature (K)	873
Ambient Pressure (MPa)	4.1
Ambient Density (kg/m <sup>3</sup> )	16
Fuel Type	JIS # 2
Injection Pressure (MPa)	100, 150 ,200
Injection Quantity (mg)	2.97

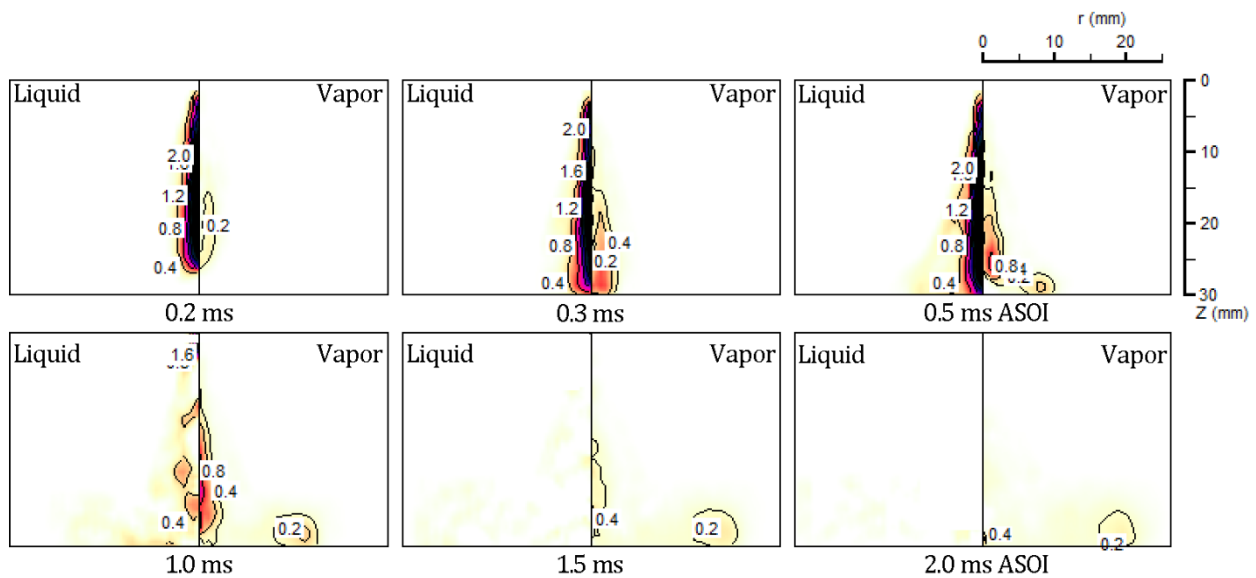
## 5.3 FLAT WALL IMPINGIGN SPRAY FLAMES CHARACTERISTICS UNDER DIFFERENT INJECTION PRESSURES

### 5.3.1 Mixture Formation Process

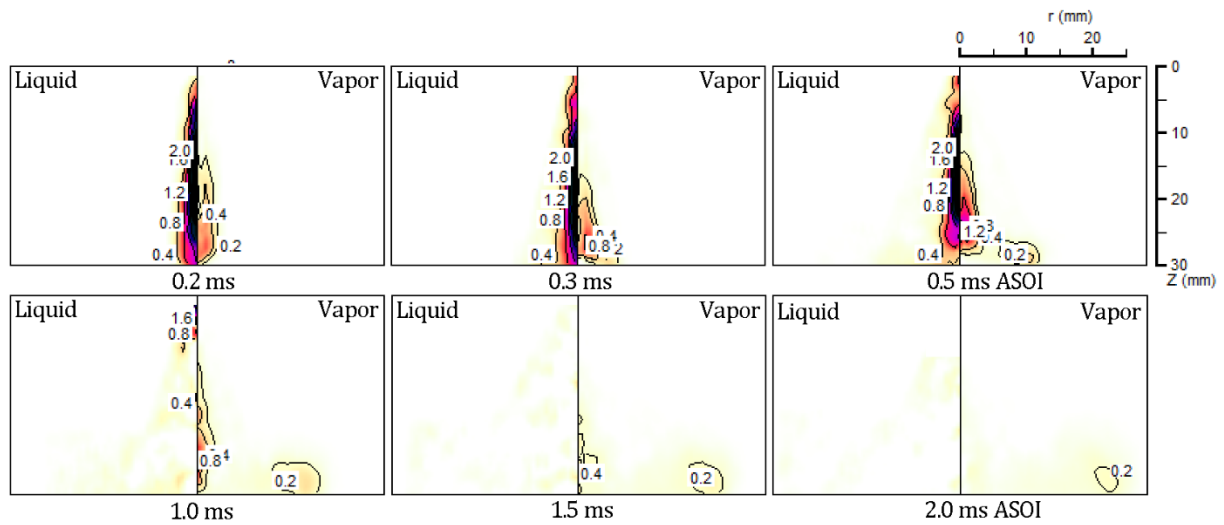
The equivalence ratio distributions of liquid phase and vapor phase of flat wall impinging spray under different injection pressures: 100, 150 and 170 MPa are shown in Fig 5.1. It should be note that the quantitative equivalence ratio of liquid phase has large error ratio because the LAS technique cannot deal with the liquid film deposited on the wall surface until now. Therefore, the liquid image in Fig 5.1 is applied to qualitatively analyze the liquid phase characteristics.

From Fig 5.1, under 100 MPa injection pressure, the impingement occurs at 0.3 ms ASOI. After impingement, the spray flow along the wall surface and evolution. It is found that the vapor phase equivalence ratios in the free spray region and wall spray region are much different. In the free spray region, the maximum vapor equivalence ratio which is appearing in the spray central region is 0.8 at 0.5 and 1.0 ms ASOI, and vapor phase mixtures are mainly distributed between the equivalence ratio regions of 0.2-0.8. However, the equivalence ratios of the wall spray mixtures are lower than 0.2 during the wall spray evolution. This is because that the air entrainment is enhanced after

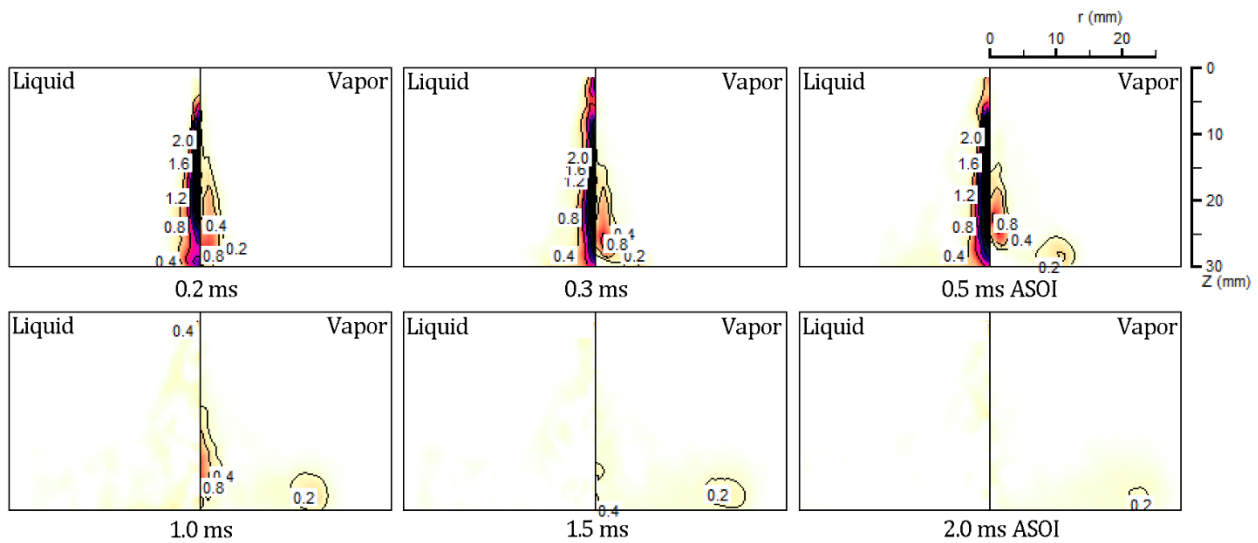
impingement which is contributed by the head vortex. The liquid phase penetration is longer than impinging distance and the dense droplets are formed in the spray free region. The droplet is evaporated with time elapsing, and all of the floating droplets are nearly evaporated before 1.5 ms ASOI. When injection pressure is increased to 150 MPa, the impingement occurs at 0.2 ms ASOI, the fuel is evaporated faster than 100 MPa which was deduce from the liquid equivalence ratio images. This is because the high injection pressure increases the spray atomization. Compared with 100 MPa injection pressure results, the vapor-air mixture of 150 MPa injection pressure is richer at the free spray region during the injection process, this is because the evaporation velocity is enlarged, as a result, the vapor mass is enlarged by increasing injection pressure. After EOI, both the liquid phase and the vapor phase has the lower equivalence ratio, which is resulted from the enhancement of ambient gas entrainment by injection pressure increasing. Under 170 MPa injection pressure, the fuel evaporation velocity fast, at 1.0 ms ASOI, the tiny floating droplets are exist. And the vapor phase equivalence ratio is small, the mixture in the wall spray region is very lean, the region of equivalence ratio near 0.2 is smaller than the other two lower injection pressures' results.



(a) 100 MPa



(b) 150 MPa



(c) 200 MPa

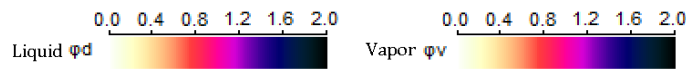


Figure 5.1 Equivalence ratio distributions of liquid phase and vapor phase of flat wall impinging spray under different injection pressures.

The temporal spray tip penetrations, ratios of entrained gas to total fuel, ratios of vapor fuel and the mean vapor phase equivalence ratios of flat wall impinging spray under different injection pressures are shown in Fig 5.2.

It is found that the spray tip penetration is increased with injection pressure increasing, which implies the spray atomization and the ambient gas entrainment are enhanced by injection pressure increasing. As a result, the ratio of vapor to total fuel, a reflector of evaporation velocity, is

increased with injection pressure increasing. The ratio of entrained gas to total fuel results reveal that the higher injection pressure gives higher ambient gas entrainment after 0.3 ms SOI. Before 0.3 ms ASOI, the ratios of entrained gas to total injected fuel under different injection pressures are disordered, this is because that the masses of existing fuel during the injection duration under different injection pressures are different with each other. As a result of the enhancement of ambient gas entrainment, the mean vapor phase ratio is decreasing with the injection pressure increasing after 0.5 ms SOI, the average vapor phase equivalence ratio at 1.0 ms ASOI which is around the start of ignition is lower than 0.2 under all the injection pressures.

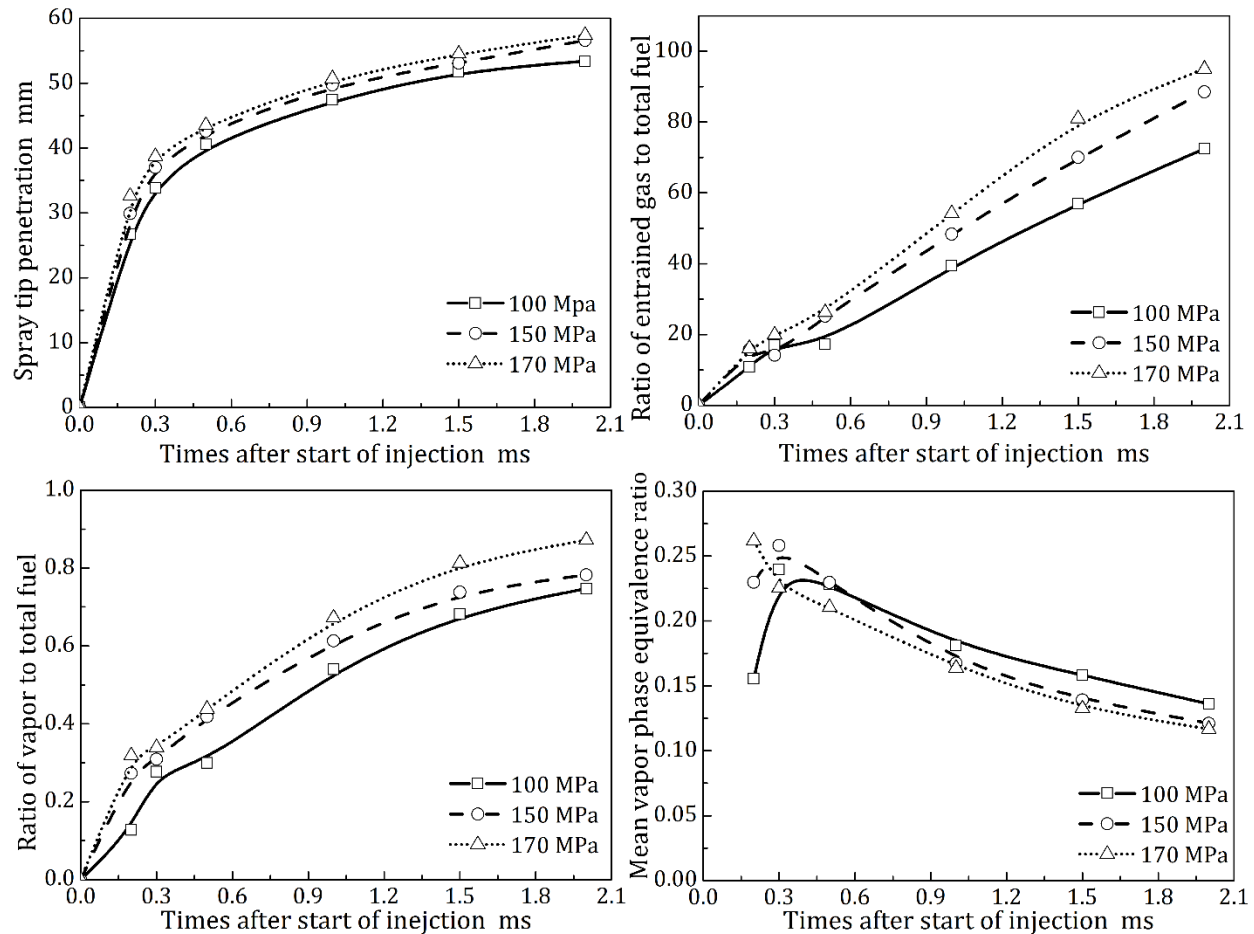


Figure 5.2 Temporal distributions of spray tip penetration, ratio of entrained gas to total fuel, ratio of vapor to total fuel and mean vapor phase equivalence ratio of flat wall impinging spray under different injection pressures.

The spatial distributions of the vapor phase equivalence ratios along the spray flowing path under different injection pressures are shown in Fig 5.3. The horizontal axis definition is described by blue line in the upper image, the horizontal line which is located at the half spray height region is

applied to reflect the radial distribution after impingement, and the radial distribution is denoted as the filling symbol in the lower images.

From Fig 5.3, it is found that the temporal variations of the vapor phase equivalence ratio distribution at the free region of impinging spray are inconsistent under different injection pressures. Under 100 MPa injection pressure, the vapor phase equivalence ratio of free region at 1.0 ms ASOI is higher than those of 0.5 and 1.5 ms ASOI whose low vapor phase equivalence ratios are contributed by the partial fuel evaporation and large amount gas entrainment respectively. However, under 150 MPa injection pressure, the vapor-air mixture of free region is the richest at 0.5 ms ASOI, and the leanest mixture is achieved at 1.5 ms ASOI. This is possibly because the evaporation velocity is enhanced by increasing the injection pressure as shown in Fig 5.2. With injection pressure increasing to 170 MPa, the equivalence ratio distribution of the free region at 1.0 ms ASOI is highest, but it should be noted that the maximum value is lower than 1. In the impinging region, the global vapor phase equivalence ratio is decreased with time elapsing under all the injection pressures. Near the impinging point, denoted by the first solid symbol, the vapor phase equivalence ratio always has the relative high value and dramatically decrease along the radial direction. And at the head vortex region, the vapor equivalence ratio has the relative peak value once again, however, the maximum value at the wall spray region is about 0.4. As discussed in Chapter 4, the impinging point undergoes misfiring under 30 mm impinging distance, thus the flat wall impinging spray undergoes lean vapor-air mixture combustion, the particles are formed by the liquid phase combustion. With the injection pressure increasing, the vapor-air mixture distribution characteristics are not changed significantly, the richest vapor-air mixture is located in the equivalence ratio regions of 0.2-0.4.

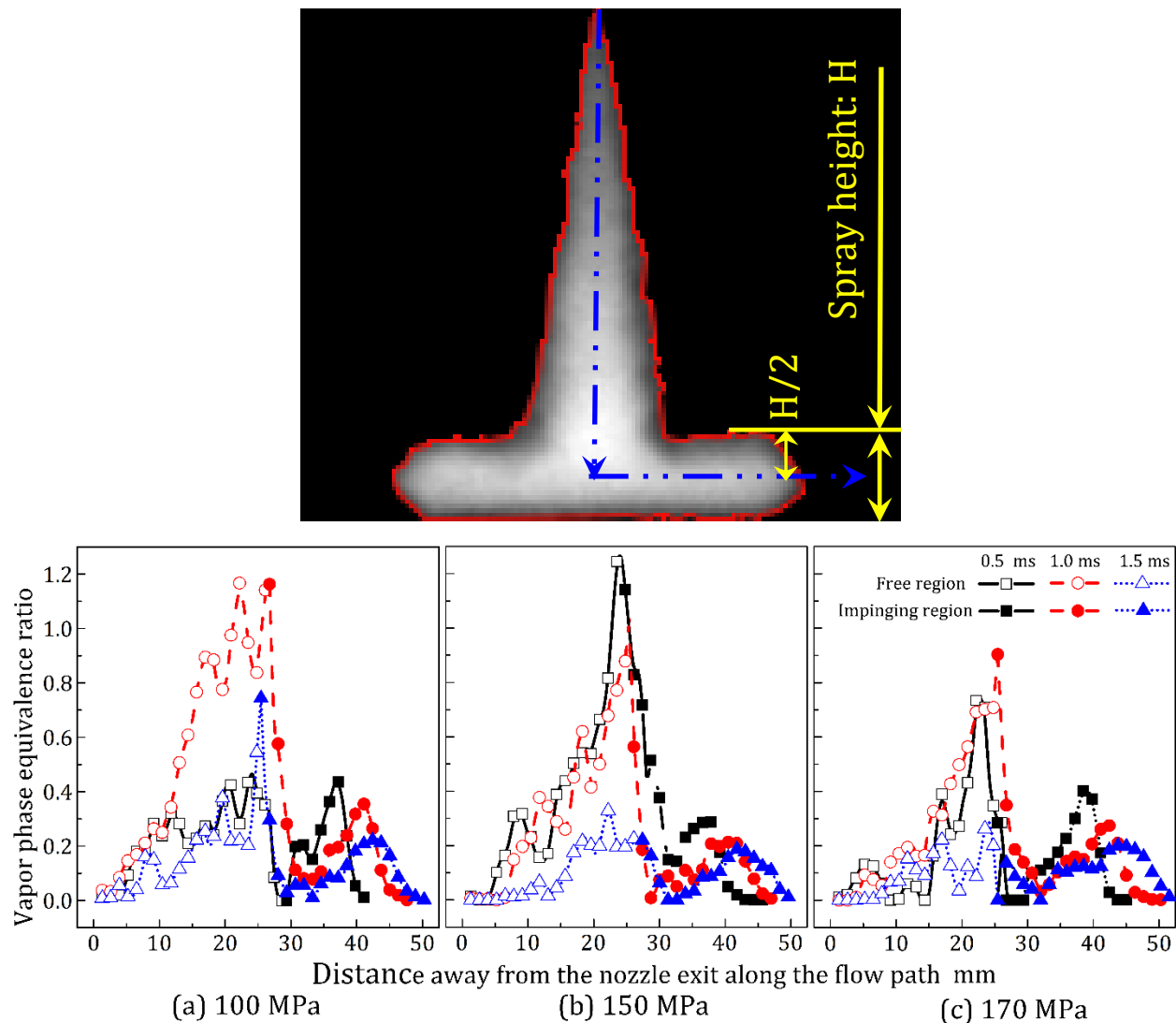


Figure 5.3 Spatial distributions of the vapor phase equivalence ratios along the spray flowing path under different injection pressures.

### 5.3.2 Combustion Process

In this section, three injection pressures were selected to investigate the influence of pressure on the impinging spray combustion. The injection pressures were 100 MPa, 150 MPa and 200 MPa. Under these injection pressures, the injection masses and the ambient conditions were kept constant. To make a comparison, the free spray flame experiments under different injection pressures were also conducted.

Figure 5.4 shows the images of  $\text{OH}^*$  chemiluminescence of impinging spray flame and Fig 5.5 shows the temporal variations of integrated  $\text{OH}^*$  chemiluminescence intensity of flat wall impinging flame (a) and free flame (b) under three injection pressures.

According to Figure 5.4, under three injection pressures, the flame tip is the intense reacting region. At the vicinity of the wall, there is a relatively high OH\* intensity region when injection pressures are 100 MPa and 150 MPa, however, the close wall region has no or low OH\* chemiluminescence intensity when injection pressure increases to 200 MPa, which implies that 200 MPa injection pressure can cause more fuel unburned.

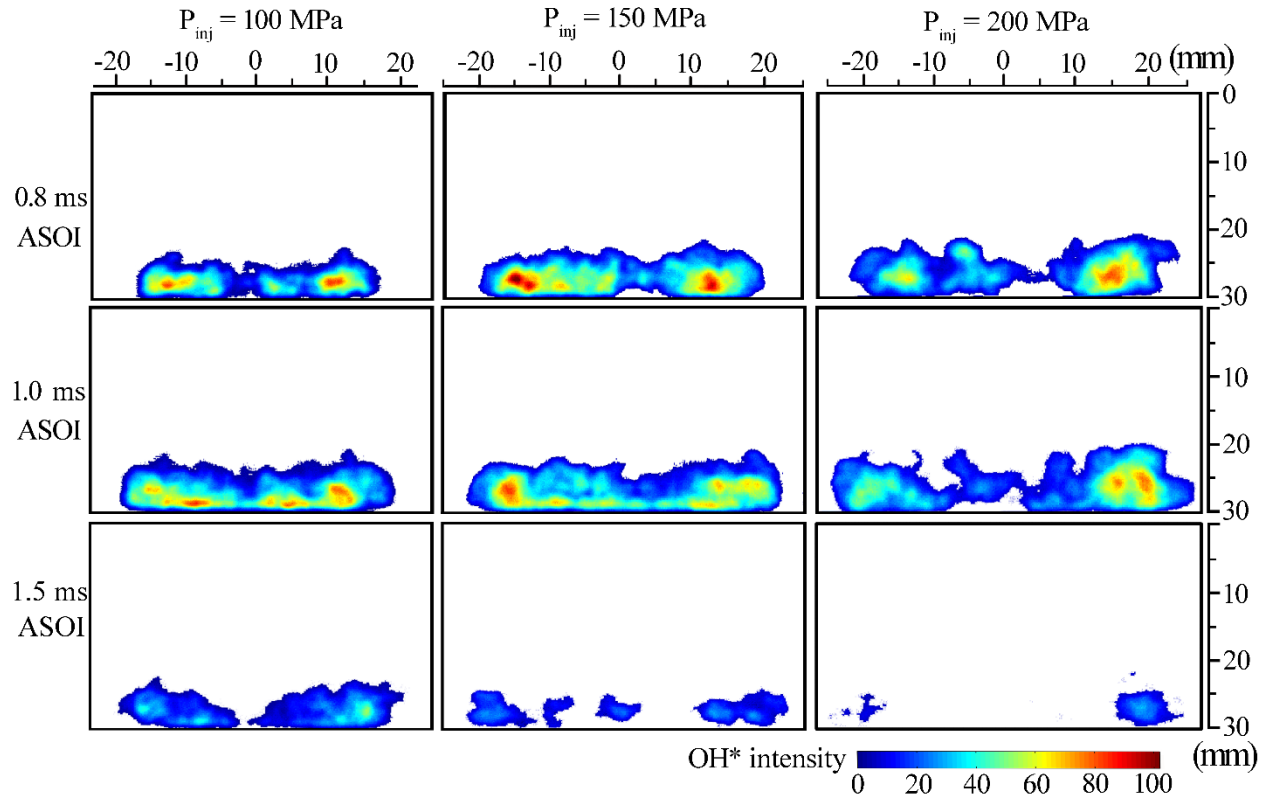


Figure 5.4 OH\* chemiluminescence images under different injection pressures: 100, 150 and 200 MPa.

From Figure 5.5, it is clear that the integrated OH\* intensity of impinging spray is much lower than that of free spray under all the injection pressures, which means that the injected fuel of impinging spray could not be burned completely as that of free spray. This is because 1: the same phenomenon with 100 MPa injection pressure, the wetting effects were also detected under 150 and 200 MPa injection pressure which means that liquid phase and pool combustion also occur under 150 and 200 MPa injection pressure; 2: as discussed above, the impinging spray flame has low upstream spreading ability which results in larger unburned region compared with free spray flame. Thus it is safe to say that the heat release is low and the unburned hydrocarbon emission is high when impingement occurs. Among these three injection pressures, the integrated OH\* chemiluminescence intensity of  $P_{inj} = 150$  MPa has the highest peak value according to Figure 5.5 (a)

which means that the optimal combustion behaviors are achieved when injection pressure is 150 MPa. It is commonly accepted that the combustion can be improved by increasing of injection pressure [Kato et al., 1989] as Figure 5.5 (b) shows: The integrated OH\* chemiluminescence intensity is improved by increasing the injection pressure of free spray flame. However, in this impinging experiment, the effect of injection pressure is not linear, when the injection pressure increases to 200 MPa, the integrated OH\* chemiluminescence intensity which reflects the combustion behavior achieves the lowest value among these three injection pressures. As Fig 5.4 shows, the OH\* intensity of 200 MPa injected pressure near the projected impinging point is very low, therefore, one explanation for the low integrated OH\* intensity at 200 MPa injected pressure is that the mixture is lean (more leaner than 170 MPa mixture which was introduced in Figs 5.1 and 5.3 (c)) and there are some regions where the mixture is not rich enough to be burned. What's more, the serious wetting effect which has been demonstrated to be a key factor for partial combustion [Matsui and Sugihara, 1986] may also play a role in low integrated OH\* intensity at 200 MPa injected pressure, the near wall liquid phase could not be burned by the surrounding low temperature flame as Fig 5.4 shows.

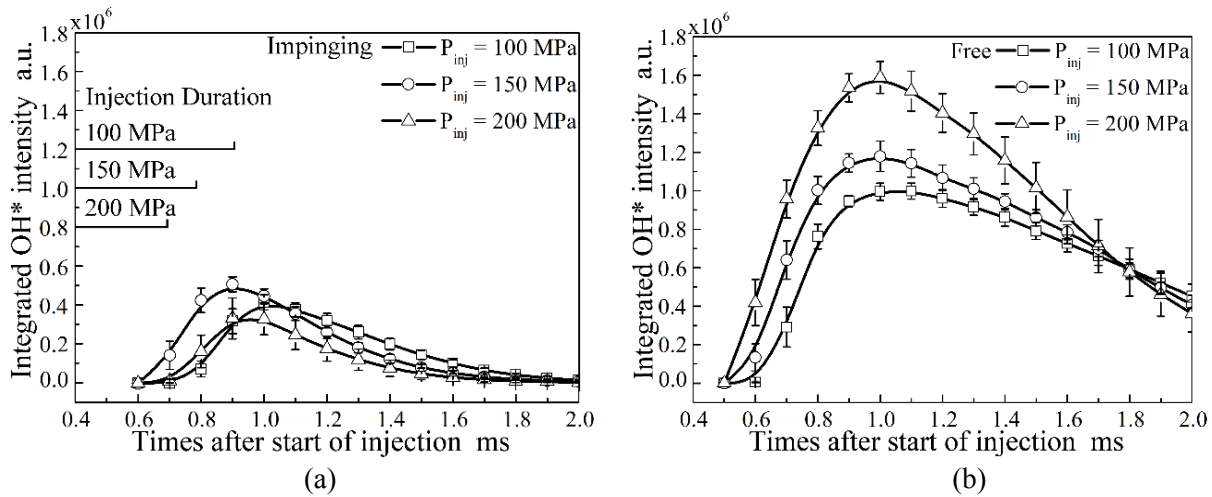


Figure 5.5 Temporal variations of integrated intensity of OH\* chemiluminescence under different injection pressures: 100, 150 and 200 MPa.

The natural luminosity images under different injection pressures are shown in Fig 5.6. In natural luminosity image recording system, the aperture size was selected as F22, the exposure timing was selected as 0.003 ms when  $P_{inj} = 100$  MPa, however, in order to receive clear natural luminosity images, the aperture size was selected as F8, the exposure timing was selected as 0.01 ms for  $P_{inj} = 150$  MPa and  $P_{inj} = 200$  MPa.

In Fig 5.6, the natural flame intensity of 200 MPa injected pressure is very weak. Since the natural luminosity mainly comes from the soot incandescence in diesel flame, 200 MPa injected pressure has the minimum soot emission. Because of the weak intensity, when applying two color method on the flame natural luminosity images of 200 MPa injected pressure, there is no soot concentration (KL factor). Consequently, the detail discussions about the soot concentration and temperature distribution are restricted to be on the injection pressures of 100 MPa and 150 MPa.

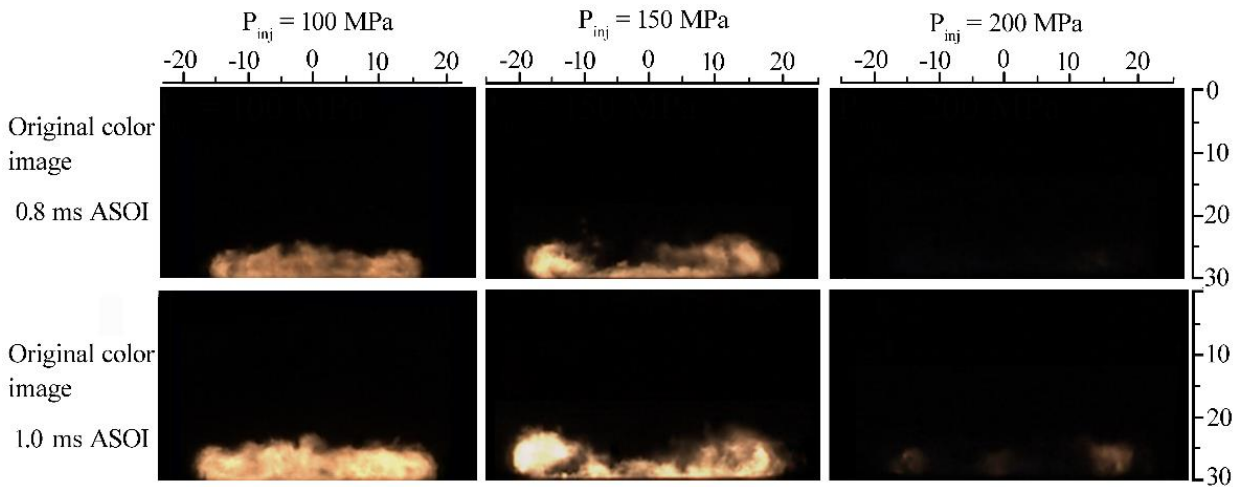


Figure 5.6 Original color images under different injection pressures: 100, 150 and 200 MPa.

The KL factor and temperature images are shown in Fig 5.7, and the temporal variations of integrated KL factor and mean temperature are shown in Fig 5.8.

According to Fig 5.8, KL factors has high value at the vicinity of the wall both under 100 and 150 MPa injected pressure because of the liquid combustion. In general, the KL factors of 150 MPa are lower than those of 100 MPa injected pressure. Figure 5.8 shows that the soot emission is improved by increasing the injection pressure both in the impinging spray flame and in the free spray flame because of the improvement of atomization and fuel-air mixing [Kato et al., 1989]. The same with 100 MPa injected pressure condition, the soot of impinging flame is oxidized faster than that of free flame at 150 MPa injected pressure. The flame temperature decreases as injection pressure increase, and the temperature of impinging flame decreases faster than that of free flame because the heat transfers from the flame to the wall. This contributes to more energy loss.

According to the analyzing above, the soot production of impinging spray flame is improved by increasing injection pressure, however, OH\* chemiluminescence intensity does not linearly increase as injection pressure increasing. The combustion of impinging spray is not as complete as that of free spray under all injection pressures.

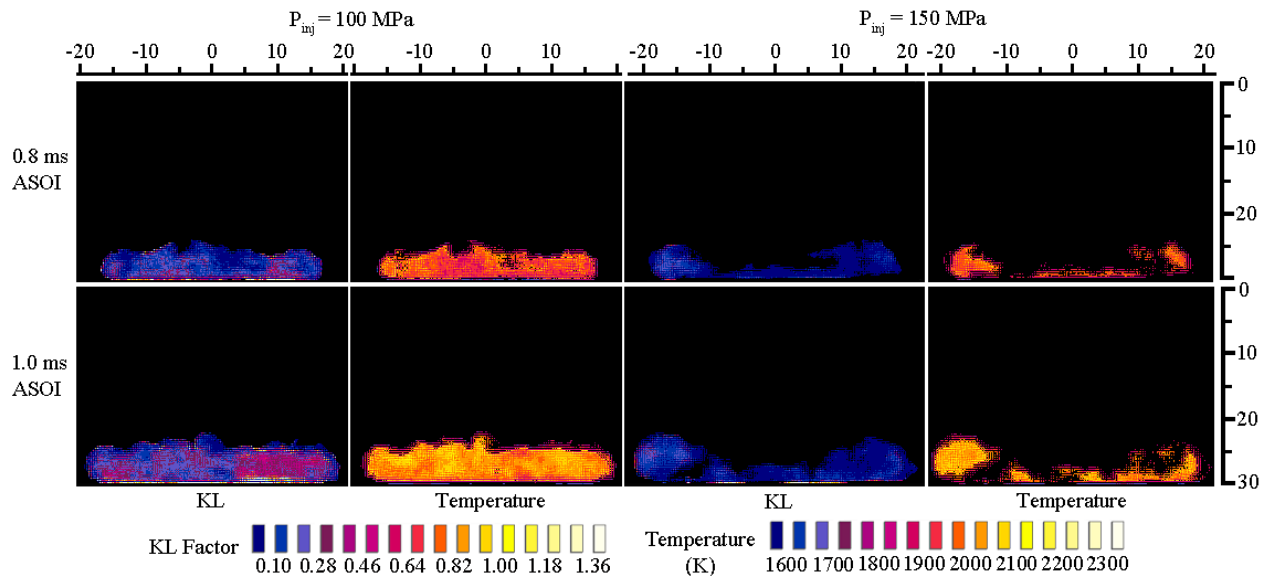


Figure 5.7 Distributions of KL factor and temperature under different injection pressures: 100 MPa and 150 MPa.

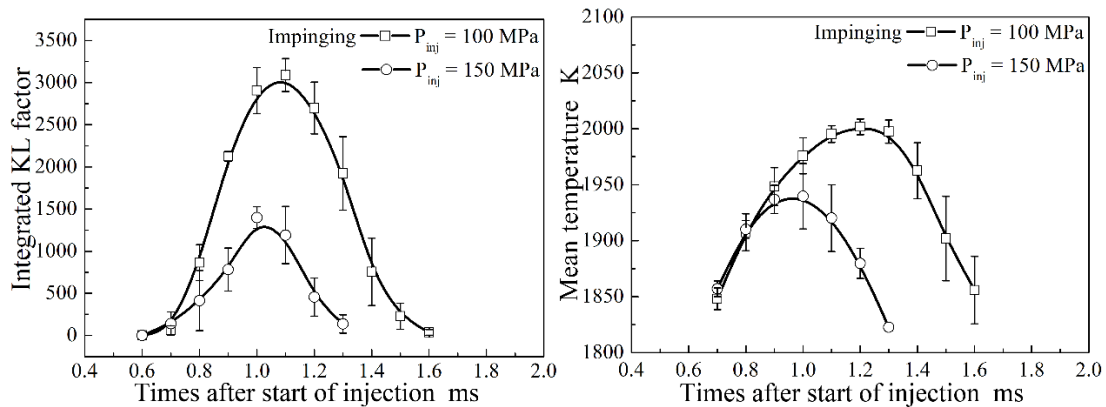


Figure 5.8 Temporal variations of integrated KL factor and mean temperature of flat wall impinging spray flame and free spray flame under different injection pressures: 100 and 150 MPa.

## 5.4 SUMMARY

In this chapter, the effect of injection pressure on flat wall impinging spray flame characteristics were investigated by applying LAS technique, OH\* chemiluminescence recording system, and two-color method. Based on this study, the following can be concluded:

1. The spray tip penetration is increased with the injection pressure increasing, as a result, the spray/wall interaction is enhanced and the ambient gas entrainment is improved.

2. The higher injection pressure results in faster fuel evaporation rate. Around the ignition timing (1.0 ms ASOI), the evaporation ratio of 170 MPa injection pressure spray is about 70%, and it is about 50% for 100 MPa injection pressure. Which implies that the liquid phase combustion is occurring during the combustion process.
3. The mean vapor phase equivalence ratio is decreased with the injection pressure increasing. Under all of the injection pressures, the relatively rich vapor-air mixture is observed in at the free and near impinging point region. Most of the ambient gas entrained into the spray at the wall spray region contributed by the head vortex. The vapor-air mixture is very lean in the wall spray region, and the wall spray maximum equivalence ratio is appeared at the head vortex region, what's more, the maximum vapor equivalence decrease with injection pressure increasing.
4. The soot emission is reduced by increasing injection pressure, however, the combustion is not linearly enhanced by increasing injection pressure, the results of OH\* chemiluminescence imply that the best combustion behavior can be obtained at the injection pressure of 150 MPa. This is possibly because that some regions of 200 MPa injection pressure spray is very lean and undergoes misfiring.
5. Combustion and soot emission are improved by increasing injection pressure for free spray flame. No matter what injection pressure is applied, the combustion of free spray flame is stronger and more completely than that of impinging spray flame. Which is resulted from the droplets combustion and pool flame under impinging conditions.

# CHAPTER 6 CHARACTERISTICS OF DIESEL IMPINGING SPRAY FLAME UNDER VARIOUS IMPINGING DISTANCES

## 6.1 INTRODUCTION

According to the discussions in Chapters 3 and 4, spray/wall impingement plays a significant role on affecting the mixture formation, combustion and emission. Under 30 mm distance impinging condition, the soot is formed because of the droplet combustion and pool flame. The evaporation and the ambient gas entrainment and the combustion completeness are deteriorated by impingement. However, the soot oxidation is enhanced by flat wall impingement due to the more utilized oxidation. Therefore, it is thought that appropriately enlarge the impinging distance, which can decrease the liquid/wall interaction effect but without significantly damage the soot oxidation, can realize the relatively complete combustion and also can limit the soot emission. In this dissertation work, finding the optimal impinging distance was also concentrated on. Different impinging distances (30, 40, 50 and 60 mm) were selected to observe the combustion behaviors, and the free spray flame is also shown to make a comparison.

## 6.2 EXPERIMENTAL CONDITIONS

The injection and impinging conditions are shown in Tab 6.1. The injection pressure was selected as 100 MPa and the injection mass was kept at 2.97 mg, and the flat wall was employed to form the impinging spray because the changing of impinging distance is simple. The impinging distances were selected as 30, 40, 50 and 60 mm. To make a comparison, the free spray flame was also carried out, it should be note that the free spray represents the limitless impinging distance. The LAS experimental conditions are shown in Tab 6.2. The ambient temperature and pressure were selected as 760 K and 3.6 MPa respectively, and the ambient gas density was 16 kg/m<sup>3</sup>, the blend fuel of n-tridecane and 1-MN was employed. For combustion experiments, as shown in Tab 6.3, the ambient temperature and pressure were kept at 873 K and 4.1 MPa respectively, and the ambient gas density was the same with that of LAS experiment. The fuel for combustion experiment was Diesel JIS #2.

Table. 6.1 Injection and impinging conditions.

Nozzle Type	Single Holes Nozzle
Hole Diameter (mm)	0.133

Injector Type	Piezo Actuator Type
Injection Pressure (MPa)	100
Injection Quantity (mg)	2.97
Impinging Wall	Flat Wall
Impinging Distance (mm)	30,40,50,60

Table. 6.2 Experimental conditions for LAS technique.

Ambient Gas	Nitrogen
Ambient Temperature (K)	760
Ambient Pressure (MPa)	3.6
Ambient Density (kg/m <sup>3</sup> )	16
Fuel Type	97.5% n-Tridecane +2.5% 1-Methylnaphthalene

Table. 6.3 Experimental conditions for combustion.

Ambient Condition	Evaporating
Ambient Gas	Air (O <sub>2</sub> ) (for Combustion)
Ambient Temperature (K)	873
Ambient Pressure (MPa)	4.1
Ambient Density (kg/m <sup>3</sup> )	16
Fuel Type	JIS # 2

### 6.3 MIXTURE FORMATION CHARACTERISTICS

Equivalence ratio distributions of liquid phase and vapor phase of flat wall impinging spray under different impinging distances are shown in Fig 6.1. At 0.3 ms ASOI, when the impingement occurs under 30 mm impinging distance, no significant variations are appearing among the liquid phase distributions under different impinging distances. The vapor-air mixtures are observed in the spray mid-downstream regions under all the impinging conditions. And the 30 mm impinging distance has the richest vapor-air mixture which is appeared at the near impinging point region, this is because the high evaporation velocity at this timing which has been discussed in Chapter 4. When impinging distance is increased to further, the spray/wall interaction does not occur at 0.3 ms ASOI, however, the 40 mm vapor-air mixture is richer than the other conditions whose impinging distance

is longer than 40 mm. This confirms that the wall existence plays a role in spray atomization even before the impingement.

When time is increased to 0.5 ms ASOI, the impingement just occurred under 40 mm impinging distance. At this timing, it is found that the vapor phase equivalence ratio is small near the impinging point under 30 mm impinging distance, this is because that the liquid phase of fuel is stagnated in this region. In 40 mm impinging distance images, the vapor phase equivalence ratio near the impinging point region runs up to 1.2. The vapor-air mixture distributions are nearly the same under 50 and 60 mm impinging distance, the equivalence ratio is mainly located between 0.2 and 1.2. Under limitless impinging distance condition, the vapor-air mixture is lean and the equivalence ratio is mainly distributed within the region of 0.2 to 0.8.

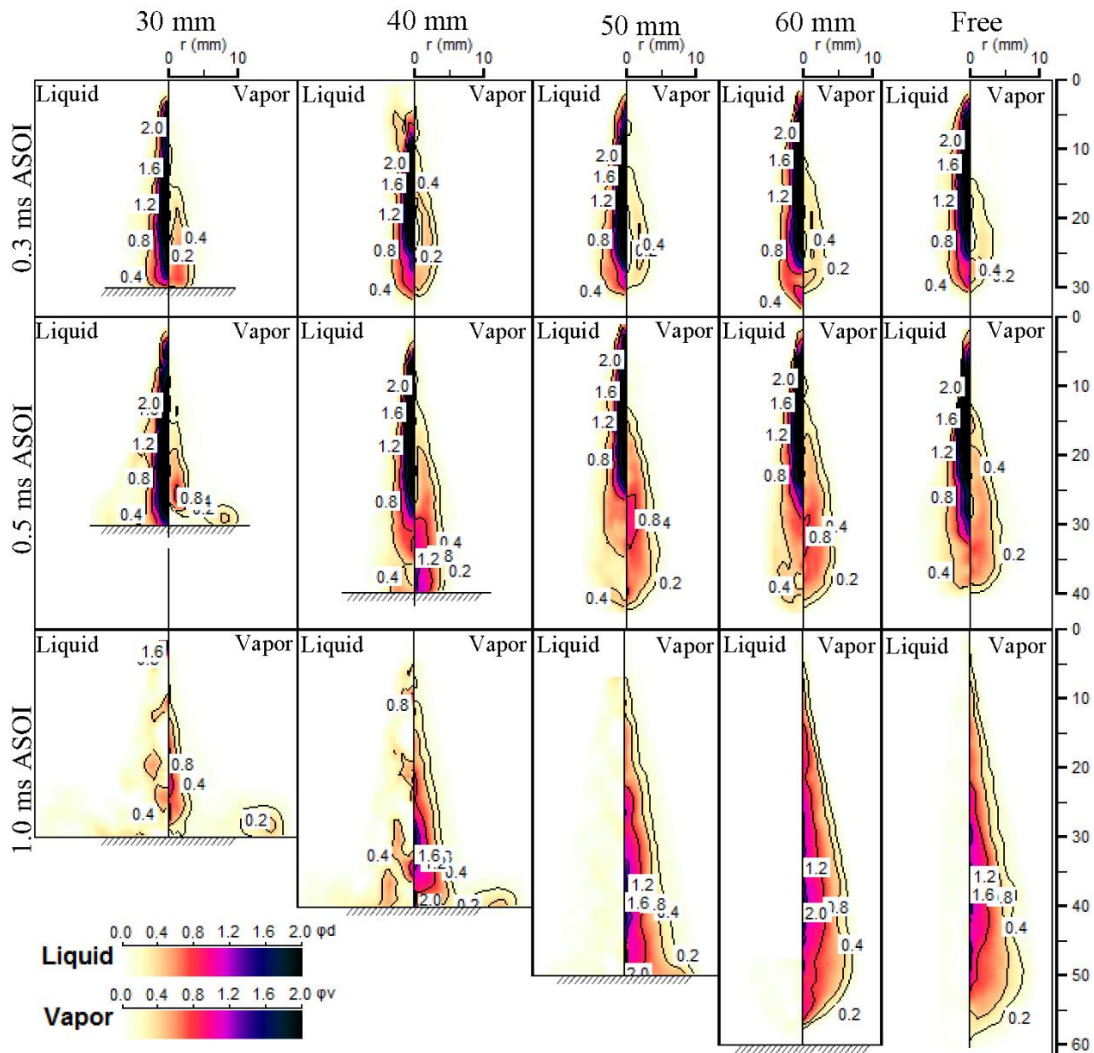


Figure 6.1 Equivalence ratio distributions of liquid phase and vapor phase of flat wall impinging spray under different impinging distances.

At 1.0 ms ASOI, the 50 mm impinging spray also undergoes impingement. At this timing, the droplets can be evidently observed under the short impinging distance (30 and 40 mm) conditions. However, the droplets-air equivalence ratios under the other impinging conditions are small which are lower than 0.2. When attention is paid to 60 mm impinging and free sprays, it is found that the spray structures of them are nearly the same except some tiny variations which include that the tip penetration of 60 mm impinging spray is a little shorter than free spray contributed by the enhancement of spray/air interaction and also include that the vapor-air mixture in the central region of the 60 mm impinging spray is a little richer than free spray because of the evaporation enhancement and entrained gas reduction.

The temporal variation of ratio of vapor to total fuel under different impinging distances are shown in Fig 6.2. At 0.2 ms ASOI, when the impingement is not occurred under all the impinging distance condition, the spray is unstable and the dependence of evaporation velocity on impinging distance cannot be analyzed. At 0.3 ms ASOI, it is found that the evaporation ratio decrease with impinging distance increasing. This confirms that the wall existence play a role in evaporation even before the impingement. At 0.5 ms ASOI, the impingement occurs under 40 mm impinging distance, unlike at 0.2 ms ASOI, the 30 mm impinging spray evaporation ratio increases slowly, this is because the long time impingement hinders the evaporation. And among the other impinging condition sprays (40, 50, 60 mm and free), the evaporation ratio is reduced by increasing impinging distance. After 0.5 ms, the effect of impinging distance on evaporation is distinct. The evaporation velocity of 60 mm impinging spray is the fastest after 0.5 ms SOI, the injected fuel is approximately completely evaporated before impingement under 60 mm impinging condition. The evaporation velocity of free spray is a little slower than 60 mm impinging spray, but it is much faster than the other impinging conditions. Among 30, 40 and 50 mm impinging sprays, the evaporation velocity is increased with impinging distance increasing, this is because that the wall wetting effect is reduced by enlarging the impinging distance.

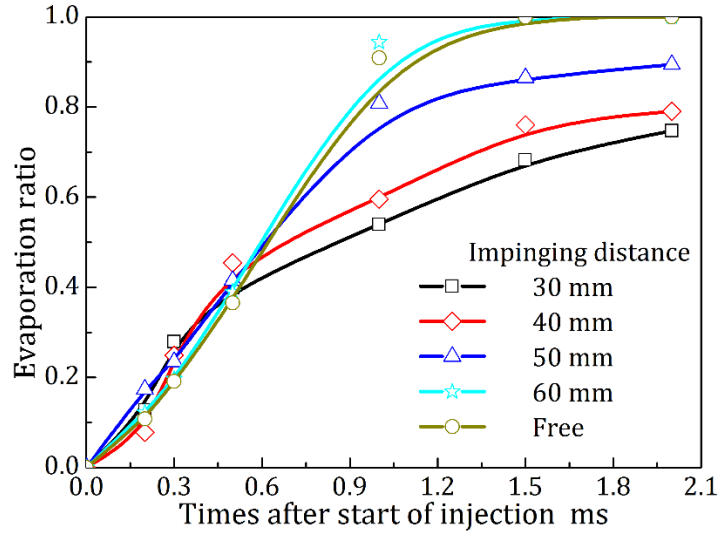


Figure 6.2 Temporal variations of ratio of vapor to total fuel under different impinging distances.

The temporal ratio of entrained gas to total fuel under different impinging distances are shown in Fig 6.3. It is clear that the free spray has the most ambient gas entrainment after 0.5 ms SOI, which is contributed by the longest spray tip penetration. And the air entrainment of 60 mm impinging spray is lower than free spray but higher than the other impinging sprays. It is interesting that the ambient gas entrainments of 30 and 50 impinging sprays are near the same, and the entrained gas of 40 mm impinging spray is the least among all the conditions. The mechanism of this phenomenon is not clear, one possible explanation is that the entrained gas quantities under different impinging conditions are determined by the combining effect of spray tip variations and head vortex intensity variations, therefore, the 40 mm impinging spray has the least ambient gas entrainment.

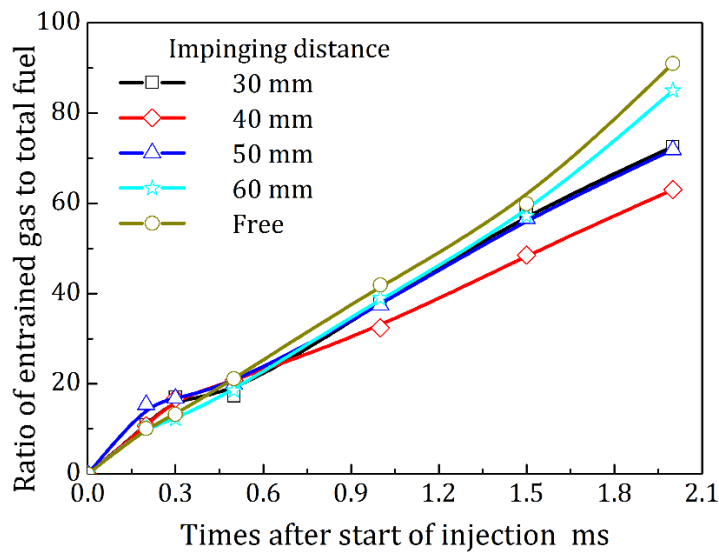


Figure 6.3 Temporal ratio of entrained gas to total fuel under different impinging distances.

The Spatial distributions of vapor phase equivalence ratio along the spray flowing path at 0.5 and 1.0 ms ASOI under different impinging distances are shown in Fig 6.4. Under 0.5 ms ASOI, during the main injection process, only the 30 mm impinging spray has the relatively evident head vortex, and the vapor phase equivalence ratio at the spray tip region. In addition, the vapor phase equivalence ratio in the mid-downstream region of free spray is lower than those of 40, 50 and 60 mm impinging sprays. This is attributed to the combined effect of low evaporation ratio and the large entrained gas quantity as shown in Figs 6.2 and 6.3 respectively. At 1.0 ms ASOI, the lean vapor-air mixtures at the head vortex regions are observed under 30 and 40 mm impinging sprays. The maximum equivalence ratios of vapor-air mixtures of 40, 50 and 60 mm impinging sprays are higher than that of free spray. This is also resulted from the combined effect of evaporated fuel and ambient gas entrainment.

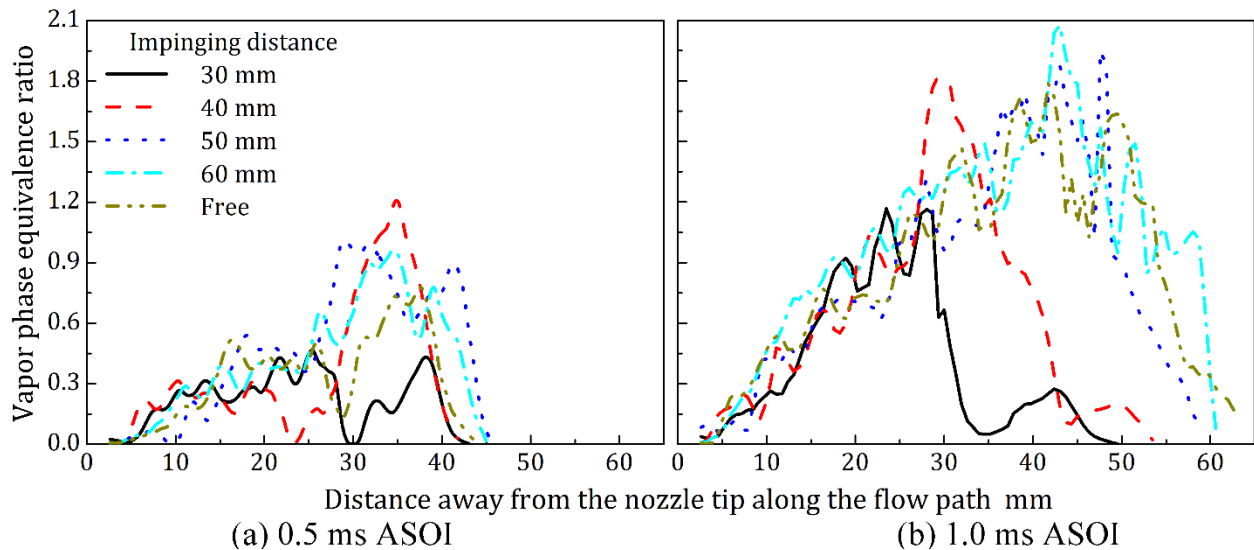


Figure 6.4 Spatial distributions of vapor phase equivalence ratio along the spray flowing path.

## 6.4 COMBUSTION CHARACTERISTICS UNDER DIFFERENT IMPINGING DISTANCES

The integrated  $\text{OH}^*$  intensities under different impinging distances are shown in Fig. 6.5. The integrated  $\text{OH}^*$  intensity is a reflector of heat release [Tinaut et al., 2011].

Figure. 6.5 shows that the maximum integrated  $\text{OH}^*$  intensity increases with the increasing of the impinging distance. This means that the combustion is more complete under larger impinging distance condition. When impinging distance increases to 60 mm, for maximum integrated intensity, there is no significant difference between impinging and free flame, what's more, before 1.3 ms ASOI, the integrated  $\text{OH}^*$  intensity of 60 mm impinging flame is higher than that of free flame which implies

that the combustion velocity at initial combustion stage of 60 mm impinging spray is faster than that of free spray.

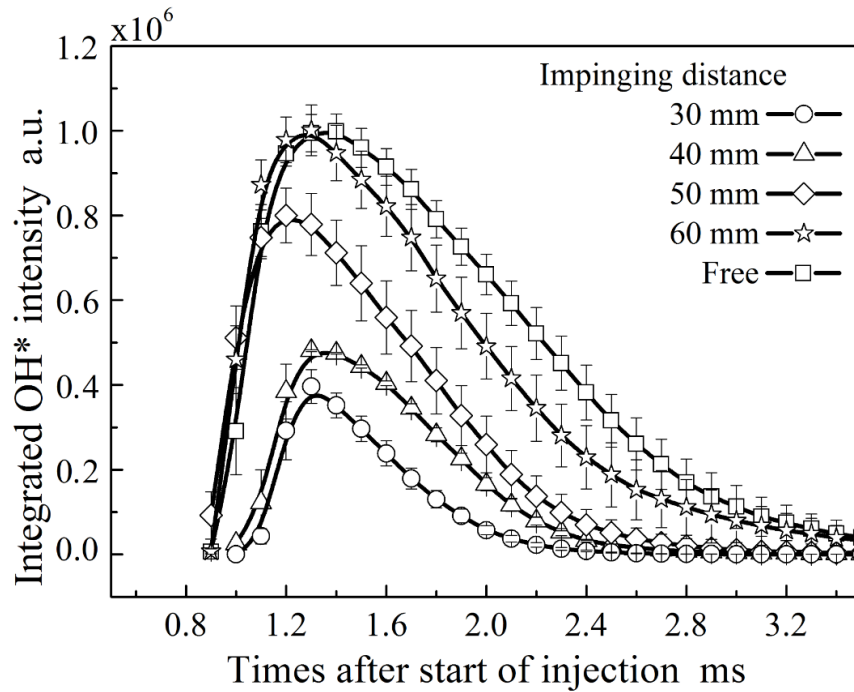


Figure 6.5 Temporal variations of integrated OH\* intensity under different impinging distances.

OH\* chemiluminescence images under different impinging distances (30, 40, 50, 60 mm and free) at 1.3 (around maximum integrated OH\* intensity and KL factor timing) and 1.6 (soot oxidation dominant timing) ms ASOI are shown in Fig 6.6. The aperture size was selected as F 8.

From Fig 6.6, it is clear that the flame width decrease with impinging distance increase which is contributed by the impinging effect. At 1.3 ms ASOI under 30 mm impinging condition, the combustion is mild which is reflected from the low OH\* chemiluminescence intensity. The relative high OH\* radical region locates at the vicinity of the flat wall. This is because that OH\* radical mainly comes from the high temperature and stoichiometric ratio region, short impinging distance results in large head vortex intensity and lean mixture is formed in the wall spray region as shown in Figs 6.1 and 6.4. Near the flat wall, there is a region where is occupied by liquid film and droplets, what's more, ambient gas entrainment in this region is difficult. Therefore, the vicinity of the flat wall undergoes relatively rich mixture diffusion combustion which has high OH\* radical emission. The liquid phase penetration under these experimental conditions is between 40 mm and 50 mm as given from Fig 6.1. Thus even the scattered droplets still has interaction with flat wall under 40 mm impinging distance condition, but the interaction is much weaker which contributes to more intense OH\* emission compared with those of 30 mm impinging distance condition. Relatively high OH\*

intensity appears at the near impinging point region because of the later injected fuel stagnation. Under 50 mm impinging distance, the projected area is enlarged and the OH\* intensity is enhanced and the reaction is intense near the impinging point region. When impinging distance comes to 60 mm and infinite (free), the OH\* flame distributions of 60 mm impinging distance and free are nearly the same except the structure. The 60 mm distance impinging flame is wider than that of free flame even at the flame upstream region, this is because the effect of impingement enhance the interaction between spray tip and the ambient gas before impingement occurs. This structure changing phenomenon could not be observed under shorter impinging distance is because that the combustion occurs after the impingement.

At 1.6 ms ASOI, the combustion undergoes soot oxidation dominant process. The OH\* chemiluminescence intensity is enhanced by enlarging impinging distance. Under 50 and 60 mm impinging distance conditions, the close wall regions have more intense OH\* emission than free flame which implies that the soot oxidation rate is faster than free flame at these regions.

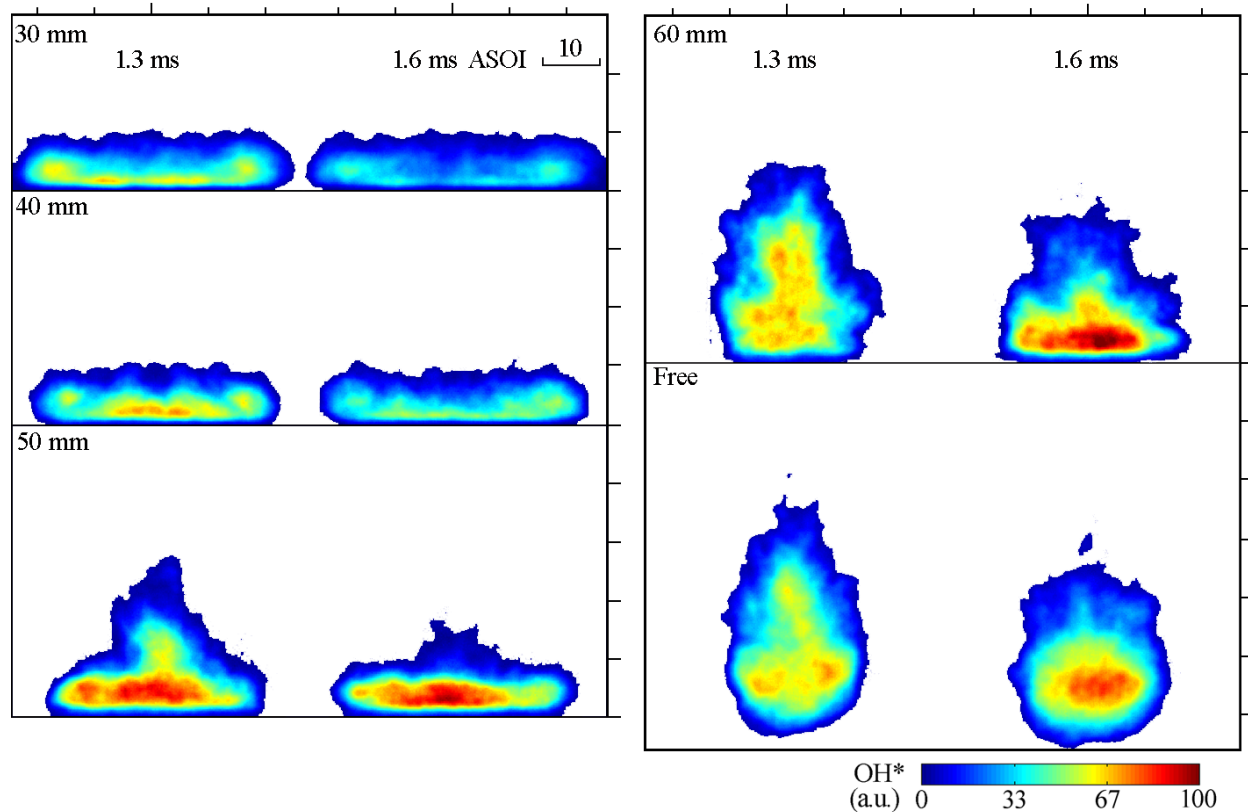


Figure 6.6 OH\* chemiluminescence images under different impinging distances (30, 40, 50, 60 mm and free) at 1.3 and 1.6 ms ASOI.

Figure 6.7 shows the temperature and KL factor images at 1.3 ms ASOI under different impinging distances (30, 40, 50, 60 mm and free). Figure 6.8 (a) and (b) show temporal variations of mean temperature and integrated KL factor under different impinging distances respectively.

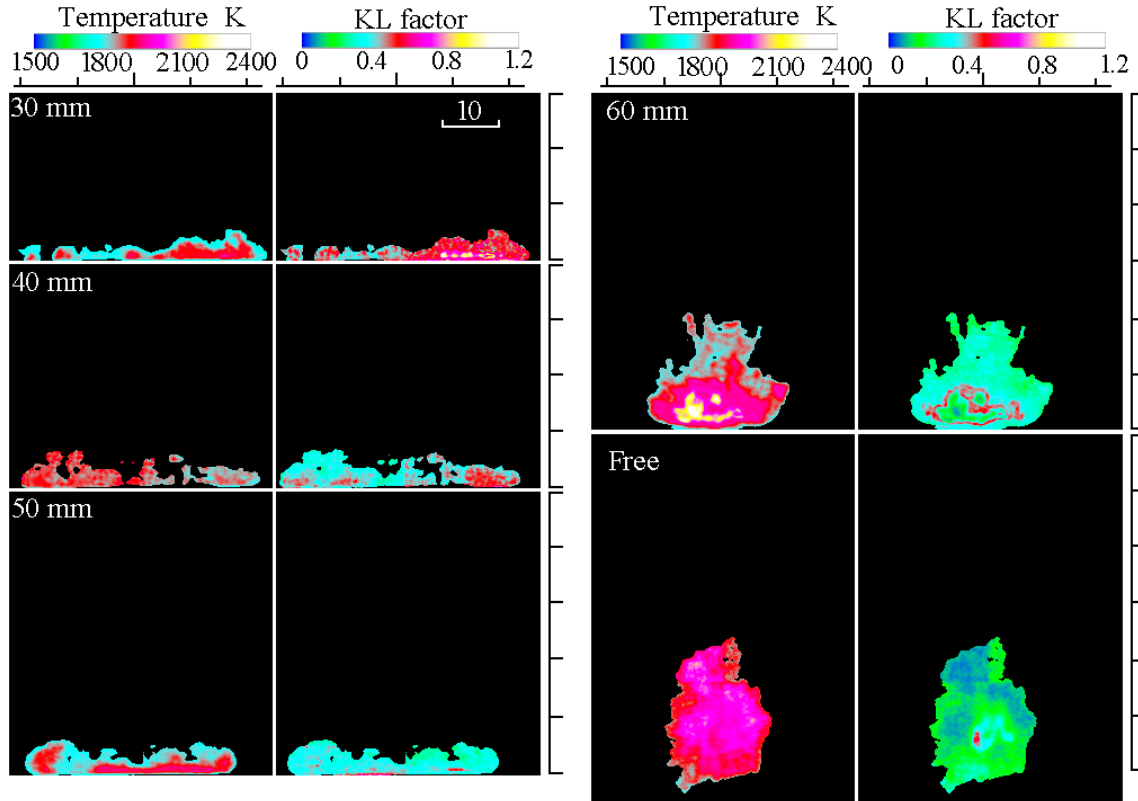


Figure 6.7. Temperature and KL factor images at 1.3 ms ASOI under different impinging distances (30, 40, 50 60 mm and free).

According to Fig 6.7, the soot particles mainly distribute at the wall vicinity region under 30 mm impinging distance, and the relatively high temperature region is also close to the wall, these are coincide with the high OH\* chemiluminescence region in Fig 6.6. Under impinging distance of 40 mm condition, the temperature increase but the KL factor intense decrease compared with 30 mm. When it comes to 50 mm impinging distance, it is clear that the high temperature particles distribute at close wall region, the KL factor becomes more uniform and the wall vicinity has a high KL factor region. This means that even at 50 mm impinging condition, the wetting effect still plays a role on combustion. It should be not that the soot flame heights under 30, 40, and 50 mm impinging conditions are lower than those of OH\* chemiluminescence as shown in Fig 6.6, which means that the higher region is no soot combustion region when flame appears after impingement. This is because the impingement enhance the head vortex intense and then enhance the air entrainment through the spray upside [Mohammadi et al., 2002]. Under 60 mm and infinite (free) impinging distance, it is

clear that the soot temperatures become much higher than other conditions. The high temperature and high soot regions of 60 mm impinging distance are near the impinging point region because the particles stagnate and be oxidized at this region.

From Fig 6.8 (a), it is clear that the mean temperature increasing with enlarging the impinging distance, this means that under these injection and ambient conditions, the larger impinging distance combustion is close to stoichiometric flame. The difference of the maximum average temperatures between 30 mm impinging distance and free flames is more than 200 K.

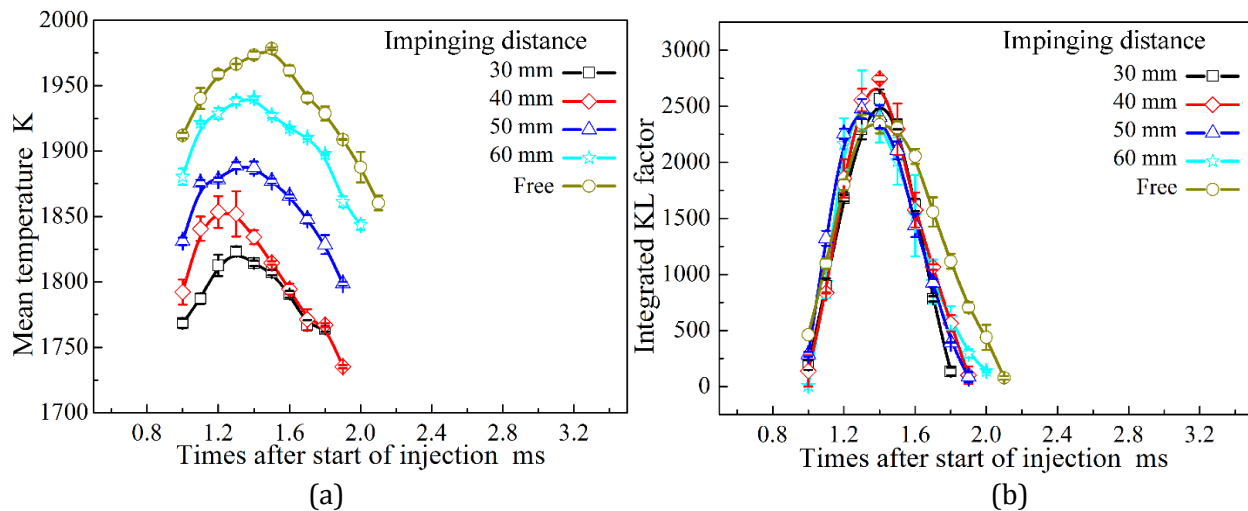


Figure 6.8. Temporal variations of mean temperature and integrated KL factor under different impinging distances (30, 40, 50, 60 mm and free).

However, different with that of mean temperature, the difference of integrated KL factors under different impinging distances is unobvious as shown in Fig 6.8 (b). The integrated KL factor increasing process implies the soot formation dominant process and the decreasing process implies soot oxidation dominant process. Fig 6.8 (b) shows that the soot formation rates are nearly the same under different impinging distance. While, the free flame cannot oxidize soot as fast as that of impinging flames. This is because the air entrainment is enhanced after impingement, which means the utilization of the oxygen atoms is enhanced. Therefore, the soot oxidation rate is fast under impinging conditions.

As the post combustion has relationship with heat release, degree of combustion completeness, and unburned HC emission, thus post combustion was simply concentrated on. The definition of post combustion process in this research is that from the disappearance timing of soot in Fig 6.8 (b) to the combustion finish timing (the combustion finish is defined as that the integrated OH\* intensity is lower than 10% of the maximum integrated OH\* intensity). Considering Fig 6.5 and

Fig 6.8 (b) simultaneously, the duration of later stage no soot combustion in this research could be regarded as that: 1.8-2.2, 1.9-2.4, 1.9-2.4, 2.0-2.9 and 2.1-3.1 ms ASOI for 30,40,50,60 mm impinging distance and free conditions respectively. It is clear that the post combustion duration is enlarged by increasing impinging distance. What's more, according Fig 6.5, the post combustion intensity is also enhanced by increasing impinging distance, thus the post combustion behaviors are improved by enlarging impinging distance

According to above discussions, the combustion intensity is deteriorated under impinging condition in general. However, the soot formation rate nearly has no dependence on impingement. On the contrary, the soot oxidation rate is enhanced by impingement. Under 60 mm impinging distance condition, the reaction rate of initial stage is faster than that of free flame without damaging maximum integrated OH\* intensity. What's more, the soot emission is reduced as discussed above. Therefore, from the view of reaction velocity and soot emission are considered to evaluate diesel spray combustion behaviors, the 60 mm impinging distance is the optimal condition according to the results of OH\* radical emission and two color method. Based on the results, a supposition is made: the optimal impinging condition is that the impingement occurs immediately after complete evaporation.

To clarify the soot formation and oxidation characteristics at the specific timings, the soot formation and oxidation behaviors were concentrated on by applying the method of combining the two-color and OH\* chemiluminescence results as introduced in Chapter 3. The results are given in Fig 6.9. In each pair of the images, the left is KL factor temporal variations at 1.2 ms ASOI when the soot formation is dominant, and the right is KL factor temporal variations at 1.6 ms ASOI when the soot oxidation is dominant.

From Fig 6.9, it is found that under soot formation dominant process, the soot is formed at the wall vicinity region and the head vortex tip region under all the impinging conditions, the soot formations under 30 and 40 mm impinging conditions are possibly attributed to the droplets combustion and pool flame, however, the soot formations under 50 and 60 mm impinging conditions are contributed by the rich mixture whose equivalence ratio is higher than 1 as introduced in Fig 6.1. The same with the soot formation behaviors which has been described in Chapter 4, the soot is mainly formed at the sooting flame downstream region of free spray flame. During the soot formation dominant process, the soot oxidation is also taking place at the soot flame upstream through where the ambient gas mainly entrained and at the wall spray periphery where is the intersection of the sooting flame and pure OH\* flame regions. In soot oxidation dominant process, it is found that the

oxidized intensity under shorter impinging distances (30, 40, 50 mm) is strong, and the oxidation regions of shorter impinging distance flame is also large, thus as Fig 6.8 shows, the oxidation velocities under impinging conditions are fast. Under 60 mm impinging distance, the soot is mainly oxidized at the head vortex region.

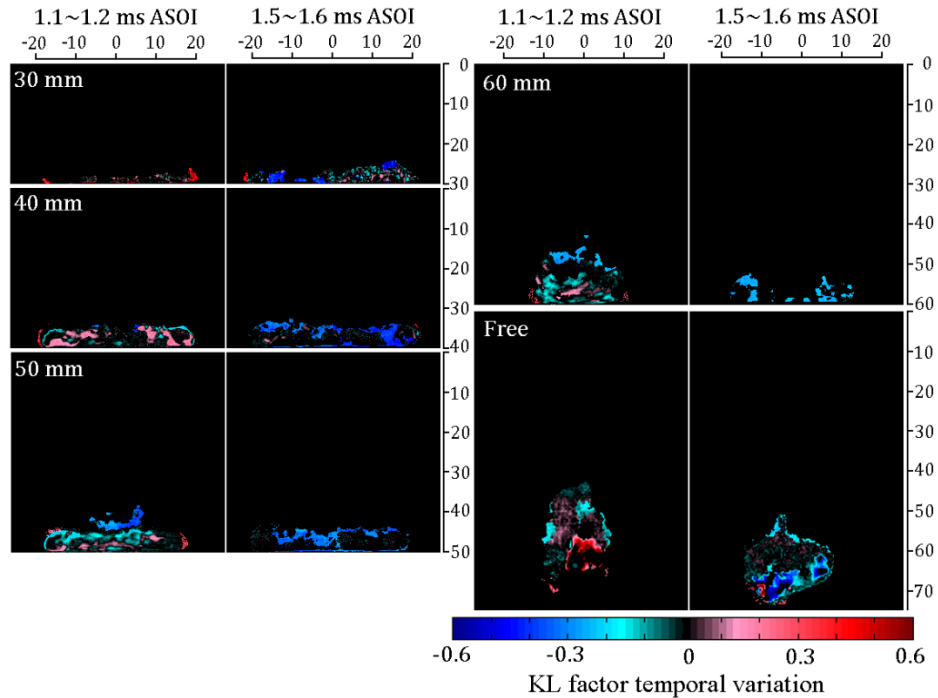


Figure 6.9 Soot formation and oxidation denoted by KL factor temporal variation under different impinging distances

## 6.5 SUMMARY

Characteristics of mixture formation, combustion and soot emission under different impinging distances were investigated by applying LAS technique, OH\* chemiluminescence recording system and two-color method respectively. The impinging distances were selected as 30, 40, 50 and 60 mm, to make a comparison, free spray flame was also concentrated on. Based on this investigation, the conclusions are summarized as follows:

1. The impinging distance plays a significant role in spray atomization. Under severe liquid/wall interaction conditions (30 and 40 mm impinging distance), the evaporation velocity of the injected fuel is much slower than the longer impinging distance sprays.
2. The flat wall plays a role in spray atomization even before the impingement occurs because of the enhancement of the interaction between the spray tip and the ambient gas.

- As a result, the shorter impinging distance spray is evaporated faster than the longer impinging distance sprays when the spray tip is approaching to the wall surface.
3. The complete evaporation of 60 mm impinging spray is observed firstly. At 1.0 ms ASOI, more than 90 percent of the total have been evaporated. On account of smaller ambient gas entrained quantity, the vapor phase equivalence is higher than that of free spray.
  4. The mean temperature increases with impinging distance increasing. Soot formation process (increasing process of integrated KL factor) does not depends on the impinging distance variations, but the soot oxidation rate (decreasing process of integrated KL factor) can be enhanced by impingement.
  5. Reactive intensity and completeness of combustion are improved by increasing impinging distance. Under 60 mm impinging distance, the reactive rate at initial combustion stage is faster than that of free spray flame without damaging maximum integrated OH\* intensity. Therefore, 60 mm impingement is thought as the optimal condition when reaction velocity and soot emission are considered to evaluate diesel spray combustion behaviors.
  6. The soot is mainly formed in the wall vicinity region and the periphery of the head vortex for impinging spray, and at the downstream of the sooting flame of the free spray. The soot oxidized intensity is enhanced and the oxidized region is enlarged by decreasing the impinging distance which can improve the fuel-air mixing in the wall spray region where the impinging flame is confined in.

# **CHAPTER 7 CHARACTERISTICS OF DIESEL SPRAY FLAME UNDER VARIOUS INJECTION AMOUNTS**

## **7.1 INTRODUCTION**

HCCI is difficult to realize in diesel engine especially in traditional type which adopts high compression ratio to achieve high power output. Thus, decreasing compression ratio is thought as one way to realize HCCI combustion mode in a diesel engine [Laget et al., 2009]. However, the combustions under cold start process and idle mode are unstable in a low compression ratio diesel engine. As a solving method, the multi-pilot injection strategy is always employed [MacMillan et al., 2009] under the cold start and idle modes. Under multi-pilot injection condition, the pilot injection mass is always selected as tiny to restrain the uncontrollability of ignition timing. Up to present, there is little investigation focused on tiny mass injection, therefore, the spray behaviors of tiny mass injection is concentrated on in this Chapter.

## **7.2 EXPERIMENTAL CONDITIONS**

The experimental conditions are included in Tabs 7.1, 7.2 and 7.3. In the non-reaction experiment, two kinds of ambient conditions were set as:  $P_a = 1.4$  MPa,  $T_a = 300$  K and  $P_a = 3.6$  MPa,  $T_a = 760$  K to represent non-evaporating and evaporating condition respectively. The ambient gas density was decided as the same condition with the real engine under cold start mode at near TDC timing. To avoid reaction, nitrogen was selected as the ambient gas. Under the reaction condition, the ambient temperature was selected as 873 K and the pressure was selected as 4.1 MPa which are the same as the conditions of a low compression ration Diesel engine near TDC. A piezo actuator type with a diameter of 0.133 mm injector, and three kinds of injection amount were selected as 0.27, 0.89 and 2.97 mg to represent pilot injection, main injection of light load, and main injection of middle load respectively.

Table. 7.1 Injection conditions.

Nozzle Type	Single Holes Nozzle
Hole Diameter (mm)	0.133
Injector Type	Piezo Actuator Type
Injection Pressure (MPa)	100
Injection Quantity (mg)	0.27, 0.89, 2.97
Impinging Wall	Non-Impinging 2-D Piston Cavity
Impinging Distance (mm)	30

Table. 7.2 Experimental conditions for LAS technique.

Ambient Condition	Non-Evaporating	Evaporating
Ambient Gas	Nitrogen	
Ambient Temperature (K)	300	760
Ambient Pressure (MPa)	1.4	3.6
Ambient Density (kg/m <sup>3</sup> )	16	
Fuel Type	97.5% n-Tridecane +2.5% 1-Methylnaphthalene	

Table. 7.3 Experimental conditions for combustion.

Ambient Gas	Air (O <sub>2</sub> )
Ambient Temperature (K)	873
Ambient Pressure (MPa)	4.1
Ambient Density (kg/m <sup>3</sup> )	16
Fuel Type	JIS # 2

## 7.3 SPRAY STRUCTURE

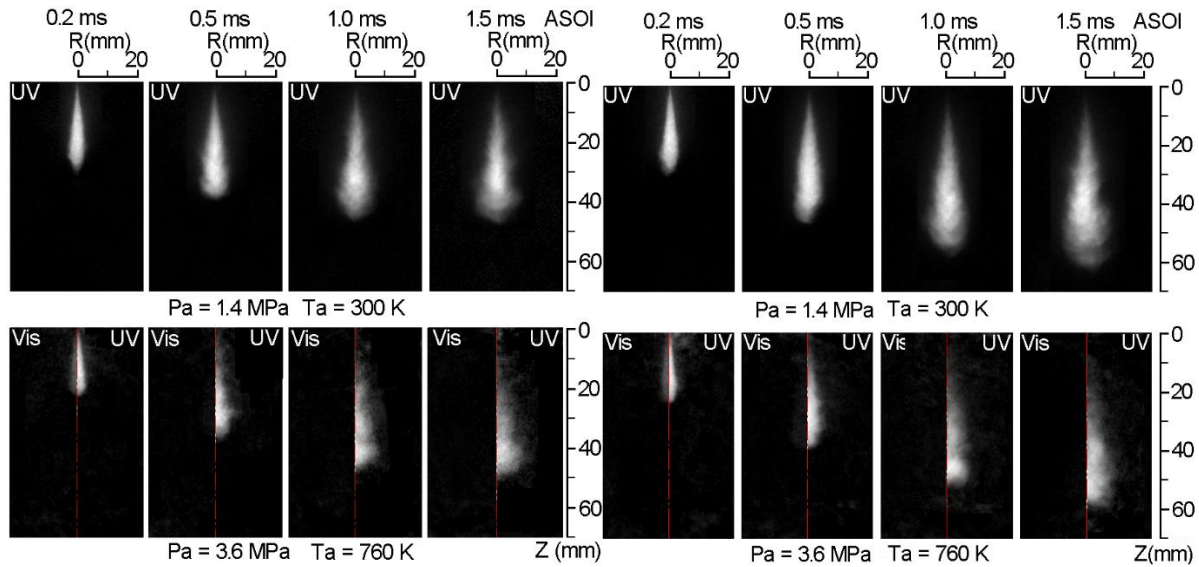
### 7.3.1 Free Spray

Figure 7.1(a), (b) and (c) respectively shows the spray images of 0.27, 0.89 and 2.97 mg in optical thickness at the visible and UV wavelengths under different conditions. The spray images under non-evaporating condition in each figure show the thickness of UV wavelength only, this is because there is no vapor phase under non-evaporating condition and the optical thicknesses of UV

and visible wavelengths are equal to each other. The bright region in non-evaporating means liquid phase only. Each spray image of mid-evaporating and evaporating conditions is composed of optical thicknesses of visible and UV wavelengths at the left half and right half of the image respectively. As discussed in Chapter 2, the optical thickness of visible wavelength is contributed by droplet attenuation and the optical thickness of UV wavelength is contributed by vapor and droplet attenuations.

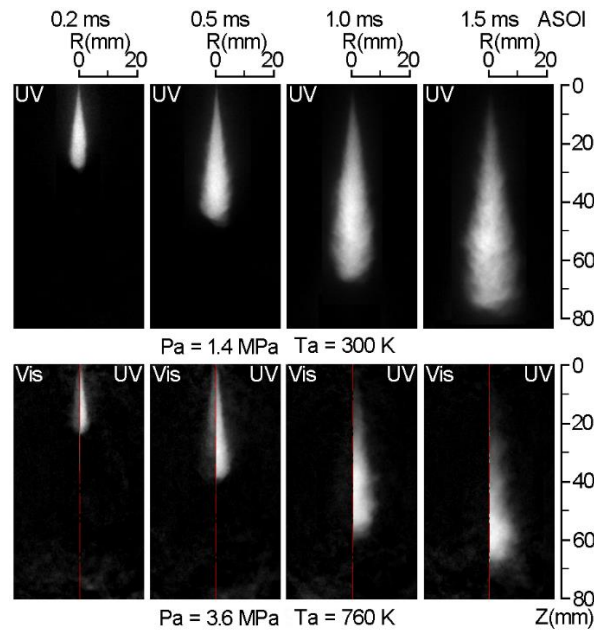
As Fig 7.1 shown, in tiny mass injection case, both the evaporating and non-evaporating conditions, the spray tip penetration is increasing with time elapsing until 1.0 ms ASOI. However, after that timing, the spray dose not penetrate further which is estimated by the same tip penetration between the images of 1.0 and 1.5 ms ASOI. This implies that the spray and ambient gas reach equilibrium after a long time of end of injection (EOI) (the injection duration is 0.31 ms as shown in Fig 2.3). Under evaporating condition, the vapor phase and liquid phase penetrations are nearly the same within the injection duration. However, it should also note that near the nozzle tip, there is a region with UV optical thickness but without visible thickness at 0.5 ms ASOI, which confirms that the more air entrained into the spray after EOI at the spray tail region [Moon et al., 2009].

When injection mass increases to 0.89 and 2.97 mg as shown in Fig 7.1 (b) and Fig. 7.1 (c) respectively, the same with that of 0.27 mg injected condition, the liquid phase penetrations are equal to the vapor phase penetration within injection duration. The around EOI timing images of 0.5 ms ASOI of 0.89mg and 1.0 ms ASOI of 2.97 mg, only tiny mass of liquid phase is existence, which implies that the injected fuel is evaporated completely soon after the EOI under this evaporating condition.



(a) 0.27 mg

(b) 0.89 mg



(c) 2.97 mg

Figure 7.1 Spray images in optical thickness at visible and UV wavelength under different ambient conditions.

Considering images of different injection masses simultaneously, it is clear that under the same ambient condition, the larger injection amount has longer spray tip penetration except within the tiny mass injection duration. This is a widely accepted phenomenon. This study focuses on this phenomenon by calculating real pressure inside the sac volume based on the ideal Bernoulli equation.

Supposing that the used fuel is the incompressible and non-viscous fluid, then the sac hole pressure could be calculated by applying Eq (7.1):

$$P_{Sac} = P_a + \frac{\rho_f}{2} \cdot \left(\frac{Q_f}{\rho_f \cdot \alpha \cdot A}\right)^2 \quad (7.1)$$

Where the  $P_a$  means the ambient pressure, the  $\rho_f$  represents fuel density,  $Q_f$  is the mass flow rate which is shown in Fig 2.3,  $\alpha$  is the flow coefficient which was selected as 0.66 according to Naber and Siebers's [1996] suggestion,  $A$  is the section area of the nozzle hole.

The estimated sac pressure results are shown in Fig 7.2. It is clear that the real sac volume pressure has the same tendency with that of mass flow rate. Even the supplied pressures by common rail are the same, the sac volume pressures which represent the real injection pressures are totally different. With injection mass decreases, the sac hole pressure decrease. This means that the real injection pressure decreases with injection mass decrease. Therefore, the spray tip penetration increases with injection mass increase as shown in Fig 7.1. According to the above discussion, the decreasing of injection mass is an effective method to decrease spray tip penetration, what's more, it is also an effective method to decrease the liquid phase penetration.

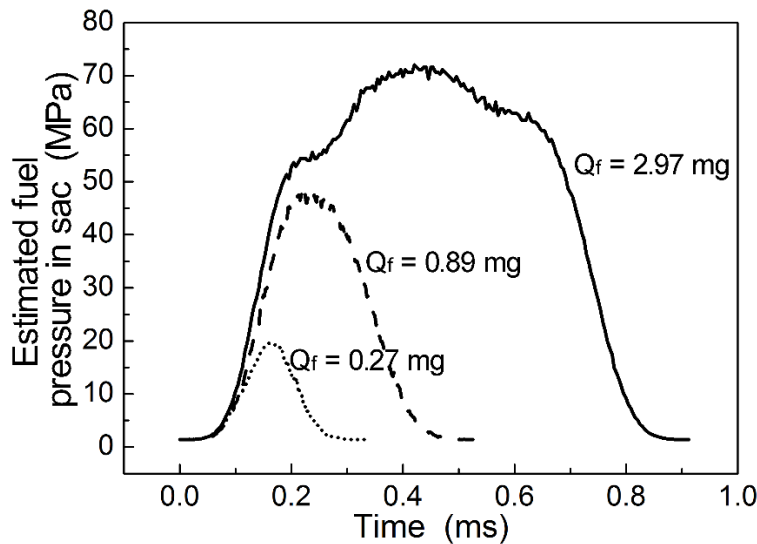


Figure 7.2 Estimated fuel pressure in sac volume.

The temporal variations of spray tip penetrations and spray angles of non-evaporating and evaporating under different injection masses are shown in Fig 7.3. The spray boundary was decided as the threshold of 20% of the saturation intensity.

According to Fig 7.3, under tiny mass injection condition, the evaporative spray has the longer spray tip penetration than that of non-evaporating spray after 0.5 ms SOI which contradicts with the former researchers' conclusions [Naber and Siebers, 1996]. The spray tip penetrations of 2.97 mg injected mass under different ambient conditions have the agreed tendency with the common acknowledgement: spray tip penetration of non-evaporating is longer than that of evaporating spray. Under 0.89 mg injection mass condition (Fig 7.3 (b)), the spray tip penetrations have the same tendency with that of 2.97 mg injection mass before 1.5 ms SOI, after 1.5 ms SOI, the opposite tendency appears which coincides with that of 0.27 mg injected mass.

The spray tip penetration can be compared with the empirical/ theoretical correlations in the literature. In this investigation, the theoretical mode developed by Desantes et al., [2006] is applied.

$$S \propto \sqrt{\sqrt{\frac{(P_f - P_a)}{\rho_a} \cdot \frac{d_0 \cdot t}{\tan(\theta/2)}}}$$

$$\propto \left(\frac{\rho_f}{\rho_a}\right)^{1/4} u_0^{1/2} d_0^{1/2} t^{1/2} \tan(\theta/2)^{-1/2} \quad (7.2)$$

In Eq (7.2),  $\rho_a$  and  $\rho_f$  represent ambient gas density and fuel density respectively,  $P_a$  and  $P_f$  represent ambient pressure and injection pressure respectively,  $d_0$  means orifice diameter,  $u_0$  is the spray velocity at the nozzle exit,  $t$  is the timing after start of injection, and  $\theta$  is the spray angle which is shown in Fig 7.3.

The spray tip penetration data can be normalized to investigate whether or not a self-similar behavior is observed as existed in steady turbulent gas jet [Payri et al., 2006]. The methods of Hill [Hill and Ouellette, 1999] and Petersen [Petersen and Gandhi, 2006] are employed, the characteristic length scale  $S^+$  and time scale  $t^+$  are defined as,

$$S^+ = \frac{d_0 \cdot \sqrt{\rho_f / \rho_a}}{\tan(\theta/2)}; \quad t^+ = \frac{d_0 \cdot \sqrt{\rho_f / \rho_a}}{u_0 \cdot \tan(\theta/2)} \quad (7.3)$$

The non-dimensional length  $S^* = S/S^+$  and non-dimensional time  $t^* = (t/t^+)^{0.5}$  can therefore be obtained. Figure 7.4 shows all of the data of Fig 7.3 recast in those non-dimensional variables. The solid line in Fig 7.4 is derived from the linear regression of all points under 2.97 mg injection mass condition which has the stable flow rate.

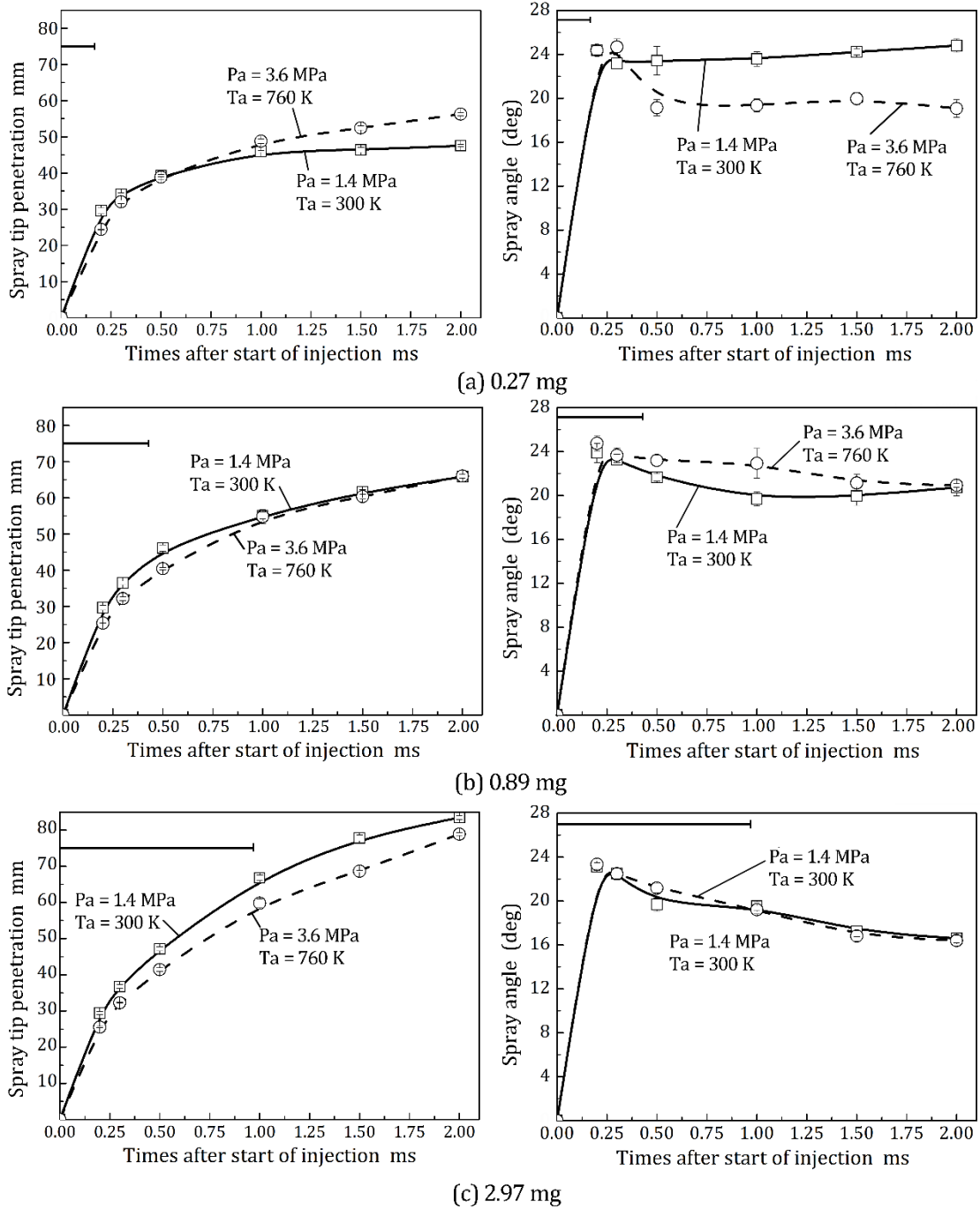


Figure 7.3 Temporal variations of spray tip penetration and spray angle of non-evaporating and evaporating under different injection masses.

From Fig 7.4, it is clear that an approximately linear relationship is established between  $S^+$  and  $t^+$  under 2.97 mg injection condition. Which implies that the relationship of Eq 7.2 is available under this condition. However, under the 0.89 mg injection mass condition, the obvious variations appear around  $T^* = 10$  time scale, this is because that the injection has finished for a long time when

the relationship of Eq 7.2 cannot be applied. Under 0.27 mg injection mass condition, large variations are observed at all the time scales except the small time scale when the injection does not finish.

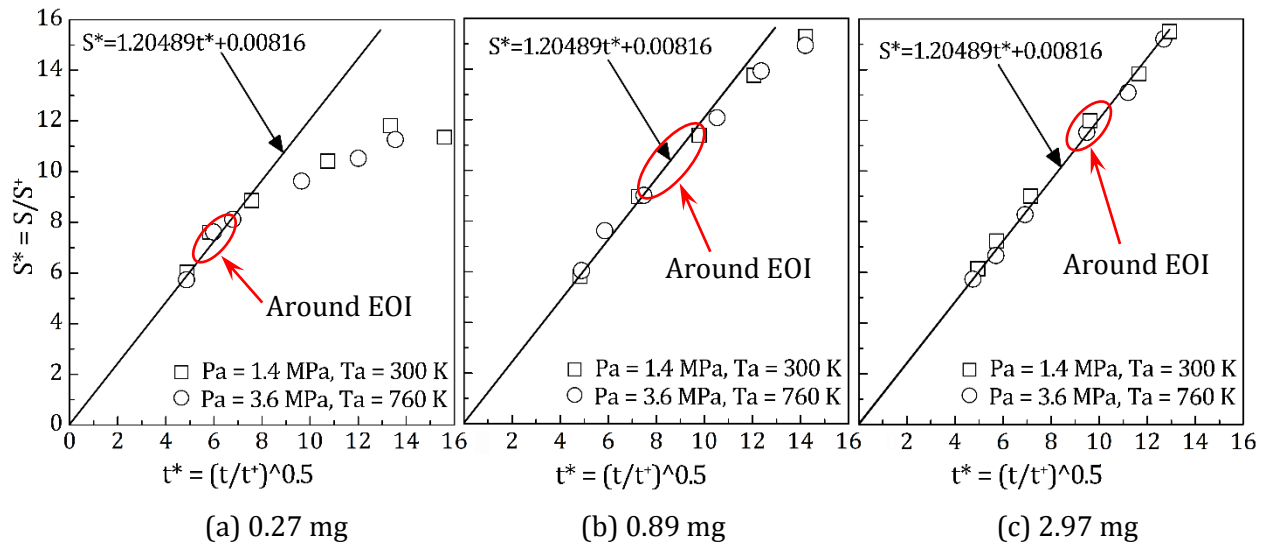


Figure 7.4 Non-dimensional form of the spray tip penetration for all the data of Fig 7.3. The solid line is derived from the linear regression of all points under 2.97 mg injection mass condition.

Therefore, the tendency of spray tip penetrations under tiny mass injection contradicts the tendency of normal mass injection after 0.5 SOI which is described above is contributed by the injection finishing. The tiny mass injection duration is about 0.31 ms, around EOI, the spray penetrative tendencies of evaporating and non-evaporating sprays are reversed, and the evaporative spray penetrate further than that of non-evaporating spray after 0.5 ms ASOI; under 0.89 mg injection mass condition, the spray tip penetrations of evaporative sprays also overpass that of non-evaporating after 1.5 ms ASOI when the injection have finished for a long time. The mechanism of the effect of EOI on spray tip penetration under evaporating and non-evaporating condition could be explained as that: the spray penetration under evaporative condition is a compromising result between the cooling effect and the air entrainment reduction effect [Naber and Siebers, 1996]. The cooling effect is that the entrained gas was cooled by droplet evaporation, and then the mixture density become higher than that of non-evaporating condition, which will result in a slower penetration velocity of evaporating spray compared with that of non-evaporating spray based on conservation of spray momentum; the air entrainment reduction effect is that the air entrainment always decrease under evaporative condition because the spray pressure consists of vapor pressure and entrained gas pressure, the entrained gas pressure of evaporative spray is lower than that of non-evaporating spray (the entrained gas pressure is equal to the ambient gas pressure under non-evaporating condition). Thus the air entrainment reduction effect resulting in a slower deceleration

of the evaporative fuel jet. During the injection duration, the cooling effect plays a significant role, thus the non-evaporating spray has longer tip penetration as Fig 7.3 (c) and the earlier timing of Fig 7.3 (a) and (b) show. However, after injection, the droplets are evaporated quickly, and the effect of cooling is diminishing, after complete evaporation, only the entrained gas reduction plays a role on spray tip penetration, thus the evaporative spray tip penetration has faster increasing rate or even is longer than those of non-evaporating spray as shown in later timing part of Fig 7.3 (a) and (b).

### **7.3.2 2-D Cavity Impinging Spray**

The effect of impingement on spray structure was concentrated on by applying a 2-D piston cavity. The spray images in optical thickness at UV and visible wavelength under different ambient conditions (non-evaporating and evaporating) and under different injection masses (0.27, 0.89 and 2.97 mg) are shown in Fig 7.5. In this section, the temporal variations of 2-D piston cavity impinging spray tip penetration are shown in Fig 7.6 which are measured from Fig 7.5.

From Fig 7.5, it can be found that the spray penetrates along the wall surface after impingement. Different with free sprays, the tip penetration and structure of liquid phase seem to be different from those of vapor phase under 2-D piston cavity impinging condition. What's more, the relative high droplet density (estimated from the brightness) does not locate at the near spray tip region which disagrees with the liquid phase distributions as shown in Fig 7.1. Lager amount of liquid phase locates at the near impinging point region and locates at the cavity's deep groove region, this is because that large momentum losing after impingement and the droplets stagnate at those regions.

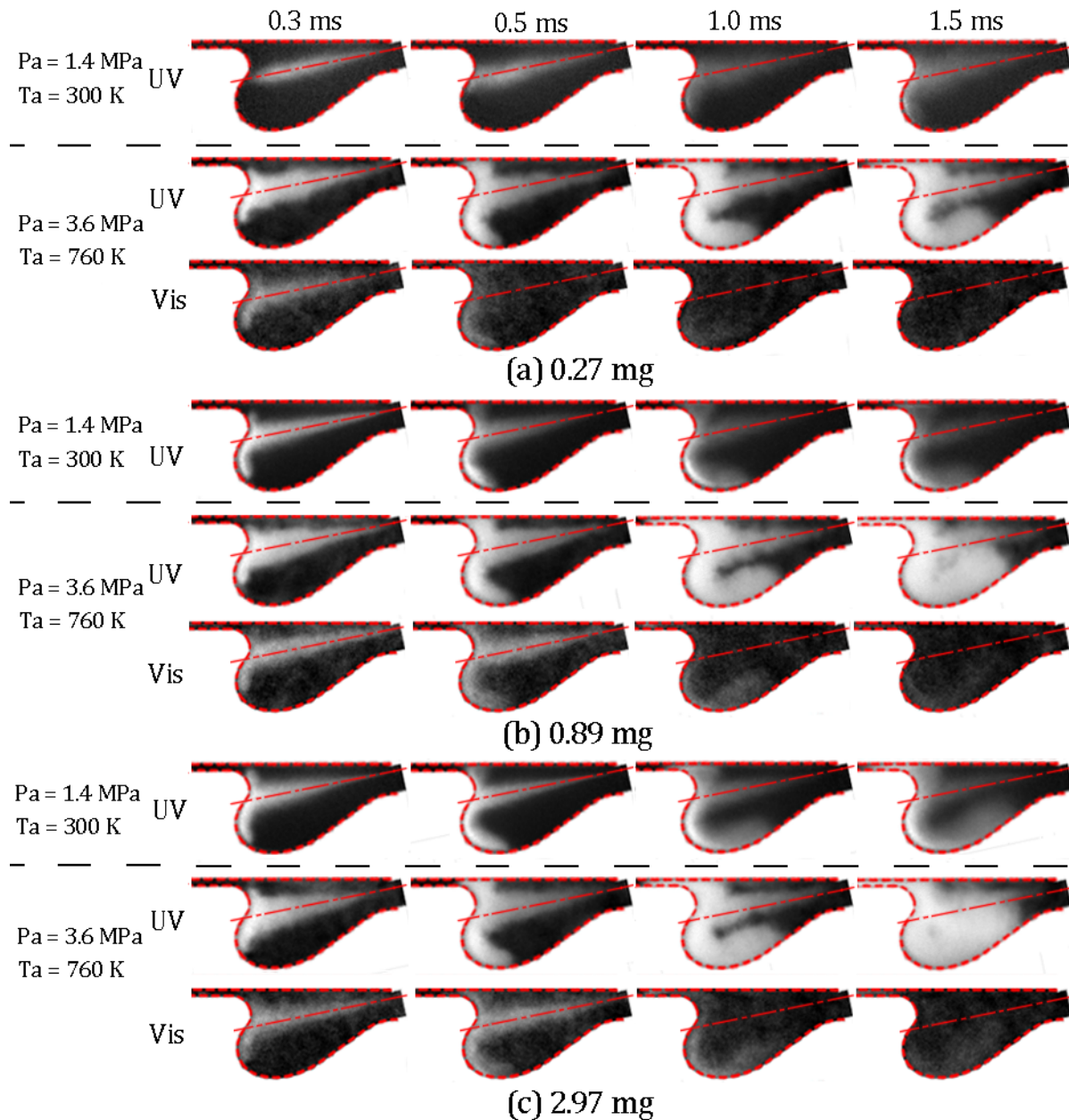


Figure 7.5 Spray images in optical thickness at visible and UV wavelength under different ambient conditions.

In Fig 7.6, it is clear that the evaporative sprays has longer spray tip penetrations than non-evaporating spray even under 2.97 mg injection mass condition when 2-D piston cavity impingement occurs. The difference between tip penetrations of evaporative spray and non-evaporating spray is evident, what's more, the gap between them is enlarged by injection mass decreasing.

As discussed in the free spray part, the evaporative spray tip penetration depends on the cooling effect and the entrained gas reduction effect. According to the former investigation [Shimo et

al., 2011], the 2-D piston cavity impinging spray has low evaporation rate because the wetting effect and Leidenfrost phenomenon [Xiong and Yuen, 1991], thus the cooling effect which results in shorter penetration under evaporative condition is weakened. What's more, the entrained gas is limited under impinging condition, and the entrained gas reduction effect is also subsistent. Therefore, the spray tip penetration of evaporative spray is longer than that of non-evaporating spray. What should be taken attention is that, the special impinging cavity shape also plays a role on the spray tip penetration. The impingement occurs around 0.3 ms ASOI, thus the tendency of penetrations under different ambient conditions is the same with that of free spray at this timing when the injection masses are 0.89 and 2.97 mg (Fig 7.6 (b) and (c)). After impinging spray pass through the cavity's deep groove region, most of the droplets are stagnated, and the spray tip is dominated by vapor where the cooling effect is feeble. This could be confirmed from Fig 7.6 (c) where the evaporative sprays penetrate further than non-evaporating spray after 0.5 ms ASOI (the spray tip pass out the cavity's deep groove region around 0.5 ms ASOI according to Fig 7.5).

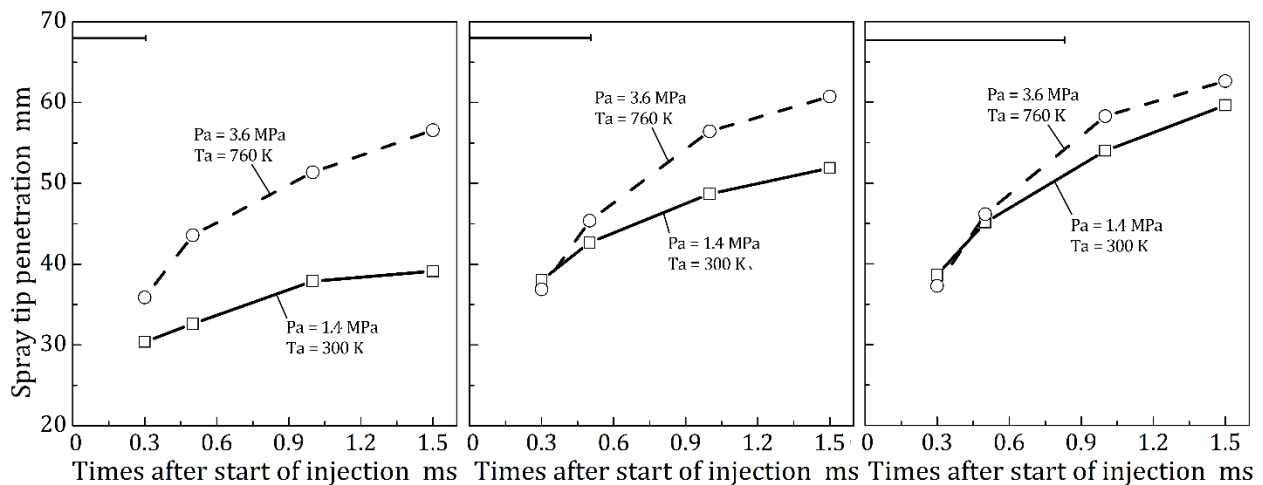


Figure 7.6 Temporal variations of spray tip penetration and spray angle of non-evaporating and evaporating under different injection masses.

## 7.4 VAPOR AND LIQUID PHASE DISTRIBUTION OF EVAPORATING SPRAY

### 7.4.1 Free Spray

The Equivalence ratio distributions of liquid phase and vapor phase of free spray under different injection mass are shown in Fig 7.7. In each pair of the image, the left part is the equivalence ratio of liquid phase and denoted as ER<sub>d</sub>, the right part is the equivalence ratio of vapor phase and denoted as ER<sub>v</sub>. The results were analyzed by applying onion reconstruction method in LAS system.

The results shows that under 0.27 mg injection condition, the injected fuel approaches to complete evaporation at 0.3 ms ASOI (close to EOI), and the maximum equivalence ratio is 1.2 (in the central region) around this timing, most of the mixtures are located within the equivalence ratio region of 0.4-0.8, thus the global mixture is lean. When injection mass increases to 0.89 mg, at 0.2 and 0.3 ms ASOI, the dense liquid fuel occupies the overall spray region, and the liquid fuel is evaporated at the spray downstream region. The vapor phase distributes at the downstream of the spray within injection duration is because the ambient gas mainly entrains into the spray through the upstream region, and then the injected fuel is evaporated and penetrates to the downstream, this structure coincides with the flame structure, and the upstream no vapor region is similar with lift-of-length. Around EOI (0.5 ms ASOI), the fuel is completely evaporated except the tiny mass later injected fuel in the spray tail region. The maximum equivalence ratio also is 1.2 in the spray central region, but the dense region area is larger than that of 0.27 mg at 0.3 ms ASOI. After that, the spray penetrates further and dispersing, the overall spray equivalence ratio goes to 0.2-0.5 region at 1.0 ms ASOI. Under 2.97 mg injection condition, the same with the 0.89 mg condition, the liquid fuel occupies the whole area of the spray, and the vapor phase appears in the downstream region. Around EOI (1.0 ms ASOI), there is no liquid fuel existing and the maximum equivalence reaches to 1.6, and the rich mixture (ERV: 1.2-1.6) is dominant inside the spray. At 1.5 ms ASOI, the ambient gas entrained more and the mixture distribution is similar with that of 0.27 mg 0.3 ms ASOI and 0.89 mg 0.5 ms ASOI.

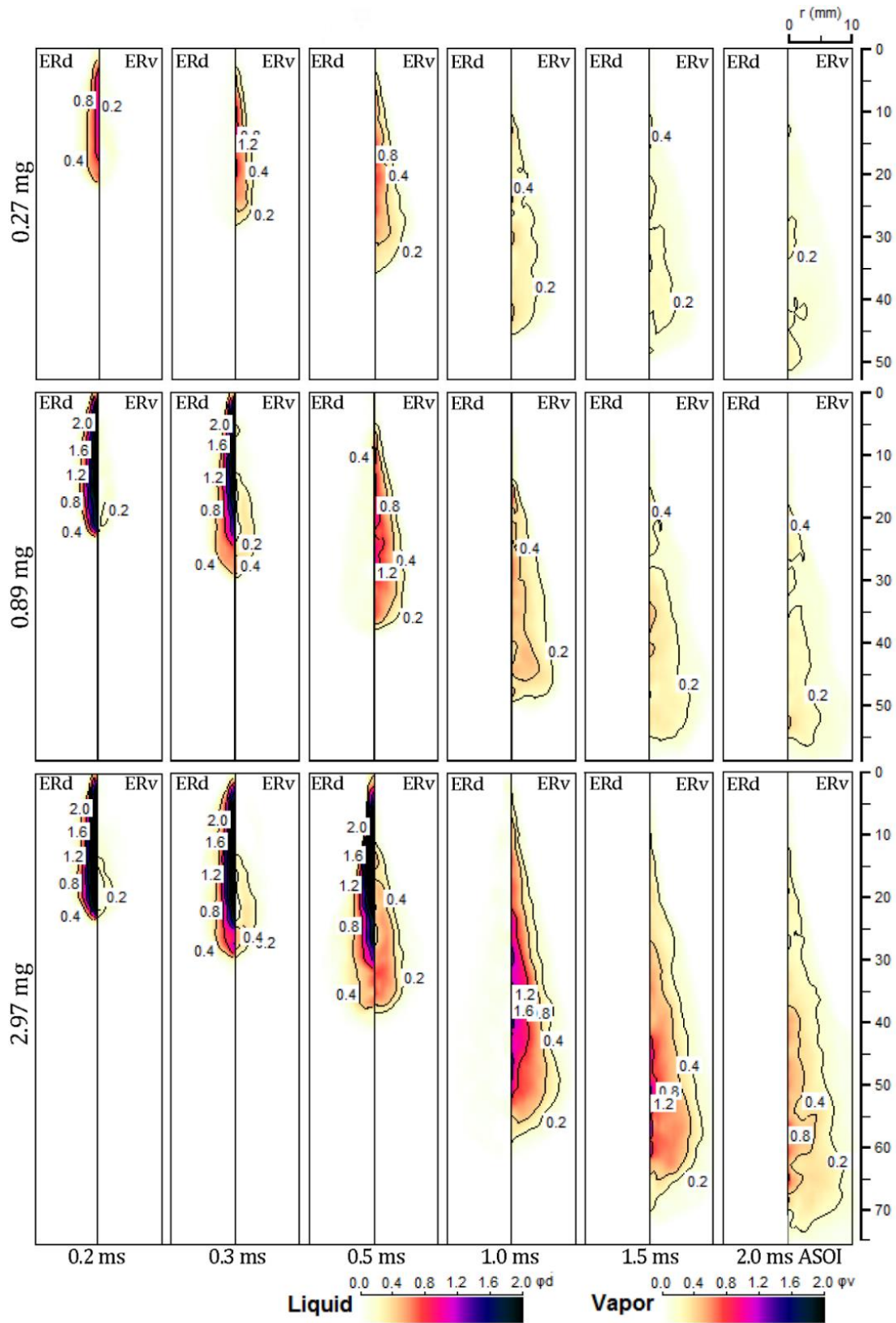


Figure 7.7 Equivalence ratio distributions of liquid phase and vapor phase of free spray under different injection mass.

The equivalence ratio spatial distributions of vapor phase of free spray under different injection mass near at the EOI timing (0.3 ms for 0.27 mg, 0.5 ms for 0.89 mg and 1.0 ms for 2.97 mg) are shown in Fig 7.8. In Fig 7.8, the image (a) is the axial distribution at the central region which is coincident with the nozzle hole axis, to compare those results directly, the horizontal axis was normalized as the percentage of the spray tip penetration  $S$ ; and the Fig 7.8 (b) is the radial distribution at different axial locations.

From Fig 7.8 (a), it is found that around EOI, the relative rich region appears at the mid-downstream region. The injection mass does not play a significant role in the mixture equivalence ratio at the upstream region (shorter than  $2S/5$ ), however, the mixture becomes dense with injection mass increasing at the spray mid-downstream region. The axial distributions' curves are not smooth but with some peaks especially at the mid-downstream region. When it comes to Fig 7.8 (b), it is clear that the radial distribution of equivalence ratio is monotone decreasing from inter to external region of the spray under all the conditions. Combined with left curve, it is clear that the mid-downstream region is the mixture region.

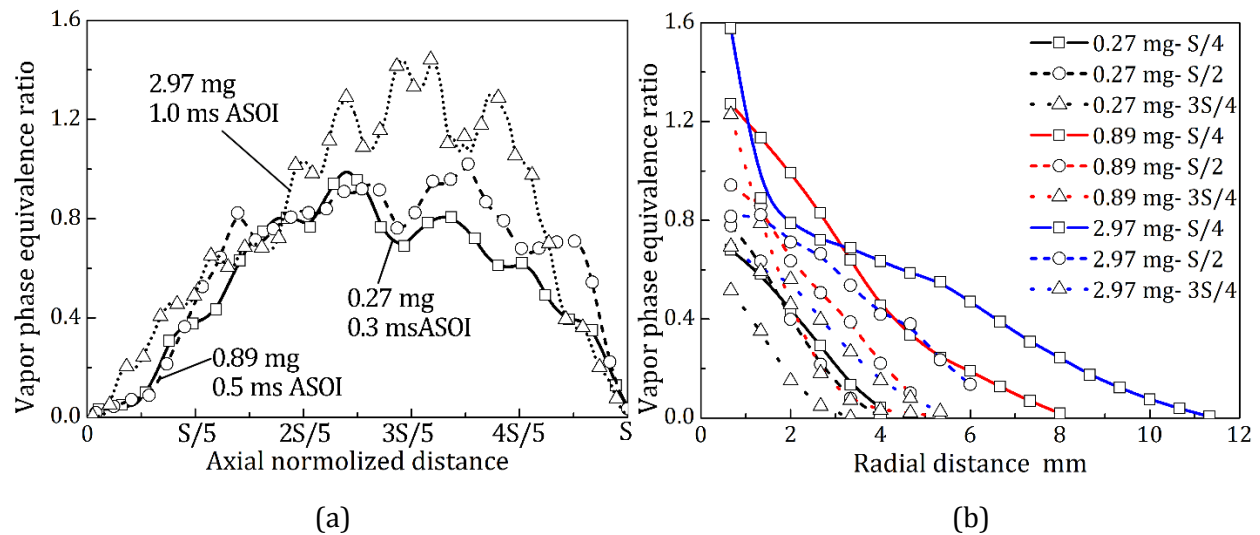


Figure 7.8 Equivalence ratio spatial distributions of vapor phase of free spray under different injection mass.

#### 7.4.2 2-D Cavity Impinging Spray

The spatial distributions of vapor mass per project area of 2-D piston cavity impinging spray under different injection masses are shown in Fig 7.9. It is found that both the spray structures and vapor mass distributions of different injection amount sprays are similar at 0.3 ms ASOI. At 0.5 ms

ASOI, around the EOI of 0.89 mg injection mass, the vapor phase of 0.89 mg injection spray per projected area is higher than that of 2.97 mg spray especially at the impinging point region, this is because that around EOI, the ambient gas entrainment is suddenly enhanced due to the momentum reduction and the fuel is evaporated rapidly, as a result, the vapor mass of 0.89 mg injection spray is more dense than 2.97 mg injection spray. At 1.0 ms AOSI, when the 2.97 mg injection has been finished, it is found that the larger injection amount gives denser vapor phase concentration and also gives the larger spray projected area. The evidently dense vapor phase is located at the spray tip region. When it comes to 1.5 ms ASOI, significant variations are appearing among different injection masses. Under 0.27 and 0.89 mg injection masses' conditions, the vapor fuel mainly distributes at the spray middle and tip regions, however, under large amount injection case, the vapor phase locates at the whole wall spray region, and the wall vicinity is very dense.

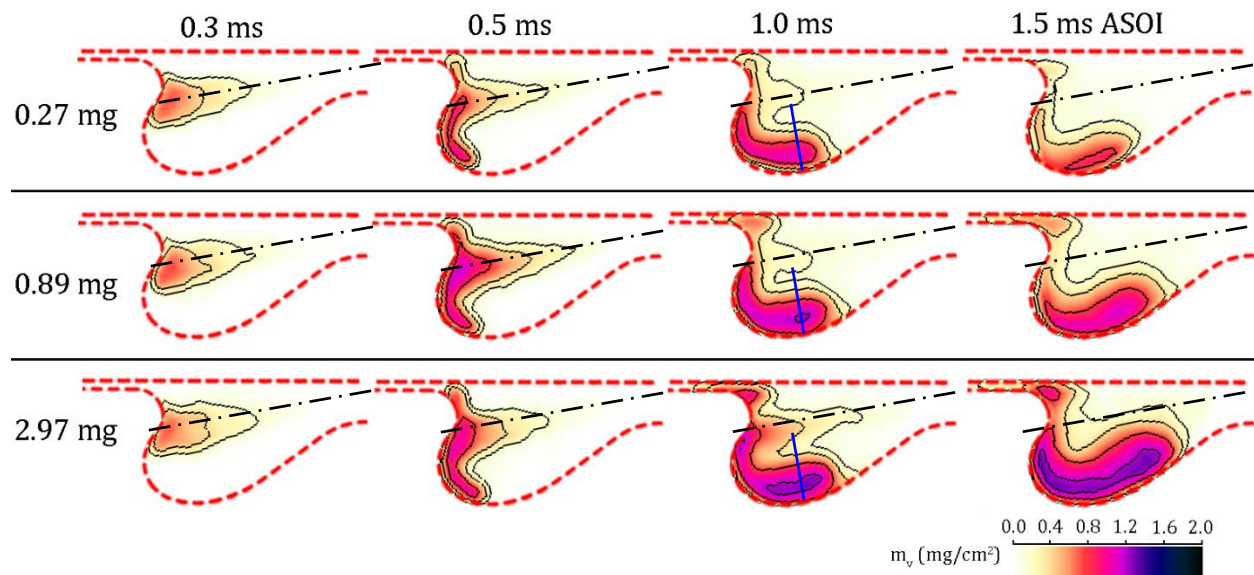


Figure 7.9 Equivalence ratio distributions of liquid phase and vapor phase of 2-D piston cavity impinging spray under different injection mass.

The spatial distributions of vapor per unit area along the flowing path under different injection masses at 1.0 ms ASOI are shown in Fig 7.10 (a), and the spatial distributions of vapor per unit area along the sectional lines at the spray tip region (as blue lines shown in Fig 7.9) under different injection amounts are shown in Fig 7.10 (b). The zero point in the horizontal axis of Fig 7.10 (b) represents the wall surface.

From Fig 7.10 (a), it is found that the spray tail regions (0-25 mm) of 0.27 and 0.89 mg have the same vapor phase distributions, however, the 2.97 mg is denser than them, this is resulted from the difference of the injection duration. The vapor fuel is mainly distributes at the wall spray region,

and the density of the vapor phase is increased with injection amount increasing. The vapor phase per unit area of 2.97 mg injection spray reveals two peaks at the wall spray region, this is because some of the droplets are stagnated at the large curvature region as shown in Fig 7.5, and then the droplets are evaporated at this region. Figure 7.10 (b) gives that the vapor fuel mainly located at the wall vicinity region, the peak values appear at 2 mm away from the wall surface region.

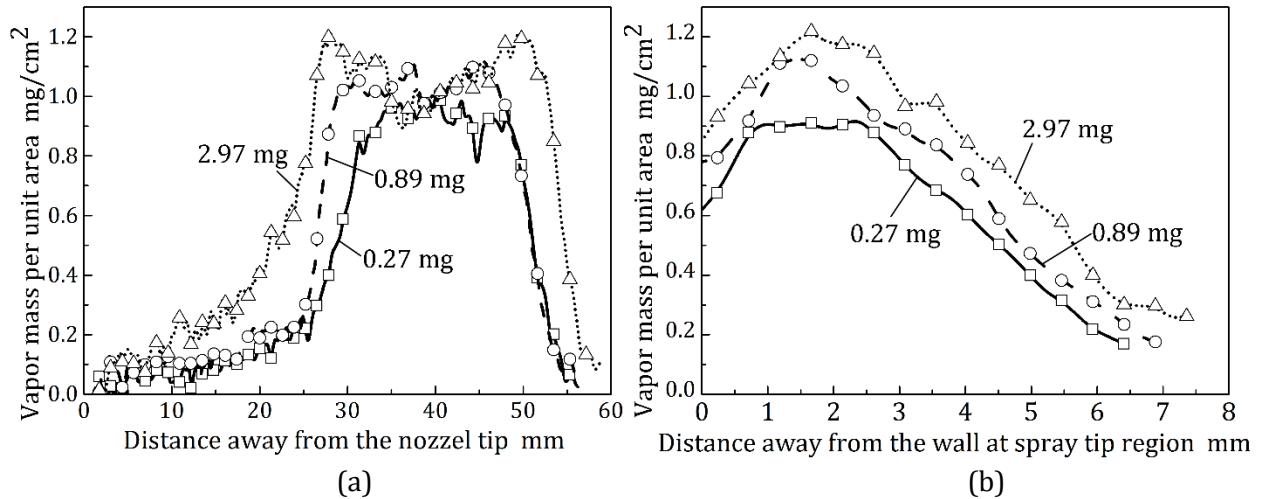


Figure 7.10 Spatial distribution of vapor per unit area along the flowing path (a) and along the sectional line (blue line in Fig 7.9) (b) at 1.0 ms ASOI.

## 7.5 COMBUSTION PROCESSES

### 7.5.1 Free Spray Flame

The flame natural luminosity images of free spray under different injection masses are shown in Fig 7.11. The camera settings were different because of the significant variations of the flame luminosity intensity under different injection masses, and the settings are shown at the bottom of each figure group. To avoid intensity saturation and also to avoid that intensity could not be perceived, the camera settings were carefully selected (F1.8 and 0.1 ms exposure timing under 0.27 mg injection condition, F8 and 0.1 ms exposure timing for 0.89 mg injection, and F22 and 0.003 ms exposure timing). In addition, a 5% transmittance neutral filter was adopted when the injection mass of 2.97 mg experiment was carried out, this is because the super strong intensity received by the high sensitivity camera sensor.

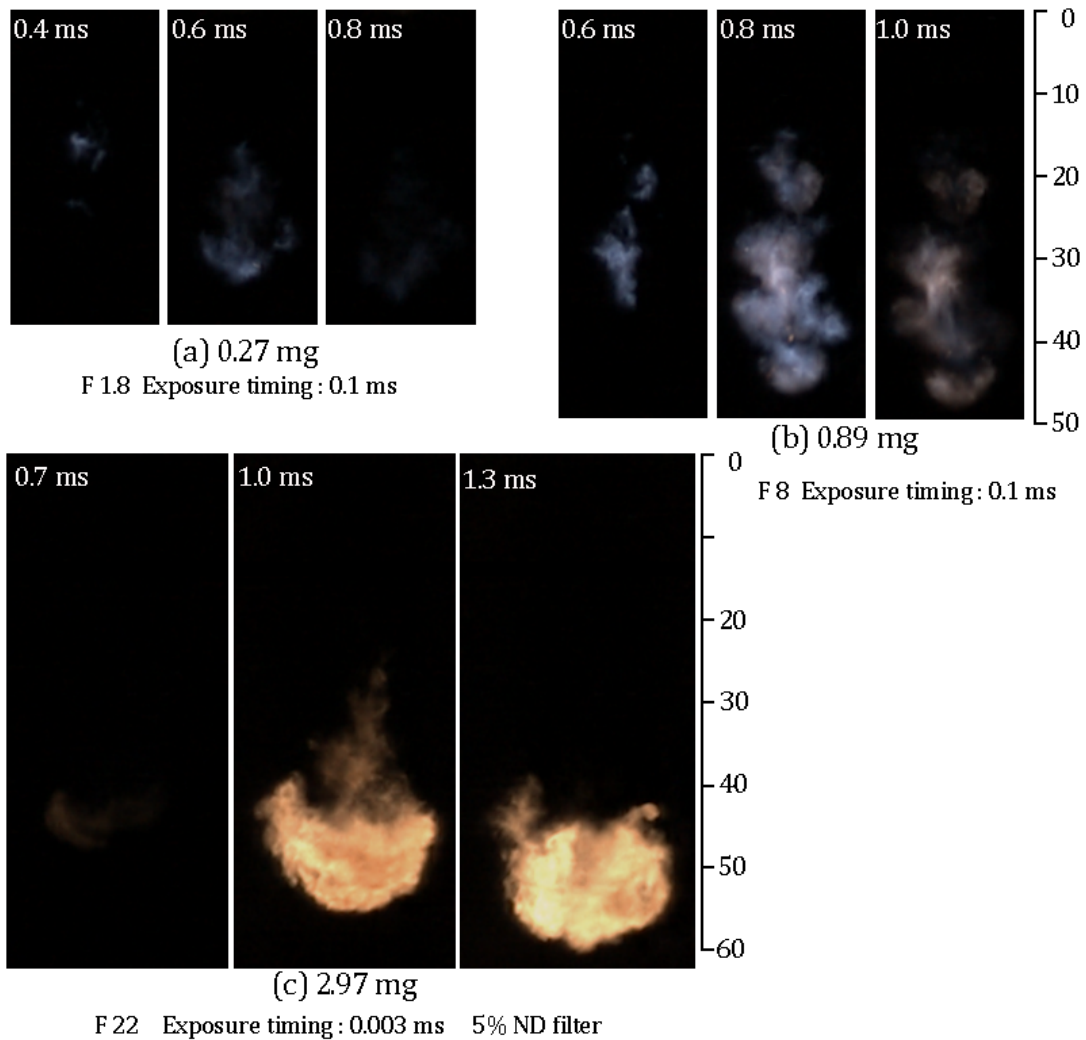


Figure 7.11 Spatial distributions of flame luminosities under different injection masses.

From Fig 7.11, the flame luminosity initially appeared at 0.4 ms ASOI when injection mass was 0.27 mg, the ignition delay is longer than the injection duration. At the auto-ignition timing, the equivalence ratio of mixture central region where the auto-ignition occurs should be belong to 0.8-1.0 which is deduced from Fig 7.7. At 0.8 ms AOSI, only weak flame luminosity could be observed, which means near the end of combustion. During the combustion process, the emitted flame is blue which implies that it is low temperature and no soot combustion. Under 0.89 mg injection condition, even the aperture size is smaller than that of 0.27 mg condition, the flame luminescence is brighter. The same with 0.27 mg injection case, the flame appeared after the EOI which ensures the relatively uniform mixture forming. The flame luminescence is dominated by the blue light, and faint yellow flame appears after 0.8 ms ASOI. The faint yellow flame is not thought as soot incandescence because the burning mixture is lean (equivalence ratio is lower than 1) and the low flame temperature (lower than 1650 K which is thought as the crucial temperature for soot formation), the two color method

also confirmed that no soot formation under this condition. When injection mass was increased to 2.97 mg, the strong soot incandescence and the camera settings result in undetectable of the blue flame, and the perceived intensities are mainly emitted from soot incandescence. The soot is initially formed at 0.7 ms ASOI, as the soot is formed a period after auto-ignition, therefore, the ignition delay is shorter than 0.7 ms, which means that the combustion occurs during the main injection period. And the diffusion combustion which results in high soot emission is forming [Dec, 1997]. The soot concentration and temperature distribution analyzed by applying two-color method will not be shown because the results of 0.27 and 0.89 mg are not precise (the two-color method is appropriately applied on the premise of soot incandescence).

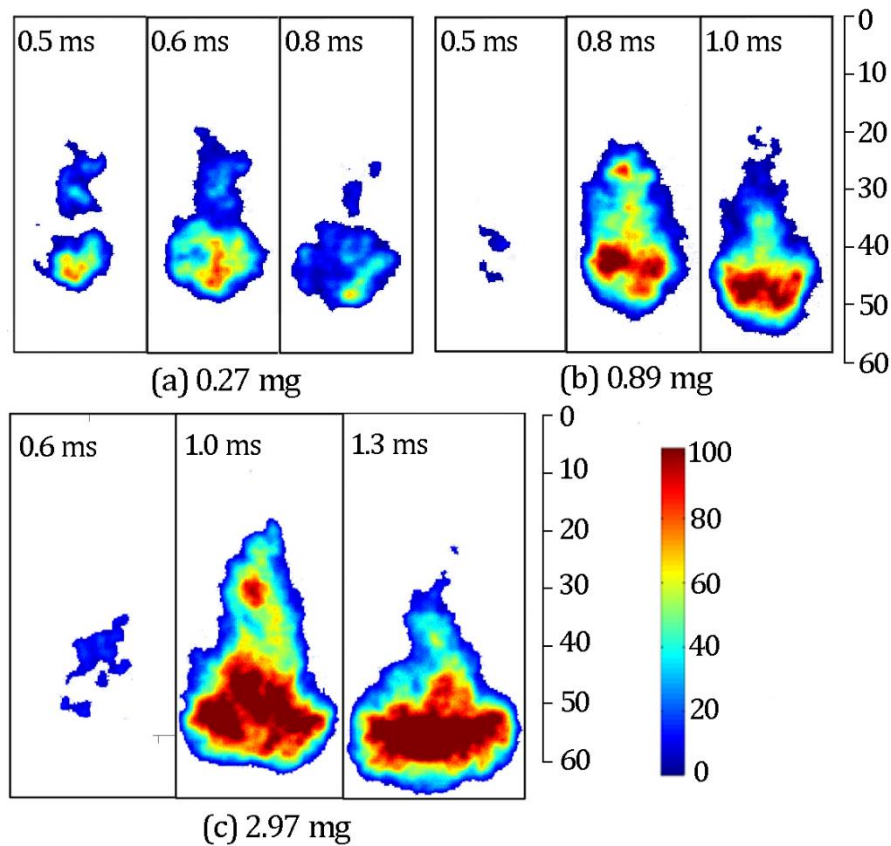


Figure 7.12 OH\* chemiluminescence images of free spray flame under different injection masses.

The OH\* chemiluminescence images of free spray under different injection masses are shown in Fig 7.12. The gain was selected as 75 us, and the aperture size was selected as F8. Under 0.27 mg injection mass, it is interesting that the OH\* chemiluminescence is initially observed at 0.5 ms ASOI, it is later than the appearing of flame luminosity, this is possibly because the jet-jet variation. When time comes to 0.6 and 0.8 ms, the OH\* structure is similar with that of flame luminosity as shown in Fig 7.11 (a), and the relative high OH\* intensities are observed at the spray mid and downstream

regions which coincides with the relative high equivalence ratio mixtures. When injection mass is increased to 0.89 mg, the OH\* intensity become intense, and the tiny OH\* intensity is observed at 0.5 ms. At 0.8 and 1.0 ms ASOI, the OH\* flame structures are similar with those of flame natural luminosity, which confirms that the faint yellow luminescence shown in Fig 7.11 is not soot incandescence (if soot is forming, upper region of sooting flame are occupied by OH\* chemiluminescence and the downstream intensity is much higher than the upstream intensity). The 2.97 mg injection condition, as discussed in Chapter 4, has high OH\* intensity at the spray downstream region which means that the stoichiometric mixture is achieved or soot oxidation is undergoing at the spray downstream region.

The temporal variations of integrated OH\* intensity and injected mass integrated OH\* intensity are shown in Fig 7.13 (a) and (b) respectively. Combining with the injection flow rate, it can be found that compared with EOI timing, the auto-ignition is considerably prolonged for 0.27 and 0.89 mg injection conditions. The auto-ignition occurs after EOI is called PCCI combustion mode, which is thought as an effective combustion mode to reduce soot emission. The integrated OH\* intensity is an indicator of heat release and a reflector of reaction intensity. As commonly recognized, the larger injection mass has the higher heat release and the stronger reaction intensity. When attention is paid to Fig 7.13 (b), it is found that the lower injection mass, the higher maximum integrated intensity, and the more advance maximum timing, which implies that the heat release fast under small injection mount condition, and the combustion completeness is enhanced by decreasing injection amount.

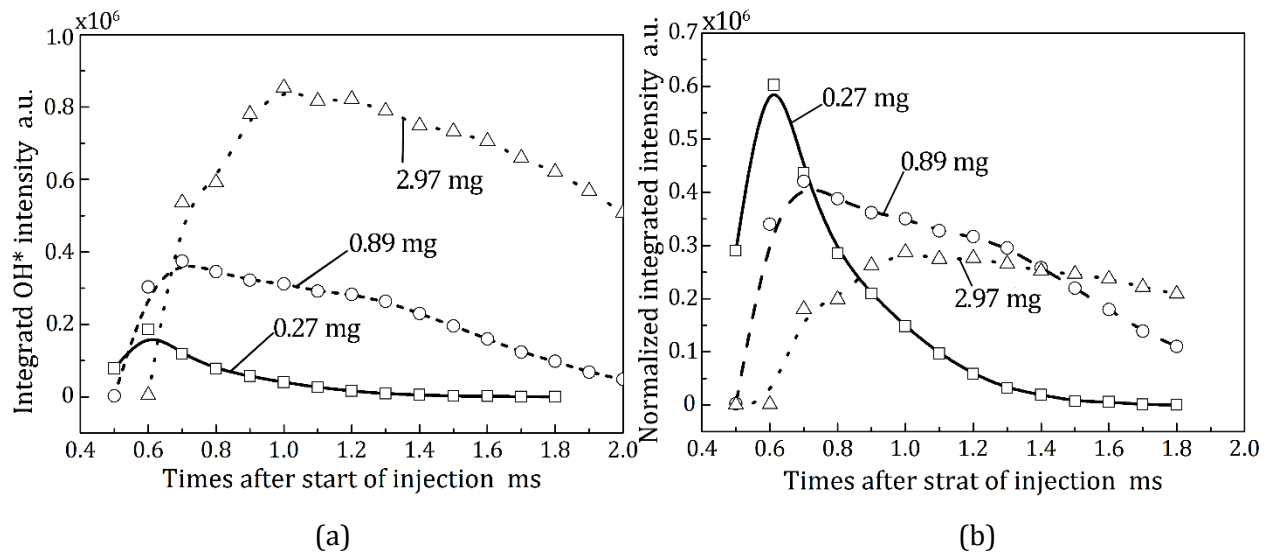


Figure 7.13 Temporal variations of integrated OH\* intensities (a) and injection mass normalized integrated OH\* intensity (b) of free spray flame.

## 7.5.2 2-D Piston Cavity Impinging Spray Flame

The 2-D piston cavity impinging flames of 0.27, 0.89, and 2.97 mg injection masses are shown in Fig 7.14, the same with free flame recording system, the camera settings are different under different injection masses.

Under 0.27 mg injection condition, the flame is initially observed at 0.4 ms ASOI which is the same with free flame, the blue flame is appeared at the impinging point region where the mixture is rich to auto-ignition as shown in Fig 7.9. At 0.4 ms ASOI, it is clear that two bright yellow flames are formed at the right and the left region symmetrically, this is attributed to soot incandescence which is contributed by liquid combustion. At the later stage of the combustion, the soot is oxidized and the natural flame is confined in the larger curvature region. Under 0.89 mg injection condition, the blue flame is simultaneously recorded near the wall vicinity, and the soot indicated by bright yellow flame is formed in the in the large curvature region and the spray tip region. This is because that both the dense liquid fuel and the vapor phase are formed in this region, and the large vortex in the spray tip region also contributes to relative high mixture and to the large liquid fuel forming. When injection mass is increased to 2.97 mg, the blue flame cannot be detected because the setting of the recording system. And the soot mainly exists at the head vortex region.

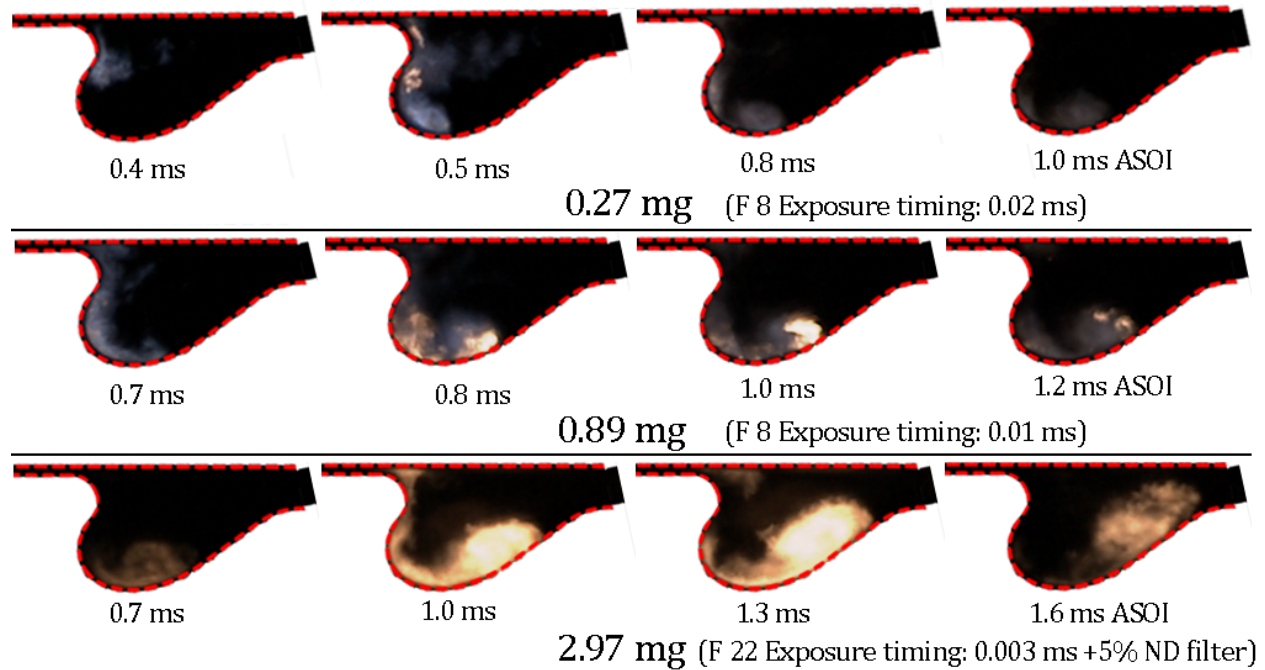


Figure 7.14 Spatial distributions of impinging flame luminosities under different injection masses.

The OH\* chemiluminescence images of 2-D impinging spray flame under different injection masses are shown in Fig 7.15. It can be found that the OH\* chemiluminescence is restricted to the large curvature region where the mixture is high as shown in Fig 7.9. This is because under tiny mass injection, the mixture is lean and the richest region approaches to stoichiometric ratio. The auto-ignition occurs at 0.6 ms ASOI under 0.89 mg injection condition, the same structures with those of soot incandescence as shown in Fig 7.14, the strong reaction represented by high OH\* intensity occurs at the large curvature region and the spray tip region. This is possibly because that the OH\* is a potential reflector of soot oxidation. When it comes to 2.97 mg injection, it is more clear that the strong OH\* chemiluminescence region coincides with the soot incandescence region distinctly.

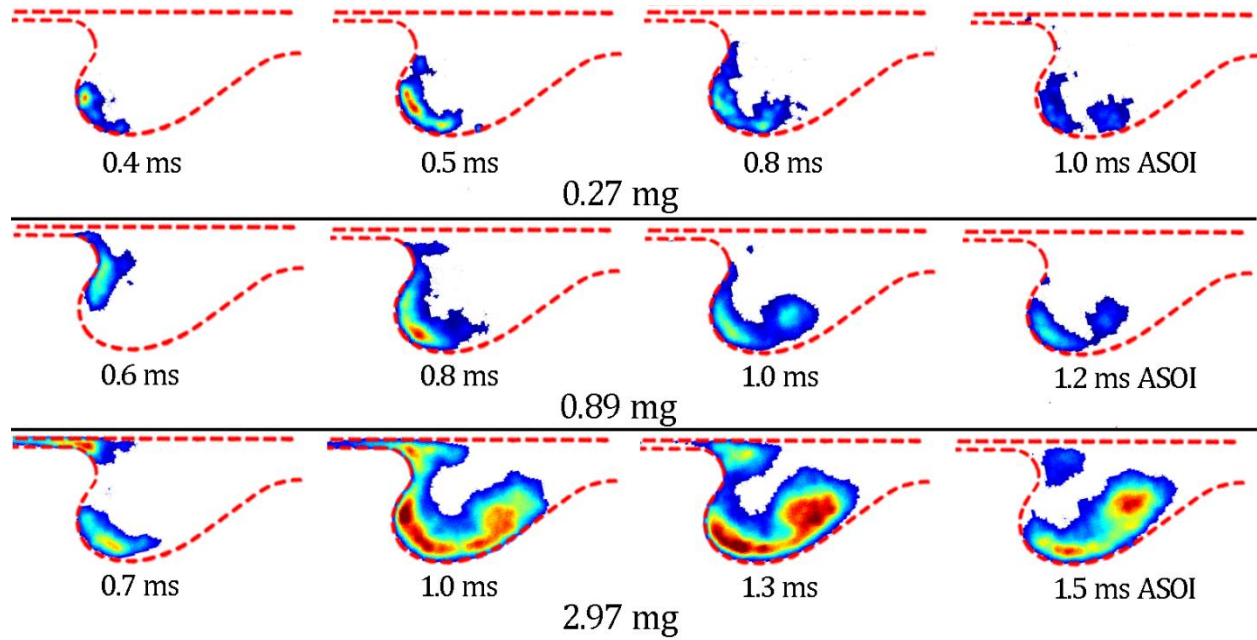


Figure 7.15 OH\* chemiluminescence images of impinging flame under different injection masses.

The temporal variations of integrated OH\* intensity and injected mass integrated OH\* intensity of 2-D impinging spray flames are shown in Fig 7.16 (a) and (b) respectively. The same with free spray flame, the higher heat release and the stronger reaction intensity. When attention is paid to Fig 7.16 (b), it is found that the lower injection mass, the higher maximum integrated intensity, and the more advance maximum timing, which implies that the heat release fast under small injection amount condition, and the combustion completeness is enhanced by decreasing injection amount.

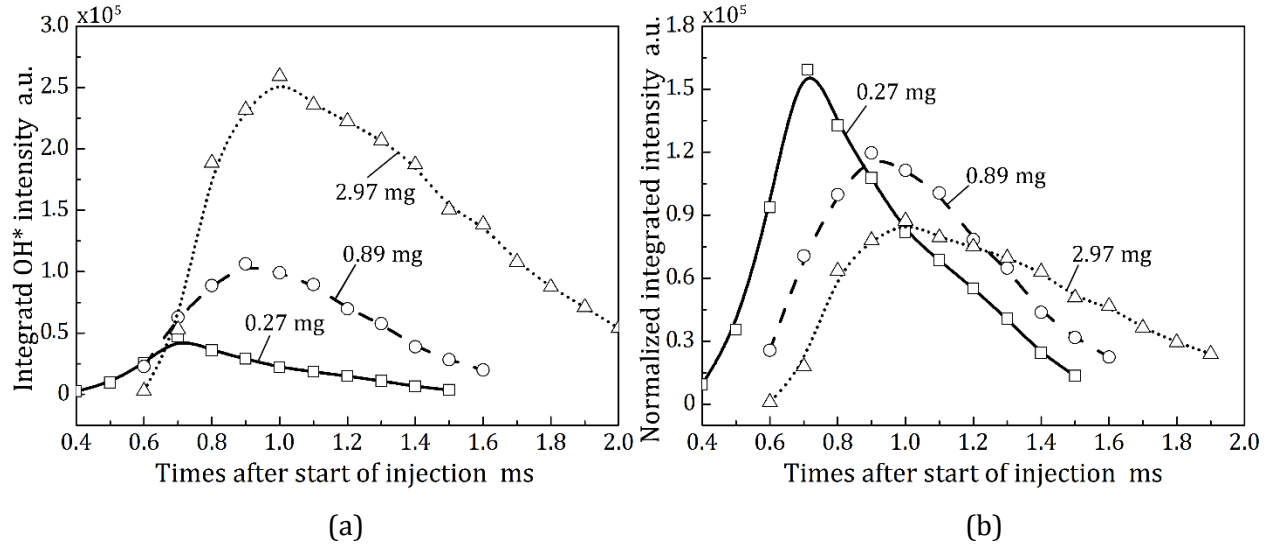


Figure 7.16 Temporal variations of integrated OH\* intensities (a) and injection mass normalized integrated OH\* intensity (b) of 2-D impinging spray flame.

Generally, the injection amount decreasing can enhance the mixture formation and soot reduction both under free spray and impinging spray conditions.

## 7.6 SUMMERY

Characteristics of mixture formation and combustion of free spray flame and 2-D impinging spray flame under different injection amounts were investigated by applying LAS technique, OH\* recording system and broadband spectrum luminosity recording system. The injection amounts are selected as 0.27, 0.89 and 2.97 mg to represent pilot injection, main injection of light load, and main injection of middle load respectively. Based on this investigation, the main conclusions are summarized as follows:

1. The spray tip penetration is increased with the injection amount increasing because the pressure of sac volume is enhanced by increasing the injection mass. Decreasing injection mass is an effective method to reduce spray tip penetration.
2. Under different ambient conditions, the spray tip penetration tendency of tiny amount injection contradicts with that of relatively large amount injection which is performed as that the evaporative spray has further tip penetration than the non-evaporating spray. This is contributed by the competition between cooling effect and entrained gas reduction effect.
3. Under 2-D piston cavity impinging condition, the evaporative spray has further spray tip penetration than the non-evaporating spray under all the injection amount conditions.

This is because the low evaporation rate, droplets stagnation and low ambient gas entrainment when impingement occurs.

4. Around EOI, under all of the injection amounts of free sprays, the vapor-air mixture is rich in the central region of the spray downstream. And the vapor phase equivalence ratio is increased with injection amount increasing. The maximum equivalence ratio for 2.97 mg injection spray is around 1.6, however, it is lower than 1 under 0.27 and 0.89 mg injection amounts conditions.
5. Under 2-D impinging condition, the vapor fuel are mainly distributes at the wall vicinity region (about 2 mm away from the wall surface). The vapor mass per projected area at the wall spray region has two peak values which represent the large curvature and spray tip region respectively.
6. The auto-ignitions of free spray under 0.27 and 0.89 mg injection conditions are occurred after the EOI, the combustions which are recognized as PCCI mode produce no soot.
7. The auto-ignition of 2-D impinging spray under 0.27 and 0.89 mg injection are occurred after the EOI. Even the combustions are PCCI mode, the particles are formed because the liquid phase combustion.
8. Even the reaction intensity and the heat release is enhanced by increasing the injection amount, the combustion completeness is improved by decreasing the injection mass.

# **CHAPTER 8 COMBUSTION AND EMISSION CHARACTERISTICS OF MULTIPLE INJECTION SPRAY**

## **8.1 INTRODUCTION**

Multiple injection, as discussed in Chapter 2, has the advantages [Ricaud and Lavoisier, 2004] of: (1) reduce combustion noise and NO<sub>x</sub> emissions through pre-injection or pilot injection of a small fuel quantity; (2) optimize the torque release without producing excessive particles through the main injection and (3) enhance soot oxidation rate through post injection of another small fuel mass. In a low compression ratio diesel engine, which is aiming to realize the HCCI combustion mode, the tiny mass pilot injection is also thought as an effective method to obtain combustion stability and the completeness under cold start and idling conditions. The interval between the pilot injection and the main injection and the pilot injection times play a significant role in the mixture formation, combustion and soot formation. What's more, the post injection which can enhance the soot oxidation is also relied on the interval between the main injection and the post injection. Therefore, this section is focused on the combustion and emission behaviors under various injection strategies. The intervals between the pilot injection and main injection and between the main injection and the post injection were also concentrated on.

## **8.2 EXPERIMENTAL CONDITIONS**

The experimental conditions are shown in Tab 8.1. A single hole piezo actuator type injector with diameter of 0.133 mm was applied. The injection pressure was 100 MPa, and Diesel JIS #2 was selected as the used fuel. In this section, both the pilot and post injections with the injection mass of 0.27 mg, and the main injection mass was 2.97 mg. The injection strategies consisted of pilot and main injections, main and post injections, twice pilots and main injections, pilot, main and post injections. Under conditions of single pilot injection and post injection, the combustion behaviors of spray flames with intervals of 0.2, 0.5 and 0.8 ms were observed. And under twice pilot injections condition and also under the pilot-main-post injection condition, the intervals were kept at 0.2 ms. The specific injection profiles of multi injection strategies are shown in Fig 8.1. 2-D piston cavity was applied to forming the impinging spray flame which was similar with that of a real engine. The ambient gas temperature and pressure were selected as 873 K and 4.1 MPa which were used to simulate the ambient conditions of a low compression ratio diesel engine at TDC.

Table. 8.1 Experimental conditions.

Nozzle Type	Single Holes Nozzle
Hole Diameter (mm)	0.133
Injector Type	Piezo Actuator Type
Injection Pressure (MPa)	100
Injection Quantity (mg)	0.27 (Pilot/Post), 2.97 (Main)
Injected Fuel	Diesel JIS #2
Interval (ms)	0.2, 0.5, 0.8
Injection Strategy	Pilot + Main, Main + Post, Pilot+ Pilot+ Main, Pilot+ Main+ Post
Impinging Wall	2-D Piston Cavity
Impinging Distance (mm)	30
Ambient Gas	Air (21% O <sub>2</sub> )
Ambient Pressure (MPa)	4.1
Ambient Temperature (K)	873
Ambient Density (kg/m <sup>3</sup> )	16

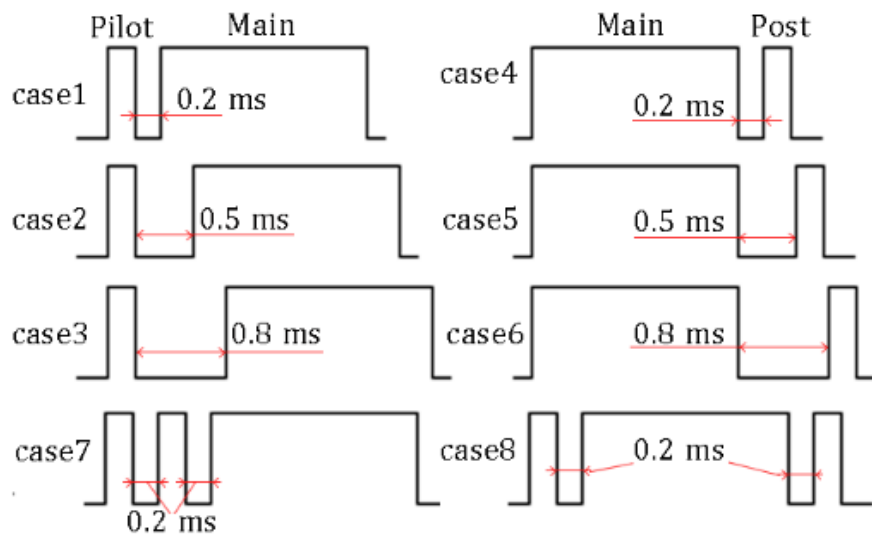


Figure 8.1 Schematic injection profiles of multi injection strategies.

## 8.3 FLAME CHARACTERISTICS OF SPRAY WITH PILOT AND POST INJECTIONS

### 8.3.1 Combustion Behaviors under Different Intervals

The flame natural luminosity images under different pilot-main injection intervals: 0.2, 0.5 and 0.8 ms which are denoted as cases 1, 2 and 3 respectively as shown in Fig 8.2. The left in Fig 8.2 is the integrated natural luminosity (NL) intensity which can roughly reflected the combustion behaviors of pilot injection (0.27 mg) spray. The color vertical lines are representing the start of main injection (SOMI) under different cases. Under multiple injection conditions, the exposure timing and aperture size were carefully selected as 0.003 ms and F16 respectively. In this figure, the perceived luminosity was emitted from the sooting flame because of the strict camera settings, therefore, the weak flame of pilot spray and start of ignition of the main injection spray were difficult to measure. To achieve the convenient description, the initial flame luminosity which was observed by the camera was decided as the start of the combustion of the main injection spray.

From Fig 8.2, it is found that the main injection of case 1 occurs at the most intense reaction duration of the pilot spray, and the main injections of cases 2 and 3 starts at the post stage of the combustion of the pilot spray. The start of ignition of the main injection spray does not depend on the pilot-main interval, all of the cases reveal that luminosity is initially detected at 0.3 ms ASOMI. As discussed in Figure 7.14, the ignition delay is about 0.7 ms without pilot injection spray. Therefore, it is safe to say that the ignition delay is decreased by applying tiny mass pilot injection strategy. As a result, the soot formation is enhanced by pilot injection. Before the EOI of the main injection, there is no significant variations of the flame structures and the intensities under different pilot-main intervals. It should be note that the evident “flames” appeared in the free spray region at 0.6 ms ASOMI of cases 1 and 2 are not the real combustion, however, they are the Mie scattering light resulted from the liquid phase existence. After the end of the main injection, it seems that the combustion intensity of case 1 is the largest. It becomes more evident at 1.5 ms ASOMI, the mechanism of this phenomenon is not clear. One possible reason is that the chamber temperature is high during the main injection of case 1, which gives more possibility for soot formation. In addition, the later injected fuel is burned by the flame tip under case 1 condition, which is estimated by that two separated bright regions are observed 1.5 ms ASOMI, however, the evident combustion of later injected fuel is not observed in cases 2 and 3.

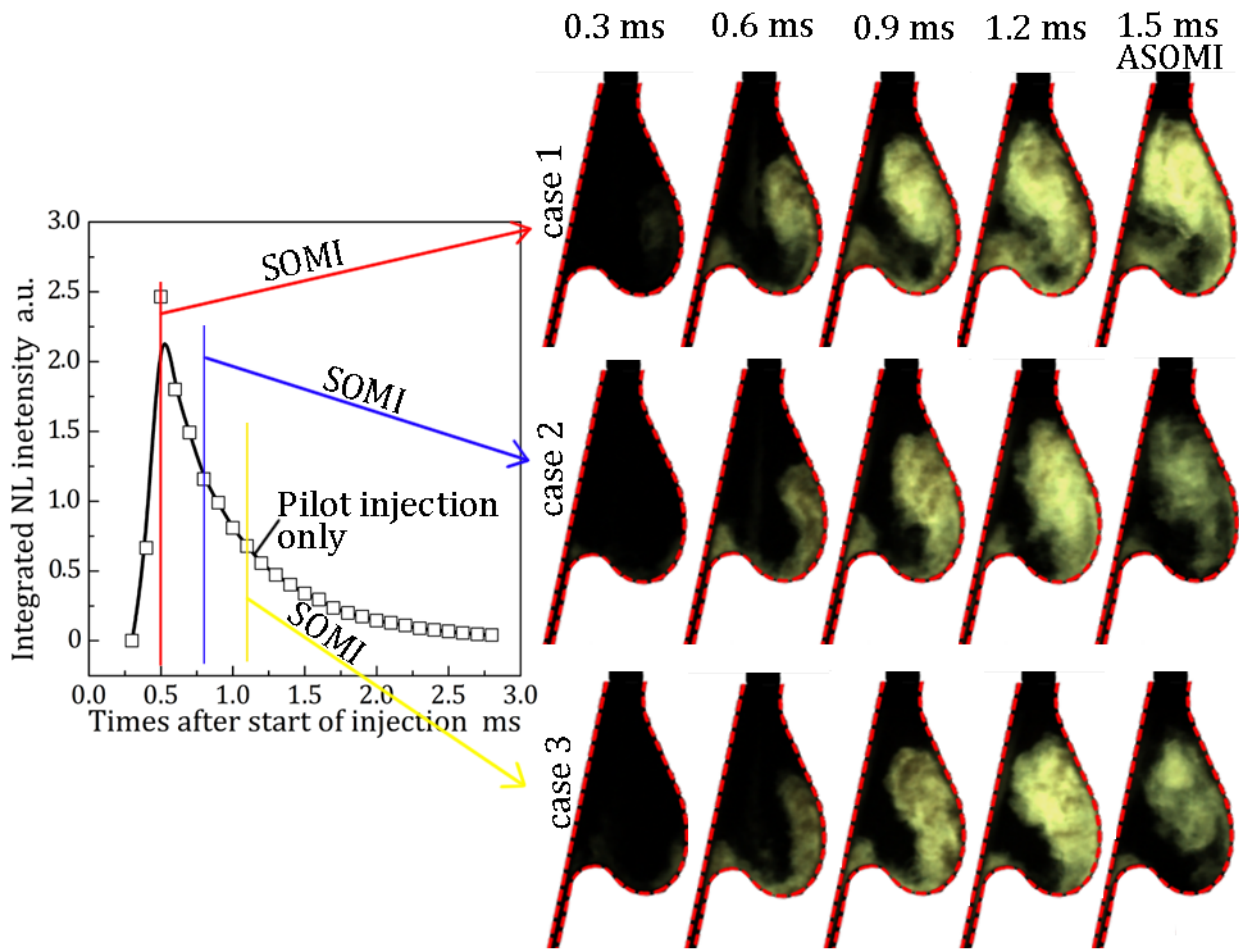


Figure 8.2 Flame natural luminosity images of spray with pilot injection under different injection intervals.

The combustion flames with post injection spray under different main-post injection intervals are shown in Fig 8.3. The left figure in Fig 8.3 is the integrated NL intensity of the main injection spray.

Unlike the interval effect of the pilot-main injection as shown in Fig 8.2, the interval plays a significant role in the luminosity intensity and the structure of the flame. Left part of Fig 8.3 reveals that the post spray injection (SOPostI) of case 4 is occurred at the early stage of the main spray combustion, the SOPostI of case 5 is occurred at the maximum reaction intensity region of the main spray, and the SOPostI of case 6 is started at the post combustion stage of main injection spray. The integrated intensity of main spray flame of cases 5 and 6 approach the same value.

It is found that there is no flame observed by camera at -0.3 ms after SOPostI (ASOPostI) because the combustion is not occurring. At 0 ms ASOPostI, the tip sooting flame at the spray tip region can be perceived under all the three cases. At 0.3 ms ASOPostI, the post injection spray is

burning of injection strategies of cases 5 and 6, however, only the main spray flame can be observed of case 4. This is because that the interaction between the main spray flame and the post injection spray is weak of case 4, and the post spray is evaporated slowly. At 0.6 ms ASOPostI, the flame is disconnect of case4, the flame region which is close to the wall surface is contributed by the combustion of the unburnt fuel of main injection spray. For cases 5 and 6, the luminosities are completely from the flame induced by post injection because the main combustion cannot be detected at 0.3 ms ASOPostI. The flame intensity is much higher than the intensity of 0.27 mg injected mass spray reveals that the unburnt fuel is numerous under impinging condition which have been proved in Chapter 4. At 1.5 ms ASOPostI, the flame characteristics are nearly the same of cases 4 and 6. The flame region is enlarged by the injection strategy of case 5.

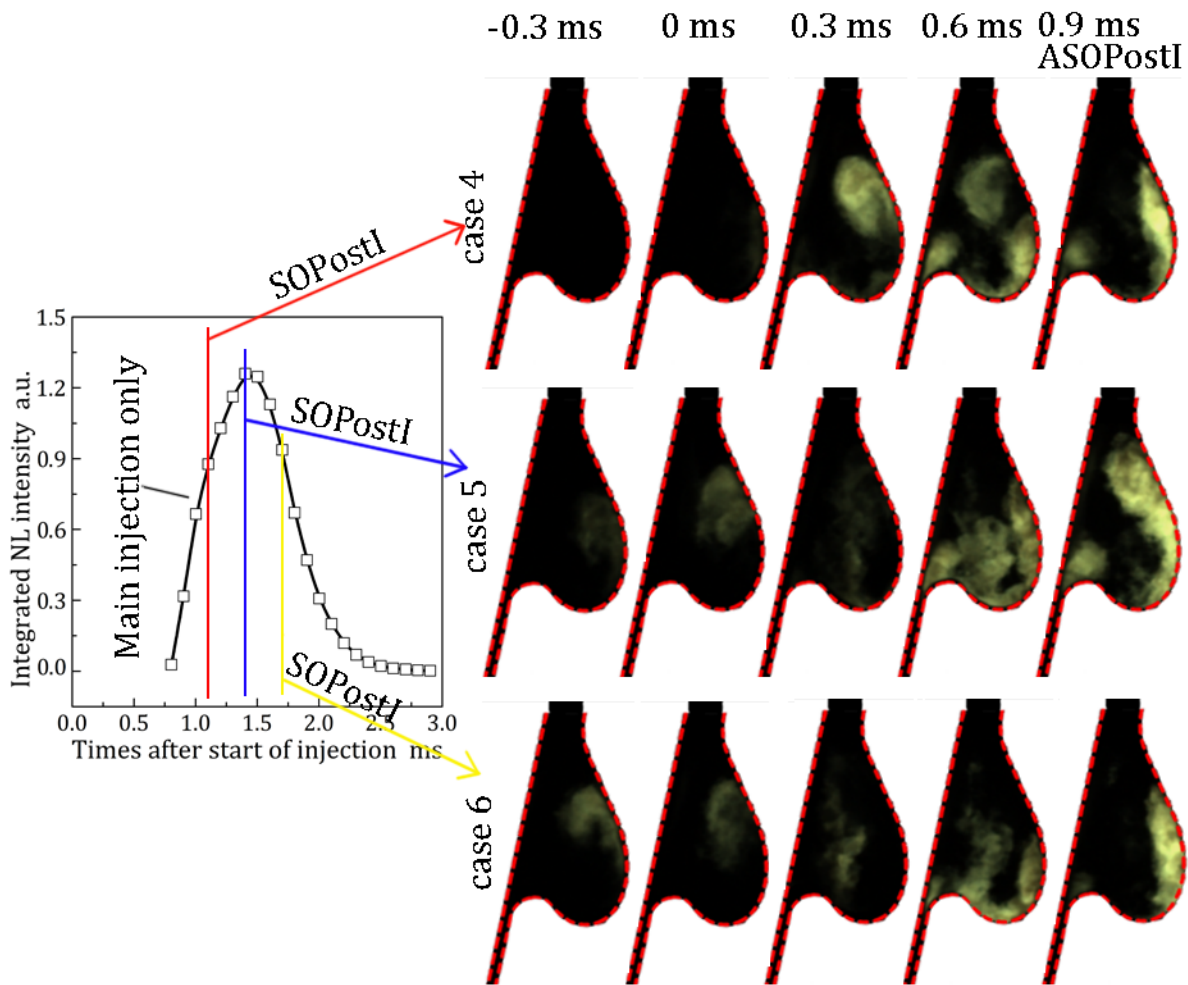


Figure 8.3 Flame natural luminosity images of spray with pilot injection under different injection intervals.

The temporal variations of integrated KL factor and mean temperature of 2-D piston cavity impinging spray under different injection strategies are shown in Figs 8.4 and 8.5 respectively.

It is found that the soot quantity is not depended on the pilot-main injection interval before 1.2 ms ASOMI, however, after that, the soot oxidation rates appearing variations. The formed soot of case 2 decreasing faster than that of cases 1 and 3, and the oxidized velocity of case 1 is the slowest one. The mechanism of this effect is not clear and need further research. In Fig 8.4 (b), the integrated KL factors of case cases 5 and 6 appear a small peaks before the post start of injection, which are contributed by the combustion of main spray. After the post of the injection, the soot quantities of cases 4 and 6 are corresponding with each other. However, evidently large quantity of soot is formed under main-post injection interval of 0.5 ms. It is difficult to estimate whether the combustion is improved or not by the main-post interval of 0.5 ms, because the large integrated KL factor, as well as the intense natural luminosity, is depend on the combustion completeness and the soot formation. The larger integrated KL factor also represents the more complete combustion of the unburnt fuel of the main injection. It should be note that the soot formation under pilot injection conditions (cases 1, 2 and 3) is higher than that of post injection conditions (cases 4, 5 and 6). This confirms that the post injection can enhance the soot oxidation. Compare with main injection spray flame, both the pilot injection and the post injection enhance the soot formation.

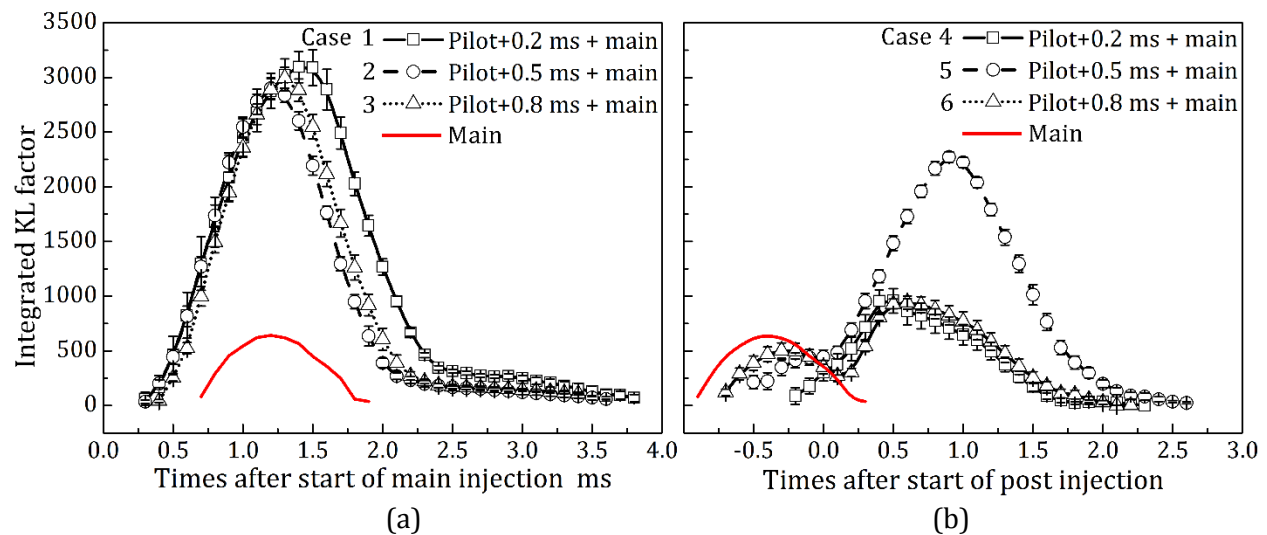


Figure 8.4 Temporal variations of integrated KL factor of 2-D piston cavity impinging spray with pilot injection (a) and post injection (b).

The temporal variations of mean temperature of 2-D piston cavity impinging spray with pilot injection (a) and post injection (b). The same trend with the KL factor of integrated KL factor of pilot injection sprays, the mean temperature of case 1 is highest at the post combustion stage. It is

interesting that the decreasing rates of the temperature and the integrated KL factor are small after 2.2 ms ASOMI under all the pilot injection conditions, this is because the fuel in the region between the cylinder head and the cavity comes back to the cavity chamber due to the tumble and also due to the high pressure in the slit region. For mean temperature of post spray strategies, the variations resulted by the different intervals are not significant, but the 0.5 ms still gives high mean temperature at the later combustion stage. The flame temperature is increased by pilot injection strategies. Under post injection conditions, the combustion temperature at the later stage of post injection is much higher than that of main injection, therefore, single post injection is thought as an effective method on unburnt fuel combustion.

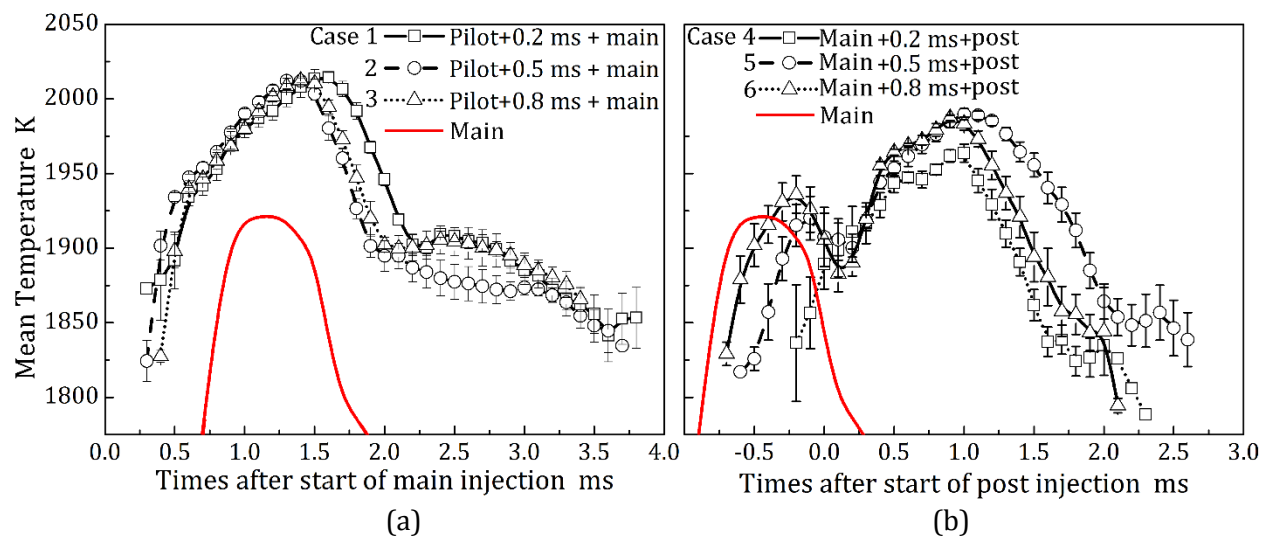


Figure 8.5 Temporal variations of mean temperature of 2-D piston cavity impinging spray with pilot injection (a) and post injection (b).

The spatial distributions of KL factor and the mean temperature under pilot-main injection and main-post injection conditions at the maximum integrated KL factor timing are shown in Fig 8.6. It is found that the high temperature and KL factor region are appeared in at the flame tip region under all the conditions. Under pilot injection conditions, the KL factor appears relatively high value at the impinging point region. Under post injection spray conditions, it is clear that the high KL factor regions are smaller than that of pilot injection flame.

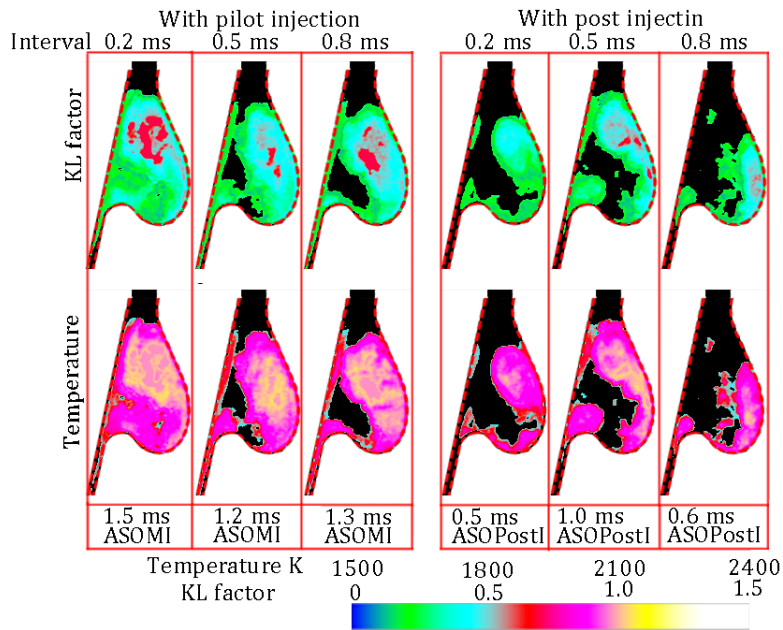


Figure 8.6 Spatial distributions of KL factor and temperature at the maximum integrated KL factor timing.

### 8.3.2 Combustion Behaviors of Three Times Injections

The pilot-pilot-main and pilot-main-post injection strategies are focused on in this section. The injection profiles are shown in Fig 8.1. Fig 8.7 gives the twice pilot injection flames at different timing of ASOMI. It is found that the sooting flame is observed at 0.1 ms ASOMI, this is not thought as the main spray ignition delay because the main spray cannot penetrate to the flame region as Fig 8.7 shows. The natural flame luminosity is much enhanced by the twice pilot injection strategy compared with the single pilot injection ones. At 1.5 and 2.0 ms ASOMI, the light is very bright at the flame tip region and also at the cylinder head vicinity region, this is contributed by the combustion of the later injected fuel of main spray.

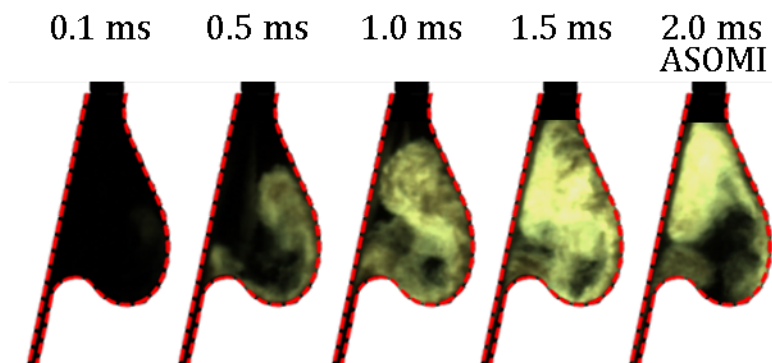


Figure 8.7 Flame natural luminosity images of spray with twice pilot injections.

The flame natural luminosity images of pilot-main-post injection spray are at specific timings are shown in Fig 8.8. Coinciding with the results of case 1, the ignition delay of main injection spray is 0.3 ms. After post spray injected, compared with the images of case 1, the post combustion intensity is suppressed. Even the same injection quantity with that of case 7 as shown in Fig 8.7, the combustion intensity in the later stage is moderate when the case 8 injection strategy is applied.

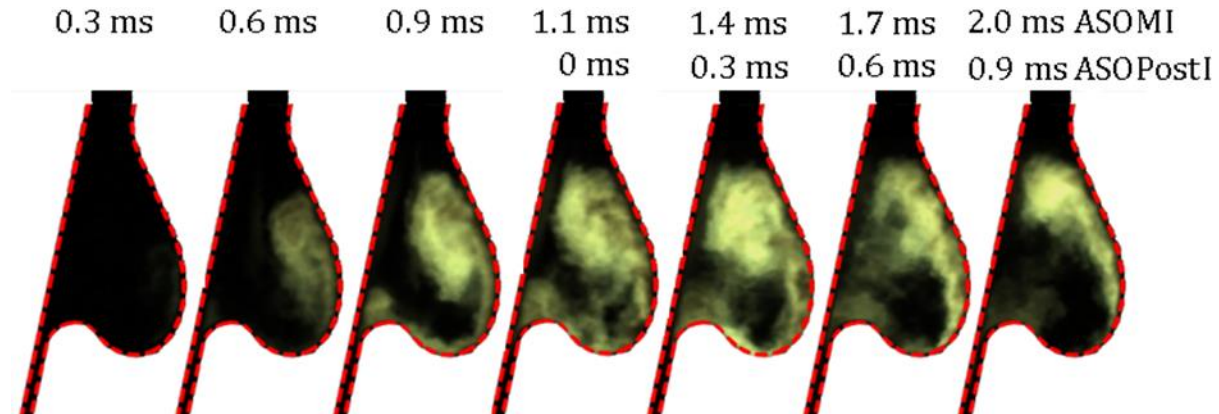


Figure 8.8 Flame natural luminosity images of spray with pilot and post injections.

The temporal variations of integrated KL factor and mean temperature are shown in Fig 8.9 (a) and (b) respectively. The horizontal value is the times after start of the first pilot injection.

From Fig 8.9, it is found that the soot formation quantity under case 7 is more than that of case 8. This is because the advanced main injection spray under twice pilot injections condition. The soot oxidation trends after 3.0 ms ASOI are nearly the same between case 7 and case 8. However, under the intense combustion stage (1.8-3.0 ms AOSI), the twice pilot injection flame produces more soot than that of case 8. The temperature also gives the same distribution. Generally, the post injection enhance the flame temperature in later combustion stage and enhance the soot oxidation, however, in this experiment, the opposite results are observed. This is because the special chamber shape: the post injection spray is injected into the flame tip directly, and the evaporation of the post injected fuel decrease the flame temperature. Even the soot formation is shrink by the post injection, but the oxidation velocity is also decreased by the low flame temperature.

Compared with the injection conditions of cases 1 and 4, it is found that the twice pilot injection enhances the soot formation and flame temperature both. When post injection is added to the pilot-main injection condition (blue line), it is found that the soot is difficult to oxidize, as discussed above, because the post injected fuel injected into the flame tip directly. Thus, the post

injection can give positive effect on combustion when the post spray has no or little interaction with spray tip.

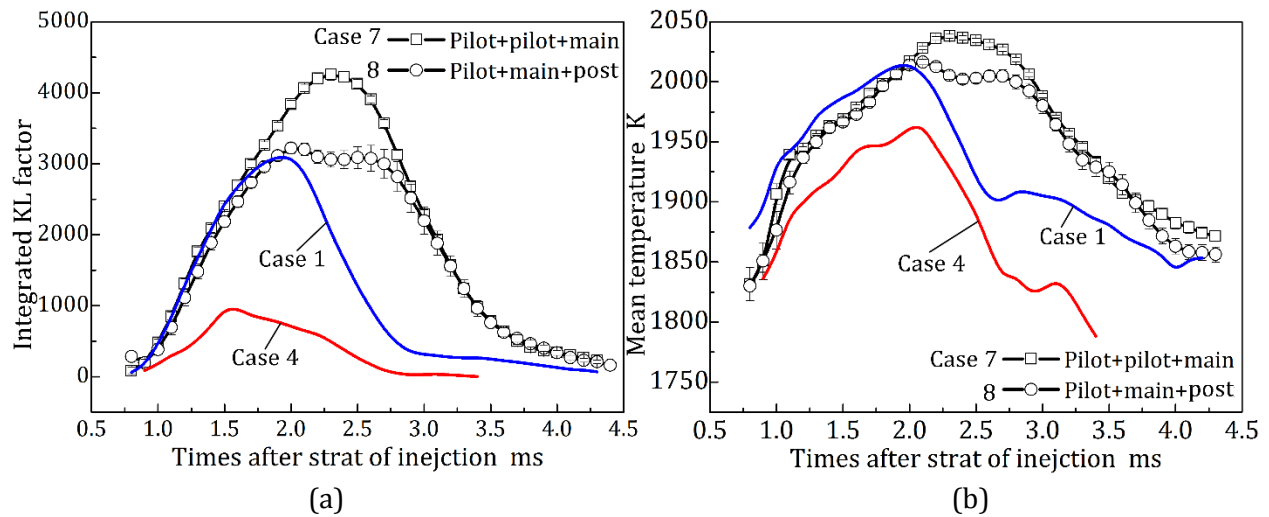


Figure 8.9 Temporal integrated KL factor and mean temperature of different injection strategies' spray flames.

## 8.4 SUMMARY

The flame characteristics of 2-D piston impinging spray with pilot injection and post injection sprays were investigated by applying two color method. Different pilot-main injection and main-post injection intervals are concentrated on. In addition, the twice pilot injections and the injection with both the pilot and the post sprays are also focused on. Based on the study, the main conclusions are summarized as follows:

1. In pilot- main injection spray, the interval has no influence on soot formation of the main spray, however, it plays a role in the soot oxidation, the 0.2 ms interval produce more particles during the later combustion stage. Compared with the only main injection spray, the soot is formation is enhanced by the pilot injection due to the ignition delay reduction.
2. In main-post injection spray, the soot formation quantity is smaller than that of pilot-main injection spray. The 0.5 ms interval gives the most soot formation, as well as, the unburned fuel of the main injection is burned more completely at this interval condition.
3. When applying the three times injection strategies: pilot-pilot-main and pilot-main-pilot injections, the soot formations are higher than that of spray with single pilot injection or with single post injection. The post injection spray cannot play a positive role in the soot oxidation because the special cavity shape.

## CHAPTER 9 CONCLUSIONS

This dissertation work is aimed at the clarifying the effects of impingement and multiple injection on mixture formation process, combustion and soot emission characteristics of D.I. Diesel spray. The spray mixture formation process was investigated using the Mie scattering technique and LAS technique to acquire the qualitative and quantitative information on the characteristics of free sprays, flat wall impinging spray, and 2-D piston cavity impinging sprays. The combustion behaviors were investigated by applying the broadband spectrum luminosity recording system and the OH\* chemiluminescence recording system. And the soot emission was quantitatively calculated by applying the two-color pyrometry on the natural luminosity images. In this investigation, three kinds of injection pressures (100,150, 200 MPa), three kinds of injection amounts (0.27,0.89 and 0.97 mg) and four kinds of impinging distances (30,40,50,60 mm) were selected to acquire a better understanding of the governing mechanisms of mixture formation and combustion processes. In addition, the multiple injection strategies such as injection frequency and injection interval were varied to estimate the effect of injection strategy on combustion behaviors. The general conclusions will be introduced gradually in this chapter.

### 9.1 MAIN FINDINGS OF THIS STUDY

In Chapter 1, the significance of this search subject was firstly introduced and a review on characterization of Diesel spray flame evolution under free and impinging condition, advanced Diesel combustion mode, multiple injection spray and its combustion in Diesel engines, and optical diagnostics for measurements of spray characteristics and flame behaviors was made.

In Chapter 2, the experimental apparatus such as fuel injection system and high temperature and high pressure high temperature acquiring system for this research was introduced. After that, brief descriptions of Mie scattering and OH\* detecting system which were applied in this dissertation work were made, and the natural luminosity recoding system as well as the two-color perometry were given subsequently. Finally, the LAS technique was introduced.

The LAS technique for Diesel spray was different with the traditional one, in this study, it is modified. 1,3-dimethlnaphthalene (1,3-DMN) had been widely used as the substituted fuel of Diesel. However, it is found that the measurement error was remarkable which was resulted in the saturation of the UV beam optical thickness, because 1,3-DMN is a strong UV light absorber. The blend fuel with 2.5 volumetric percentage of  $\alpha$ -MN and 97.5 volumetric percentage of n-tridecane was

found as an appropriate substituted fuel of Diesel, whose LAS images are both sharpness and unsaturation.

In Chapter 3, the combustion characteristics of free spray formed by using a three holes injector were investigated by applying OH\* and natural luminosity recording systems synchronously. The investigation was aimed to clarify the relationship between OH\* chemiluminescence and soot oxidation. And also wanted to give some information of soot formation and oxidation locations. The detection view of the three holes injector was changed to make clear the dependence of perceived intensity on the light path length, and this dependence was a crucial factor for the precision of this dissertation work. It has been found that, firstly, in a three jets free spray diesel flame, the natural luminosity is dominated by the soot incandescence, and the sooting flame is surrounded by OH\* chemiluminescence. Soot is distributed in the mid-downstream of the flame and the flame upstream is purely emitted from OH\* chemiluminescence because the large momentum of particles and the lean mixture in the flame upstream region, respectively. The maximum integrated KL factor and OH\* chemiluminescence are not appeared at the same timing and the flames in the post combustion stage are contributed by OH\* emission, which demonstrate that the OH\* intensity does not depend on soot incandescence. Secondly, the normalized images gave that the spray dense soot emission region and the intense OH\* chemiluminescence are complementary, the intense OH\* emission region appears at the jet-jet interferential region, this also confirmed that the soot incandescence has no effect on OH\* radical perceiving. Thirdly, the soot incandescence is dominated by the temperature at the sooting flame periphery region due to the soot oxidation by OH\*, however, it is dominated by soot concentration in the sooting flame inner region due to the soot formation where the mixture is rich. Finally, the OH\* chemiluminescence intensities of in frontal view and side view images are corresponding very after the auto-ignition, which confirmed that the light attenuation by the soot scattering and absorption at the light path is negligible.

In Chapter 4, the effect of impingement on mixture formation, combustion, and soot emission were concentrated on. The impinging distance of flat wall and 2-D piston cavity were kept at 30 mm. It is found that, firstly, the spray tip penetration is shorten by impingement, and the flat wall impinging spray penetrates shortest because the large momentum losing. As a result, the evaporation velocity of impinging spray is slower than that of free spray, as well as, the ambient gas entrainment is deteriorated by impingement. The liquid/wall interaction occurs under 30 mm impinging distance, and the droplets are deposited at the wall vicinity and difficult to be evaporated due to the Leidenfrost effect. The evaporative velocity under the 2-D impinging condition is the slowest and the liquid phase mainly distribute at the large curvature region. Secondly, the vapor fuel mostly locates

at the mid-downstream of the free spray, and locates at the wall jet regions of impinging sprays. However, the vapor-air mixtures in the free region of free spray and the same location of free spray are much richer than that of wall spray region of flat impinging spray, which implies that the ambient gas entrainment in the partial region (wall jet region) is enhanced by flat wall impingement. Thirdly, the combustion of impinging sprays are not as complete as that of free spray. The droplets burning resulted from floating droplets and pool flame contributed by liquid film play a positive role on combustion completeness. Besides, the flame under impinging conditions cannot spread to upstream as further as that of free spray due to the stagnation of droplets at the impinging point. Finally, under free spray condition, the soot is formed in the near tip region of the sooting flame and is oxidized at the upstream of the sooting flame where is close to the pure OH\* combustion. For flat wall impinging spray flame, soot is formed at the wall vicinity due to the droplets combustion and pool flame, and also formed at the periphery region of the head vortex due to the droplets coalescence. For 2-D piston cavity impinging spray flame, the soot is formed at the large curvature region where the liquid phase is evident, and is also formed in the periphery region of the head vortex, during the later combustion stage, the soot is still formed in the central region of the cavity which is contributed by the combustion of later injected fuel. And soot is mainly oxidized in the inner region of head vortex.

In Chapter 5, the effect of injection pressure on flat wall impinging spray flame characteristics were focused on, it is found that, firstly, the spray tip penetration highly depends on the injection, the higher injection pressure gives longer spray tip penetration. As a result, the atomization is enhanced by increasing injection pressure which is also reflected by the faster evaporative velocity under higher injection pressure. Secondly, due to the different flow rates, the ratio of entrained gas to total fuel and the average vapor phase equivalence ratio are complex during the initial stage of the injection, however, the air entrainment and the mean vapor phase equivalence ratio during the main injection and after the injection stages are improved and decreased respectively by increasing the injection pressure. Thirdly, compared with free spray flame, the combustion is incomplete under all the injection pressure duo to the wall wetting effect. For flat wall impinging spray flame under different injection pressures, the combustion is not linearly enhanced by increasing injection pressure, the results of OH\* chemiluminescence imply that the best combustion behavior can be obtained at the injection pressure of 150 MPa. This is possibly because that some regions of 200 MPa injection pressure spray is very lean and undergoes misfiring. Finally, the soot formation is reduced with injection pressure increasing. Under 200 MPa injection pressure, even the combustion is not as complete as that of 150 MPa injection pressure, the incomplete combustion part are possibly emitted as the unburnt hydrocarbons but not as soot.

As the impingement still plays a negative role in mixture formation and combustion due to the wall wetting effect even under the high injection pressure, increasing the impinging distance was paid attention which is thought as an effective method to reduce the liquid/wall interaction.

In Chapter 6, the experiments under various impinging distances were carried out. The results reveal that, firstly, the impinging distance plays a significant role in spray atomization. Under severe liquid/wall interaction conditions (30 and 40 mm impinging distance), the evaporation velocity of the injected fuel is much slower than the longer impinging distance sprays. The flat wall effect occurs even before the impingement occurs, as a result, the injected fuel under 60 mm impinging distance is evaporated faster than that of free spray. Secondly, the ambient gas entrainment under free spray condition and 60 mm impinging condition are better than the other shorter impinging distances conditions, and no liquid phase exists around the ignition timing. Thirdly, the combustion intensity and combustion completeness is increased by increasing the impinging distance, under 60 mm impinging distance, the reaction velocity at initial stage is even higher than that of free spray flame without damaging the maximum integrated OH\* intensity, which implies the 60 mm impingement enhances the combustion velocity. Thirdly, the dependence of soot production on impinging distance is negligible, which is contributed by the liquid phase combustion under 30-50 mm impinging distance conditions and the rich vapor-air mixture combustion under 60 mm impinging and free spray conditions. The average KL factor which represents the soot concentration distraction is decreased by increasing the impinging distance, this is because the liquid phase combustion reduction. The soot oxidation rate under impinging conditions are faster than that under free condition contributed to the enhancement of air entrainment at the wall jet region. Therefore, in this investigation, 60 mm is thought as the optimized impinging distance. From this part of investigation, a supposition was made that the optimal impinging distance is equal to the penetration length when the injected fuel is completely evaporated.

In a small bore diesel, it is not possible to enlarge the piston chamber size, to reduce the wall wetting effect, adjusting the injection amount is thought as an effective approach. What's more, in multiple injection strategies, the tiny amount injection is widely applied to act as the pilot injection, therefore, the injection amount effect was focused on.

In Chapter 7, the effects of injection amount on the mixture formation and combustion was investigated. It is found that, firstly, for free spray, the spray tip penetration is enlarged by injection spray amount due to the actual injection pressure in the sac volume is higher under large injection amount conditions. Under normal (2.97 mg) and middle (0.89) masses injection conditions, the spray

tip penetration under non-evaporating condition is longer than that under evaporating conditions, however, when it comes to fine mass injection spray, the spray tip penetration tendency under non-evaporating and evaporating conditions is contradicted, which is reflected as that the evaporating spray penetrates further than non-evaporating spray. This is contributed by the competition between cooling effect and entrained gas reduction effect. Secondly, under 2-D piston cavity impinging condition, the evaporative spray has further spray tip penetration than the non-evaporating spray under all the injection amount conditions. This is because the low evaporation rate, droplets stagnation and low ambient gas entrainment when impingement occurs. Thirdly, the auto-ignitions of free spray under 0.27 and 0.89 mg injection conditions are occurred after the EOI, and there is no soot produced since the completely evaporate and the lean mixture, however, the soot is formed under 2-D impinging condition even the ignition delay is longer than injection duration when injection amount is tiny, the particles are formed because the liquid phase combustion. Finally, even the reaction intensity and the heat release is enhanced by increasing the injection amount, the combustion completeness is improved by decreasing the injection mass.

In Chapter 8, the combustion and soot emission under various multiple injection conditions are investigated, it is found that, firstly, the single pilot injection can enhance the combustion intensity, however, the soot formation is also increased, the pilot-main injection interval does not plays a role in the ignition delay of main injection spray. Secondly, the main-post injection strategy can burn the unburnt fuel of the main injection spray, accompanied with the large quantity of soot formation at the later stage of combustion. Thirdly, the combustion intensity is increased with the pilot injection frequency increasing. When the post injection is added after pilot-main injection, the post injection plays a negative role in the combustion and soot oxidation, which is because that the post injected fuel is injected into the flame tip directly, as a result, the flame temperature is decreased and the droplets combustion is occurred.

In summary, the findings of this dissertation work are those:

The wall/spray interaction deteriorates the combustion when the liquid/wall interaction occurs. The combustion of free spray is the rich vapor-air mixture burning, as a result, the soot formation is contributed by the high equivalence ratio mixture combustion. Under flat wall impinging condition, the combustion flame is confined in the wall vicinity region where the lean vapor-air mixture observed, and the liquid phase exist for a long time during the combustion process which results in liquid phase combustion, therefore, the soot formation under flat impinging condition is contributed by the droplet combustion (floating droplets) and pool flame (liquid film). What's more,

the dense vapor and liquid phase in the impinging point region is misfiring when flat wall impingement occurs. Under 2-D impinging condition, the fuel vaporization is the worst, and the liquid phase combustion is occurring at the large curvature and the spray tip regions which are corresponding with the region of soot formation.

When liquid/wall interaction occurs, the increasing of injection pressure decreases the soot formation, however, the combustion behavior which is reflected by OH\* intensity is not monotonously improved by injection pressure increasing. The combustion is enhanced by enlarging the impinging distance possibly due to the reduction of liquid/wall interaction. Under 100 MPa injection pressure condition, the 60 mm impinging distance receive the optimized spray flame characteristics (high reaction rate and high soot oxidation rate) which implies that there is an appropriate distance under the specific condition. When injection amount is decreased, which also means the reduction of liquid/wall interaction, the soot formation is decreased and the ratio of stoichiometric combustion is increased.

Both the pilot injection and the post injection increase the combustion intensity as well as the soot formation quantity.

## **9.2 RECOMMENDATIONS FOR FUTURE WORKS**

Several recommendations can be made for future work in this field.

The detail mechanism of the effect of liquid/wall interaction on spray evolution and combustion need to be further investigated. Until now, the LAS technique cannot deal with the liquid film on the wall surface, to resolve, the precision of LAS technique on the liquid phase should be improved. Besides, the computational fluid dynamics should applied to simulate the spray evolution and to further investigate the liquid film behaviors.

Current result shows that the optimal impinging condition is that the impingement occurs immediately after complete evaporation. It is under specific injection and ambient conditions. Therefore, more fundamental experiments with systematically varying more parameters are recommended to provide data for calibrating the predicative models.

The ultimate purpose of this research is to improve the performance in a real engine. Although the physical ambient conditions in a real engine are similar with this work, the turbulent flow may play a role in mixture formation and combustion process. Therefore, it is recommended to

investigate the mixture and combustion characteristics in an optical engine by applying different chamber shapes, injection pressures, injection amount and multiple injection strategies.

## REFERENCE

1. **Akagawa, H., Miyamoto, T., Harada, A., Sasaki, S., Shimazaki, N., Hashizume, T., and Tsujimura, K.** (1999) Approaches to Solve Problems of the Premixed Lean Diesel Combustion. *SAE paper* 1999-01-0183.
2. **Alock, J., and Scott, W.** (1962) Some More Light on Diesel Combustion. *Proc. Instn. Mecj. Eng*, 5: 179-191.
3. **Andresen, P., Meijer, G., Schlüter, H., Voges, H., Koch, A., Hentschel, W., Oppermann, W., and Rothe, E.** (1990) Fluorescence Imaging inside an Internal Combustion Engine using Tuable Excimer Lasers. *Applied optics*, 26:2392-2404.
4. **Anezaki, Y., Yamashita, H., Hashizume, T., and Nishida, K.** (2013) RGR Gas Effects on Soot Formation and Oxidation. *The 24th Internal Combustion Engine Symposium*, Kobe, Japan.
5. **Arai, M., Shimizu, M., and Hiroyasu, H.** (1991) Similarity between the Breakup Lengths of a High Speed Liquid Jet in Atmospheric and Pressurized Conditions. *ICLASS*, Gaithersburg, MD, USA.
6. **Araneo, L., Coghe, A., Brunello, G., and Cossali, G. E.** (1999) Experimental Investigation of Gas Density Effects on Diesel Spray Penetration and Entrainment. *SAE paper* 1999-01-0525.
7. **Arcoumanis, C., and Chang, J. C.** (1994) Flow and Heat Transfer Characteristics of Impinging Transient Diesel Sprays. *SAE paper* 940678.
8. **Arcoumanis, C., and Enotiadis, A. C.,** (1991) In-Cylinder Fuel Distribution in a Port-Injected Model Engine Using Rayleigh Scattering. *Expts. Fluid* 11: 375-387.
9. **Arcoumanis, C., Flora, H., Gavaises, M., and Badami, M.** (2000) Cavitation in Real-Size Multi-Hole Diesel Injector Nozzles. *SAE paper* 2000-01-1249.
10. **Arcoumanis, C., Gavaises, M., and French, B.** (1997) Effect of Fuel Injection Processes on the Structure of Diesel Sprays. *SAE paper* 970799.
11. **Arcoumanis, C., Green, H.G., and Whitelaw, J.** (1985) Velocity and Concentration Measurement in a Model Diesel Engine. *Expts. Fluids* 3:270-276.
12. **Arcoumanis, C., Whitelaw, J. H., Hentschel, W., and Schindler, K. P.** (1994) Flow and combustion in a transparent 1.9 liter direct injection diesel engine. *Proc. IMechE Part D: J Automob Eng*, 208:191-205.
13. **Baby, X. and Floch, A.** (1997) Investigation of the In-Cylinder Tumble Motion In a Multi-Valve Engine: Effect of the Piston Shape. *SAE paper* 971643.
14. **Bai, C. and Gosman, A. D.** (1995) Development of Methodology for Spray Impingement Simulation. *SAE paper* 950283.

15. **Baumgarten, C.** (2006) *Mixture Formation in Internal Combustion Engine*. Berlin Heidelberg, Springer-Verlag.
16. **Benajes, J., Molina, S., and García, J.** (2001) Influence of Pre- and Post-Injection on the Performance and Pollutant Emissions in a HD Diesel Engine. *SAE paper* 2001-01-0526.
17. **Bergstrand, P., and Denbratt, I.** (2001) Diesel Combustion with Reduced Nozzle Orifice Diameter. *SAE paper* 2001-01-2010.
18. **Bergwerk, W.** (1959) Flow Pattern in Diesel Nozzle Spray Holes. *Proc Inst Mech Eng*, 173: 665-660.
19. **Bobba, M., Musculus, M., and Neel, W.,** (2010) Effect of Post Injections on In-Cylinder and Exhaust Soot for Low-Temperature Combustion in a Heavy-Duty Diesel Engine. *SAE paper* 2010-01-0612.
20. **Bruneaux, G.** (2001) Liquid and Vapor Spray Structure in High-Pressure Common Rail Diesel Injection. *Atomization and Sprays*, 11: 533-556.
21. **Bruneaux, G.** (2002) A Study of Mixture Formation in Direct Injection Diesel Like Conditions Using Quantitative Fuel Concentration Visualizations in a Gaseous Fuel Jet. *SAE paper* 2002-01-1632.
22. **Bruneaux, G.** (2005) Mixing Process in High Pressure Diesel Jets by Normalized Laser Induced Exciplex Fluorescence Part II: Wall Impinging Versus Free Jet. *SAE paper* 2005-01-2097.
23. **Bruneaux, G.** (2008) Combustion Structure of Free and Wall-Impingement Diesel Jets by Simultaneous Laser-Induced Fluorescence of Formaldehyde, Poly-Aromatic Hydrocarbons, and Hydroxides. *International Journal of Engine Research*, 9: 249-265.
24. **Bruneaux, G., Causse, M., and Omrane, A.** (2011) Air Entrainment in Diesel-Like Gas Jet by Simultaneous Flow Velocity and Fuel Concentration Measurements, Comparison of Free and Wall Impinging Jet Configurations. *SAE paper* 2011-01-1828.
25. **Bruneaux, G., Verhoeven, D., and Baritaud, T.** (1999) High Pressure Diesel Spray and Combustion Visualization in a Transparent Model Diesel Engine. *SAE paper* 1999-01-3648.
26. **Castleman, R. A.** (1931) The Mechanism of the Atomization of Liquids. *J. Res. Natl. Bur. Std*, 6: 369-376.
27. **Chemla, F., Jager, P., Herzog, P., and Wirbeleit, F.** (1999) Reducing Exhaust Emissions of Direct Injection Diesel Engines via Injection Rate Shaping. *MTZ Worldwide*, 60: 5-8.
28. **Chomiak, J., and Karlsson, A.** (1996) Flame Lift-off in Diesel Spray. *Symposium (International) on Combustion*, 26: 2557-2564.

29. **Chraplyvy, A. R.** (1981) Nonintrusive Measurements of Vapor Concentrations inside Sprays. *Appl. Opt.*, 20: 2620-2624.
30. **Corcione, F. E., and Valentino, G.** (1990) Turbulence Length Scale Measurements by Two-Probe-Volume LDA Technique in a Diesel Engine. *SAE paper* 902080.
31. **Cossali, G. E., Brunello, G., and Coghe, A.** (1991) LDV Characterization of Air Entrainment in Transient Diesel Sprays. *SAE paper* 910178.
32. **Cossali, G. E., Coghe, A., and Brunello, G.** (1993) Effect of Spray-Wall Interaction on Air Entrainment in a Transient Diesel Spray. *SAE paper* 930920.
33. **Cossali, G. E., Gerla, A., Coghe, A., and Brunello, G.** (1996) Effect of Gas Density and Temperature on Air Entrainment in a Transient Diesel Spray. *SAE paper* 960862.
34. **Costa, M., Vaglieco, B., and Corcione, F.** (2005) Radical Species in the Cool-Flame Regime of Diesel Combustion: A Comparative Numerical and Experimental Study. *Experiments in Fluids*, 39:514-526.
35. **Dec, J. E., and Tree, R. D.** (2001) Diffusion-flame/wall Interactions in a Heavy-Duty DI Diesel Engine. *SAE paper* 2001-01-1295.
36. **Dec, J. E.** (1992) Soot Distribution in a D.I. Diesel Engine Using 2-D Imaging of Laser-Induced Incandescence, Elastic Scattering, and Flame Luminosity. *SAE paper* 920115.
37. **Dec, J. E.** (1997) A Conceptual Model of DI Diesel Combustion Based on Laser-Sheet Imaging. *SAE paper* 970873.
38. **Dec, J. E., and Espey, C.** (1995) Ignition and Early Soot Formation in a D.I. Diesel Engine Using Multiple 2-D Imaging Diagnostics. *SAE paper* 950456.
39. **Dec, J. E., and Espey, C.** (1998) Chemiluminescence Imaging of Autoignition in a DI Diesel Engine. *SAE paper* 982685.
40. **DeJuhasz, K. J.** (1931) Dispersion of Sprays in Solid Injection Oil Engines. *Trans. ASME*, 53: 65-77.
41. **Dent, J. C.** (1971) A Basis for the Comparison of Various Experimental Methods for Studying Spray Penetration. *SAE paper* 710571.
42. **Desantes, J. M., Payri, R., Salvador, F. J., and Gil, A.** (2006) Development and Validation of a Theoretical Model for Diesel Spray Penetration. *Fuel*, 85: 910-917.
43. **Desantes, J., Arrègle, J., Pastor, J., and Delage, A.** (1998) Influence of the Fuel Characteristics on the Injection Process in a D.I. Diesel Engine. *SAE paper* 980802.

44. **Egermann, J., Göttler, A., and Leipertz, A.** (2001) Application of Spontaneous Raman Scattering for Studying the Diesel Mixture Formation Process under Near-Wall Conditions. *SAE paper* 2001-01-3496.
45. **Endo, S.** (2011) Powertrain Technologies of Commercial Vehicles for Today and Future. *2011 SAE/JSAE International, Keynotes*. Kyoto, Japan.
46. **Espey, C., and Dec, J. E.** (1993) Diesel Engine Combustion Studies in a Newly Designed Optical-Access Engine Using High-Speed Visualization and 2-D Laser Imaging. *SAE paper* 930971.
47. **Espey, C., Dec, J. E., Litzinger, T. A., and Santavicca, D. A.** (1997) Planar Laser Rayleigh Scattering for Quantitative Vapor-Fuel Imaging in a Diesel Jet. *Combustion and Flame*, 109: 65-78.
48. **Fajardo, C., and Sick, V.** (2009) Development of a High-Speed UV Particle Image Velocimetry Technique and Application for Measurements in Internal Combustion Engines. *Exp. Fluids*, 46:43-53.
49. **Farrell, P. V., Chang, C. T, and Su, T. F.** (1996) High Pressure Multiple Injection Spray Characteristics. *SAE paper* 960860.
50. **Flynn, P. F., Durrett, R. P., Hunter, G. L., zur Loye, A. O., Akinyemi, O. C., Dec, J. E., and Westbrook, C. K.** (1999) Diesel Combustion: An Integrated View Combining Laser Diagnostics, Chemical Kinetics, And Empirical Validation. *SAE paper* 1999-01-0509.
51. **Fujimoto, H., Iids, H., Aoyama, T., and Senda, J.** (1994) Analysis of Combustion Characteristics in Diesel Flame by Means of Chemiluminescence. *COMODIA*, Yokohama, Japan.
52. **Fujimoto, H., Kusano, S., and Senda, J.** (1997) Distribution of Vapor Concentration in a Diesel Spray Impinging on a Flat Wall by Means of Exciplex Fluorescence Method -In Case of High Injection Pressure. *SAE paper* 972916.
53. **Fujimoto, H., Saitou, M., Monoura, A., and Senda, J.** (1987) Characteristics of a Diesel Spray Impinging on a Flat Wall (1<sup>st</sup> Report). *JSME*, 54:2252-2259.
54. **Gao, J., Matsumoto, Y., Namba, M., and Nishida, K.** (2007) Group-Hole Nozzle Effects on Mixture Formation and In-cylinder Combustion Processes in Direct-Injection Diesel Engines. *SAE paper* 2007-01-4050.
55. **Gaydon, A. G.** (1974) *The Spectroscopy of Flames*. 2nd, London, Chapman and Hall.
56. **Gray, A.W., and Ryan, T.W.** (1997) Homogeneous Charge Compression Ignition (HCCI) of Diesel Fuel. *SAE paper* 971676.
57. **Gulder, O. L., Smallwood, G. J., and Snelling, D. R.** (1992) Diesel Spray Structure Investigation by Laser Diffraction and Sheet Illumination. *SAE Paper* 920577.

58. **Ha, J. Y., Iida, N., Sato, G. T., Hayashi, A. and Tanabe, H.** (1984) Experimental Investigation of the Entrainment into Diesel Spray. *SAE paper* 841078.
59. **Hammond, D. C.** (1981) Deconvolution Technique for Line-of-Sight Optical Scattering Measurements in Axisymmetric Sprays. *Applied Optics*, 20:493-499.
60. **Hardalupas, H., and Orain, M.** (2004) Local Measurement of the Time-Dependent Heat Release Rate and Equivalence Ratio using Chemiluminescence Emission from a Flame. *Combustion and flame*, 139:188-207.
61. **Hardalupas, Y., Panoutsos, C. S., and Taytor, A.M.K.P.** (2010) Spatial Resolution of a Chemiluminescence Sensor for Local Heat-Release Rate and Equivalence Ratio Measurements in a Model Gas Turbine Combustor. *Exp Fluid*, 49: 883-909.
62. **Hasegawa, R., and Yanagihara, H.** (2003) HCCI Combustion in DI Diesel Engine. *SAE paper* 2003-01-0745.
63. **Hashizume, T., Miyamoto, T., Hisashi, A., and Tsujimura, K.** (1999) Combustion and Emission Characteristics of Multiple Stage Diesel Combustion. *SAE paper* 980505.
64. **Hashizume, T., Miyamoto, T., Hisashi, A., and Tsujimura, K.** (1999) Emission Characteristics of a MULDIC Combustion Diesel Engine: Effects of EGR. *JSAE Review*, 20: 428-430.
65. **Heinze, T., and Schmidt, T.** (1989) Fuel-Air Ratios in a Spray, Determined between Injection and Autoignition by Pulsed Spontaneous Raman Spectroscopy. *SAE paper* 892102.
66. **Heinze, T., and Schmidt, T.,** (1989) Fuel-Air Ratios in a Spray, Determined between Injection and Autoignition by Pulsed Spontaneous Raman Spectroscopy. *SAE paper* 892102.
67. **Helmantel, A., and Denbratt, I.** (2004) HCCI Operation of a Passenger Car Common Rail DI Diesel Engine With Early Injection of Conventional Diesel Fuel. *SAE paper* 2004-01-0935.
68. **Heywood, J. B.** (1988) *Internal Combustion Engine Fundamentals*. New York, McGraw-Hill.
69. **Higgins, B., and Siebers, D.** (2001) Measurement of the Flame Lift-Off Location on DI Diesel Sprays Using OH Chemiluminescence. *SAE paper* 2001-01-0918.
70. **Higgins, B., Siebers, D., and Aradi, A.** (2000) Diesel-Spray Ignition and Premixed-Burn Behavior. *SAE paper* 2000-01-0940.
71. **Hill, P.G., and Ouellette, P.** (1999) Transient Turbulent Gaseous Fuel Jets for Diesel Engines. *Journal of Fluids Engineering*, 121: 93-101.
72. **Hiroyasu, H., and Arai, M.** (1990) Structures of Fuel Sprays in Diesel Engines. *SAE paper* 900475.
73. **Hiroyasu, H., Shimizu, M., and Arai, M.** (1991) Breakup Length of a Liquid Jet and Internal Flow in a Nozzle. *ICLASS*, Gaithersburg, MD, USA.

74. **Hodges, J. T., Baritaud, T. A., and Heinza, T. A.** (1997) Planer Liquid and Gas Fuel and Droplet Size Visualization in a DI Diesel Engine. *SAE Paper* 910726.
75. **Hotta, Y., Inayoshi, M., Nakakita, K., Fujiwara, K., and Sakata, I.** (2005) Achieving Lower Exhaust Emissions and Better Performance in an HSDI Diesel Engine with Multiple Injection. *SAE paper* 2005-01-0928.
76. **Hottel, H., and Broughton, F.** (1932) Determination of True Temperature and Total Radiation from Luminous Gas Flames. *Ind and Eng. Chem.* 4-2: 166-174.
77. **Hurle, I. R., Price, R. B., Sugden, T. M., and Thomas, A.** (1968) Sound Emission from Open Turbulent Premixed Flames. *Proc. Roy. Soc.*, 303:409-427.
78. **Ikeda, Y., Kaneko, M., and Nakajima, T.** (2001) Local A/F Measurement by Chemiluminescence OH\*, CH\* and C2\* in SI Engine. *SAE paper* 2001-01-0919.
79. **Jain, A. K.** (1989) *Fundamentals of Digital Image Processing*. Prentice-Hall, New York, 1989.
80. **Jakob, M., Hülser, T., Janssen, A., Adomeit, P., Pischinger, S., and Grünefeld, G.** (2012) Simultaneous High-Speed Visualization of Soot Luminosity and OH\* Chemiluminescence of Alternative-Fuel Combustion in a HSDI Diesel Engine under Realistic Operating Conditions. *Combustion and Flame*, 159: 2516-2529.
81. **Johnston, S.,** (1979) Precombustion Fuel/Air Distribution in a Stratified Charge Engine Using Laser Raman Spectroscopy. *SAE paper* 790433.
82. **Kamimoto, T., and Kobayashi, H.** (1991) Combustion Processes in Diesel Engines. *Progress in Energy and Combustion Science*, 17:163-189.
83. **Kamimoto, T., Yokota, H., and Kobayashi, H.** (1989) A New Technique for the Measurement of Sauter Mean Diameter of Droplets in Unsteady Dense Sprays. *SAE paper* 890316.
84. **Karnani, S., and Dunn-Rankin, D.** (2013) Visualizing CH\* Chemiluminescence in Sooting Flame. *Combustion and Flame*, 160:2275-2278.
85. **Kato, T., Tsujimura, K., Shintani, M., Minami, T., and Yamaguchi, I.** (1989) Spray Characteristics and Combustion Improvement of DI Diesel Engine with High Pressure Fuel Injection. *SAE paper* 890265.
86. **Katsura, N., Saito, M., Senda, J., and Fujimoto, H.** (1989) Characteristics of a diesel spray impinging on a flat wall. *SAE paper* 890264.
87. **Katsura, N., Saito, M., Senda, J., and Fujimoto, H.** (1990) Characteristics of a Diesel Spray Impinging on a Flat Wall (2<sup>nd</sup> Report). *JSME*, 56: 227-234.

88. **Kim, Y., Kim, M., Yeom, J., and Min, K.** (2002) LIEF Measurement and Calculation Analysis of Evaporation Spray. *THIESEL 2002 Conference on Thermo- and Fluid Dynamic Process in Diesel Engines*, Valencia, Spain.
89. **Kimura, S., Aoki, O., Kitahara, Y., and Aiyoshizawa, E.** (2001) Ultra-Clean Combustion Technology Combining a Low-Temperature and Premixed Combustion Concept for Meeting Future Emission Standards. *SAE paper* 2001-01-0200.
90. **Kimura, S., Aoki, O., Ogawa, H., Muranaka, S., and Enomoto, Y.** (1999) New Combustion Concept for Ultra-Clean and High-Efficiency Small DI Diesel Engines. *SAE paper* 1999-01-3681.
91. **Ko, K. and Arai, M.** (2002) The Characteristics of Post Impingement Diesel Spray, Part I: Penetration and Volume. *Atomization Spray*, 12: 403-17.
92. **Kohse-Hoinghaus, K., and Jeffries, J. B.** (2002) *Applied Combustion Diagnostics*. New York, Taylor & Francis.
93. **Kojima, J., Ikeda, Y., and Nakajima, T.** (2000) Spatially Resolved Measurement of OH\*, CH\*, and C2\* Chemiluminescence in the Reaction Zone of Laminar Methane/Air Premixed Flames. *Proceedings of the Combustion Institute*, 28: 1757-1764.
94. **Kompenhans, J., and Kähler, C.** (2002) Particle Image Velocimetry- an advanced Experimental Tool for the Investigation of Turbulent Flow Fields. *Engineering Turbulence Modelling and Experiments*, 79-94.
95. **Kosaka, H., Aizawa, T., and Kamimoto, T.** (2005) Two-Dimensional Imaging of Ignition and Soot Formation Process in a Diesel Flame. *International Journal of Engine Research*, 6(1): 21-42.
96. **Kosaka, H., Drewes, V., Catalfamo, L., Aradi, A. A., Iida, N., and Kamimoto, T.** (2000) Two-Dimensional Imaging of Formaldehyde Formed During the Ignition Process of a Diesel Fuel Spray. *SAE paper* 2000-01-0236.
97. **Kosaka, H., Won, Y.H., and Kamimoto, T.** (1992) A Study of the Structure of Diesel Sprays Using 2-D Imaging Techniques. *SAE paper* 920107.
98. **Laget, O., Pacaud, P., and Perrin, H.** (2009) Cold Start on Low Compression Ratio Diesel Engine: Experimental and 3D RANS Computation Investigations. *Oil & Gas Science and Technology*, 64: 407-429.
99. **Lee, J. G., Kim, K., and Stantavicca, D. A.** (2000) Measurement of equivalence ratio fluctuation and its effect on heat release during unstable combustion. *Proceedings of the Combustion Institute*, 28: 415-421.
100. **Lee, J., Nishida, K., and Yamakawa, M.** (2002) An Analysis of Ambient Air Entrainment into Split Injection D.I. Gasoline Spray by LIF-PIV Technique. *SAE paper* 2002-01-2662.

101. **MacMillan, D., La Rocca, A., Shayler, P. J., Morris, T., Murphy, M., and Pegg, I.** (2009) Investigating the Effects of Multiple Pilot Injections on Stability at Cold Idle for a DI Diesel Engine. *SAE paper 2009-01-0612*.
102. **Matsui, Y., and Sugihara, K.** (1986) Sources of Hydrocarbon Emissions from a Small Direct Injection Diesel Engine. *JSAE Review*, 7:4-11.
103. **Matsuo, Y., Yanagisawa, A., and Yamashita, Y.** (2013) A Global Energy Outlook to 2035 with Strategic Considerations for Asia and Middle East Energy Supply and Demand Interdependencies. *Energy Strategy Reviews*, 2: 79-91.
104. **Meingast, U., Staudt, M., Reichelt, L., Renz, U., and Sommerhoff, F.A.** (2000) Analysis of Spray/Wall Interaction under Diesel Engine Conditions. *SAE paper 2000-01-0272*.
105. **Melton, L. A. and Verdieck, J. F.** (1985) Vapor/Liquid Visualization in Fuel Sprays. 20th Symposium (International) on Combustion, 1283-1290.
106. **Mendez, S., and Thirouard, B.** (2008) Using Multiple Injection Strategies in Diesel Combustion: Potential to Improve Emissions, Noise and Fuel Economy Trade-Off in Low CR Engines. *SAE paper 2008-01-1329*.
107. **Miles, P., and Hinze, P.** (1998) Characterization of the Mixing of Fresh Charge with Combustion Residuals Using Laser Raman Scattering with Broadband Detection. *SAE paper 981428*.
108. **Mohammadi, A., Kidoguchi, Y., and Miwa, K.** (2002) Effect of Injection Parameters and Wall-Impingement on Atomization and Gas Entrainment Processes in Diesel Sprays. *SAE paper 2002-01-0497*.
109. **Montgomery, D. T., Chan, M., Chang, C. T., Farrell, P. V., and Reitz, R. D.** (1996) Effect of Injector Nozzle Hole Size and Number on Spray Characteristics and the Performance of A Heavy-Duty D.I. Diesel Engine. *SAE paper 962002*.
110. **Moon, S., Gao, J., Nishida, K., Matsumoto, Y., and Zhang, Y. Y.** (2008) Ignition and Combustion Characteristics of Wall-Impinging Sprays Injected by Group-Hole Nozzles for Direct-Injection Diesel Engines. *SAE paper 2008-01-2469*.
111. **Moon, S., Matsumoto, Y., and Nishida, K.** (2009) Entrainment, Evaporation and M Characteristics of Diesel Spray Around End-of-Injection. *SAE paper 2009-01-0849*.
112. **Morawski, P., Coutinho, J.A.P., and Domanaka, U.** (2005) High Pressure (Solid + Liquid) Equilibria of n-Alkane Mixtures: Experimental Results, Correlation and Prediction. *Fluid Phase Equilibria*, 230: 72-80.

113. **Mueller, C. J., and Martin, G. C.** (2002) Effects of Oxygenated Compounds on Combustion and Soot Evolution in a DI Diesel Engine: Broadband Natural Luminosity Imaging. *SAE paper* 2002-01-1631.
114. **Musculus, M.P.B,** (2006) Multiple Simultaneous Optical Diagnostic Imaging of Early-Injection Low-Temperature Combustion in a Heavy-Duty Diesel Engine. *SAE paper* 2006-01-0079.
115. **Naber, J. D., and Siebers, D. L.,** (1996) Effects of Gas Density and Vaporization on Penetration and Dispersion of Diesel Sprays. *SAE paper* 960034.
116. **Nagao, F., and Kakimoto, H.** (1962) Swirl and Combustion in Divided Combustion Chamber Type Diesel Engines. *SAE paper* 620558.
117. **Najm, H. N., Paul, P. H., Mueller, C. J., and Wyckoff, P. S.** (1998) On the Adequacy of Certain Experimental Observables as Measurements of Flame Burning Rate. *Combustion and Flame*, 113: 312-332.
118. **Najt, P., and Foster, D.** (1983) Compression-Ignited Homogeneous Charge Combustion. *SAE paper* 830264.
119. **Noguchi, M., Tanaka, Y., Tanaka, T., and Takeuchi, Y.** (1979) A Study on Gasoline Engine Combustion by Observation of Intermediate Reactive Products during Combustion. *SAE paper* 790840.
120. **O'Connor, J., and Musculus, M.** (2013) Post Injections for Soot Reduction in Diesel Engines: A Review of Current Understanding. *SAE paper* 2013-01-0917.
121. **Oguma, M., Hyun, G., Goto, S., Konno, M., and Oyama, K.** (2002) Spectroscopic Investigation of the Combustion Process in DME Compression Ignition Engine. *SAE paper* 2002-01-1707.
122. **Onishi, S., Jo, S. H., Shoda, K., Jo, P. D., and Kato, S.** (1979) Active Thermo-Atmosphere Combustion (ATAC) - A New Combustion Process for Internal Combustion Engines. *SAE paper* 790501.
123. **Osses, M., Andrews, G. E., and Greenhough, J.** (1998) Diesel Fumigation Partial Premixing for Reduced Particulate Soot Fraction Emissions. *SAE paper* 980532.
124. **Pacaud, P., Perrin, H., and Laget, O.** (2008) Cold Start on Diesel Engine: Is Low Compression Ratio Compatible with Cold Start Requirements. *SAE paper* 2008-01-1310.
125. **Panoutsos, C.S., Hardalupas, H., and Taylor, A.M.K.P.** (2009) Numerical Evaluation of Equivalence Ratio Measurement using OH\* and CH\* Chemiluminescence in Premixed and Non-Premixed Methane-Air Flames. *Combustion and Flame*, 156: 273-291.
126. **Payri, F., Benajes, J., Pastor, J. V, and Molina, S.** (2002) Influence of the Post-Injection Pattern on Performance, Soot and NO<sub>x</sub> Emissions in a HD Diesel Engine. *SAE paper* 2002-01-0502.

127. **Payri, F., Broatch, A., Salavert, J. M., and Martin, J.** (2010) Investigation of Diesel Combustion Using Multiple Injection Strategies for Idling after Cold Start of Passenger-Car Engines. *Experimental Thermal and Fluid Science*, 34:857-865.
128. **Payri, F., Pastor, J. V., Pastor, J. M., and Juliá, J. E.** (2006) Diesel Spray Analysis by Means of Planar Laser-Induced Exciplex Fluorescence. *International Journal of Engine Research*, 7:77-89.
129. **Payri, R., Tormos, B., Salvador, F. J., and Araneo, L.** (2008) Spray Droplet and Velocity Characterization for Convergent Nozzles with Three Different Diameters. *J. Fuel*, 87:3176-3182.
130. **Peng, Z., Zhao, H., and Ladommatos, N.** (2003) Effects of Air/Fuel Ratios and EGR Rates on HCCI Combustion of n-heptane, a Diesel Type Fuel. *SAE paper 2003-01-0747*.
131. **Peter, L., Kelly-Zion., and Dec, J. E.** (2000) A Computational Study of the Effect of Fuel Type on Ignition Time in Homogenous Charge Compression Ignition Engines. *Proceeding of the Combustion Institute*, 28:1187-1194.
132. **Peterson, B. R., and Gandhi, J. B.** (2006) Transient High-Pressure Hydrogen Jet Measurements, *SAE paper 2006-01-0652*.
133. **Pickett, L. M., and López, J. J.** (2005) Jet-Wall Interaction Effects on Diesel Combustion and Soot Formation. *SAE paper 2005-01-0921*.
134. **Pickett, L.M., Kook, S., and Williams, T. C.** (2009) Visualization of Diesel Spray Penetration, Cool-Flame, Ignition, High-Temperature Combustion, and Soot Formation Using High-Speed Imaging. *SAE paper 2009-01-0658*.
135. **Pilch, M., and Erdman, C. A.** (1987) Use of Breakup Time Data and Velocity History Data to Predict the Maximum Size of Stable Fragments for Acceleration-Induced Breakup of a Liquid Drop. *Int. J. Multiphase Flow*, 13:741-757.
136. **Rabenstein, F., Egermann, J., and Leipertz, A.** (1998) Quantitative Analysis of Vapor Phase Structures in Transient Liquid Fuel Sprays. *COMODIA*, Kyoto, Japan.
137. **Rajalingam, B. V., and Farrell, P. V.** (1999) The Effect of Injection Pressure on Air Entrainment into Transient Diesel Sprays. *SAE paper 1999-01-0523*.
138. **Reid, R.C., Pravsnitz, J. M., and Sherwood, T. K.** (1985) *Properties of Gases and Fluids*, 3<sup>rd</sup> ed. McGraw-Hill, Inc., New York.
139. **Reitz, R., and Diwakar, R.** (1986) Effect of Drop Breakup on Fuel Sprays. *SAE paper 860469*.
140. **Rhim, D.R., and Farrell, P. V.** (2002) Air Flow Characteristics Surrounding Evaporating Transient Diesel Sprays. *SAE paper 2002-01-0499*.
141. **Ricaud, J. C., and Lavoisier, F.** (2004) Optimizing the Multiple Injection Settings on an HSDI Diesel Engine. *Thermo-and Fluid Dynamic Processes in Diesel Engine*, Springer, 2004, 199-234.

142. **Ricou, D. R., and Spalding, D. B.** (1961) Measurement of Entrainment by Axis-Symmetrical Turbulent Jets. *J. Fluid Mech.*, 11:21-32.
143. **Rothrock, A.M., and Waldon, C. D.** (1935) Some Effects of Injection Advanced Angle, Engine-Jacket Temperature, and Speed on Combustion in a Compression-Ignition Engine. *NACA Technical Report*, 525.
144. **Rupe, J. H.** (1953) The Liquid-Phase Mixing of a Pair of Impinging Stream. *Jet Propulsion Lab. Progress Report.20-195*, California Inst. of Technology, Pasadena.
145. **Ryan, T. W., and Callahan, T. J.** (1996) Homogeneous Charge Compression Ignition of Diesel Fuel. *SAE paper* 961160.
146. **Sawersyn, J. P., Sochet, L., Desenne, D., Crunelle-Cras, M., Grase, F., and Bridoux, M.** (1986) A Study of Spatial Distribution of Molecular Species in an Engine by Pulsed Multichannel Raman Spectroscopy. *Proc. 21<sup>st</sup> Symposium (International) on Combustion*, 491-496.
147. **Schmalzing, C. O., Stapf, P., Maly, R. R., Renner, G., Stetter, H., and Dwyer, H. A.** (1999) A Holistic Hydraulic and Spray Model- Liquid and Vapor Phase Penetration of Fuel Sprays in DI Diesel Engines. *SAE paper* 1999-01-3549.
148. **Schugger, C., and Renz, U.** (2001) Experimental Investigations on the Primary Breakup of High Pressure Diesel Sprays. *ILASS-Europe*, Zurich, Switzerland.
149. **Schugger, C., and Renz, U.** (2003) Experimental Investigation of the Primary Breakup Zone of High Pressure Diesel Sprays from Multi-Orifice Nozzles. *ICLASS*, Sorrento, Italy.
150. **Schweitzer, P. H.** (1937) Mechanism of Disintegration of Liquid Jets. *Journal of Applied Physics*, 8: 513-521.
151. **Scott, W. M.** (1969) Looking in on Diesel Combustion. *SAE paper* 690002.
152. **Senda, J., Kanda, T., Kobayashi, M., and Fujimoto, H.** (1997) Quantitative Analysis of Fuel Vapor Concentration in Diesel Spray by Exciplex Fluorescence Method. *SAE paper* 970796.
153. **Senda, J., Kobayashi, M., Iwashita, S., and Fujimoto, H.** (1994) Modeling of Diesel Spray Impingement on a Flat Wall. *SAE paper* 941894.
154. **Senda, J., Tanabe, Y., Fujimoto, H., and Fukami, Y.** (1992) Visualization of Evaporative Diesel Spray Impinging Upon Wall Surface by Exciplex Fluorescence Method. *SAE paper* 920578.
155. **Sepret, V., Bazile, R., Marchal, M., and Couteau, G.** (2010) Effect of Ambient Density and Orifice Diameter on Gas Entrainment by a Single-Hole Diesel Spray. *Exp. Fluids*, 49:1293-1305.
156. **Settles, G. S.** (2001) *Schlieren and Shadowgraph Techniques: Visualizing Phenomena in Transparent Media*. Berlin, Springer.

157. **Shimazaki, N., Tsurushima, T., and Nishimura, T.** (2003) Dual Mode Combustion Concept with Premixed Diesel Combustion by Direct Injection near Top Dead Center. *SAE paper* 2003-01-0742.
158. **Shimo, D., Kato, Y., Kim, S., Miyazaki, M., and Kanzaki, J.** (2011) Vertical Vortex Formation and Combustion Process by Diesel Sprays Impinging on a Combustion Chamber Wall. *The 22nd Internal Combustion Engine Symposium*, Tokyo, Japan.
159. **Siebers, D. L.** (1998) Liquid-Phase Fuel Penetration in Diesel Sprays. *SAE paper* 980809.
160. **Siebers, D., and Higgins, B.** (2001) Flame Lift-Off on Direct-Injection Diesel Sprays Under Quiescent Conditions. *SAE paper* 2001-01-0530.
161. **Smallwood, G. J., and Gülder, Ö. L.** (2000) Views on the Structure of Transient Diesel Sprays. *Atomization and Spray*, 10: 355-386.
162. **Song, L., and Abraham, J.** (2003) The Structure of Wall-Impinging Jets: Computed Versus Theoretical and Measured Results. *ASME J Fluids Eng*, 125: 997-1005.
163. **Soteriou, C., Andrews, R., and Smith, M** (1995) Direct Injection Diesel Sprays and the Effect of Cavitation and Hydraulic Flip on Atomization. *SAE paper* 950080.
164. **Stanglmaier, R., and Roberts, C.** (1999) Homogeneous Charge Compression Ignition (HCCI): Benefits, Compromises, and Future Engine Applications. *SAE paper* 1999-01-3682.
165. **Stojkovic, B. D., Fansler, T. D., Drake, M. C., and Sick, V.** (2005) High-speed imaging of OH\* and soot temperature and concentration in a stratified-charged direct-injection gasoline engine. *P Combust Inst*, 30: 2657-2665.
166. **Su, T. F., and Farrell, P. V.** (1998) Characterization of High Injection Pressure Diesel Sprays with Relation to Particulate and NO<sub>x</sub> Emissions. *Atomization Spray*, 8: 83-107.
167. **Su, T. F., Patterson, M. A., Reitz, R. D., and Farrell, P. V.** (1996) Experimental and Numerical Studies of High Pressure Multiple Injection Sprays. *SAE paper* 960861.
168. **Suh, H. K., Lee, Park, S. W., and Lee, C. S.** (2007) Effect of Piezo-Driven Injection System on the Macroscopic and Microscopic Atomization Characteristics of Diesel Fuel Spray. *Fuel*, 86: 2833-2845.
169. **Suzuki, M., Nishida, K., and Hiroyasu, H.** (1993) Simultaneous Concentration Measurement of Vapor and Liquid in an Evaporating Diesel Spray. *SAE paper* 930863.
170. **Svensson, K. I., Mackrory, A, J., Richards, M. J., and Tree, D. R.** (2005) Calibration of an RGB, CCD Camera and Interpretation of its Two-Color Images for KL and Temperature. *SAE paper* 2005-01-0648.

171. **Takamura, A., Ohta, T., Fukushima, S., and Kamimoto, T.** (1992) A Study on Precise Measurement of Diesel Fuel Injection Rate. *SAE paper* 920630.
172. **Takeda, Y., Keiichi, N., and Keiichi, N.** (1996) Emission Characteristics of Premixed Lean Diesel Combustion with Extremely Early Staged Fuel Injection. *SAE paper* 961163.
173. **Tamaki, N., Shimizu, M., and Hiroyasu, H.** (2001) Enhancement of the Atomization of a Liquid Jet by Cavitation in a Nozzle Hole. *Atomization Spray*, 11: 125-137.
174. **Tinaut, F. V., Reyes, M., Gimenez, B., and Pastor, J. V.** (2011) Measurements of OH\* and CH\* Chemiluminescence in Premixed Flames in a Constant Volume Combustion Bomb under Autoignition Conditions. *Energy and Fuel*, 25:119-129.
175. **Tomonaga, T., Murai, K., Takano, T., and Sami, H.** (1996) A study on combustion behavior of a diesel fuel spray impinging on a wall. *SAE paper* 960028.
176. **Tree, D. R., and Svensson, K. I.** (2007) Soot Processes in Compression Ignition Engines. *Progress in Energy and Combustion Science*, 33: 272-309.
177. **Varde, K. S., and Watanabe, T.** (2000) Characteristics of High Pressure Spray and Exhaust Emissions in A Single Cylinder DI Diesel Engine. *SAE paper* 2000-05-0333.
178. **Velji, A., Günthner, M., and Spicher, U.** (2003) Direkteinspritzung im Ottomotor mit Fremd- und Kompressionszündung- Brennvverfahren der Zukunft? In *Direkteinspritzung im Otto-motor IV*, herausgegeben von U. Spicher, Expert Verlag.
179. **Wakuri, Y., Fujii, M., Amitani, T. and Tsuneya, R.** (1960) Studies of the Penetration of a Fuel Spray in a Diesel Engine. *JSME* 3(9): 123-130.
180. **Wakuri, Y., Fujii, M., Amitani, T., and Tsuneya, R.** (1959) Studies on the Penetration of Fuel Spray of Diesel Engine. *Trans. JSME* 25: 820-826.
181. **Wang, X. G., Huang, Z. H., Zhang, W., Kutti, O. A., and Nishida, K.** (2011) Effects of Ultra-High Injection Pressure and Micro-Hole Nozzle on Flame Structure and Soot Formation of Impinging Diesel Spray. *Applied Energy*, 88: 1620-1628.
182. **Whitelaw, J. H., and Payri, F.** (2000) *Thermo-and Fluid-dynamic Processes in Diesel Engines*. Verlag Berlin Heidelberg New York, Springer.
183. **Wu, P. K., and Faeth, G. M.** (1995) Onset and End of Drop Formation along the Surface of Turbulent Liquid Jets in Still Gases. *Phy. of Fluids*, 7 (11): 2915-2917.
184. **Wu, Z., Zhu, Z., and Huang, Z.** (2006) An Experimental Study on the Spray Structure of Oxygenated Fuel using Laser-Based Visualization and Particle Image Velocimetry. *Fuel*, 85: 1458-1464.
185. **Xiong, T. Y., and Yuen, M. C.** (1991) Evaporation of a liquid droplet on a hot plate. *Int J. Heat*

*Mass Tran*, 34 (7):1881-1894.

186. **Yanagihara, H.** (2001) Ignition Timing Control at Toyota "UNIBUS" Combustion System. Proceedings of the IFP International Congress, 35-42.
187. **Yeh, C., Kamimoto, T., Kosaka, H., and Kobori, S.** (1994) Quantitative Measurement of 2-D Fuel Vapor Concentration in a Transient Spray via Laser-Induced Fluorescence Technique. *SAE paper* 941953.
188. **Yokota, H., Kamimoto, T., Kosaka, H., and Tsujimura, K.** (1991) Fast Burning and Reduced Soot Formation via Ultra-High Pressure Diesel Fuel Injection. *SAE paper* 910225.
189. **Yokota, H., Kudo, Y., Nakajima, H., Kakegawa, T., and Suzuki, T.** (1997) A New Concept for Low Emission Diesel Combustion. *SAE paper* 970891.
190. **Yokota, H., Nakajima, H., and Kakegawa, T.** (1998) A New Concept for Low-Emission Diesel Combustion (2nd Report: Reduction of HC and CO Emission, and Improvement of Fuel Consumption by EGR and MTBE Blended Fuel). *SAE Paper* 981933.
191. **Yun, H., and Reitz, R. D.** (2007) An Experimental Investigation on the Effect of Post-Injection Strategies on Combustion and Emissions in the Low-Temperature Diesel Combustion Regime. *J. Eng. Gas Turb. Power*, 129:279-286.
192. **Zeldovich, Y. B.,** (1946) The Oxidation of Nitrogen in Combustion and Explosions. *Acta Physicochim.* 21:577.
193. **Zhang, Y. Y.,** (2001) A Study on Mixture Formation in Diesel Sprays with Split Injection Strategy. *Dissertation*, University of Hiroshima.
194. **Zhang, Y. Y., and Nishida, K.** (2004) Imaging of Vapor/Liquid Distributions of Split-Injected Diesel Sprays in a Two-Dimensional Model Combustion Chamber. *Combustion Science and Technology*, 176, 1465- 1491.
195. **Zhao, H., and Ladammatos, N.** (2001) *Engine Combustion Instrumentation and Diagnostics*. Warrendale, SAE.
196. **Zhao, H., and Ladommatos, N.** (1998) Optical Diagnostics for Soot and Temperature Measurement in Diesel Engines. *Prog. Energy Combust. Sci*, 24: 221-255.

## ACKNOWLEDGEMENTS

This thesis was accomplished at the Fluid Engineering Laboratory, Faculty of Engineering, University of Hiroshima. I would like to express my gratitude to all those who helped me during the working of this dissertation.

My deepest gratitude goes first and foremost to Professor. Keiya Nishida, my academic advisor, for his constant encouragement, earnest guidance, constructive criticism and invaluable discussions throughout the three years.

Gratefulness is also given to Prof. Yoichi Ogata and Prof. Baolu Shi, for their extremely valuable comments and helpful suggestions in directing me to fulfill this thesis. Also, my sincere appreciation goes to the thesis committee members: Professors Satoru Ishizuka and Takuma Endo.

Thanks are also given to Dr. Shimo (Mazda Co), Mr. Naber (Mazda Co), Mr. Ido (Komatsu Co), Mr. Dong, Mr. Matsuo, Mr. Tomoda and Mr. Itamochi, for their assistance in the experiment.

Thanks are also given to Prof. Wuqiang Long (Dalian University of Technology) for his moral support and encouragement during this 3-year research and in the previous studies.

I would like to appreciate the Ministry of Education, Japan (Monbukagakusho), for sponsoring my studies by providing scholarship and tuitions fees.

Last but not least, my deepest gratitude goes to my family, especially to my wife, Bingbing Liu, for her consistent love, encouragement, and support.